Olivine in the Polaris Alaskan-type Intrusion of North-central British Columbia: Implications for the Magmatic Evolution of Primitive Arc Magmas and for Convergent Margin Ni-Cu-PGE Ore-forming Systems

By

Dylan Wilson Spence

A THESIS SUBMITTED IN PARTIAL FULFILLMENT OF

THE REQUIREMENTS FOR THE DEGREE OF

BACHELOR OF SCIENCE

in

THE FACULTY OF SCIENCE

(Geological Sciences)

This thesis conforms to the required standard

……

Supervisor

THE UNIVERSITY OF BRITISH COLUMBIA

(Vancouver)

April 2020

Abstract

The Jurassic Polaris Alaskan-type ultramafic-mafic intrusion is a 14 km by 3 km sill-like intrusion hosted by sedimentary and volcanic rocks of the Lay Range Assemblage in the Quesnel terrane of north-central British Columbia. Olivine, the dominant mineral in the intrusion, displays a wide range of textures and compositions that reflect different environments of crystallization. Olivine compositions (n = 326) determined by electronprobe microanalysis (EPMA) span a range of forsterite contents (Fo_{94-79}), with the most Mg-rich olivine present in chromitite, due to subsolidus exchange with chromite, and most Mg-poor olivine present in olivine clinopyroxenite. Nickel concentrations in olivine vary significantly from 3108 ppm Ni at Fo_{89} to 275 ppm Ni at Fo_{81}. The lack of systematic Fo-Ni-Mn zonation from core-to-rim in Polaris olivine is indicative of pervasive diffusion and re-equilibration at high temperatures. The Mg-rich compositions of olivine in dunite, olivine wehrlite, and werhlite ($Fo_{87.5-92}$) are evidence for the involvement of primitive, mantle wedge-derived parent magmas that experienced little fractionation prior to emplacement in the crust. The Fo-Ni relationships of olivine are consistent with a fractional crystallization control from dunite-olivine werhlite-wehrlite ($Fo_{87.5-92}$, 1605-3108 ppm Ni) through magnetite-rich olivine clinopyroxenite (Fo_{79-84}, 275-550 ppm Ni), whereas Ni-rich olivine in magnetite-poor olivine clinopyroxene ($Fo_{81.5-84}$, 1305-2090 ppm Ni) is accounted for by mixing between fractionated and primitive magmas. Outcrop-scale field relationships (i.e., chaotic mixing, ultramafic dikes, chromitite schlieren) in the Polaris intrusion support the operation of periodic recharge and mixing processes. Polaris olivine is distinguished by extremely low Ca concentrations (<1000 ppm, and mostly <500 ppm) compared to olivine from volcanic rocks globally, including those from subduction zone environments. Low-Ca olivine is also typical of ultramafic-mafic plutonic rocks in general (e.g., Skaergaard, Kiglapait, Bushveld, Duke Island) and may be related to pervasive diffusional loss of Ca from olivine to interstitial melt. The shallow emplacement depth of the Polaris intrusion (~12 km) requires that ascent of primitive, unfractionated magmas was relatively rapid from the mantle wedge source to maintain the observed Mg-rich olivine compositions. The Polaris intrusion shares common petrogenetic characteristics with mafic-ultramafic ore-forming conduit systems in other settings, highlighting the similarities between extensional and convergent margin Ni-Cu-PGE ore-forming systems.

Table of Contents

List of Figures

List of Tables

List of Abbreviations

Am – amphibole
Ap – apatite
Bn – bornite
BSE – backscatter electron
Carb – carbonate
Cal – calcite
Ccp – chalcopyrite
Chl – chlorite
Chr – chromite
Cpx – clinopyroxene
Cv – covellite
EDS – energy-dispersive spectrometry
EPMA – electronprobe microanalysis
Fa – fayalite content, 100 - Fo
Fo – forsterite content, [$Mg/(Mg+Fe^{2+}) \times 100$]
Hbl – hornblende
Idd – iddingsite
Ilm – ilmenite
Mt – magnetite
Ol – olivine
Opx – orthopyroxene
PGE – platinum group element
PGM – platinum group mineral
Phl – phlogopite
Pn – pentlandite
Po – pyrrhotite
PPL – plane-polarized light
RL – reflected light
SEM – scanning electron microscope
Sp – sphalerite
Srp – serpentine
XPL – cross-polarized light

Acknowledgements

This thesis was only made possible with the guidance, knowledge, patience, and feedback provided by my supervisor Dr. James S. Scoates (UBC). His constant interest and enthusiasm on this thesis fueled my own, and for that, I am very thankful. Many thanks also to Dr. Lori Kennedy (UBC) for discussion about olivine deformation, diking mechanisms, and magmatic fabrics.

The training, mentorship, and knowledge provided by Dr. Dejan Milidragovic (BCGS) in both the field and for the duration of the project is greatly appreciated and is largely the reason I became inspired to pursue research on this topic in the first place. Dr. Graham Nixon (BCGS) is thanked for help with field work conducted in 1988, 2018, and 2019, and for his constant enthusiasm and input on this thesis. I further acknowledge Luke Ootes (BCGS) and the rest of "Team Hogem" for assistance and discussion while in the field. Thanks also to James Nott (UBC) for frequent discussions about the 2019 mapping results of the Polaris intrusion, field relationships, and interpretations, and to his field assistant Abigail Fraser (UBC) for further discourse about the Polaris intrusion. I have the utmost gratitude to SilverKing Helicopters in Smithers, B.C., for comfortable and safe flying provided by their expert team of pilots while in the field.

Jenny Lai and Lan Kato (UBC) are thanked for SEM instruction and Edith Czech (UBC) is thanked for help with operation of EPMA at the Electron Microbeam & X-Ray Diffraction Facility at UBC. I owe many thanks to my undergraduate thesis group and close friends, Eric Vandenburg, Connor Lyons, and Lars Gibbard, for making light of the various stresses of writing a thesis and their compassion in doing so. To my many other friends, I am fortunate enough in having: thank you for making my time at UBC an irreplaceable adventure. To my parents and my sister: thank you for always supporting me through all of my endeavors and instilling me with the confidence to follow them through. Funding for this project was provided by a SEG Canada Foundation scholarship to Dylan Spence, a UBC EOAS Fund for Research awarded to Dylan Spence, and a NSERC Discovery Grant to James Scoates.

1. Introduction

Alaskan-type intrusions, elsewhere referred to as ultramafic-mafic zoned or Ural-Alaskan complexes, are small, convergent margin-hosted ultramafic-mafic intrusions. Alaskan-type intrusions occur in two broad lineaments in North America: the Duke-Klukwan belt, which most notably includes the Duke Island Alaskan-type intrusion, and a parallel belt in the Mesozoic Quesnel terrane of British Columbia containing the Tulameen, Turnagain, and Polaris Alaskan-type intrusions, among others (Fig. 1.1) (Nixon *et al*., 1997). Alaskan-type intrusions have typically been described as concentrically zoned ultramafic to mafic intrusions ranging from peridotite cores to gabbroic rims and they are defined by the absence of orthopyroxene (Fig. 1.2) (Nixon *et al*., 1997; Nixon *et al*., 2015). The characteristic lithologies of Alaskan-type intrusions are dunite, chromitite, wehrlite, olivine clinopyroxenite, clinopyroxenite, hornblende clinopyroxenite, hornblendite, and gabbro to diorite. Alaskan-type intrusions are interpreted to form in magma conduits or magma storage chambers in magmatic arc systems (Findlay, 1969; Murray, 1972; Irvine, 1974b; Nixon *et al*., 1990; Himmelberg and Loney, 1995).

The general association of Ni-Cu-PGE mineralization with ultramafic-mafic bodies hosted in intraplate tectonic settings exists because the world's largest deposits and most active Ni-Cu-PGE producers are found in these settings (Naldrett and Cabri, 1976; Naldrett, 2004; Naldrett, 2010; Nixon *et al*., 2015). The presence of Ni-Cu-PGE mineralization in convergent margin ultramafic-mafic deposits is not unprecedented, however. In British Columbia, there are two notable styles of Ni-Cu-PGE mineralization: orthopyroxene-rich Giant Mascot-type (ultramafic-mafic volcanic plug) and orthopyroxene-absent Alaskan-type (Naldrett, 2011; Nixon *et al*., 2015). The Giant Mascot Ni-Cu-PGE deposit located in the Southern Canadian Cordillera of British Columbia has ~4.2 Mt of ore grading 0.77% Ni and 0.34% Cu and is British

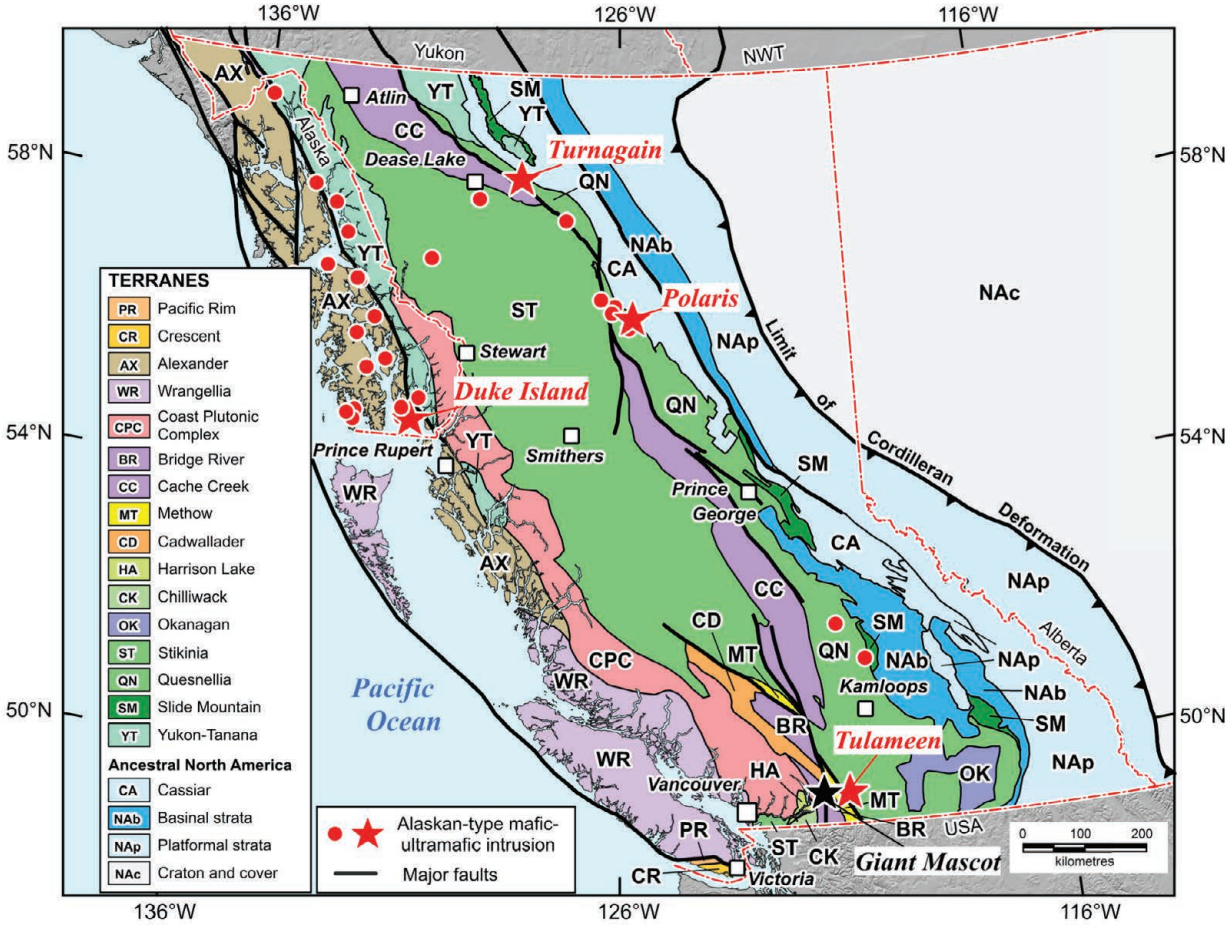

Figure 1.1. Locations of Alaskan-type mafic-ultramafic intrusions including the Polaris intrusion with respect to the terranes of the Canadian Cordillera. Modified from Nelson et al. (2013) and Nixon et al. (2019).

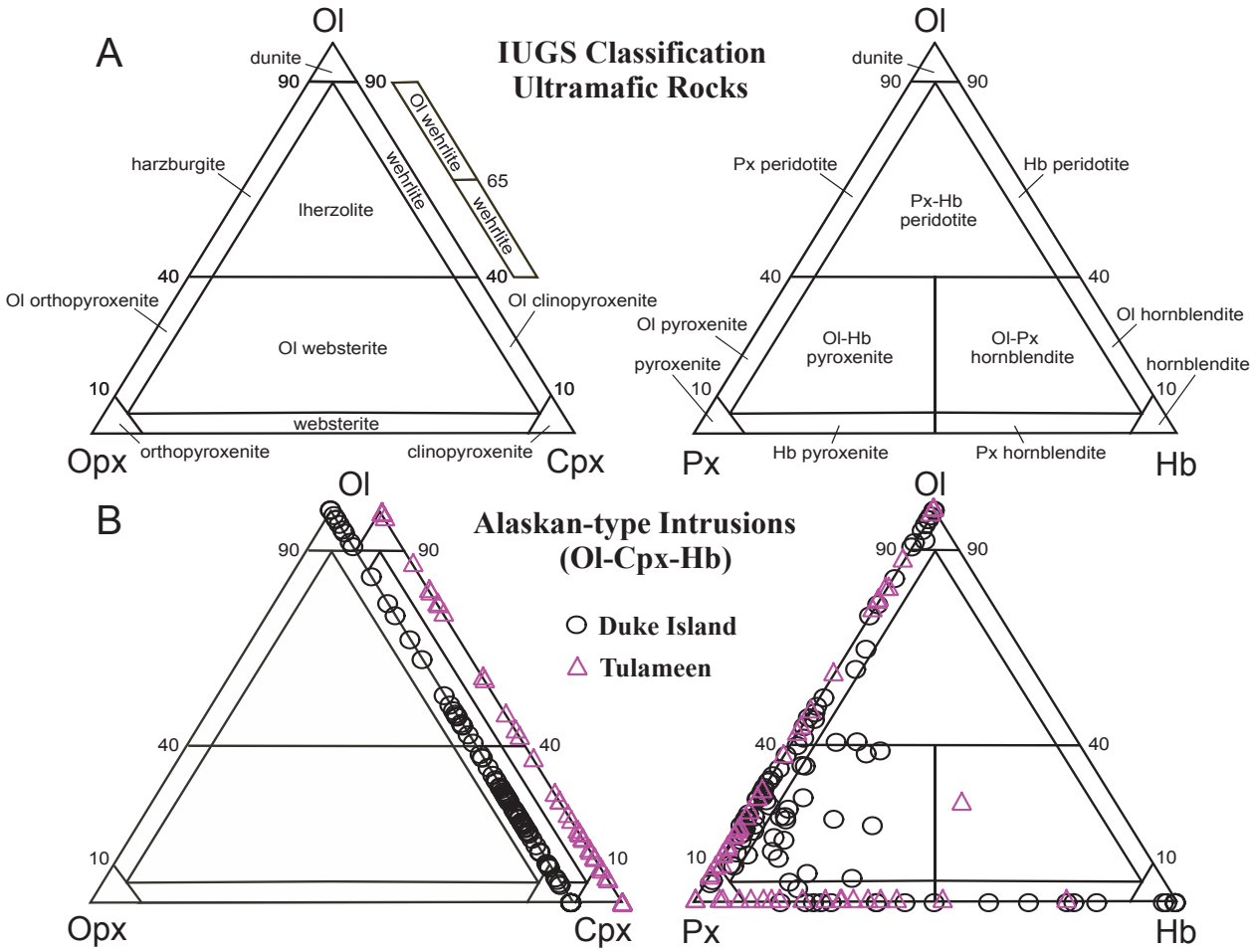

Figure 1.2. Classification plots for ultramafic rocks. A) IUGS ternary classification of ultramafic rocks (Le Maitre, 1989). B) Modal analyses for typical ultramafic rocks in the Duke Island (Irvine, 1959, 1974b) and Tulameen (Findlay, 1963) Alaskan-type intrusions demonstrating their characteristic lack of orthopyroxene. Adapted from Nixon et al. (2015).

Columbia's only past-producing nickel mine (1958-1974) (Manor *et al*., 2016; Nixon *et al*., 2015). The Turnagain Alaskan-type intrusion has ~1842 Mt of ore with an average grade of 0.21 wt% Ni and 0.013 wt% Co making it one of the world's largest deposits of contained Ni metal (Scheel, 2007; Scheel *et al.,* 2009; Mudd and Jowitt, 2014; Nixon *et al*., 2015; Jackson-Brown, 2017; Nixon *et al*., 2019). The Polaris Alaskan-type intrusion is not considered sulfide-rich and has an average Ni grade of 0.25 wt% (Nixon *et al*., 1990; Nixon *et al*., 2015). Nevertheless, information about conduit systems in arc-settings determined by the Polaris intrusion may be useful in aiding in the development of convergent margin Ni-Cu-PGE mineralization models.

Olivine (nesosilicate, $(Mg,Fe)_2SiO_4$) is generally the first silicate to precipitate out of basaltic and ultramafic magmas (e.g., Bowen 1928) and crystallizes from primitive, hydrous arc magmas to form cumulate piles (Nandedkar *et al*., 2014). The early crystallization and simple chemical structure of olivine make it an important tool for determining magmatic histories. The major element composition of olivine, described as the forsterite content ($Fo_{olivine}$ = $[Mg/(Mg+Fe^{2+}) \times 100]$), can illustrate how primitive or evolved olivine compositions are from equilibrium with their initial melt. The partitioning of Mg-Fe into olivine between liquid and olivine (K_D^{Fe-Mg}) is mainly dependent on the composition of the melt from which olivine crystallized from and is constant over a large range of temperatures (e.g., Roeder and Emslie, 1970; Langmuir and Hanson, 1981; Ulmer, 1989; Putirka, 2005). Hence, the ratio of Mg to Fe in olivine preserves compositional information about the melt from which it is derived (Straub *et al*., 2008).

The Ni content of olivine in association with forsterite content can be used as a powerful tracer for fractional crystallization and magma-mixing trends in ultramafic-mafic cumulus systems because the olivine partition coefficient of Ni (Kd^{Ni}) is a function of the Mg content of

the melt (e.g., Hart and Davis, 1978; Kinzler *et al*., 1990; Beattie *et al*., 1991; Straub *et al*., 2008; Matzen *et al*., 2017). In a closed system, it can be expected that Ni will decrease with the forsterite content of olivine predictably. However, if Ni concentrations are above or below levels expected by fractional crystallization trends, there must be some other process controlling these compositions. One way to increase Ni concentrations in olivine is by magma mixing or recharge with Ni-rich and Mg-rich magmas (Straub *et al*., 2008; Herzberg *et al*., 2013; Herzberg *et al*., 2016; Gordeychik *et al*., 2018). Ni concentrations in olivine can be lower than expected as a result of depletion due to sulfide saturation (Li *et al.,* 2007; Scheel, 2007; Thakurta *et al*., 2008; Li *et al*., 2013; Manor *et al*., 2016).

The Ca concentration in olivine is highly dependent on the composition of the melt from which it is derived including the Ca content of the melt, the H_2O content, and the relative activity of iron (i.e., fayalite content of olivine) in the melt (e.g., Stormer, 1973; Watson, 1979; Jurewicz and Watson, 1988; Libourel, 1999; Feig *et al*., 2006; Kamenetsky *et al*., 2006). This relationship remains true over wide range of pressures, temperatures, and oxygen fugacity (Jurewicz and Watson, 1988; Libourel, 1999). On average, plutonic olivine has lower olivine concentrations than their volcanic counterparts (Simkin and Smith, 1970). This low-Ca trend has been described in various plutonic cumulate rocks globally including multiple Alaskan-type intrusions (i.e., Duke Island, Ural Mountains) (e.g., Krause *et al*., 2007; Li *et al*., 2012; Yao *et al*., 2017). Ca-depletion of arc-derived magmatic olivine has been historically linked to the high H_2O contents of arc magmas (Feig *et al*., 2006; Gavrilenko *et al*., 2016) or a low-Ca and high-Si magmas (Kamenetsky *et al*., 2006). These explanations, however, do not explain the Ca-depletion of plutonic olivine relative to volcanic olivine.

Olivine is the predominant mineral in Alaskan-type intrusions (Himmelberg and Loney, 1995; Nixon *et al*., 1997). Although past studies have been conducted on olivine chemistry in Alaskan-type intrusions (e.g., Findlay, 1969; Clark, 1980; Batanova *et al*., 2005; Krause *et al*., 2007; Thakurta *et al*., 2008; Su *et al*., 2012; Li *et al*., 2013), olivine compositions for Alaskan-type intrusions are underrepresented in the global database of ultramafic-mafic rocks. For this reason, electronprobe microanalysis (EPMA) of olivine in the Polaris Alaskan-type intrusion was employed to determine high-precision major and minor olivine compositions for the various olivine-bearing lithologies. The aim of this thesis is to 1) add to the global database for olivine in Alaskan-type intrusions, 2) discern fractional crystallization, recharge trends, and other magma chamber processes, and 3) utilize the powerful petrological archive provided by the chemical composition of olivine as a window into magma conduits in arc settings.

2. Geological Background

2.1. Previous work

The Polaris Alaskan-type intrusion was initially mapped by Armstrong (1946) while mapping the Aiken Lake area. Armstrong and Roots (1948) and Roots (1954) produced the first detailed descriptions of the ultramafic-mafic assemblages of the Polaris intrusion. Irving (1974a) and Foster (1974) provided more complete rock descriptions of the Polaris intrusion and Nixon *et al*. (1997) published detailed geological maps and platinum group element (PGE) analyses. A regional 1:50,000 scale map of the area was produced by Ferri *et al*. (2001). The most recent mapping of the intrusion was conducted by Nott *et al*. (2020) (Fig. 2.1).

The age of the Polaris intrusion is not well-established. Wanless *et al*. (1968) published K-Ar dates of 167 ± 9 Ma for biotite and 156 ± 15 Ma for hornblende in peridotite. This Jurassic age has been considered too young, however, considering the likely association of the Polaris intrusion with the older (Late Triassic to Early Jurassic) volcanic packages of Stikinia and Quesnellia, and these dates are considered to represent cooling ages or the timing of metamorphic overprint (Nixon *et al*., 1997). A multigrain U-Pb TIMS zircon date for a pegmatitic quartz-hornblende-plagioclase-rich pod found in hornblendite yielded a date of 186 ± 2 Ma and was interpreted as the age of crystallization of the Polaris intrusion (Nixon *et al*.,1997). This sample was later reprocessed for single-grain analysis using the chemical abrasion or CA-TIMS technique resulting in a higher precision date of 186.26 ± 0.14 Ma (Nixon *et al*., 2019).

2.2. Regional geology

The Polaris Alaskan-type ultramafic-mafic intrusion is located in the Lay Range of the Omineca Mountains of British Columbia, approximately 200 km northeast of Smithers (56˚30’

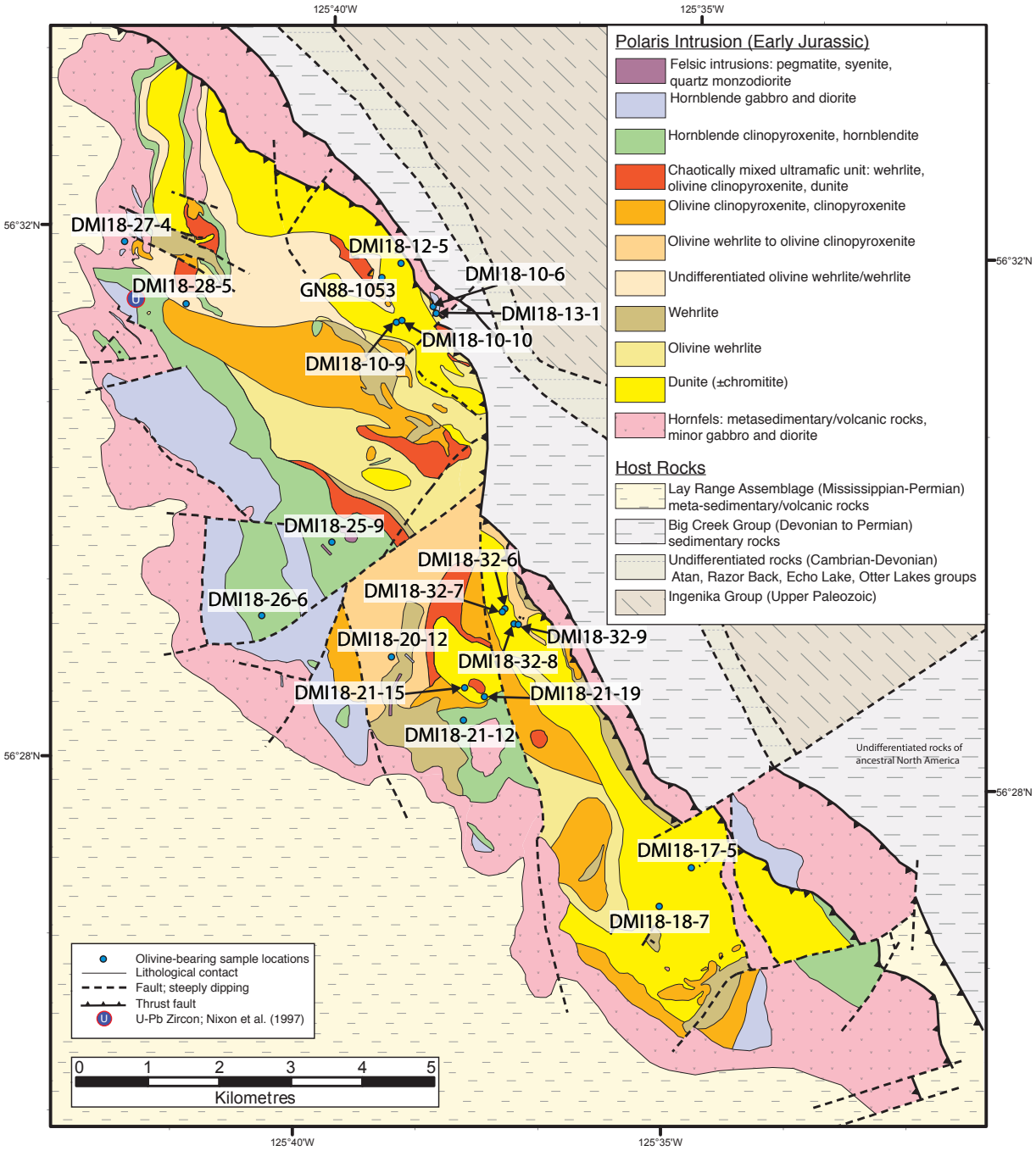

Figure 2.1. Geological map and olivine-bearing sample locations of the Polaris Alaskan-type ultramafic-mafic intrusion (from Nixon et al., 1997; revised and modified by Nott et al., 2020) illustrating host lithologies, contact relationships, and intrusive rock types. Note the distribution of dunite and olivine wehrlite primarily on the eastern and central parts of the Polaris intrusion.

N, 125˚40’W). The host rocks of the Polaris intrusion are the Mississippian to Permian sedimentary, volcaniclastic, and volcanic rocks of the Quesnellia Lay Range Assemblage (Ferri, 1997). These rocks were formed in an arc-terrane setting outboard of the continental margin of ancestral North America, separated by the back-arc Slide Mountain ocean (Nelson and Colpron, 2007). Westerly subduction of the Slide Mountain terrane in the Permian resulted in the subsequent closure of the Slide Mountain ocean, which concluded in the Late Triassic through Early Jurassic. No fragments of the Slide Mountain terrane are present at the latitude of the Polaris intrusion (Ferri, 1997).

2.3. Geology of the Polaris intrusion

The Polaris intrusion is an elongate sill-like body approximately 14 km long and 4 km wide at its widest point (Nixon *et al*., 1997). It consists of non-stratified ultramafic rocks ranging from dunite to wehrlite concentrated on the eastern margin of the intrusion and hornblende-bearing gabbro, diorite, and clinopyroxenite concentrated on the western margin of the intrusion (Fig. 2.2).

On the eastern edge of the intrusion dunite predominates and displays smooth yellow-brown weathering with dark green-grey fresh surfaces. Irregular and remobilized schlieren of chromitite are found predominantly hosted within and interlayered within dunite (Fig. 2.3 A). More rarely, chromitite schlieren are found in olivine wehrlite and wehrlite. The nature of contacts between dunite and other lithologies is quite variable (Nixon *et al*., 1997; Nott *et al*., 2020). Dunite often exhibits gradational contacts with orange-brown weathering and rough-surfaced olivine wehrlite and wehrlite and may exhibit sharp contacts with grey-green weathering olivine clinopyroxenite when present in local chaotically intermingling zones (Fig.

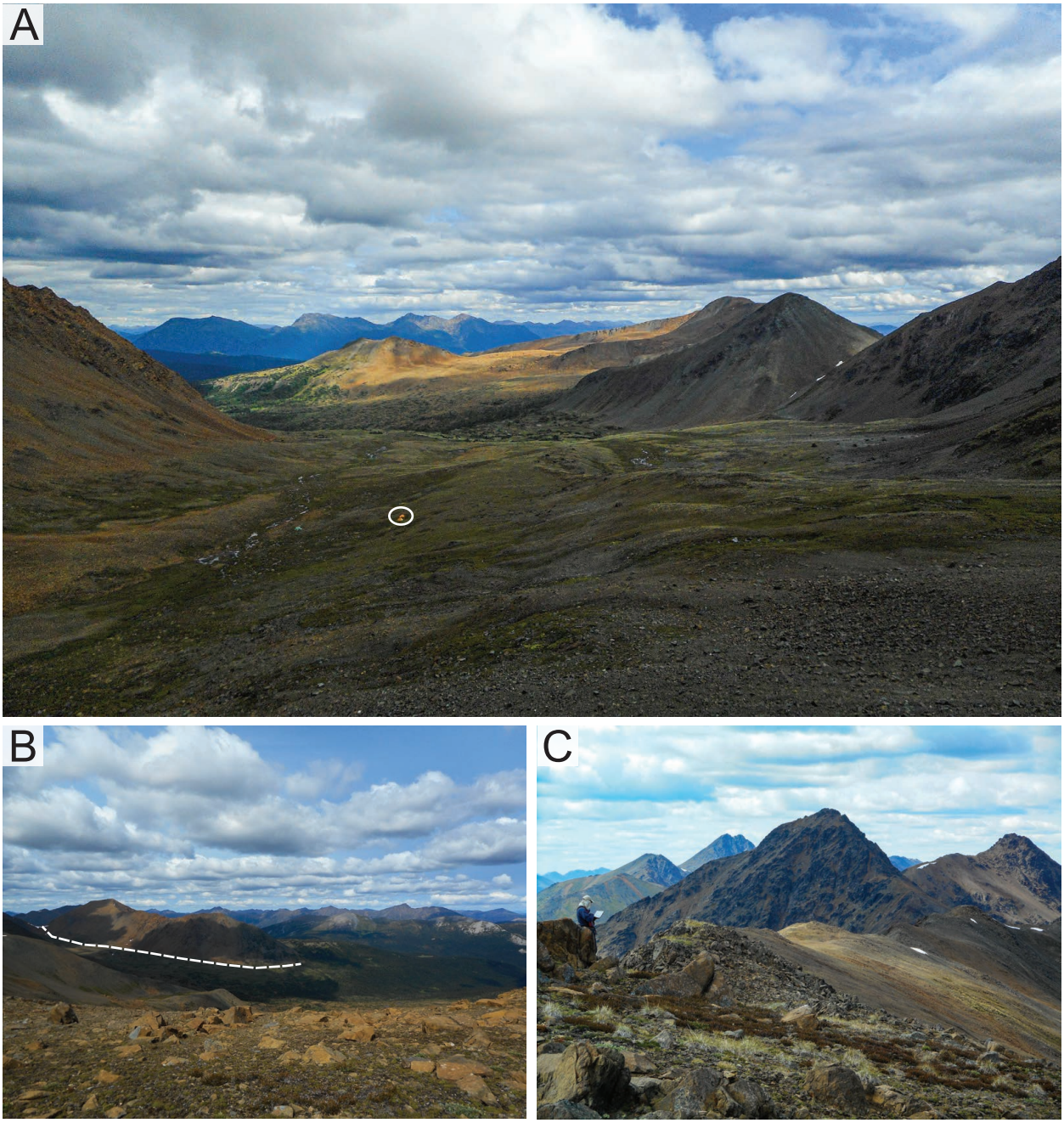

Figure 2.2. Photographs showing representative views of the Polaris Alaskan-type intrusion. A) Looking southeast towards the southern dunite "core" of the Polaris intrusion. Two tents cirled for scale. B) Looking northeast across the intrusion towards the central dunite "core" of the Polaris intrusion. Dashed line is approximately 1.9 km. C) Looking northwest from the southern part of the intrusion towards a hornblende clinopyroxenite unit. Person for scale. All photographs taken in summer 2018.

2.3 B-C). Ultramafic dikes with sharp tabular to irregular contacts ranging from dunite to olivine clinopyroxenite are also present throughout the eastern and central parts of the intrusion and are often only visible due to different weathering colors caused by slight compositional variations, or where chromitite schlieren or other lithologies are cross-cut by these dikes (Fig. 2.3 D-F) (Nixon *et al*., 1997; Nott *et al*., 2020).

Olivine wehrlite, wehrlite, olivine clinopyroxenite, and clinopyroxenite are distributed extensively in central areas of the Polaris intrusion. These units often show meter-scale gradational boundaries between them, but contacts may be sharp to diffuse (Nixon *et al*. 1997; Nott *et al*., 2020). Chaotically mixed ultramafic cumulates are also common in the central Polaris intrusion and often show sharp to diffuse contacts between dunite, olivine wehrlite, and olivine clinopyroxenite (Nixon *et al*. 1997; Nott *et al*., 2020). The large variation between lithological contact styles, chaotically intermingled cumulate ultramafics, sheared and folded chromitite schlieren, and ultramafic dikes are evidence for emplacement consisting of multi-stage intrusion and magma mingling at different thermal and rheological conditions (Nott *et al*., 2020).

Hornblendite and hornblende clinopyroxenite are found in the northwest part of the Polaris intrusion and weather dark greenish-black. The two units show decimeter scale gradation and are indistinguishable on a map scale (Nott *et al*., 2020). Hornblende crystals occasionally exhibit mineral elongation lineations and magmatic layering is present in some locations, defined by varying grain size, grain orientation, and interstitial feldspar fabrics (Nott *et al*., 2020). Hornblende gabbro-diorite is present on the margins of the intrusion and is most common on the western margin. The Polaris intrusion also hosts felsic dikes that cross-cut major lithologies and are most prevalent in the central part of the intrusion.

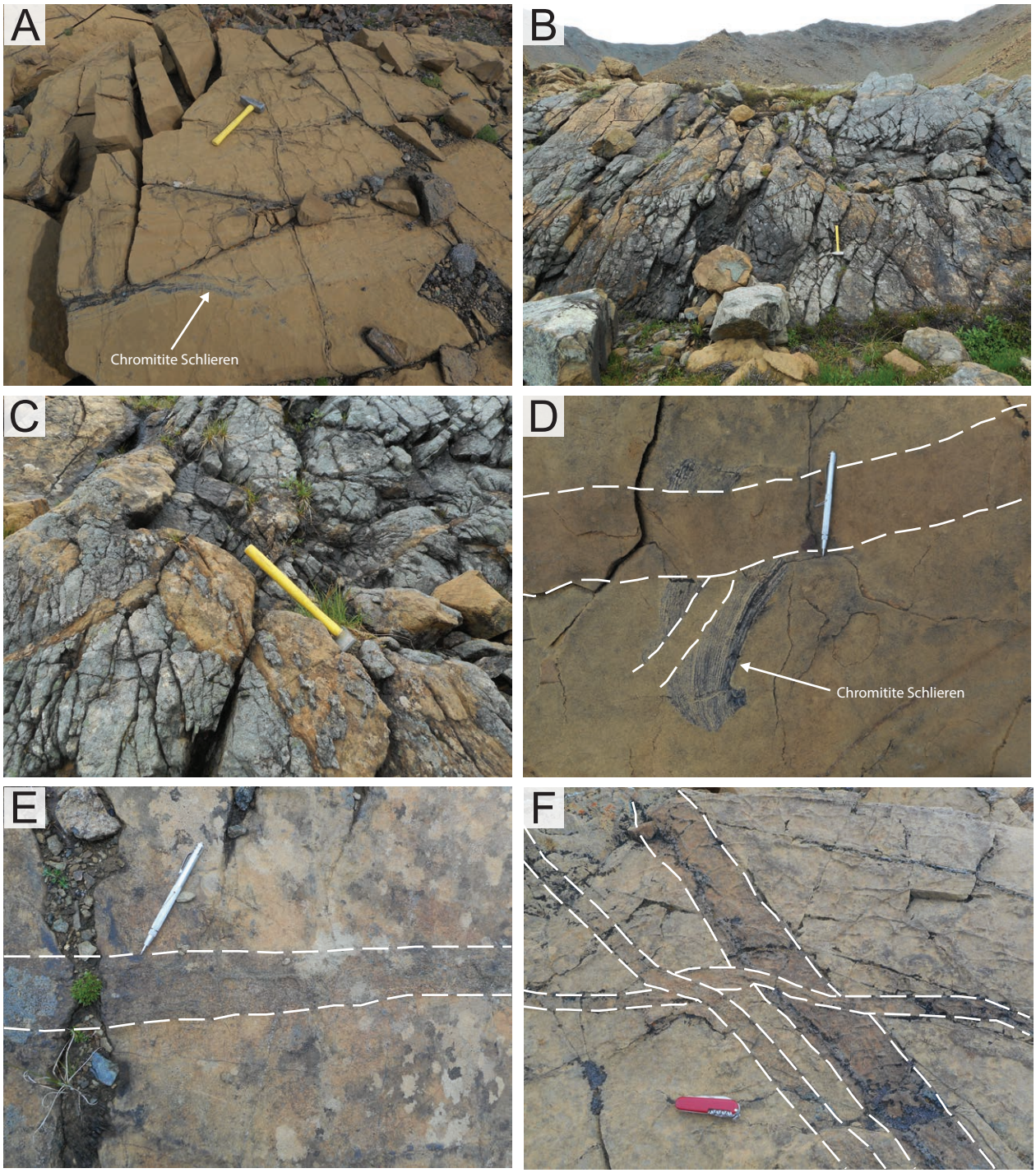

Figure 2.3. Photographs depicting intrusive relationships between olivine-bearing rocks of the Polaris intrusion. A) Outcrop of dunite with sheared chromitite schlieren. B) Chaotically intermingled ultramafic unit consisting of olivine clinopyroxenite (grey-green) and dunite (yellow-brown). C) Same outcrop as B) with close-up view of intrusive relationship between olivine clinopyroxenite and dunite. D) Dunite with chromitite schlieren that has been cross-cut by two different phases of ultramafic dikes (delineated by dashed white lines); the earliest dike is only visible where it cross-cuts the chromitite schlieren. E) Dunite cross-cut by tabular wehrlite dike (delineated by dashed white lines). F) Dunite cross-cut by three different olivine wehrlite dikes (delineated by dashed white lines). Hammer is approximately 45 cm in length. Swing-magnet is 13 cm in length. Swiss-army knife is 8.5 cm in length.

The rocks immediately bounding the Polaris intrusion are southwest dipping (40-50˚) argillites, siltstones, sandstones, carbonates, volcaniclastic, and volcanic rocks of the Lay Range Assemblage that have been hornfelsed by the intrusion's metamorphic contact aureole (Roots, 1954; Nixon *et al*., 1997). On the eastern margin, the Polaris intrusion has been thrust onto Devonian to Permian rocks of the Big Creek group, which have locally been hornfelsed. Nixon *et al*. (1997) placed a maximum emplacement depth of 12 km (3-4 kb) to the Polaris intrusion due to the presence of andalusite in various rocks of the contact aureole.

3. Samples and Analytical Techniques

3.1. Samples

Representative rock samples from the Polaris intrusion were collected by the British Columbia Geological Survey (BCGS) during its 1988 summer mapping program of the intrusion. Further samples were collected by the BCGS during the 2018 and 2019 summer mapping programs of the intrusion. Of these, twenty-three representative olivine-bearing samples (Table 1) were collected to determine the mineralogical and textural diversity of the olivine-bearing rocks of the Polaris intrusion and to complete a high-precision study on the olivine-chemistry of these representative samples. The twenty-three collected samples include four dunites (DMI18-10-10, DMI18-17-5, DMI18-21-15, DMI18-32-8), four dunites containing chromitite schlieren (DMI18-10-9, DMI18-18-7, DMI18-32-6, DMI18-32-7A), two olivine wehrlites (DMI18-10-6B, DMI18-21-19), one chromitite schlieren-bearing olivine werhlite (GN88-1053), four wehrlites (DMI18-12-5A, DMI18-13-1, DMI18-21-12, DMI18-27-4), and four olivine clinopyroxenites (DMI18-20-12, DMI18-25-9, DMI18-26-6, DMI18-28-5). Additionally, four samples consisting of a host-lithology cross-cut by an ultramafic dike were collected to investigate the mechanism of diking. These samples include dunite containing a chromitite schlieren cross-cut by a dunite dike (DMI18-32-7C), dunite cross-cut by a dunite dike (DMI18-32-9A), dunite cross-cut by an olivine wehrlite dike (DMI18-32-9B), and dunite cross-cut by a wehrlite dike (DMI18-32-9C).

3.2. Petrographic Analysis

All twenty-three samples were sent to Vancouver Petrographics, Ltd. to obtain polished thin sections for petrographic analysis. A Nikon Eclipse E600 POL polarizing petrographic microscope was used for the petrographic analysis of the olivine-bearing rocks of the Polaris

Table 1. List of olivine-bearing samples from the Polaris Alaskan-type intrusion

Sample #	Lithology	Year Collected	Easting	Northing	Electronprobe Microanalysis[1]
DMI18-10-6B	olivine wehrlite	2018	337499	6267626	N
DMI18-10-9	dunite, chromitite	2018	336988	6267406	Y
DMI18-10-10	dunite	2018	337063	6267432	N
DMI18-12-5A	wehrlite	2018	337051	6268230	Y
DMI18-13-1	wehrlite	2018	337541	6267532	Y
DMI18-17-5	dunite	2018	341110	6259778	Y
DMI18-18-7	dunite, chromitite	2018	340659	6259242	N
DMI18-20-12	olivine clinopyroxenite	2018	336917	6262726	Y
DMI18-21-12	phlogopite-rich wehrlite	2018	337921	6261843	Y
DMI18-21-15	dunite	2018	337940	6262297	N
DMI18-21-19	hornblende-olivine wehrlite	2018	338216	6262169	Y
DMI18-25-9	magnetite-olivine clinopyroxenite	2018	336083	6264333	Y
DMI18-26-6	magnetite-olivine clinopyroxenite	2018	335104	6263306	Y
DMI18-27-4	wehrlite	2018	333189	6268539	N
DMI18-28-5	olivine clinopyroxenite	2018	334047	6267666	Y
DMI18-32-6	dunite, chromitite	2018	338500	6263402	Y
DMI18-32-7A	dunite, chromitite	2018	338466	6263356	N
DMI18-32-7C	dunite, chromitite, dunite dike	2018	338466	6263356	N
DMI18-32-8	dunite	2018	338629	6263189	N
DMI18-32-9A	dunite, dunite dike	2018	338691	6263181	N
DMI18-32-9B	dunite, olivine wehrlite dike	2018	338691	338691	Y
DMI18-32-9C	dunite, wehrlite dike	2018	338691	338691	Y
GN88-1053	olivine wehrlite, chromitite	1988	336763	6268059	Y

[1]Y = yes; N = no

intrusion. Each thin section was described, and photomicrographs were taken of all thin sections by a Rebel EOS T21 camera under and polarized, cross-polarized, and reflected light. Each thin section was also scanned using transmitted light and cross-polarized light by an Epson Perfection 4490 PHOTO scanner (Fig. 3.1). Complete photomicrographs and scans of all twenty-three samples are continued in Appendix A.

3.3. Scanning Electron Microscopy

A Phillips XL30 electron microscope equipped with a Bruker Quantax 200 energy-dispersion X-ray microanalysis system was used at the University of British Columbia, Vancouver, British Columbia to obtain backscattered electron (BSE) micrographs and energy-dispersive spectrometry (EDS) of carbon-coated, polished thin sections of note and for preliminary determination of olivine grains to be analyzed using an electron microprobe. The scanning electron microscope was operated at 15 kV with a spot diameter of 6 μm and a peak count time of 30 s.

3.4. Electronprobe Microanalysis

Electronprobe microanalyses (EPMA) of olivine were conducted at the Electron Microbeam and X-Ray Diffraction Facility (EMXDF) at the University of British Columbia, Vancouver, British Columbia on a fully automated CAMECA SX-50 instrument, operating in the wavelength-dispersion mode with the following operating conditions for transects across olivine grains analyzed during winter of 2019/2020 (Table 1): excitation voltage, 15 kV; beam current, 20 nA; peak count time, 20 s; background count time, 10 s; spot diameter, 10 μm. Data reduction was done using the 'PAP' $\phi(\rho Z)$ method (Pouchou and Pichoir 1985). For the elements

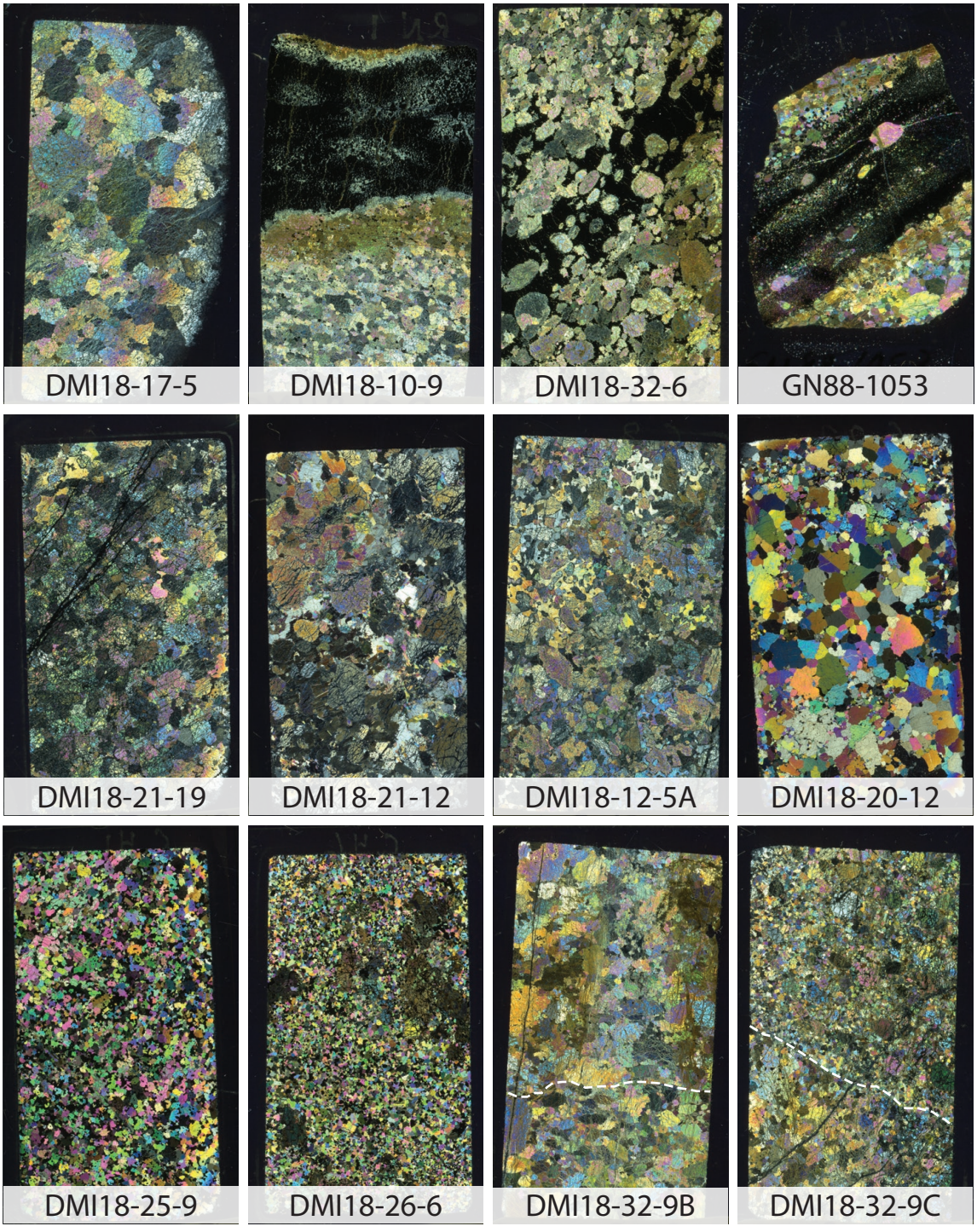

Figure 3.1. Representative scans of thin sections (2 x 4 cm) in cross-polarized light (XPL) of olivine-bearing rocks from the Polaris intrusion. DMI18-17-5: dunite; DMI18-10-9: dunite with chromitite schlieren; DMI18-32-6: dunite with olivine hosted in chromitite schlieren; GN88-1053: olivine wehrlite with olivine hosted in interstitial clinopyroxene-hosting chromitite schlieren; DMI18-21-19: hornblende-phlogopite-olivine wehrlite; DMI18-21-12: phlogopite-rich wehrlite; DMI18-12-5A: wehrlite; DMI18-20-12: olivine clinopyroxenite; DMI18-25-9: magnetite-olivine clinopyroxenite; DMI18-32-6: magnetite-olivine clinopyroxenite with interstitial phlogopite; DMI18-32-9B: dunite (top) cross-cut by olivine wehrlite dike (bottom). DMI18-32-9C: dunite (bottom) cross-cut by wehrlite dike (top). A complete list of olivine-bearing samples and lithologies is listed in Table 1.

considered, the following standards, X-ray lines, and crystals were used: olivine, Mg$K\alpha$, TAP; kyanite, Al$K\alpha$, TAP; olivine, Si$K\alpha$, TAP; diopside, Ca$K\alpha$, PET; rutile, Ti$K\alpha$, PET; synthetic magnesiochromite, Cr$K\alpha$, LIF; synthetic rhodonite, Mn$K\alpha$, LIF; olivine, Fe$K\alpha$, LIF; synthetic Ni-Olivine, Ni$K\alpha$, LIF. A second analysis of Ca and Ni on the same spots was then conducted with the following operating conditions: excitation voltage, 15 kV; beam current, 100 nA; peak count time, 100 s; background count-time, 50 s; spot diameter, 10 μm. Ca and Ni were analyzed in trace mode. All other elements were set to nominal olivine values. Data reduction was done using the 'PAP' $\phi(\rho Z)$ method (Pouchou and Pichoir 1985). For the elements considered, the following standards, X-ray lines, and crystals were used: diopside, Ca$K\alpha$, PET; synthetic Ni-Olivine, Ni$K\alpha$, LIF. For all samples analyzed, the core, midpoint, and rim of each olivine grain and a transect across one olivine gain was completed. Four to six olivine grains were analyzed per lithology.

4. Results

4.1. Petrography

4.1.1 Dunite

Dunite occurs in two main elongate bodies extending NW-SE in the Polaris intrusion (Fig. 4.1 A-C) and extends along the eastern edge of the intrusion. Dunite is also locally found elsewhere throughout the intrusion and commonly grades into other lithologies (i.e. olivine wehrlite). Dunite is composed of >90 vol.% medium- to coarse-grained olivine (Fo_{89-92}). Olivine crystals typically display re-equilibration textures in the form of polygonal sutures (120˚ grain boundary angles) and is commonly kink-banded (deformation banding) or exhibits subgrains (Fig 4.2). These latter features are likely a result of solid-state, high-temperature deformation of olivine similar to what has been described from the Duke Island intrusion, Alaska, as well as other Alaskan-type intrusions globally (e.g., Li *et al.,* 2012). The extent of kink-banding and subgrain development varies from sample to sample and is common in olivine-bearing lithologies (dunite, olivine wehrlite, wehrlite), but also other lithologies with relatively minor olivine (olivine clinopyroxenite). Olivine is locally found with an interdigitated texture indicative of mutual growth interference (Fig. 4.1 C). Chromite, typically fine-grained (<1 mm), is present as cumulus crystals and is either disseminated between olivine grains or found as inclusions in olivine. More rarely, both clinopyroxene and phlogopite are found interstitially (Fig. 4.3 A). Olivine grains are 20-70 vol.% altered to serpentine and magnetite in the form of veins that typically show fabrics both internal to individual grains and coarser parallel fabrics across samples. Chromite commonly contains rims of Fe-rich chromite to magnetite that formed as a result of alteration. Serpentinization is more pervasive along boundaries with chromitite

schlieren perhaps due to a higher degree of porosity caused by schlieren-parallel fractures and subsequent ingress of water.

4.1.2. Chromitite

Chromitites consist of >90 vol.% fine- to medium-grained, subhedral to euhedral chromite crystals and are found within dunite (and locally in olivine wehrlite) as syn-emplacement sheared and folded layers and veinlets (denoted "schlieren") ranging from sub-centimeter scales to centimeters in size (Fig. 4.1 D-F). Chromite is typically recrystallized to form equigranular, sutured crystals. Within schlieren, medium-grained olivine (Fo_{90-94}) is often found intact (Fig. 4.1 D-E). Fine-grained olivine is usually 100 vol.% serpentinized and most cracks within sutured chromite are filled with serpentine. Locally, interstitial clinopyroxene is present between grains of chromite (GN88-1053).

4.1.3. Olivine Wehrlite

Olivine wehrlite (Fig. 4.1 G-H) occurs dispersed in bodies within the Polaris intrusion and commonly exhibits gradational contacts with dunite and wehrlite. Olivine wehrlite has 65-90 vol.% medium- to coarse-grained, subhedral to euhedral cumulus olivine (Fo_{89-92}) and 10-35 vol.% interstitial oikocrysts of clinopyroxene 1-8 cm in size (Nixon *et al*., 1990), forming "heteradcumulates" due to the co-crystallization of olivine and clinopyroxene with different nucleation and growth rates (e.g., Wager *et al*., 1960; Barnes *et al*., 2016a). Olivine is 10-70 vol. % altered to serpentine and clinopyroxene shows 10-20 vol.% alteration to chlorite and carbonate. Minor phases present in olivine wehrlite include chromite (<10 vol.% except in cases of chromitite schlieren), interstitial phlogopite (1-2 vol.%), hornblende (1-15 vol.%), and apatite

(<1 vol.%). Apatite is locally found forming interdigitated textures with grains of hornblende. Hornblende is locally present in higher abundances than clinopyroxene as primary interstitial grains (Fig. 4.1 H).

4.1.4. Wehrlite

Wehrlite (Fig. 4.1 I-J) is dispersed in bodies throughout the Polaris intrusion and exhibits gradational contacts with dunite, olivine wehrlite, and olivine clinopyroxenite. Wehrlite consists of 40-65 vol.% medium- to coarse-grained, subhedral to euhedral cumulus olivine ($Fo_{87.5-91}$) and 35-60 vol.% interstitial oikocrysts of clinopyroxene forming a "heteradcumulate" texture. In some locations, wehrlite is found with blocky crystals of clinopyroxene rather than interstitial oikocrysts. Hornblende and phlogopite are commonly present as minor interstitial grains (Fig. 4.3 C), and trace chromite is typically present as small euhedral inclusions within clinopyroxene grains and, more rarely, olivine. Olivine is 20-50 vol.% serpentinized, and clinopyroxene shows approximately 1-5 vol.% alteration to chlorite, amphibole, and carbonate.

4.1.5. Olivine Clinopyroxenite

Olivine clinopyroxenite (Fig. 4.1 K-L) is also dispersed throughout the Polaris intrusion, but predominantly forms NW-SE-trending elongate bodies located on the western margin of the intrusion (Fig. 2.1). Olivine clinopyroxenite typically grades into bodies of wehrlite. Characteristically, olivine clinopyroxenite consists of 10-40 vol.% cumulus olivine (Fo_{80-84}) and 60-90 vol.% cumulus clinopyroxene. Olivine is generally anhedral to subhedral and fine to coarse-grained. Clinopyroxene is fine- to coarse-grained, subhedral to euhedral, and commonly exhibits twinning.

Olivine clinopyroxenite can be further divided into sub-lithologies based on accessory minerals. Hornblende- and phlogopite-bearing (Fig. 4.3 D) and magnetite-rich olivine clinopyroxenite is denoted as “magnetite-olivine clinopyroxenite”, and magnetite-poor olivine clinopyroxenite is simply referred to as “olivine clinopyroxenite”. Magnetite-olivine clinopyroxenite contains ilmenite as a common accessory phase along with Cu-bearing sulfides. Magnetite-poor olivine clinopyroxenite exhibits the same mineralogy—magnetite, hornblende, phlogopite—but in minor and trace amounts. Olivine clinopyroxenite contains trace amounts of Ni-bearing sulfides. In both types of olivine clinopyroxenite, olivine is less altered to serpentine (0-10 vol.%) on average than in olivine-dominant lithologies, except in areas where serpentine vein networks are pervasive throughout the sample. Clinopyroxene typically shows 0-10 vol.% alteration to chlorite.

The two types of olivine clinopyroxenite are also distinguished by olivine with kink-banding and subgrain olivine-deformation textures. Olivine clinopyroxenite commonly has strongly kink-banded olivine grains. Whereas, magnetite-olivine clinopyroxenite shows rare kink-banding. In samples where olivine records deformation textures, clinopyroxene is typically pristine and undeformed.

4.1.6. Ultramafic Dikes

Ultramafic dikes (up to 30 cm wide) are common in the east and central parts of the Polaris intrusion and often exhibit irregular contacts (Nott *et al*., 2020). These dikes can typically be distinguished from their dunite host rocks by variations in mineralogy that manifest as differences in weathering color (Fig. 2.3 D-F). These dikes are rarely laterally traceable due to their irregularity. Further distinguishing features are present as chromitite schlieren that have

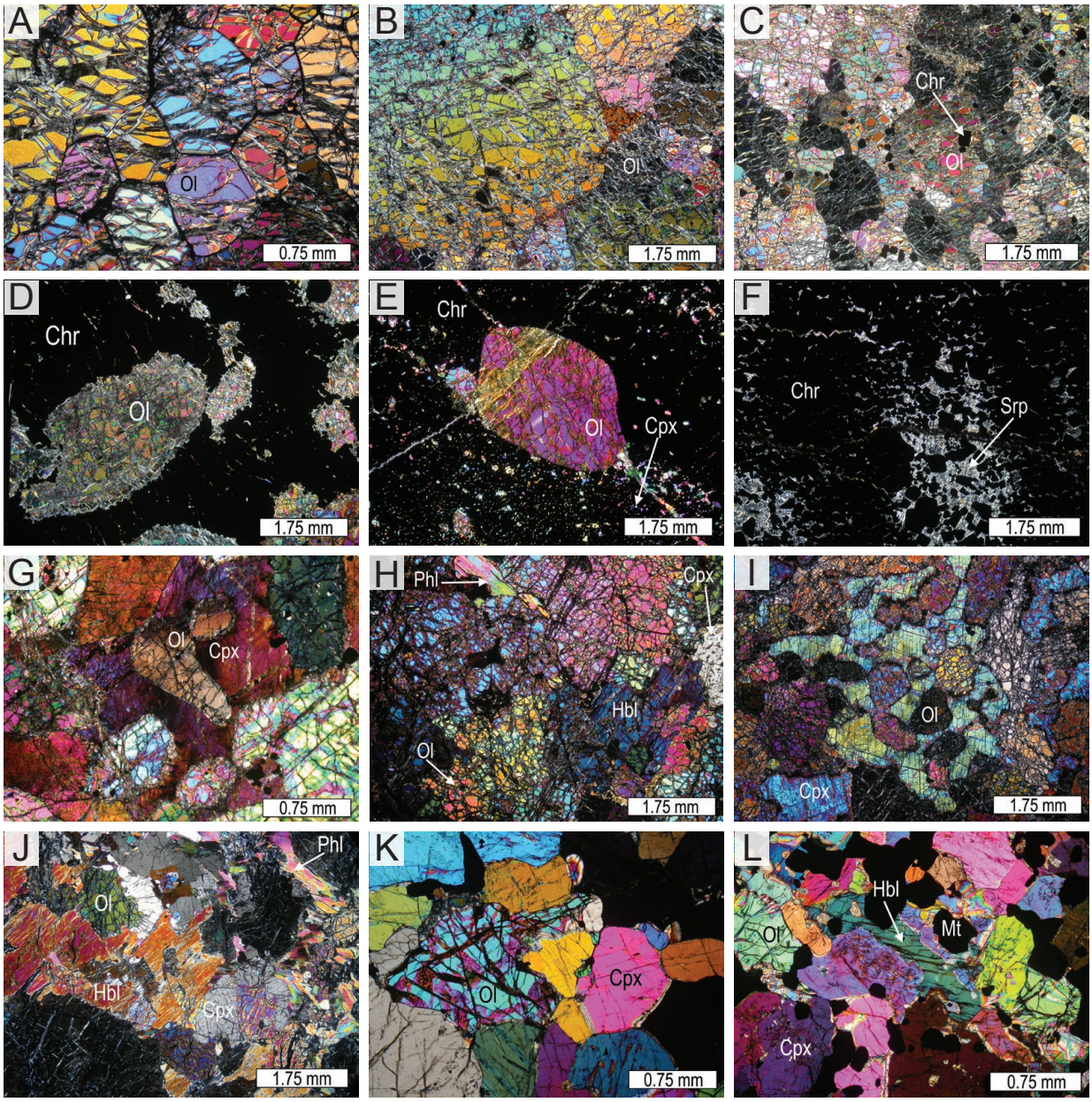

Figure 4.1. Photomicrographs in cross-polarized light (XPL) of representative olivine-bearing rocks and textures from the Polaris intrusion. A-B) Cumulus olivine with 120˚ intersecting grain boundaries indicative of high-temperature textural maturation and recrystallization (DMI18-21-15, DMI18-17-5). C) Olivine showing an interdigitated texture between grains of olivine. Chromite is present as inclusions within olivine or at grain boundaries. D) Olivine within dunite-hosted chromitite schlieren that is completely isolated from other olivine grains (DMI18-32-6). E) Olivine within olivine wehrlite-hosted chromitite schlieren with interstitial clinopyroxene within schlieren (GN88-1053). F) Dunite-hosted chromitite schlieren with completely serpentinized olivine (DMI18-10-9). G) Cumulus olivine in olivine wehrlite with interstitial clinopyroxene forming oikocrysts (DMI18-10-6B). H) Olivine wehrlite with cumulus olivine and interstitial hornblende, phlogopite, and clinopyroxene; hornblende is more abundant than clinopyroxene in this sample (DMI18-21-19). I) Oikocrysts of interstitial clinopyroxene around cumulus olivine in wehrlite (DMI18-12-5A). J) Phlogopite and hornblende-rich wehrlite with hornblende, phlogopite, and clinopyroxene as major interstitial phases (DMI18-21-12). K) Anhedral olivine in olivine clinopyroxenite with cumulus clinopyroxene (DMI18-20-12). L) Cumulus olivine and clinopyroxene in magnetite-olivine clinopyroxenite, cross-cut by hornblende-rich vein (DMI18-25-9). Scales as indicated on individual panels.

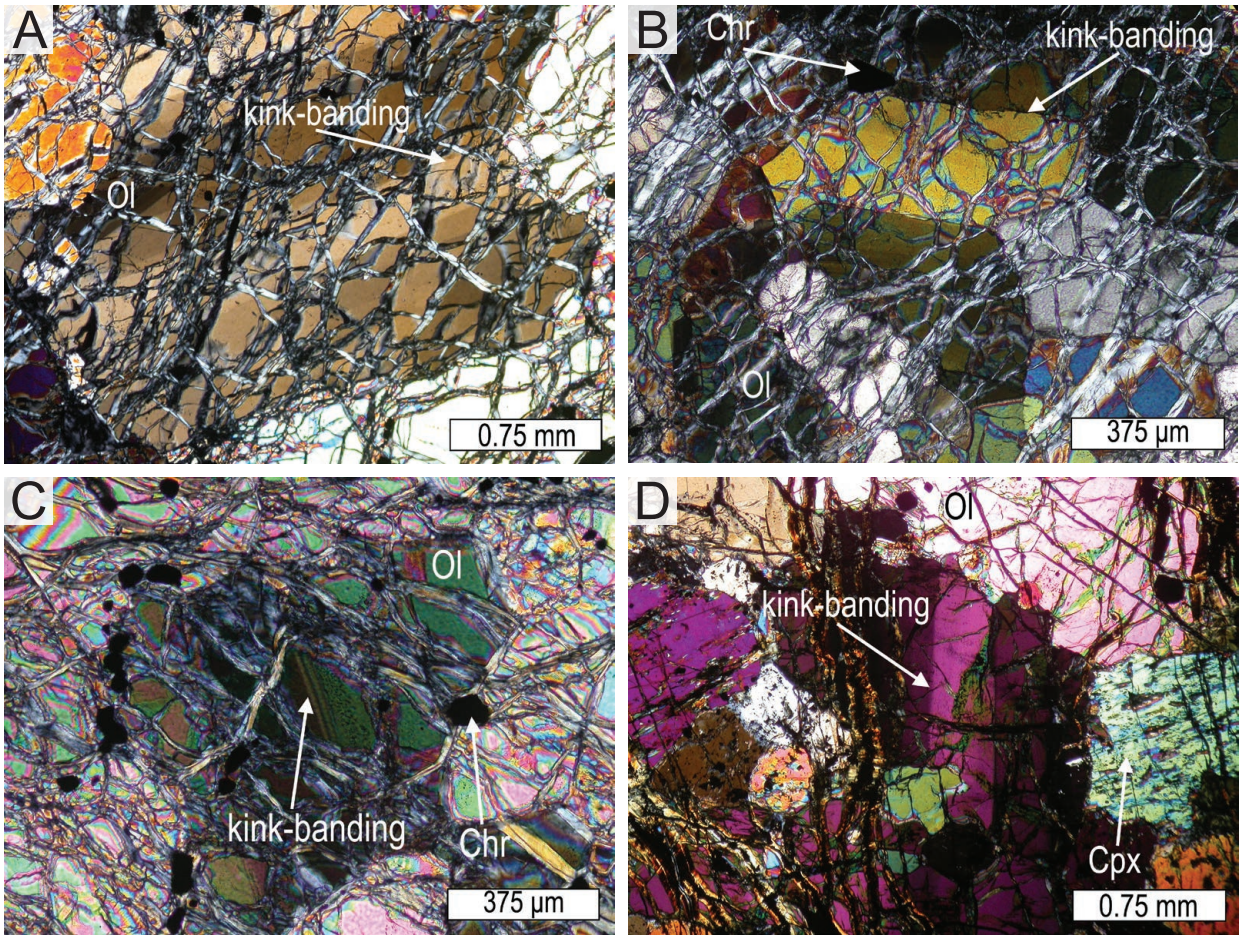

Figure 4.2. Representative photomicrographs in cross-polarized light (XPL) of kink-banded olivine from the Polaris intrusion. A) dunite (DMI18-17-5); B) dunite (DMI18-10-10); C) dunite (DMI18-32-7C); D) olivine clinopyroxenite (DMI18-28-5). Kink-banding is present in olivine across all olivine-bearing lithologies in the Polaris intrusion. Scales as indicated on individual panels.

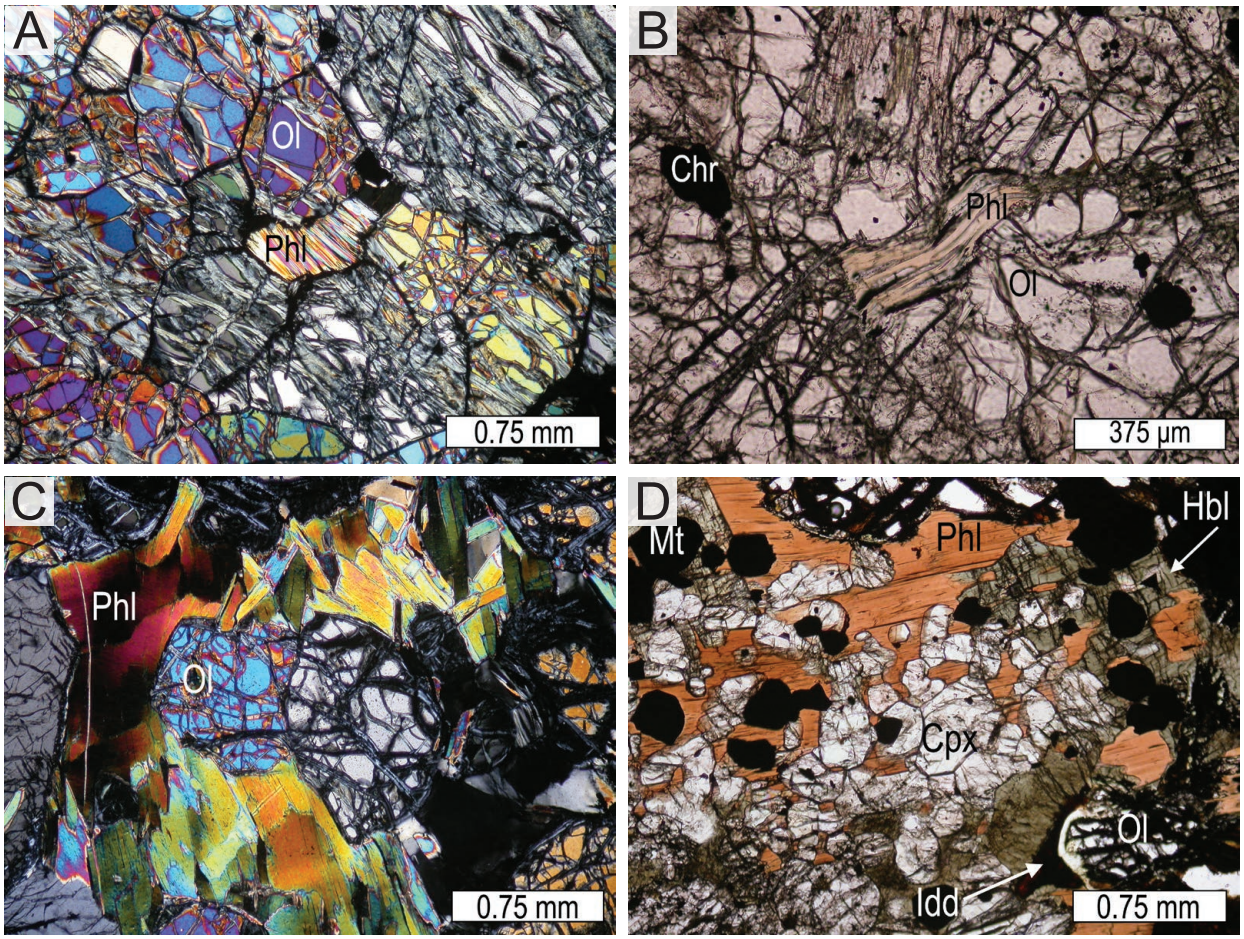

Figure 4.3. Representative photomicrographs of primary interstitial phlogopite in various lithologies in the Polaris intrusion. A) Interstitial phlogopite in dunite in cross-polarized light (XPL) (DMI18-21-15). B) Interstitial phlogopite in olivine wehrlite in plane-polarized light (PPL) (DMI18-10-6B). C) Interstitial phlogopite in phlogopite-rich wehrlite (DMI18-21-12). D) Interstitial phlogopite in magnetite-olivine clinopyroxenite (DMI18-32-6). Primary interstitial phlogopite exists within all major olivine-bearing rock types of the Polaris intrusion. Scales as indicated on individual panels.

been cross-cut by otherwise invisible dikes (Fig. 4.4 A), compositional differences between olivine grains, or textural differences (Fig. 4.4 B-D). The main mineralogical difference between ultramafic dikes and their hosts is the relative amount of clinopyroxene to olivine. On average, ultramafic dikes have more clinopyroxene than their hosts, and it is typically present as interstitial grains. The more clinopyroxene that is present, the more likely it is for the dikes to be visible in outcrop. The ultramafic dikes commonly contain less chromite than their hosts. As chromite is generally fine-grained (<1 mm), this mineralogical difference is commonly not visible in hand samples or at outcrop scales, and these dikes may be recognized where pre-existing chromite schlieren have been cross-cut by these generally indistinct dikes. Olivine chemistry may be distinct between dikes and host-rocks (see below under "Olivine Chemistry").

Textural differences between ultramafic dikes and host dunites are typically present as grain size differences or shape-oriented fabrics. On average, ultramafic dikes are finer-grained than their host dunites. The dikes also locally exhibit olivine shape-oriented fabrics that may be indicative of magmatic flow. The ultramafic dikes rarely contain kink-banded olivine, whereas olivine in the host rocks typically shows kink-banding in sub-orthogonal directions to the dike orientation.

4.1.7. Ni-Cu-PGE Sulfides

Primary base metal sulfides occur as disseminated grains throughout the Polaris intrusion and include pyrrhotite ($Fe_{1-x}S$), pentlandite ($(Fe,Ni)_9S_8$), chalcopyrite ($CuFeS_2$), and bornite (Cu_5FeS_4). Pentlandite is found in lithologies ranging from olivine clinopyroxenite to olivine wehrlite (Fig. 4.5 A-C). Except in cases of remobilization, dunite is devoid of base metal sulfides. Pentlandite occurs as blocky grains intergrown with pyrrhotite and chalcopyrite as

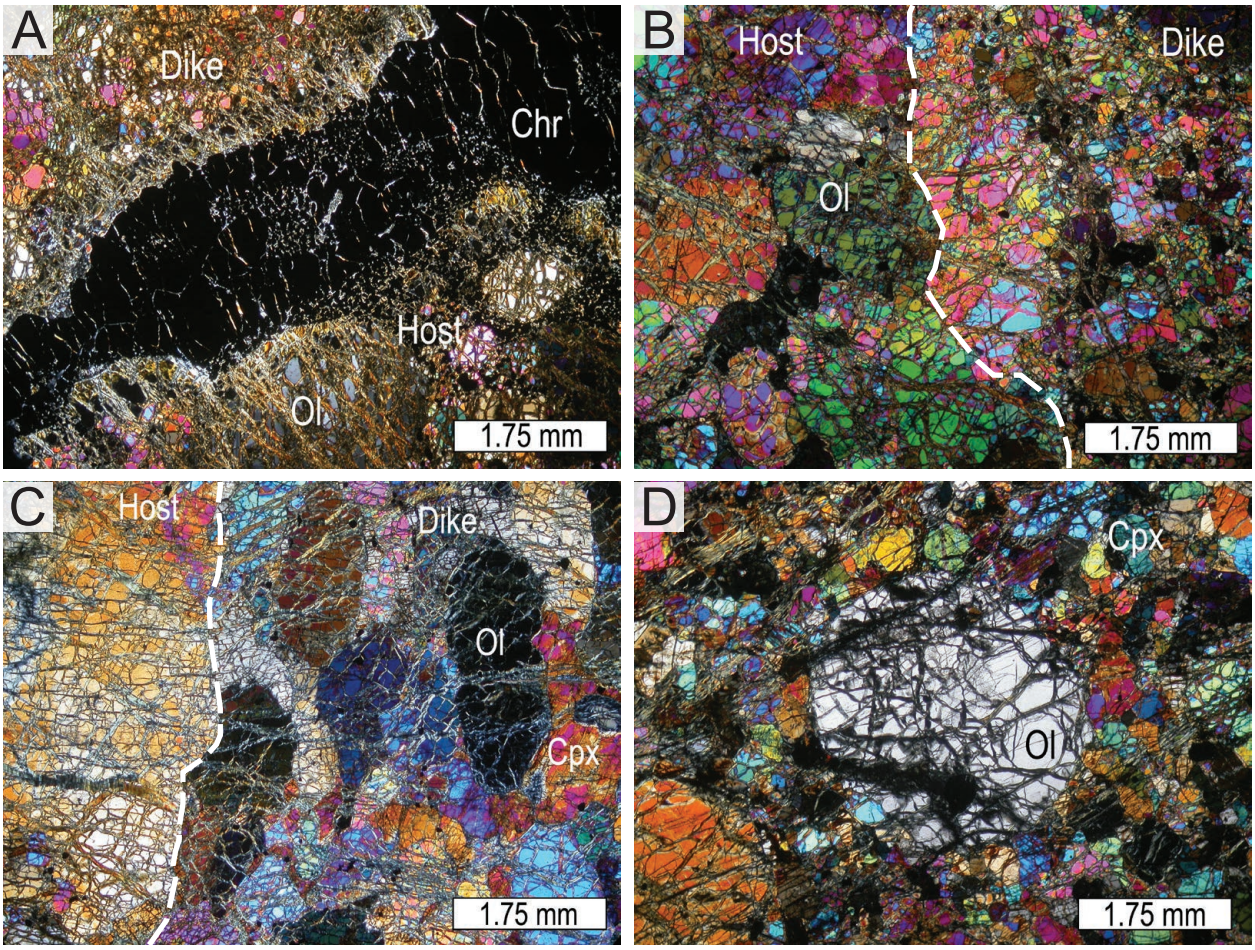

Figure 4.4. Photomicrographs in cross-polarized light (XPL) of representative textures of the ultramafic dikes in the Polaris intrusion. White dashed line delineates dike boundary. A) Dunite dike cross-cutting dunite-hosted chromitite schlieren (DMI18-32-7C). Olivine in dike is finer grained than host dunite. In outcrop, dunite dike is only visible where it is found cross-cutting chromitite schlieren. B). Dunite dike cross-cutting dunite (DMI18-32-9A). Olivine in dike is finer grained than in the host dunite. C) Olivine wehrlite dike cross-cutting dunite (DMI18-32-9B). In the olivine wehrlite dike, olivine has a shape-oriented fabric and there is interstitial clinopyroxene. D). Olivine in wehrlite dike (DMI18-32-9C) that is coarser grained than clinopyroxene and does not appear to have crystallized in the same environment as the clinopyroxene. Scales as indicated on individual panels.

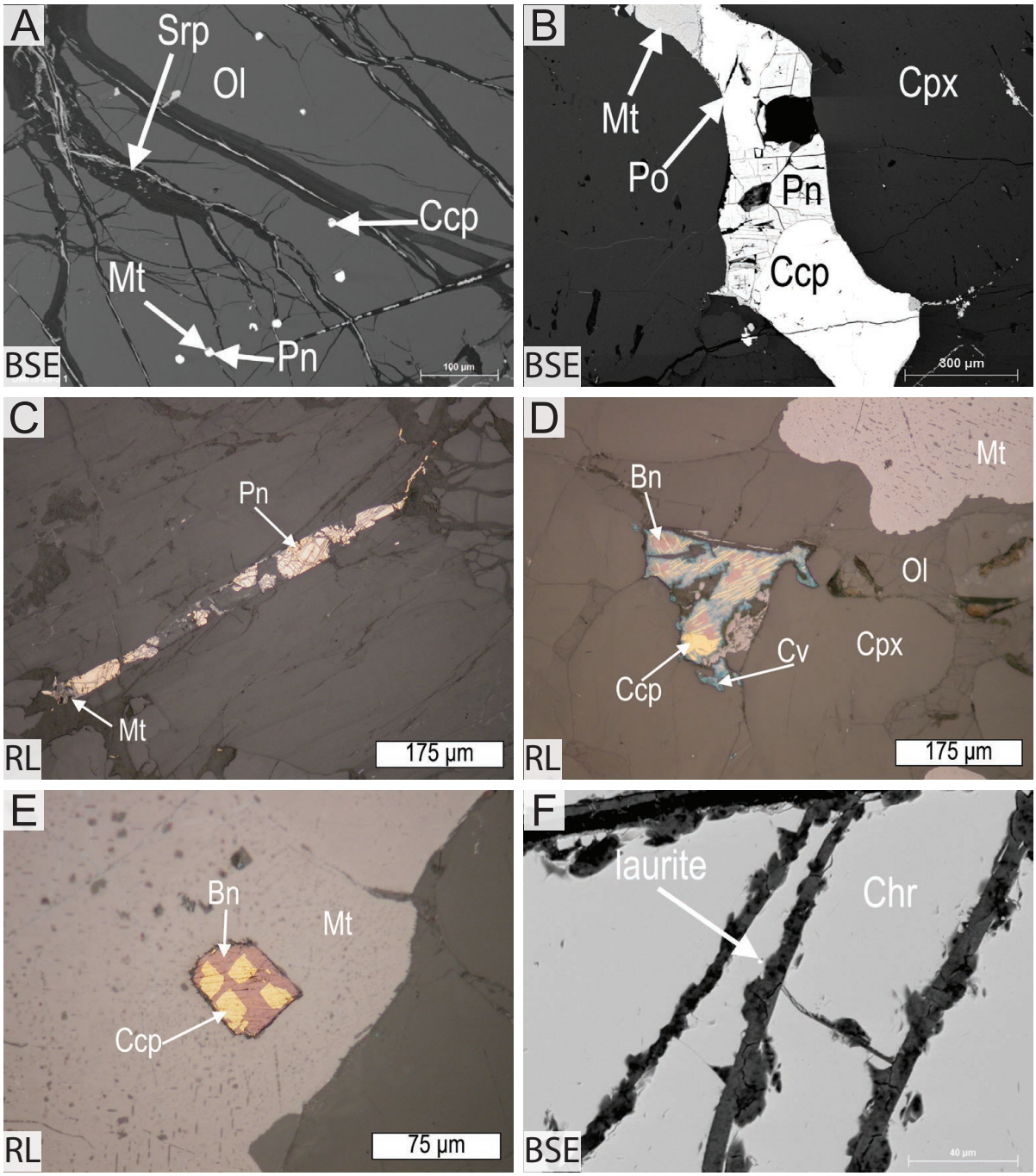

Figure 4.5. Reflected light photomicrographs (RL) and backscatter electron (BSE) images of sulfides in olivine-bearing rocks of the Polaris intrusion. A) Primary inclusions of pentlandite, chalcopyrite, and magnetite in a grain of olivine hosted in olivine clinopyroxenite (DMI18-28-5). B) Primary interstitial sulfide bleb comprised of pyrrhotite, pentlandite, chalcopyrite, and magnetite hosted in olivine clinopyroxenite (DMI18-20-12). C) Remobilized pentlandite present in hornblende-olivine wehrlite (DMI18-21-19) within vein of serpentinite. Pentlandite is brecciated by magnetite. D). Completely exsolved chalcopyrite-bornite grain interstitial to clinopyroxene in magnetite-olivine clinopyroxenite (DMI18-26-6). Rims of this Cu-rich sulfide have been supergene-enriched to covellite. Magnetite-rich olivine clinopyroxenites are dominated by Cu-sulfides, whereas magnetite-poor olivine clinopyroxenites contain Ni-sulfides. E). Bornite-chalcopyrite inclusion in magnetite, hosted by magnetite-olivine clinopyroxenite (DMI18-26-6). F). The platinum group mineral (PGM) laurite (RuS2) found as a small (<5 µm diameter) inclusion in chromitite (DMI18-32-7C). Scales as indicated on individual panels.

interstitial blebs. These sulfides are also present as small circular inclusions within olivine crystals. Pentlandite is locally found remobilized in serpentine veins and is brecciated by veinlets of magnetite.

Chalcopyrite and bornite are more commonly found in magnetite olivine clinopyroxenite as primary sulfide droplets (Fig. 4.5 D-E). They occur both interstitially and within magnetite grains and make up volumetrically more of this lithology (1-3 vol.%) than base metal sulfides do for the other lithologies (<1 vol.%). Chalcopyrite is predominant over bornite and both show primary exsolution textures. The rims of these Cu-bearing sulfide grains locally show supergene enrichment to covellite.

Although volumetrically unimportant, the platinum group mineral (PGM) laurite (Ru_2S) was discovered in chromitite (Fig. 4.5 F). Alaskan-type intrusions are known to host PGM within chromitites as exsolved minerals on the edge of chromite grains and there are likely more primary PGM present as other alloys or sulfides (e.g., Nixon *et al*., 1997).

4.2. Olivine Chemistry

The forsterite content of olivine, where $Fo_{olivine} = [Mg/(Mg+Fe^{2+}) \times 100]$, in the olivine-bearing rocks of the Polaris intrusion span a relatively large range from $Fo_{93.5}$ (olivine in chromitite) to Fo_{79} (olivine in olivine clinopyroxenite) (Table 2; Fig. 4.6). The forsterite content does not vary significantly across grains of olivine (Fig. 4.7). In some samples, there is slight reverse zoning (i.e. rims are slightly more Mg-rich than cores). In chromitites, olivine shows an enrichment in magnesium towards the rim of grains due to re-equilibration with chromite and records the highest forsterite content within the Polaris intrusion of $Fo_{93.5}$ (GN88-1053).

Table 2. Average forsterite, Ni, Ca, and Mn compositions of olivine from the Polaris Alaskan-type intrusion.

Sample #	Lithology	n	Average Fo (mol. %)	Average Ni (ppm)	Average Ca (ppm)	Average Mn (ppm)
DMI18-10-9	dunite	21	91.2	2320	740	1313
DMI18-12-5A	wehrlite	20	90.4	2173	212	1373
DMI18-13-1	wehrlite	19	89.4	1717	165	1453
DMI18-17-5	dunite	22	89.4	2075	434	1404
DMI18-20-12	ol clinopyroxenite	23	82.3	1741	204	2238
DMI18-21-12	phl-rich ol wehrlite	18	89.3	3042	181	1341
DMI18-21-19	hbl phl ol wehrlite	17	90.1	2205	152	1425
DMI18-25-9	mt ol clinopyroxenite	18	82.4	409	262	2611
DMI18-26-6	mt ol clinopyroxenite	19	80.6	365	261	3214
DMI18-28-5	ol clinopyroxenite	19	83.4	1994	156	2072
DMI18-32-6	dunite	17	90.0	2148	718	1410
DMI18-32-6	chromitite	14	91.0	2177	790	1283
DMI18-32-9B	dunite	17	89.8	1837	281	1328
DMI18-32-9B	ol wehrlite dike	15	89.6	1831	239	1418
DMI18-32-9C	dunite	21	87.2	1111	219	1829
DMI18-32-9C	wehrlite dike	16	87.9	2236	293	1549
GN88-1053	chromitite	12	91.9	2565	301	1036
GN88-1053	ol wehrlite	18	89.5	2737	392	1454
	Total	326				
		Max	91.9	3042	790	3214
		Min	80.6	365	152	1036

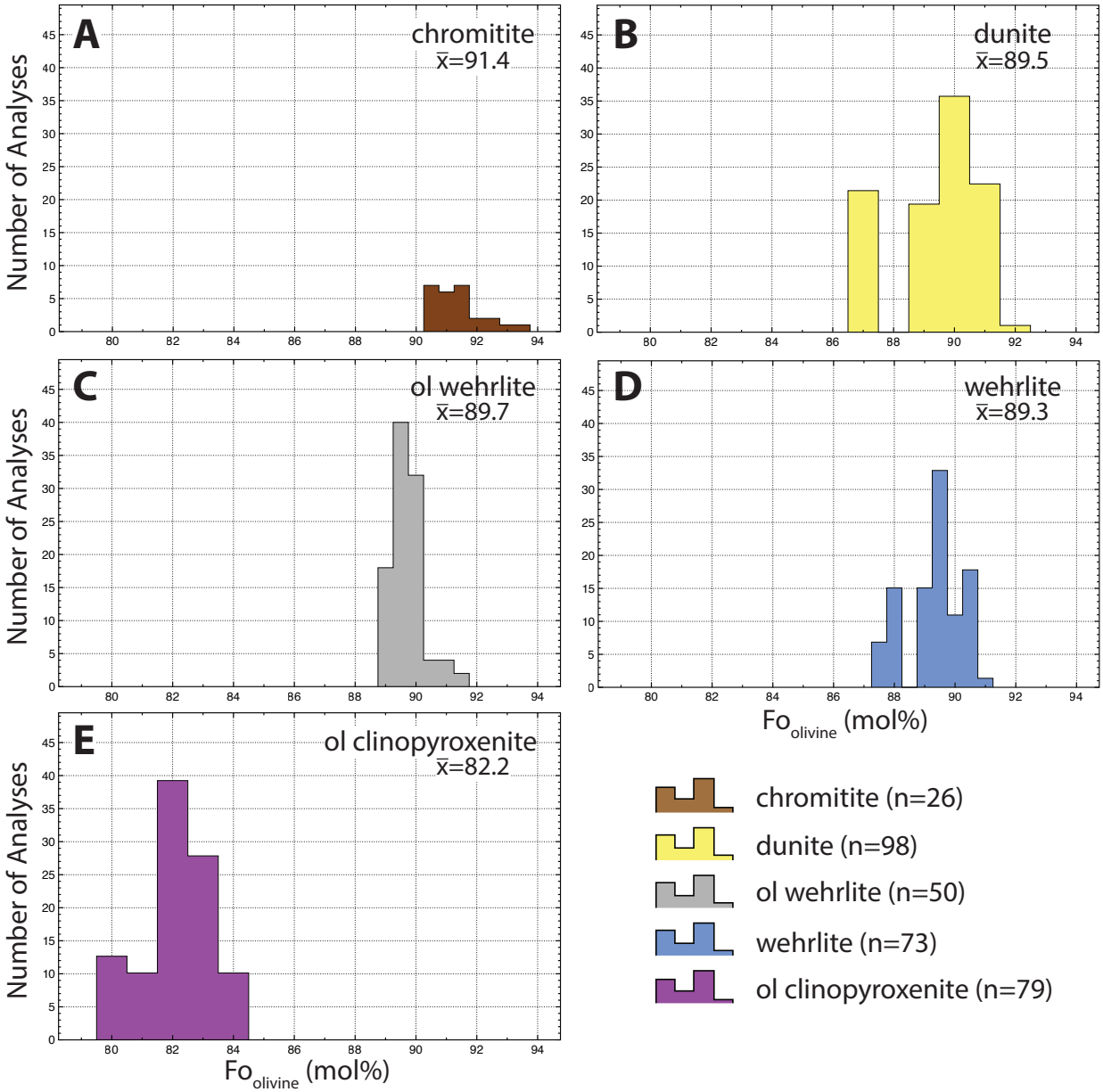

Figure 4.6. Histograms of the forsterite (Fo) content (mol. %) of olivine for representative olivine-bearing rocks from the Polaris intrusion where Fo = [Mg/(Mg+Fe)]*100. A) Chromitite contains very Mg-rich olivine with a limited range of forsterite contents from Fo_{90-94}. B) Dunite contains Mg-rich olivine with a restricted range of forsterites content mostly from Fo_{89-92} with one more evolved sample (DMI18-32-9C) with about Fo_{87} olivine. C) Olivine wehrlite contains olivine with a forsterite content of Fo_{89-92}, indistinguishable from dunite. D) Wehrlite contains olivine with a forsterite content of $Fo_{87.5-91}$. E) Olivine clinopyroxenite contains olivine analyses with a range of forsterite contents from Fo_{80-84}. The total number of analyses per lithology is denoted in the legend as "n=x". The mean (x) forsterite content for each lithology is indicated on each plot. Note that each panel has the same scale for comparative purposes.

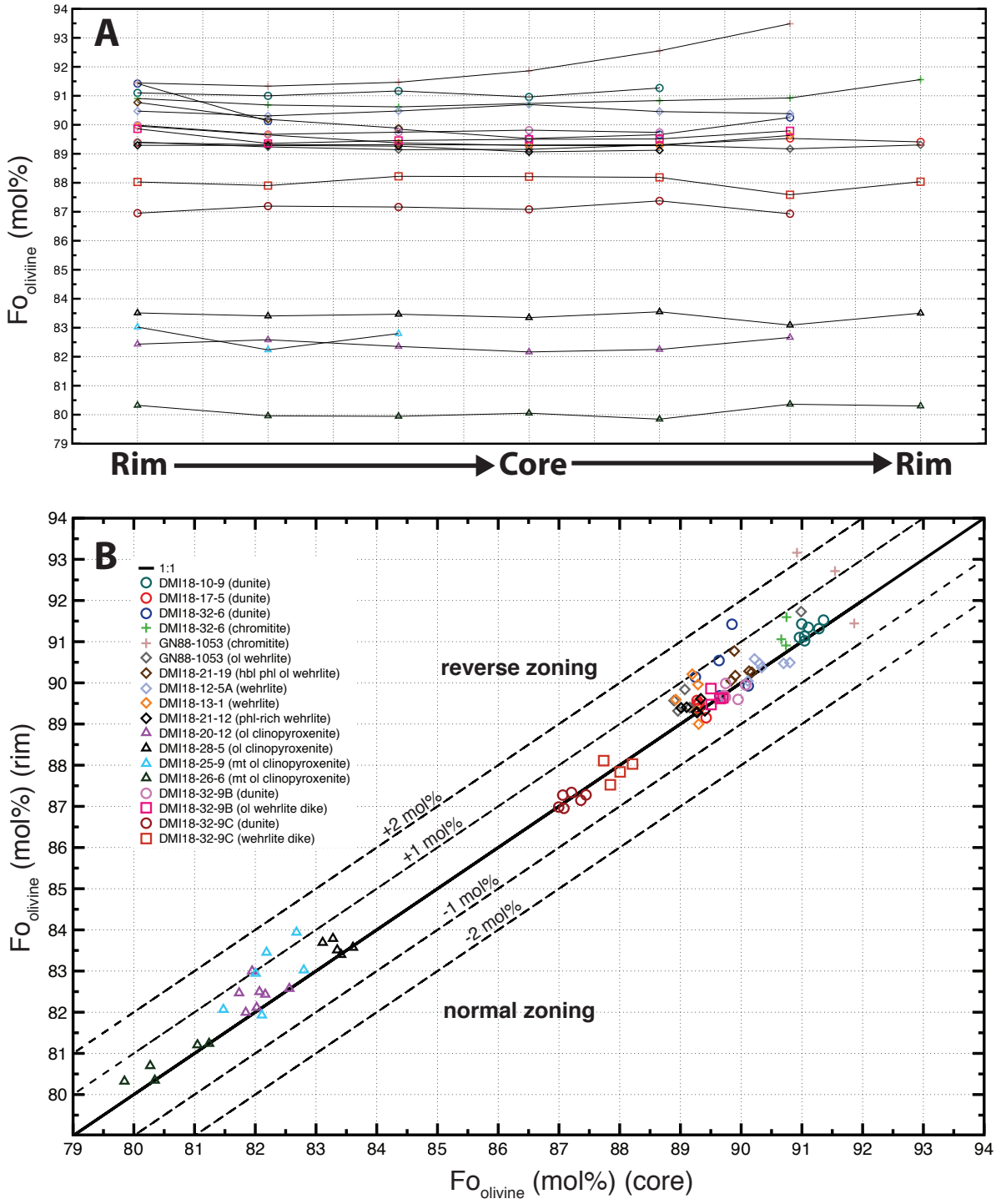

Figure 4.7. Plots of the forsterite content (mol. %) of olivine across individual grains for representative olivine-bearing rocks from the Polaris intrusion. A) Forsterite content of representative olivine grain profiles from each thin section analyzed, from rim to core to rim (note that the x-axis scale is relative and does not show absolute distances). The forsterite content does not vary significantly across nearly all analyzed grains of olivine. There is very slight reverse zoning in some samples. B) Forsterite contents of rims vs. cores for each olivine grain analyzed compared to the solid 1:1 line (i.e., no zoning). The field above the solid line indicates reverse zoning and the field below indicates normal zoning. Labeled dashed lines show relative difference between forsterite contents (mol. %) of core and rim. Note that Fo contents of olivine cluster closely around the 1:1 line for all lithologies.

Table 3 shows representative olivine chemistry for all samples measured. Contents of Al_2O_3, Cr_2O_3, and TiO_2 are below detection limits in all samples. Olivine from the Polaris intrusion has a wide range of Ni concentrations from ~275 ppm at Fo_{81} (DMI18-26-6; magnetite-olivine clinopyroxenite) to ~3108 ppm at Fo_{89} (DMI18-21-12; phlogopite-rich wehrlite) (Fig. 4.8). There is no significant Ni zonation in olivine (Fig. 4.9). Olivine from the Polaris intrusion typically has low-Ca concentrations (<1000 ppm) (Fig. 4.10). Ca contents of olivine frequently exhibit reverse zoning (i.e. cores are more Ca-rich than rims) (Fig. 4.11). The Mn concentrations in olivine show a general increasing trend with decreasing forsterite content, with an overall range from ~605 ppm (GN88-1053, chromitite) to 3670 ppm (DMI18-26-6, magnetite olivine clinopyroxenite) (Fig. 4.12). There is no significant zonation in Mn across olivine grains (Fig. 4.13).

In dunite, olivine compositions show a relatively limited range (Fo_{89-92}) and they are similar to the primitive olivine compositions measured from arc mantle xenoliths globally (Arai and Ishimaru, 2007). The Ni content of olivine in dunite shows a significant range from ~1750-2450 ppm. The Ni contents of chromitite-hosted olivine grains are similar to those from dunites. Olivine in dunite and chromitite contain a wide range of Ca concentrations from ~215-1020 ppm. All other olivine-bearing lithologies have a range of Ca concentrations ranging from below detection limits to ~500 ppm.

Olivine wehrlite (Fo_{89-92}) and wehrlite ($Fo_{87.5-91}$) have relatively limited range of forsterite contents and show significant overlap with the forsterite contents of dunite. The olivine forsterite contents of olivine wehrlite and wehrlite are also similar to primitive olivine compositions measured from arc mantle xenoliths (Arai and Ishimaru, 2007). The Ni content of olivine in olivine wehrlite ranges from ~1964-2886 ppm, whereas the Ni content of olivine in wehrlite

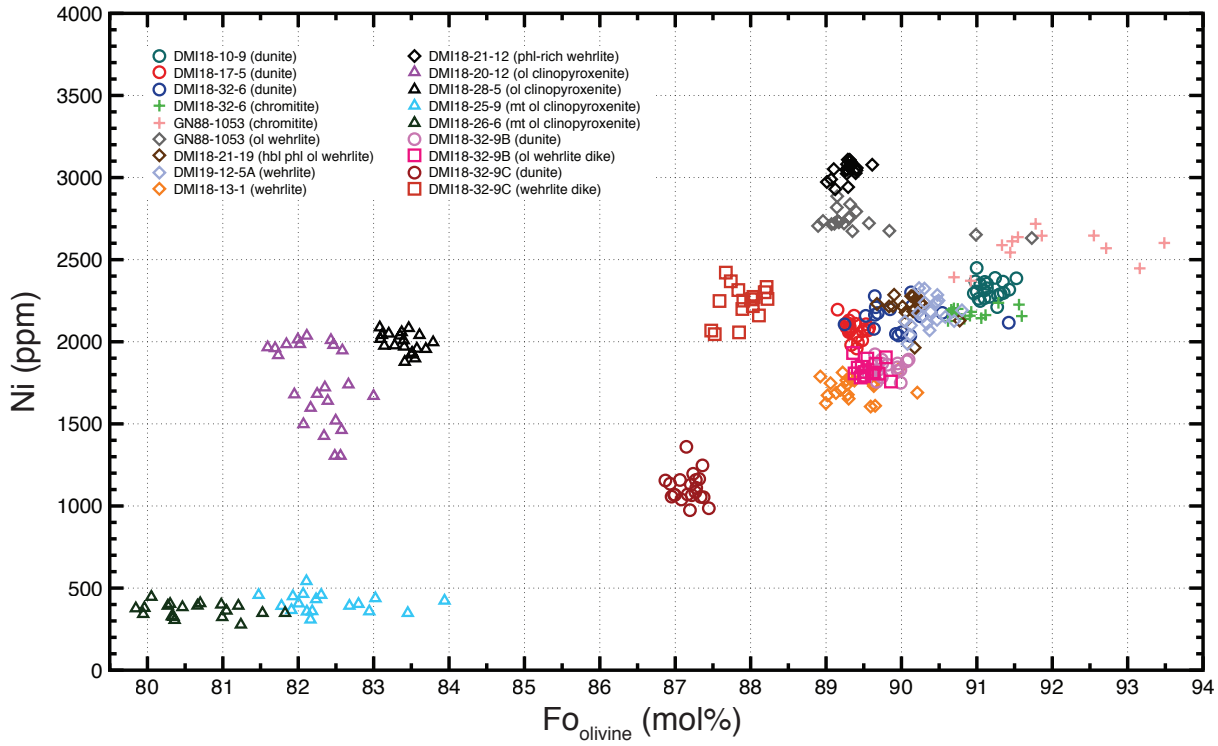

Figure 4.8. Plots of Ni concentrations (ppm) vs. forsterite content (mol. %) of olivine for representative olivine-bearing lithologies from the Polaris intrusion. The Ni concentrations in olivine range from ~1750-2450 ppm in dunites (with a similar range for chromitites), from ~1964-2886 ppm in olivine wehrlites, from ~1605-3108 ppm in wehrlites, ~1305-2090 ppm in magnetite-poor olivine clinopyroxenites, and from ~275 to 550 ppm in magnetite-rich olivine clinopyroxenites.

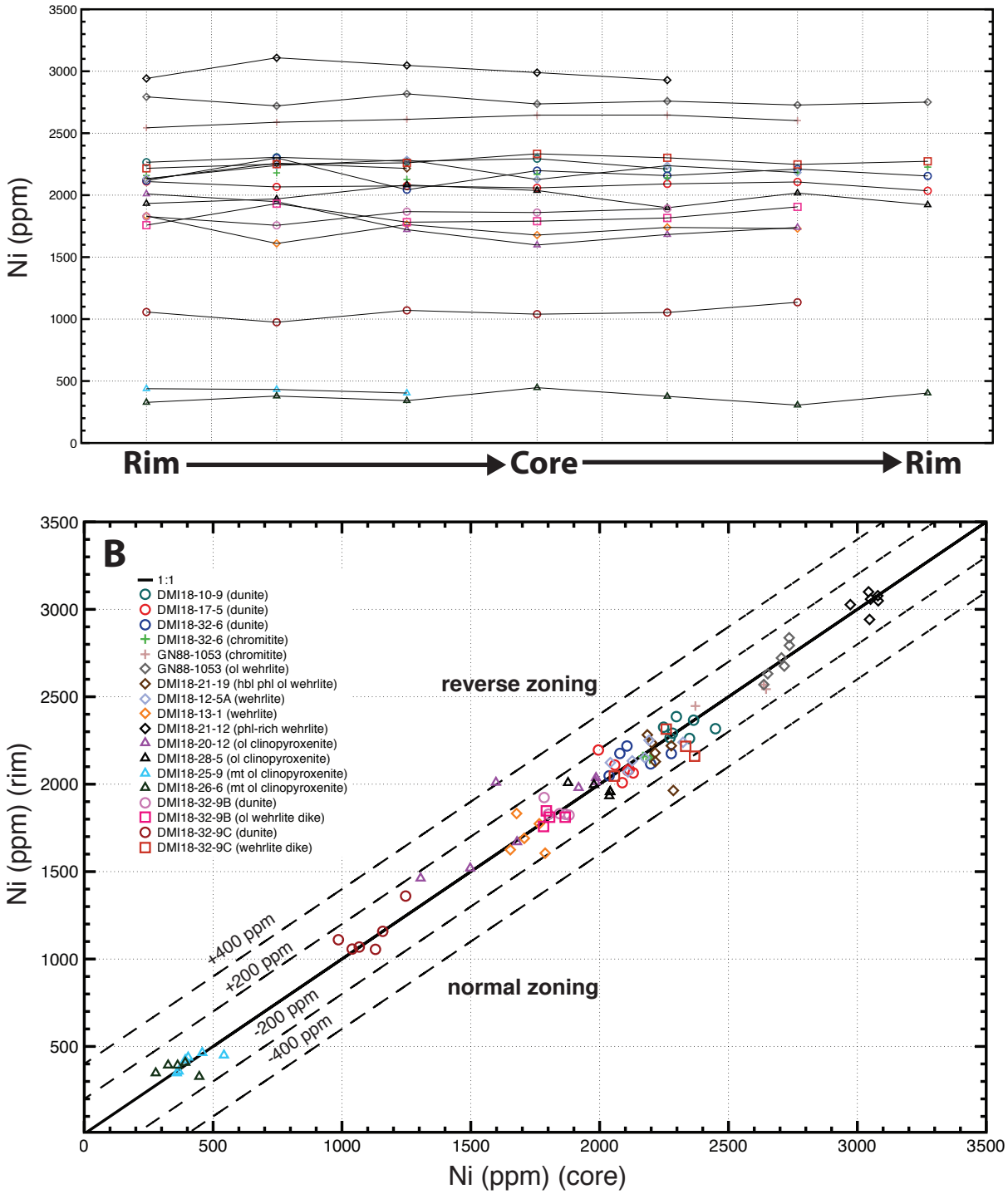

Figure 4.9. Plots of Ni concentration (ppm) of olivine across individual grains for representative olivine-bearing rocks from the Polaris intrusion. A) Ni concentrations of representative olivine grains from each thin section analyzed, from rim to core to rim (note that the x-axis scale is relative and does not show absolute distances). There is no significant Ni zonation in olivine. B) Ni concentrations of rims vs. cores for each olivine grain analyzed compared to the solid 1:1 line (i.e., no zoning). The field above the solid line indicates reverse zoning and the field below indicates normal zoning. Labeled dashed lines show relative difference between Ni concentrations (ppm) of core and rim. Ni concentrations of olivine cluster closely around the 1:1 line for all lithologies.

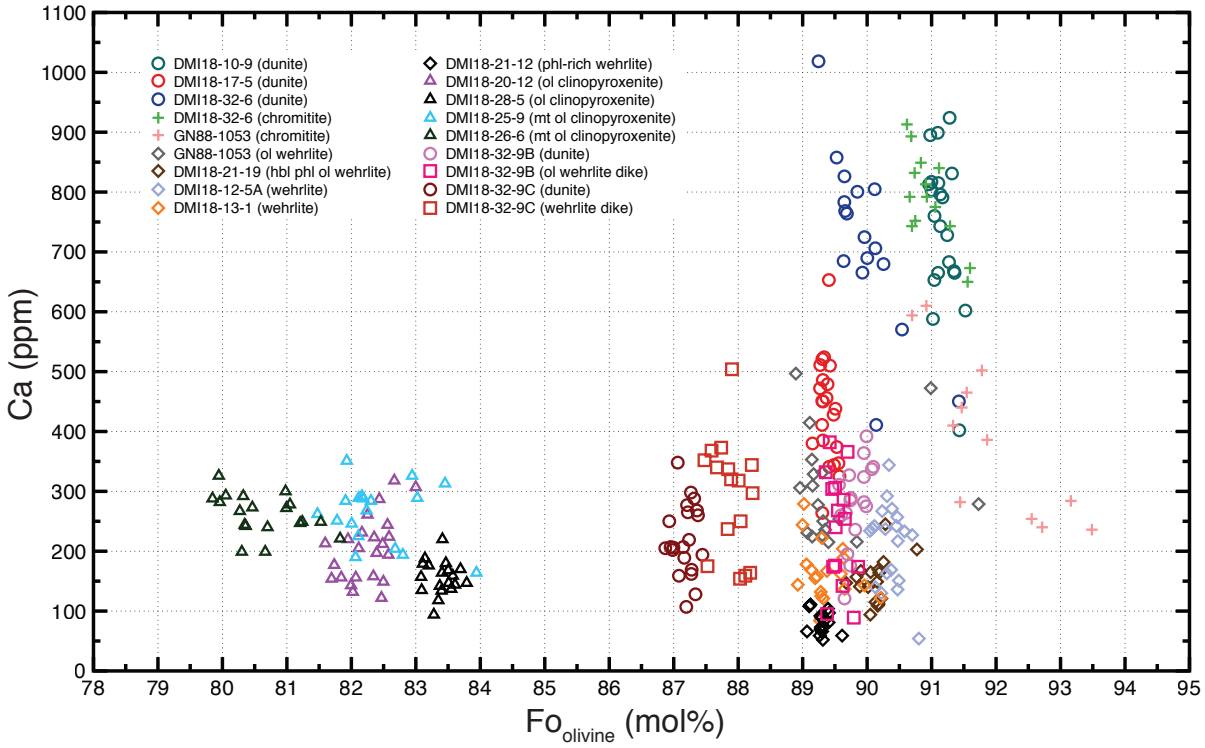

Figure 4.10. Plots of Ca concentrations (ppm) vs. forsterite content (mol. %) of olivine for representative olivine-bearing lithologies from the Polaris intrusion. All samples have low-Ca olivine (<1,000 ppm) with dunite and chromitite representing the most Ca-rich lithologies (~215-1020 ppm). All other olivine-bearing lithologies have Ca concentrations of olivine ranging from below detection limits to ~500 ppm.

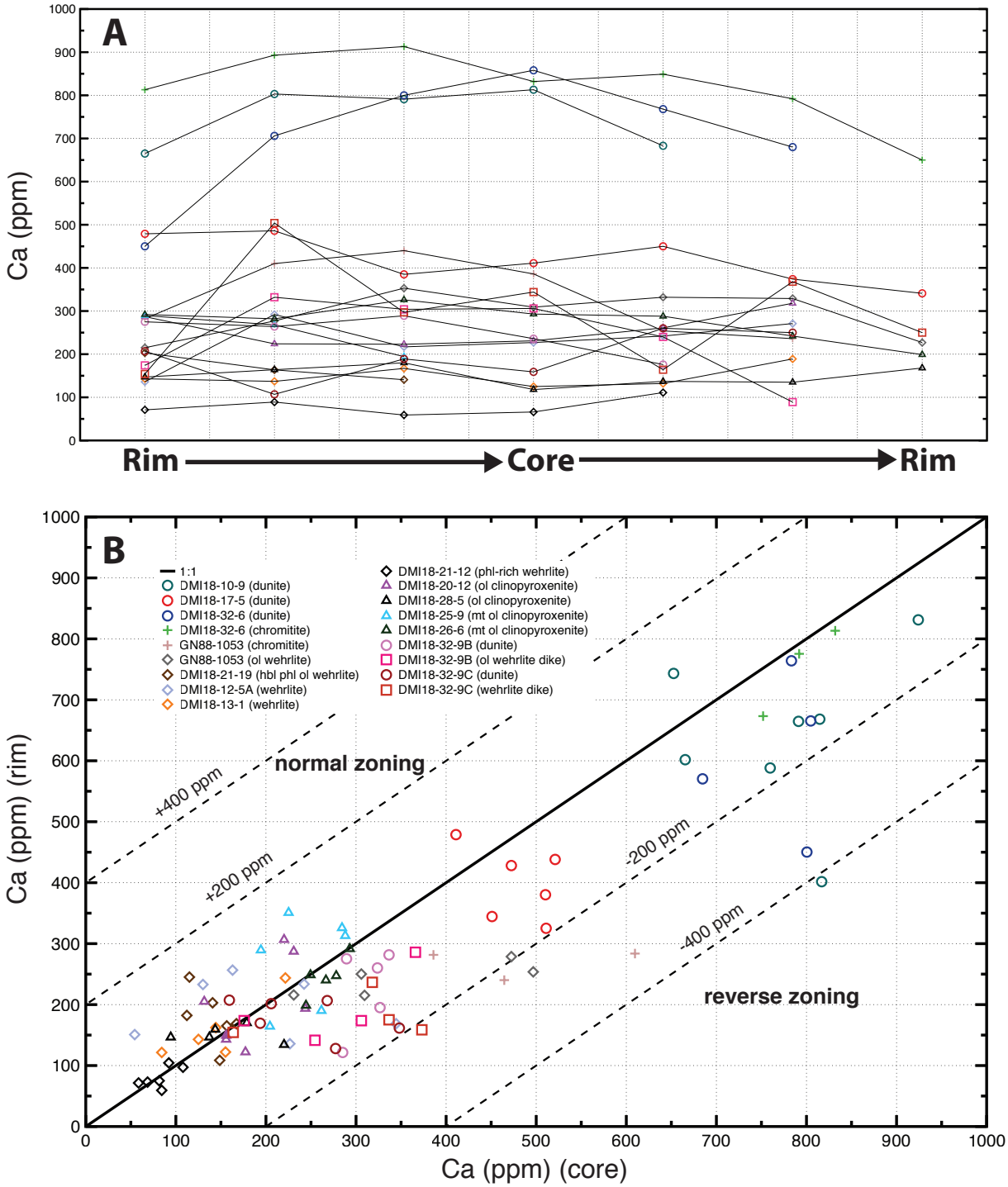

Figure 4.11. Plots of Ca concentration (ppm) of olivine across individual grains for representative olivine-bearing rocks from the Polaris intrusion. A) Ca concentrations of representative olivine grain from each thin section analyzed, from rim to core to rim (note that the x-axis scale is relative and does not show absolute distances). Ca concentrations show reverse zoning, predominantly in dunites and chromitites. B) Ca concentrations of rims vs. cores for each olivine grain analyzed compared to the solid 1:1 line (i.e., no zoning). The field above the solid line indicates normal zoning and the field below indicates reverse zoning. Labeled dashed lines show relative difference between Ca concentrations (ppm) of core and rim. Ca concentrations of olivine primarily cluster below the 1:1 line, indicative of reverse zoning.

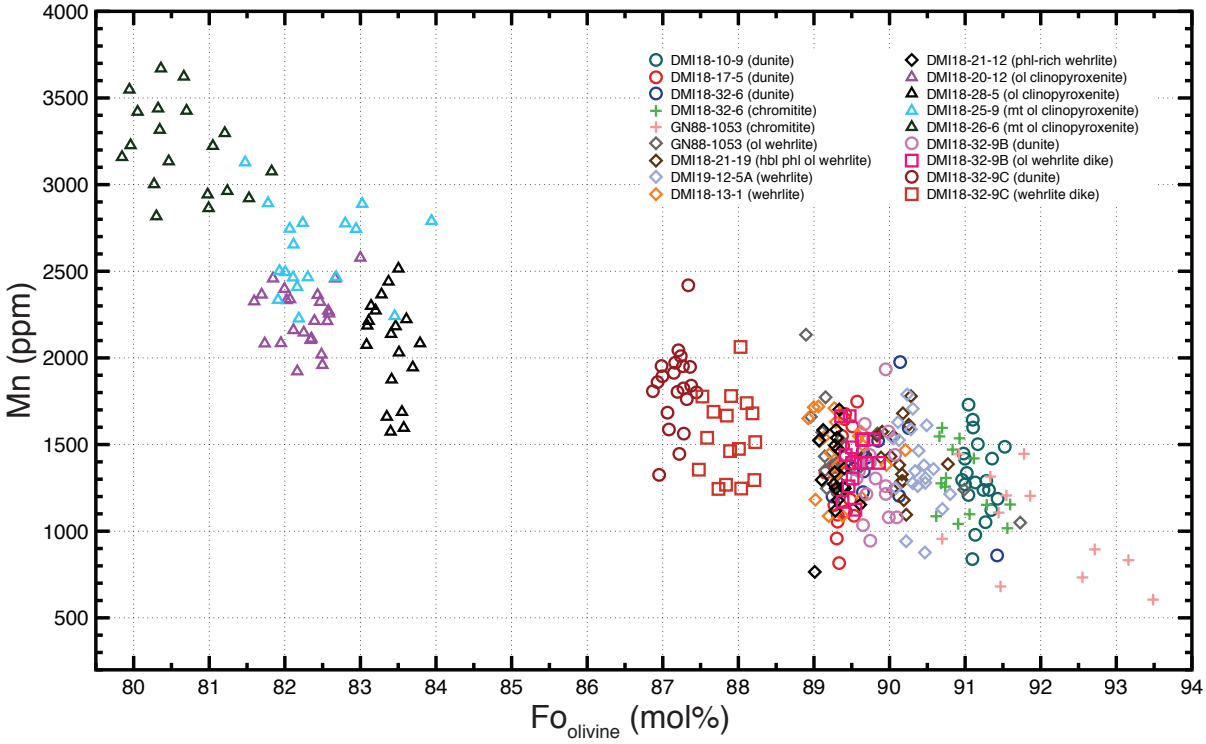

Figure 4.12. Plots of Mn concentrations (ppm) vs. forsterite content (mol. %) of olivine for representative olivine-bearing lithologies from the Polaris intrusion. Mn concentrations in olivine show a general increasing trend with decreasing forsterite content, with a total range of ~605 ppm at $Fo_{93.5}$ to 3670 ppm at Fo_{80}.

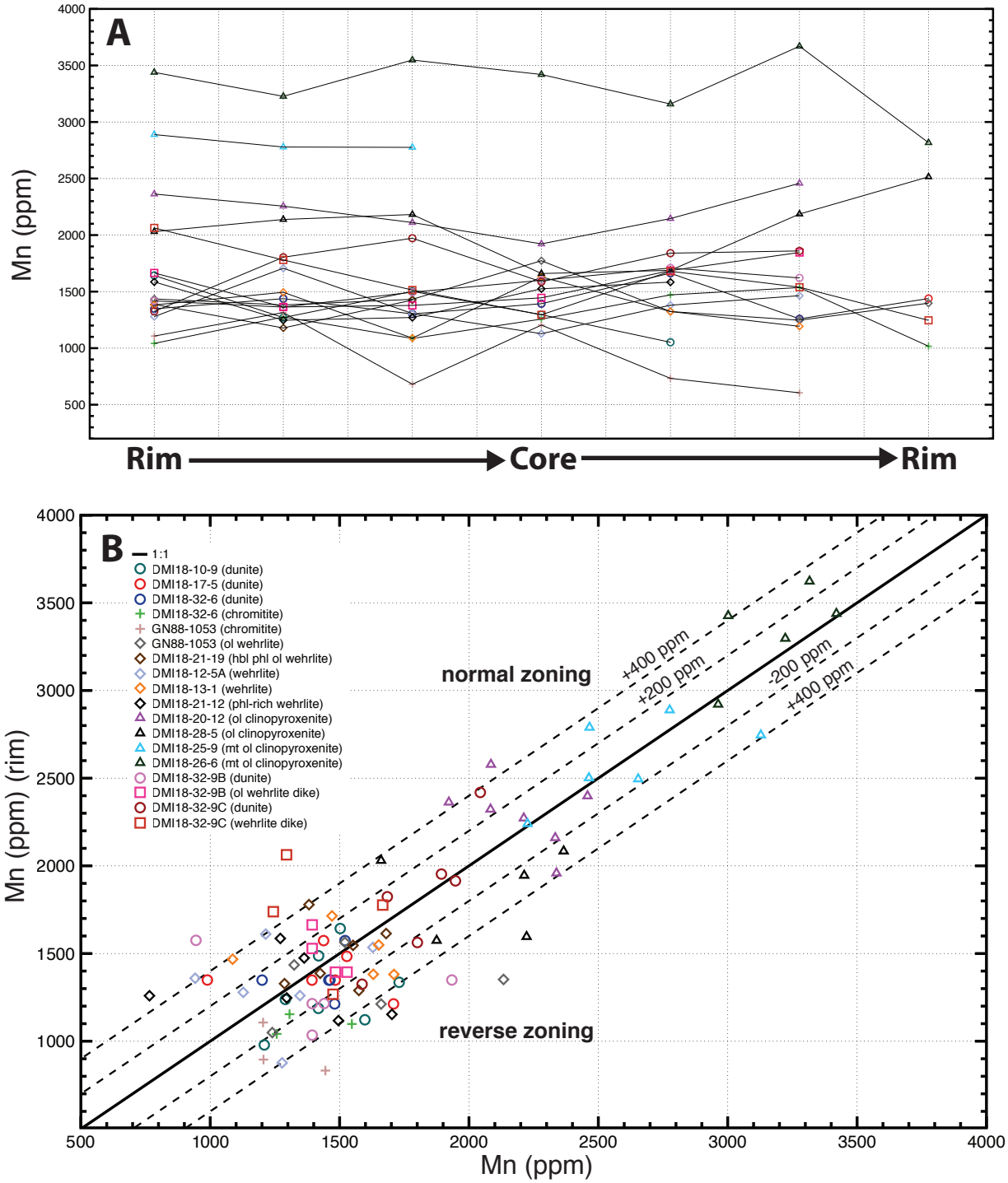

Figure 4.13. Plots of Mn concentration (ppm) of olivine across individual grains for representative olivine-bearing rocks from the Polaris intrusion. A) Mn concentrations of representative olivine grains from each thin section analyzed, from rim to core to rim (note that the x-axis scale is relative and does not show absolute distances). There is no systematic Mn zonation across grains of olivine. B) Mn concentrations of rims vs. cores for each olivine grain analyzed compared to the solid 1:1 line (i.e., no zoning). The field above the solid line indicates normal zoning and the field below indicates reverse zoning. Labeled dashed lines show relative difference between Mn concentrations (ppm) of core and rim. Mn concentrations of olivine cluster on either side of the 1:1 line for all lithologies.

spans a wide range from (1605-3108 ppm). A phlogopite-rich wehrlite (DMI18-21-12; $Fo_{89.0-89.6}$) has the highest Ni concentrations of all the samples analyzed (2972-3108 ppm).

In olivine clinopyroxenite, olivine compositions are relatively Fe-rich (Fo_{79-84}). There is a significant overlap in olivine compositions between the magnetite-poor olivine clinopyroxenite and magnetite olivine clinopyroxenite with a slightly more limited range of forsterite contents for the magnetite-poor olivine clinopyroxenite ($Fo_{81.5-84}$). The two types of olivine clinopyroxenite do, however, have distinct Ni concentrations. In magnetite-poor olivine clinopyroxenites, Ni ranges from ~1305-2090 ppm, which is well within the same ranges defined by dunite, olivine wehlrite, and wehrlite. In magnetite-olivine clinopyroxenite Ni concentrations of olivine are the lowest recorded in the Polaris intrusion with a range from ~275 to 550 ppm.

One of the ultramafic dike samples shows slight differences in olivine compositions compared to its host dunite (DMI18-32-9C), whereas there is a significant overlap in olivine compositions from another ultramafic dike sample and its host dunite (DMI18-32-9B). In sample DMI18-32-9C, the dunite host has olivine of $Fo_{87-87.5,}$ compared to $Fo_{87.5-88.5}$ olivine for the wehrlite dike; however, the Ni concentrations are very different (~975-1360 ppm in the dunite host; ~2050-2420 ppm in the wehrlite dike). The mineralogically more “primitive host” shows olivine compositions with slightly lower forsterite contents and lower Ni concentrations, indicative of a more evolved melt, than the mineralogically more “evolved” dike. Sample DMI18-32-9B shows less mineralogical diversity between the host dunite and the olivine wehrlite dike, which may explain the lack of chemical difference between the two populations of olivine grains.

Table 3. Representative electronprobe microanalyses (EPMA) of olivine from the Polaris Alaskan-type intrusion

Spot	Oxides (wt.%)									Cations (p.f.u.)								End Members (mol. %)	
	Location	SiO_2	Cr_2O_3	MgO	MnO	FeO	CaO	NiO	Total	Si	Cr	Mg	Mn	Fe	Ca	Ni	Sum	Fo[1]	Fa[1]
DMI18-10-9-2-1-c1	core	41.13	0.00	49.87	0.18	8.79	0.11	0.31	100.40	1.000	0.000	1.808	0.004	0.179	0.003	0.006	3.00	91.0	9.0
DMI18-10-9-2-1-m2	mid	40.90	0.02	49.79	0.19	8.80	0.13	0.30	100.12	0.998	0.000	1.811	0.004	0.180	0.003	0.006	3.00	91.0	9.0
DMI18-10-9-2-1-r3	rim	40.85	0.04	50.26	0.15	8.40	0.06	0.29	100.05	0.996	0.001	1.826	0.003	0.171	0.001	0.006	3.00	91.4	8.6
DMI18-12-5A-1-1-c1	core	41.07	0.01	50.14	0.17	9.56	0.05	0.27	101.27	0.994	0.000	1.809	0.004	0.193	0.001	0.005	3.01	90.3	9.7
DMI18-12-5A-1-1-m2	mid	40.64	0.07	49.56	0.21	9.51	0.03	0.27	100.29	0.994	0.001	1.806	0.004	0.194	0.001	0.005	3.01	90.3	9.7
DMI18-12-5A-1-1-r3	rim	40.84	0.00	49.86	0.16	9.47	0.02	0.26	100.63	0.994	0.000	1.809	0.003	0.193	0.001	0.005	3.01	90.4	9.6
DMI18-13-1-2-1-c1	core	40.57	0.00	48.68	0.14	10.51	0.02	0.22	100.14	0.997	0.000	1.783	0.003	0.216	0.001	0.004	3.00	89.2	10.8
DMI18-13-1-2-1-m2	mid	40.97	0.00	48.83	0.19	10.52	0.02	0.23	100.75	1.000	0.000	1.777	0.004	0.215	0.001	0.005	3.00	89.2	10.8
DMI18-13-1-2-1-r3	rim	41.06	0.00	49.63	0.19	9.60	0.02	0.22	100.71	0.999	0.000	1.799	0.004	0.195	0.000	0.004	3.00	90.2	9.8
DMI18-17-5-1-1-c1	core	40.82	0.00	48.78	0.13	10.45	0.07	0.27	100.51	0.999	0.000	1.779	0.003	0.214	0.002	0.005	3.00	89.3	10.7
DMI18-17-5-1-1-m2	mid	40.76	0.00	48.86	0.16	10.32	0.09	0.25	100.44	0.998	0.000	1.783	0.003	0.211	0.002	0.005	3.00	89.4	10.6
DMI18-17-5-1-1-r3	rim	40.55	0.00	48.35	0.17	10.13	0.06	0.26	99.53	1.001	0.000	1.779	0.004	0.209	0.002	0.005	3.00	89.5	10.5
DMI18-20-12-1-1-c1	core	39.04	0.02	43.09	0.27	17.17	0.02	0.24	99.86	0.994	0.000	1.635	0.006	0.365	0.001	0.005	3.01	81.7	18.3
DMI18-20-12-1-1-m2	mid	38.93	0.00	43.25	0.31	17.28	0.02	0.25	100.04	0.990	0.000	1.640	0.007	0.367	0.001	0.005	3.01	81.7	18.3
DMI18-20-12-1-1-r3	rim	39.66	0.00	44.03	0.30	16.69	0.02	0.25	100.94	0.995	0.000	1.647	0.006	0.350	0.000	0.005	3.00	82.5	17.5
DMI18-21-12-1-1-c1	core	40.36	0.00	48.77	0.22	10.38	0.01	0.39	100.14	0.993	0.000	1.788	0.005	0.213	0.000	0.008	3.01	89.3	10.7
DMI18-21-12-1-1-m2	mid	40.66	0.00	48.81	0.15	10.41	0.01	0.40	100.44	0.996	0.000	1.783	0.003	0.213	0.000	0.008	3.00	89.3	10.7
DMI18-21-12-1-1-r3	rim	41.12	0.02	48.67	0.15	10.06	0.01	0.39	100.41	1.005	0.000	1.773	0.003	0.206	0.000	0.008	2.99	89.6	10.4
DMI18-21-19-1-1-1c	core	40.76	0.01	50.01	0.18	9.76	0.02	0.29	101.03	0.990	0.000	1.811	0.004	0.198	0.000	0.006	3.01	90.1	9.9
DMI18-21-19-1-1-2m	mid	40.58	0.00	49.51	0.14	9.57	0.02	0.29	100.10	0.994	0.000	1.807	0.003	0.196	0.000	0.006	3.01	90.2	9.8
DMI18-21-19-1-1-3r	rim	40.35	0.00	49.19	0.20	9.85	0.02	0.29	99.91	0.992	0.000	1.803	0.004	0.202	0.001	0.006	3.01	89.9	10.1

[1] $Fo = Mg^{2+}/(Mg^{2+}+Fe^{2+}) \times 100$; Fa = 100-Fo

Table 3. (continued) Representative electronprobe microanalyses of olivine from the Polaris Alaskan-type intrusion

Spot	Oxides (wt.%)									Cations (p.f.u.)								End Members (mol. %)	
	Location	SiO_2	Cr_2O_3	MgO	MnO	FeO	CaO	NiO	Total	Si	Cr	Mg	Mn	Fe	Ca	Ni	Sum	Fo[1]	Fa[1]
DM118-25-9-1-2-1c	core	39.41	0.05	44.57	0.36	16.51	0.03	0.05	100.98	0.988	0.001	1.666	0.008	0.346	0.001	0.001	3.01	82.8	17.2
DM118-25-9-1-2-2m	mid	39.17	0.00	43.69	0.36	16.82	0.04	0.05	100.13	0.992	0.000	1.650	0.008	0.356	0.001	0.001	3.01	82.2	17.8
DM118-25-9-1-2-3r	rim	39.58	0.02	44.52	0.37	16.23	0.04	0.06	100.82	0.992	0.000	1.664	0.008	0.340	0.001	0.001	3.01	83.0	17.0
DMI18-26-6-3-1-c1	core	39.38	0.00	42.10	0.39	18.45	0.04	0.05	100.41	1.001	0.000	1.595	0.008	0.392	0.001	0.001	3.00	80.3	19.7
DMI18-26-6-3-1-m2	mid	39.34	0.01	42.91	0.37	17.95	0.04	0.04	100.67	0.996	0.000	1.619	0.008	0.380	0.001	0.001	3.00	81.0	19.0
DMI18-26-6-3-1-r3	rim	39.49	0.01	42.42	0.44	18.09	0.03	0.05	100.53	1.001	0.000	1.603	0.009	0.383	0.001	0.001	3.00	80.7	19.3
DMI18-28-5-1-1-c1	core	39.23	0.00	44.47	0.31	15.92	0.01	0.25	100.20	0.990	0.000	1.673	0.007	0.336	0.000	0.005	3.01	83.3	16.7
DMI18-28-5-1-1-m2	mid	38.95	0.05	44.12	0.27	16.02	0.02	0.27	99.70	0.989	0.001	1.669	0.006	0.340	0.001	0.005	3.01	83.1	16.9
DMI18-28-5-1-1-r3	rim	39.61	0.00	44.87	0.27	15.47	0.02	0.25	100.50	0.993	0.000	1.677	0.006	0.325	0.001	0.005	3.01	83.8	16.2
DMI18-32-6-3-1-c1	core	40.57	0.01	48.94	0.16	10.51	0.14	0.27	100.59	0.993	0.000	1.786	0.003	0.215	0.004	0.005	3.01	89.2	10.8
DMI18-32-6-3-1-m2	mid	40.66	0.01	49.02	0.16	10.09	0.12	0.28	100.33	0.996	0.000	1.790	0.003	0.207	0.003	0.005	3.00	89.6	10.4
DMI18-32-6-3-1-r3	rim	40.92	0.00	49.47	0.26	9.64	0.06	0.28	100.63	0.997	0.000	1.797	0.005	0.197	0.002	0.006	3.00	90.1	9.9
DMI18-32-6-4-2-c1	core	41.21	0.03	49.89	0.20	9.16	0.11	0.28	100.89	0.999	0.001	1.803	0.004	0.186	0.003	0.005	3.00	90.7	9.3
DMI18-32-6-4-2-m2	mid	41.24	0.00	50.05	0.21	9.15	0.10	0.28	101.04	0.998	0.000	1.806	0.004	0.185	0.003	0.005	3.00	90.7	9.3
DMI18-32-6-4-2-r3	rim	41.35	0.01	50.24	0.14	8.79	0.11	0.27	100.91	1.000	0.000	1.811	0.003	0.178	0.003	0.005	3.00	91.1	8.9
DMI18-32-9B-1-1-c1	core	40.65	0.03	48.47	0.18	10.13	0.02	0.23	99.72	1.001	0.001	1.779	0.004	0.209	0.001	0.005	3.00	89.5	10.5
DMI18-32-9B-1-1-m2	mid	40.70	0.00	49.06	0.15	10.39	0.01	0.23	100.55	0.996	0.000	1.788	0.003	0.213	0.000	0.005	3.00	89.4	10.6
DMI18-32-9B-1-1-r3	rim	40.45	0.00	48.69	0.21	10.21	0.02	0.24	99.83	0.996	0.000	1.788	0.004	0.210	0.001	0.005	3.00	89.5	10.5
DMI18-32-9B-4-1-c1	core	40.52	0.00	49.28	0.18	10.04	0.04	0.23	100.30	0.993	0.000	1.800	0.004	0.206	0.001	0.004	3.01	89.7	10.3
DMI18-32-9B-4-1-m2	mid	40.69	0.00	49.36	0.16	9.83	0.05	0.24	100.34	0.995	0.000	1.799	0.003	0.201	0.001	0.005	3.00	89.9	10.1
DMI18-32-9B-4-1-r3	rim	40.83	0.00	49.39	0.13	10.17	0.02	0.24	100.78	0.995	0.000	1.795	0.003	0.207	0.000	0.005	3.00	89.6	10.4

[1] $Fo = Mg^{2+}/(Mg^{2+}+Fe^{2+}) \times 100$; Fa = 100-Fo

Table 3. (continued) Representative electronprobe microanalyses (EPMA) of olivine from the Polaris Alaskan-type intrusion

Spot	Oxides (wt.%)									Cations (p.f.u.)								End Members (mol. %)	
	Location	SiO_2	Cr_2O_3	MgO	MnO	FeO	CaO	NiO	Total	Si	Cr	Mg	Mn	Fe	Ca	Ni	Sum	Fo[1]	Fa[1]
DMI18-32-9C-1-1-1c	core	40.57	0.00	47.45	0.25	12.24	0.04	0.16	100.71	0.999	0.000	1.741	0.005	0.252	0.001	0.003	3.00	87.4	12.6
DMI18-32-9C-1-1-m2	mid	40.36	0.00	47.47	0.26	12.38	0.03	0.15	100.65	0.995	0.000	1.745	0.005	0.255	0.001	0.003	3.00	87.2	12.8
DMI18-32-9C-1-1-r3	rim	40.23	0.02	47.65	0.25	12.53	0.03	0.17	100.88	0.991	0.000	1.750	0.005	0.258	0.001	0.003	3.01	87.1	12.9
DMI18-32-9C-6-1-c1	core	40.72	0.02	47.53	0.22	11.72	0.05	0.26	100.52	1.002	0.000	1.743	0.004	0.241	0.001	0.005	3.00	87.8	12.2
DMI18-32-9C-6-1-m2	mid	40.66	0.00	47.82	0.17	12.20	0.05	0.26	101.17	0.996	0.000	1.747	0.004	0.250	0.001	0.005	3.00	87.5	12.5
DMI18-32-9C-6-1-r3	rim	40.18	0.00	47.47	0.23	12.06	0.02	0.26	100.23	0.994	0.000	1.751	0.005	0.250	0.001	0.005	3.01	87.5	12.5
GN88-1053-1-1-c1	core	41.15	0.00	48.85	0.28	10.88	0.07	0.34	101.57	0.999	0.000	1.768	0.006	0.221	0.002	0.007	3.00	88.9	11.1
GN88-1053-1-1-m2	mid	40.31	0.04	48.52	0.20	10.57	0.06	0.35	100.03	0.993	0.001	1.782	0.004	0.218	0.002	0.007	3.01	89.1	10.9
GN88-1053-1-1-r3	rim	40.82	0.07	49.24	0.17	10.22	0.04	0.35	100.91	0.995	0.001	1.789	0.004	0.208	0.001	0.007	3.00	89.6	10.4
GN88-1053-3-1-c1	core	40.85	0.01	50.78	0.16	8.36	0.07	0.34	100.57	0.991	0.000	1.836	0.003	0.170	0.002	0.007	3.01	91.5	8.5
GN88-1053-3-1-m2	mid	40.80	0.01	50.90	0.19	8.13	0.07	0.35	100.44	0.990	0.000	1.842	0.004	0.165	0.002	0.007	3.01	91.8	8.2
GN88-1053-3-1-r3	rim	41.41	0.05	51.83	0.12	7.26	0.03	0.33	101.03	0.994	0.001	1.855	0.002	0.146	0.001	0.006	3.01	92.7	7.3

[1] $Fo = Mg^{2+}/(Mg^{2+}+Fe^{2+}) \times 100$; $Fa = 100-Fo$

5. Discussion

5.1. Constraints on magmatic differentiation processes in the Polaris intrusion from olivine Fo-Ni relationships

5.1.1. Nature of the primitive initial melt

The forsterite content of olivine, described as $Fo_{olivine} = [Mg/(Mg+Fe^{2+}) \times 100]$, is closely related to the melt composition from which it crystallizes (Roeder and Emslie, 1970). The partitioning of Mg-Fe into olivine, expressed as the partition coefficient K_D^{Fe-Mg} $([X_{Fe}/X_{Mg}]^{ol}/[X_{Fe}/X_{Mg}]^{liq}$ where X represents the mole fraction of the element, is constant over a relatively wide range of temperatures (1150-1300˚C) and pressures (e.g., Roeder and Emslie, 1970; Ulmer, 1989; Putirka, 2005). The constancy of this coefficient ($K_D^{Fe-Mg} = 0.3$; Roeder and Emslie, 1970) over a wide range of conditions means that the ratio of Mg to Fe in olivine provides direct information on the melt-olivine equilibrium composition (Langmuir and Hanson, 1981). The forsterite content of olivine can thus be used to determine the degree of differentiation a melt has undergone from derivation as partial melt from its source (i.e., primitive melt) prior to crystallization. In contrast, the Ni concentrations of olivine are much more variable across different mantle sources (e.g., Sobolev *et al*., 2005; Sobolev *et al*., 2007; Putirka *et al*., 2011; Lynn *et al*., 2017) as demonstrated by the compositional variations of Hawaiian olivine (Fig. 5.1). The Ni partition coefficient between olivine and melt (Kd^{Ni}) is directly affected by the Mg-content of the melt (e.g., Hart and Davis, 1978; Kinzler *et al*., 1990; Beattie *et al*., 1991; Straub *et al*., 2008; Matzen *et al*., 2017).

Olivine, typically the first silicate phase to crystallize from basaltic and ultramafic magmas (e.g., Bowen 1929), is the dominant phase in the Polaris Alaskan-type intrusion. The major element composition of olivine in the olivine-dominant lithologies (i.e., dunite, olivine

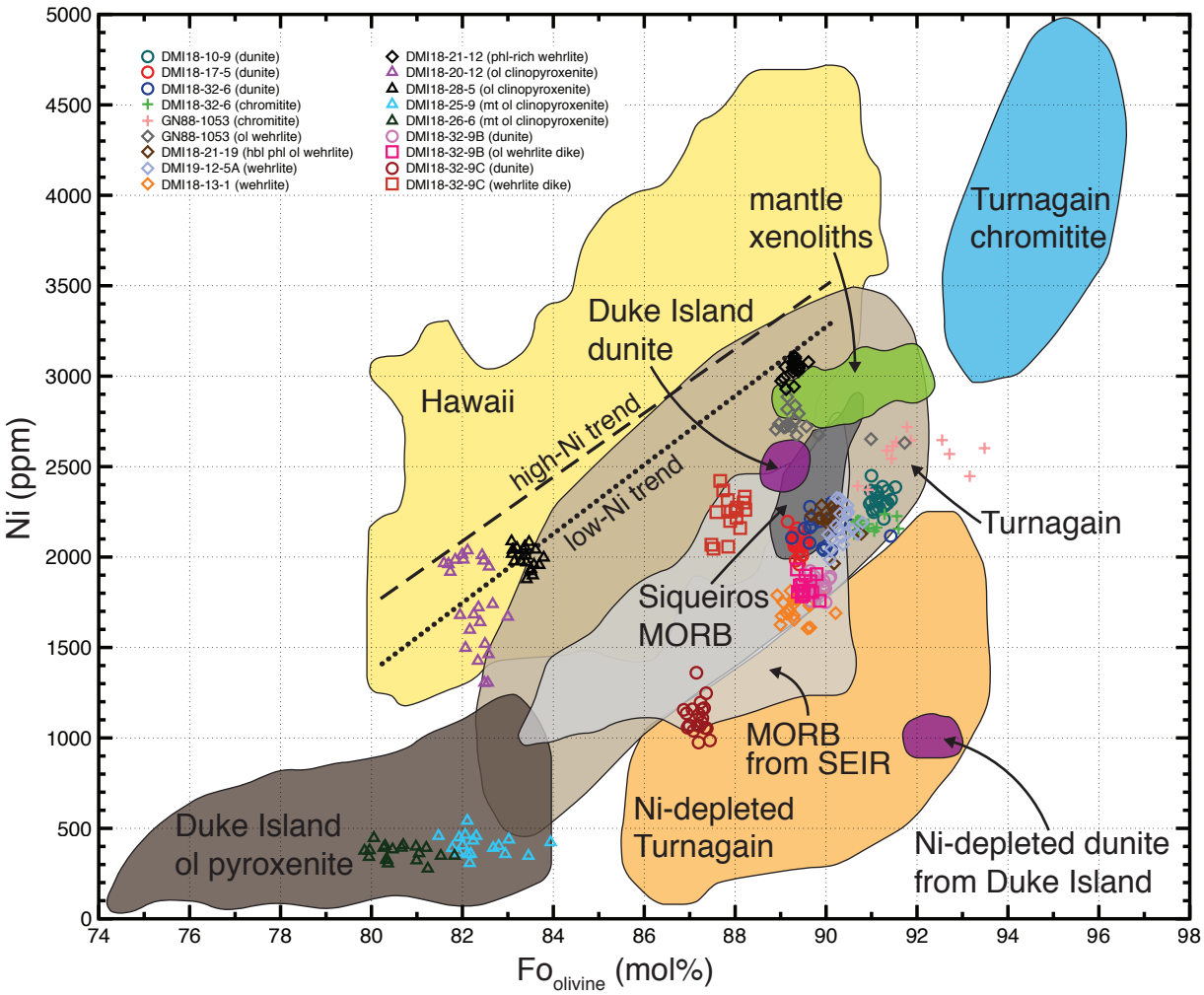

Figure 5.1. Ni concentrations (ppm) vs. forsterite content (mol. %) of olivine for representative olivine-bearing lithologies from the Polaris intrusion compared to olivine from the Duke Island Alaskan-type intrusion (modified from Thakurta et al., 2008), the Turnagain Alaskan-type intrusion (modified from Scheel, 2007), and olivine from various tectonic settings. Dunites from the Duke Island intrusion (purple fields) show dunite with "normal" Ni compositions, and Ni-depleted dunite as a result of sulfide-saturation. Olivine clinopyroxenite from the Duke Island intrusion are shown in the dark-brown field. Olivine compositions from the Turnagain intrusion form three distinct groups: "normal" dunite, wehrlite, and olivine clinopyroxenite (beige field); Ni-depleted dunite, wehrlite, and olivine clinopyroxenite (orange field) caused by sulfide-saturation; and olivine from chromitite (blue field) with high-Ni and Fo content. Hawaiian olivine compositions (yellow field) are modified from Lynn et al. (2017) and include a low-Ni and high-Ni trend denoted by the dotted black line and dashed black line, respectively. Mantle xenolith compositions (green field) are from various tectonic settings globally and are restricted to a relatively limited range of compositions (Herzberg et al., 2013). The field for olivine compositions from the South East Indian Rise (SEIR) MORB (light-grey field) has been modified from Sobolev et al. (2007). The field for olivine compositions from the Siqueiros MORB (dark-grey field), modified from Herzberg et al. (2016), is likely compositionally representative of all MORB.

wehrlite, wehrlite) is representative of the degree of differentiation that the parental magma underwent between separation from the mantle wedge source and emplacement in the shallow crust. The average forsterite content in Polaris olivine from dunite, olivine wehrlite, and wehrlite is essentially identical, ranging from $Fo_{89.5}$ (dunite) to $Fo_{89.3}$ (wehrlite) (Fig. 4.6). The composition of mantle olivine, determined through the analysis of olivine in peridotite mantle xenoliths, generally ranges from Fo_{88}-Fo_{92} (Fig. 5.1) (Ulmer, 2001; Herzberg *et al*., 2013). Olivine compositions from mantle xenoliths in the Canadian Cordillera also span this range, implying that primitive melts derived from the mantle wedge below British Columbia should be in equilibrium with olivine compositions spanning this range (Arai and Ishimaru, 2008). Because of the pressure and temperature independence of $K_D^{Fe\text{-}Mg}$, this equilibrium relationship holds for a variety of emplacement and crystallization depths and conditions. Given that the relationship between the melt composition and the forsterite content of olivine is direct when expressed as a ratio, very little needs to be known about the actual composition of the parental magma to assess the degree of differentiation that has occurred between the melt and its mantle source prior to crystallizing olivine. Although the parent melt composition for the Polaris intrusion is not known, the Mg-rich olivine compositions from dunite, olivine wehrlite, and wehrlite ($Fo_{89\text{-}91}$) are consistent with melts that were also in equilibrium with mantle olivine (Fo_{88}-Fo_{92}). The Mg-rich olivine compositions from the Polaris intrusion indicate that very little differentiation occurred between derivation from the mantle wedge before crystallization in a crustal magma chamber.

The Mg-rich olivine compositions from the Polaris intrusion overlap with olivine from other subduction zone mantle-derived primary melts, including the Mexican Volcanic Belt and the Kamchatka arc (Fig. 5.2). Mg-rich olivine from basaltic andesites and andesites from the Mexican Volcanic Belt is considered to be derived from heterogeneous primary mantle melts of

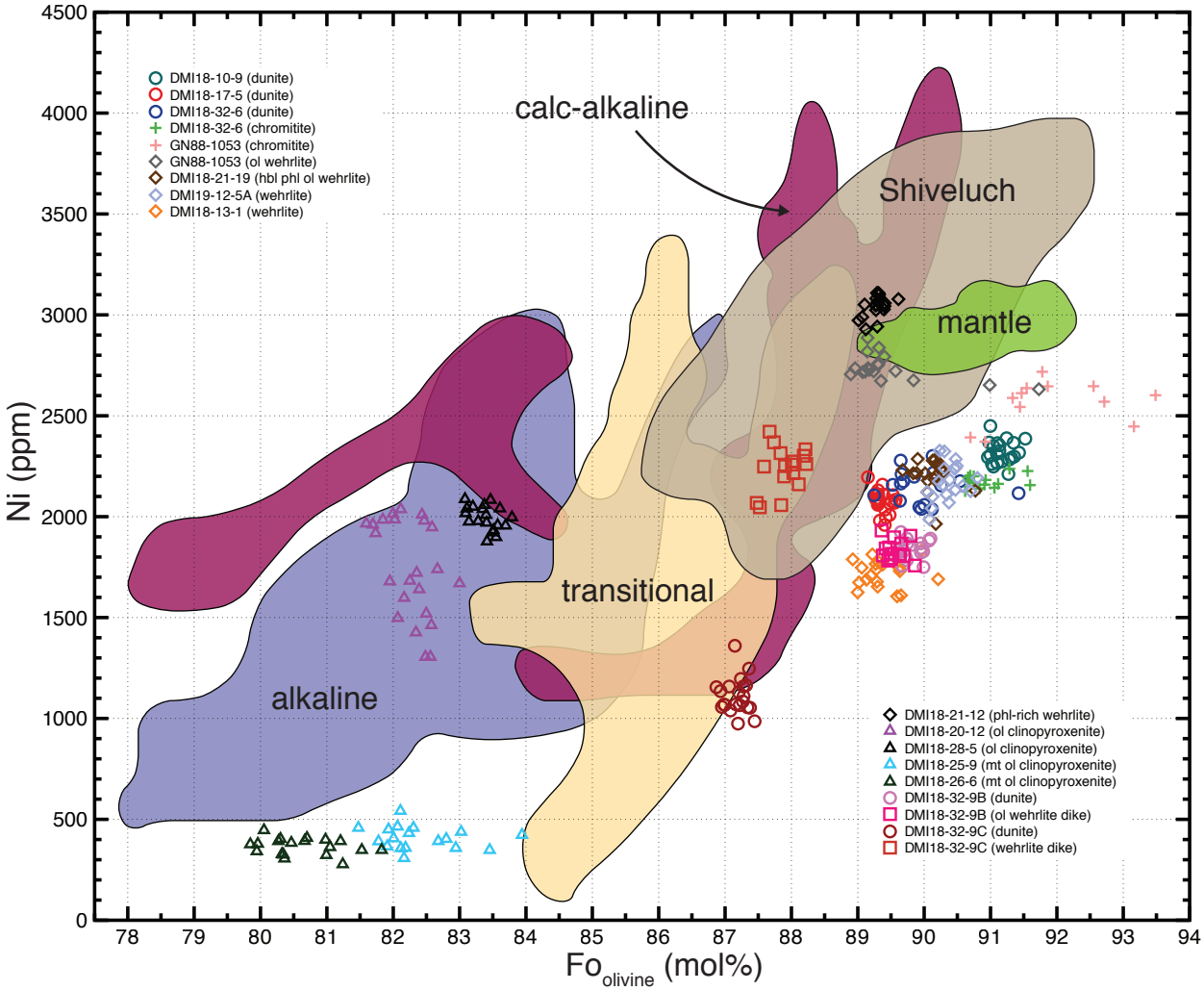

Figure 5.2. Ni concentrations (ppm) vs. forsterite content (mol. %) of olivine for representative olivine-bearing lithologies from the Polaris intrusion compared to olivine from the central Mexican Volcanic Belt (modified from Straub et al., 2008) and olivine from the Kamchatka arc (modified from Gordeychik et al., 2018). Alkaline (lavender field), transitional (yellow field), and calc-alkaline (maroon fields) olivine compositions from the Mexican Volcanic Belt are shown. Olivine core compositions from the Shiveluch volcano (Kamchatka arc) (beige field) represent primitive compositions. Mantle xenolith compositions (green field) are from various tectonic settings globally and are restricted to a relatively limited range of compositions (Herzberg et al., 2013). The forsterite content of olivine from dunite, olivine wehrlite, and werhlite from the Polaris intrusion overlap with the olivine compositions of mantle xenoliths and the most primitive olivine from the Shiveluch volcano and the Mexican Volcanic Belt.

both peridotite and pyroxenite (Straub *et al*., 2008). Zoned olivine from the Shiveluch volcano in the Kamchatka arc captures the entire evolution of the melt from its mantle source to eruption due to the fast-erupting nature of the volcanic system as demonstrated by the abundance of mantle peridotite xenoliths (Gordeychik *et al*., 2018). Shiveluch olivine records primary olivine forsterite contents of Fo_{92}, re-equilibration due to mixing with evolved melts that produced olivine overgrowths of Fo_{86}, and later overgrowths (Fo_{90}) formed from recharged melts (Gordeychik *et al*., 2018). Mg-rich olivine (Fo_{89-91}) from the Polaris Alaskan-type intrusion overlap with the forsterite contents of primary and recharge olivine forsterite contents from Shiveluch and the Mexican Volcanic belt suggesting that the initial melts forming the Polaris Alaskan-type intrusion are also highly undifferentiated and primitive.

5.1.2. Fractional crystallization trends

As noted above, the olivine Ni partition coefficient (Kd^{Ni}) is a strong function of the Mg content of the melt (e.g., Hart and Davis, 1978; Kinzler *et al*., 1990; Beattie *et al*., 1991; Matzen *et al*., 2017). This means that the Ni concentration and forsterite content of olivine have a systematic relationship during closed fractional crystallization – the Ni concentration of olivine will decrease with decreasing forsterite content (e.g., Sobolev *et al*., 2007; Straub *et al*., 2008; Putirka *et al*., 2011; Herzberg *et al*., 2013; Herzberg *et al*., 2016; Gordeychik *et al*., 2018). In general, the most Mg-rich crystals will contain the highest Ni concentrations and olivine compositions will define a curve during fractional crystallization as the melt becomes more and more depleted in Mg relative to its initial state.

The Fo-Ni relationships of olivine in the Polaris intrusion indicate a strong fractional crystallization control from dunite, olivine werhlite, and wehrlite to magnetite-rich olivine

clinopyroxenite based on comparison to fractional crystallization trends defined for olivine from volcanic rocks in the central Mexican Volcanic Belt (MVB) using different partial melting models of peridotite (Straub *et al*., 2008) (Fig. 5.3). Ni contents vary significantly in olivine globally (i.e., Hawaii: Lynn *et al*., 2017) and the most primitive olivine compositions in the Polaris intrusion are similar to olivine from other primitive mantle peridotite-derived magmas (i.e., Siqueiros MORB: Herzberg *et al*., 2016) (Fig. 5.1). In Figure 5.3, three fractional crystallization curves from Straub *et al*. (2008), at 1% increments, are depicted: 1) olivine compositions derived from a serial-melted peridotite that has just started undergoing melting; 2) olivine compositions derived from a serial-melted peridotite that has undergone melt extraction of 70% at 2% steps; 3) olivine compositions derived from approximately 30% batch melting from a single peridotite source. For Polaris, the distribution of many of the measured olivine compositions is consistent with these fractional crystallization trends and most closely follows curve 2 noted above. However, several samples, including both magnetite-poor olivine clinopyroxenites (DMI18-20-12, DMI18-28-5), contain olivine with distinctively elevated Ni concentrations for a given Fo content and do not follow the fractional crystallization trends (Fig. 5.3) and these unusual compositions are addressed below.

5.1.3. Effects of recharge and magma mixing

Several processes can account for elevated Ni concentrations in olivine for a given forsterite content compared to a system dominated by fractional crystallization. Crystallization of olivine from magmas derived a pyroxenite or hybrid pyroxenite-peridotite mantle source can produce relatively Ni-rich olivine (e.g., Sobolev *et al*., 2005; Sobolev *et al*., 2007; Straub *et al*., 2008; Lynn *et al*., 2017) and this process is advocated for the high-Ni olivine in Hawaiian basalts

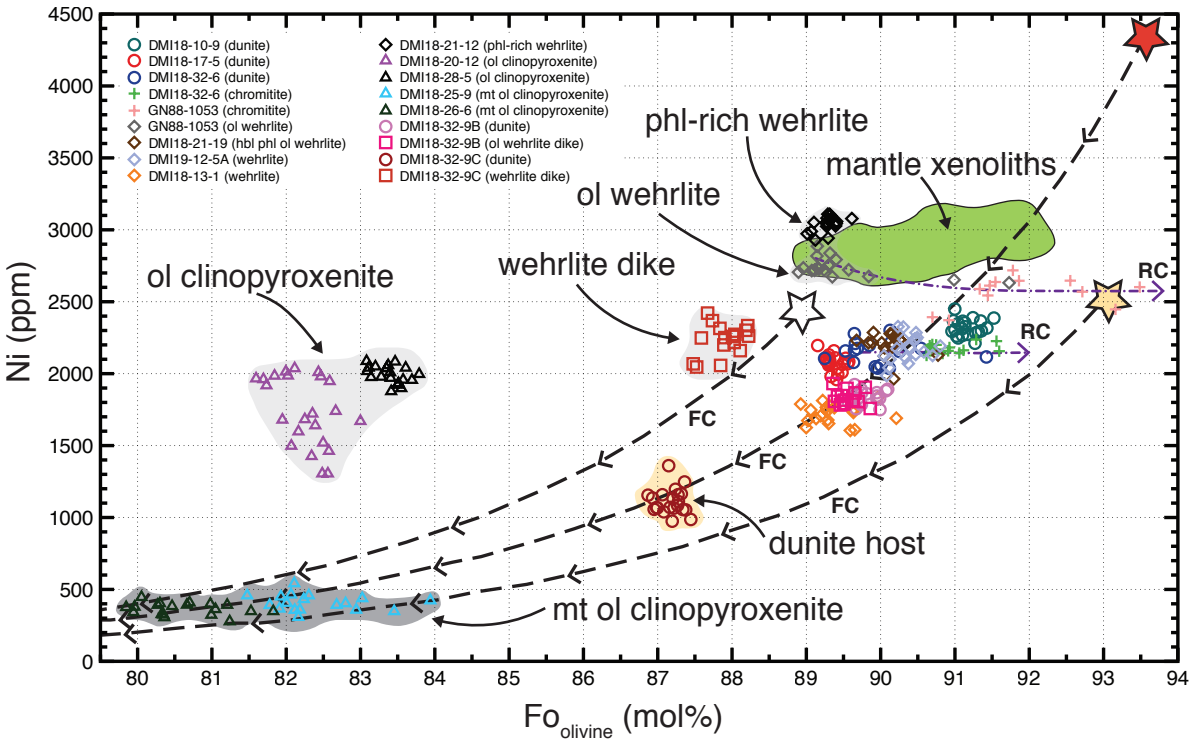

Figure 5.3. Ni concentrations (ppm) vs. forsterite content (mol. %) of olivine for representative olivine-bearing lithologies from the Polaris intrusion showing representative fractional crystallization and chromite re-equilibration trends. The nearly horizontal purple dash-dot lines (labelled RC) represent Mg-enrichment trends of olivine following re-equilibration with chromite (RC). The thick dashed lines (labelled FC) have been modified from Straub et al. (2008) and show the evolution of olivine compositions modelled by 1% increments of fractional crystallization (FC) for subduction zone magmas in the central Mexican Volcanic Belt for comparison. The white-filled star represents the starting olivine composition from a serial melting peridotite that has just started undergoing melting. The red-filled star represents the starting olivine composition from a serial melting peridotite that has undergone melt extraction of 70% at 2% steps. The yellow-filled star represents the starting olivine composition from approximately 30% batch melting from a single peridotite source. Most of the Polaris olivine compositions plot roughly along these fractional crystallization trends. Note that olivine compositions in magnetite-poor olivine clinopyroxenites (DMI18-20-12; DMI18-28-5), a wehrlite dike (DMI18-32-9C), an olivine wehrlite (GN88-1053), and a phlogopite-rich wehrlite (DMI18-21-12) are too high in Ni (light-grey fields) to be explained by these olivine fractional crystallization trends. Low-Ni olivine clinopyroxenites (dark-grey field) and the dunite host of DMI18-32-9C (yellow field) plot along fractional crystallization trends.

(Sobolev *et al*., 2005; Lynn *et al*., 2017). In the central Mexican Volcanic Belt (MVB), the high Ni concentrations in olivine are considered to result partially from mixing between a pyroxenite and peridotite source (Straub *et al*., 2008). Olivine that crystallizes from a pyroxenite source, however, will generally exhibit steep fractional crystallization trends, or partial fractional crystallization trends, that start with higher Ni concentrations than those anticipated from a peridotite source (Straub *et al*., 2008). There is no evidence from Polaris olivine for fractional crystallization trends originating with high-Ni, high-Fo compositions that may be indicative of a pyroxenite, and partly pyroxenitic, source.

Magma mixing between evolved and primitive melts as a result of magma recharge in a crustal reservoir is another process that can account for high Ni concentrations in olivine for a given forsterite content (Straub *et al*., 2008; Herzberg *et al*., 2013; Herzberg *et al*., 2016; Gordeychik *et al*., 2018). The evolved melt that is produced will crystallize olivine with an excess of Ni (e.g., Beattie *et al*., 1991). Such a process has been invoked for olivine from the central Mexican Volcanic Belt (Straub *et al*., 2008) and olivine from Theistareykir, Iceland (Herzberg *et al*., 2016). Magma mixing may account for the Ni-rich olivine in the Polaris intrusion (Fig. 5.4). In Figure 5.4, mixing lines (red lines) from Herzberg *et al*. (2016) are used to illustrate this effect and show mixing between a conventional crystal-line-of-descent (blue line) and an initial olivine composition representative for MORB (blue-filled star). The Fo-Ni relationships of olivine from the wehrlite dike (DMI18-32-9B) and the two magnetite-poor olivine clinopyroxenites (DMI18-20-12, DMI18-28-5) are consistent with crystallization from mixed magmas. These magnetite-poor clinopyroxenites, with Ni-rich olivine, also contain small amounts of sulfide with a Ni-rich assemblage (pentlandite, pyrrhotite + minor chalcopyrite)

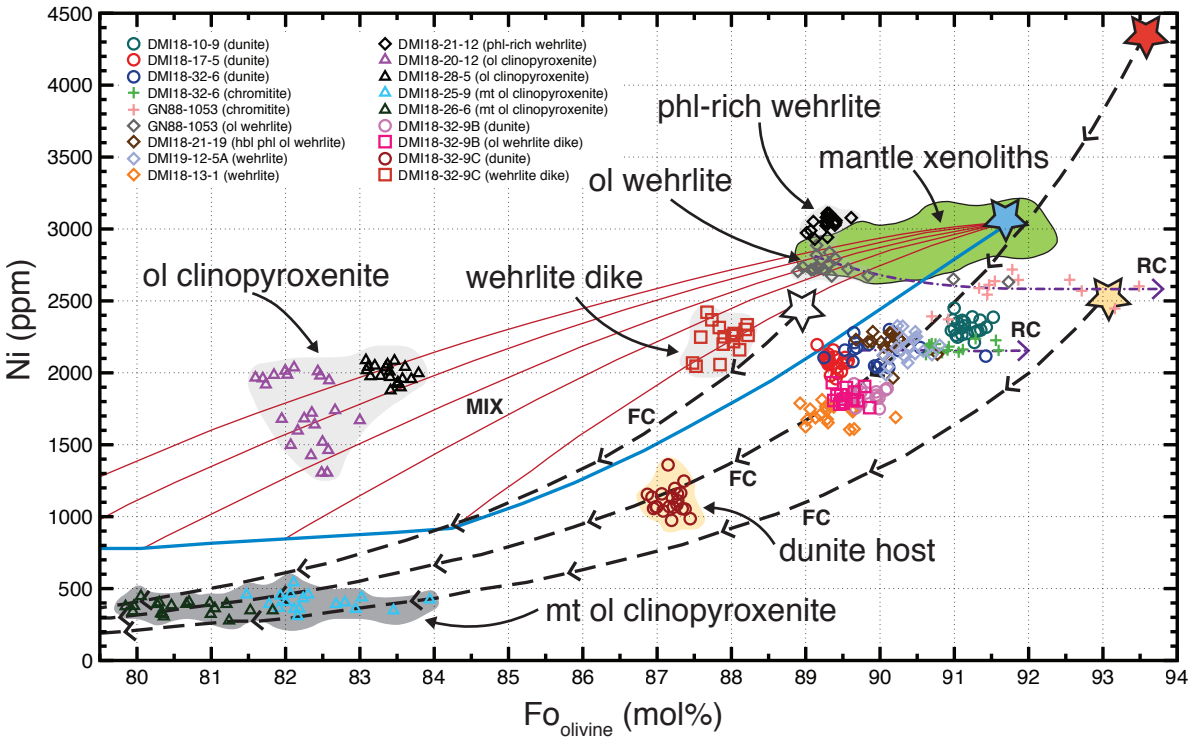

Figure 5.4. Ni concentrations (ppm) vs. forsterite content (mol. %) of olivine for representative olivine-bearing lithologies from the Polaris intrusion showing mixing lines (MIX) compared to fractional crystallization (FC) trends. The solid blue line has been modified from Herzberg et al. (2016) and represents olivine compositions that would crystallize along a liquid line of descent from an initial composition depicted by the blue-filled star and is likely representative of a MORB trend. Solid red lines are mixing lines that represent olivine compositions that would crystallize due to mixing of primary magmas (blue-filled star) with derivative magmas produced by fractional crystallization (solid blue line). All other trends and symbols are described in the caption to Figure 21. Mixing could explain the relatively Ni-rich olivine compositions in magnetite-poor olivine clinopyroxenites (DMI18-20-12; DMI18-28-5), a wehrlite dike (DMI18-32-9C), an olivine wehrlite (GN88-1053), and a phlogopite-rich wehrlite (DMI18-21-12).

compared to the magnetite-rich olivine clinopyroxenites, with low-Ni olivine, that contain small amounts of Cu-rich sulfide (chalcopyrite, bornite).

Outcrop-scale field relationships in the Polaris intrusion support the hypothesis of recharge and magma mixing. Ultramafic dikes with both sharp and irregular contacts are present throughout the intrusion and their emplacement has been interpreted to be evidence for multi-stage emplacement (Nott *et al*., 2020). One sample, DMI18-32-9C, contains a wehrlite dike cross-cutting dunite and olivine from the dike has a slightly higher forsterite content and a significantly higher Ni concentration on average than its host dunite. The composition of olivine in the dunite can be explained by fractional crystallization, whereas the olivine compositions in the wehrlite dike are best explained by a recharge and magma mixing process (Fig. 5.4). Chaotically mixed ultramafic cumulates are common in the central Polaris intrusion (Nixon *et al*., 1997; Nott *et al*., 2020). They have sharp to diffuse contacts between dunite, olivine wehrlite, and olivine clinopyroxenite. Chromitite schlieren, primarily hosted by dunite, are also found throughout the Polaris intrusion and are commonly disrupted and sheared (Nixon *et al*., 1997; Nott *et al*., 2020). Combined, the presence of ultramafic dikes, chaotically mixed ultramafic cumulates, and chromitite schlieren, and geochemical evidence for Ni-rich olivine that cannot be explained by simple fractional crystallization processes, indicates that magma recharge and mixing was likely an integral part to the emplacement and crystallization of the Polaris Alaskan-type intrusion.

5.1.4. Lack of zoning in Polaris olivine: diffusion and re-equilibration processes

Olivine from the Polaris intrusion shows compositions indicative of high-temperature diffusion and re-equilibration processes. Re-equilibration is most distinguished in chromitite-

hosted olivine (Fig. 5.3). Olivine gains that are entirely enveloped by chromite grains are enriched in Mg (up to $Fo_{93.5}$) relative to the host olivine (i.e., DMI18-32-6; GN88-1053). This effect has been described for olivine in other Alaskan-type intrusions, including the Turnagain intrusion in north-central B.C. (Fig. 5.1) (Clark, 1978; Scheel, 2007) and is ascribed to subsolidus Mg-Fe^{2+} re-equilibration between olivine and chromitite (Clark, 1978). The distribution coefficient for this relationship is described as $(Mg/Fe^{2+})^{Ol} \bullet (Fe^{2+}/Mg)^{Chr}$ and indicates that olivine will become richer in Mg relative to Fe^{2+} and chromite grains richer in Fe^{2+} relative to Mg, especially at high temperatures when exchange by diffusion is optimal (Clark, 1978).

Olivine from the Polaris intrusion is typically unzoned and does not show systematic zonation from core-to-rim of forsterite content, Ni concentration, or Mn concentration (Figs. 4.7, 4.9, 4.13). The diffusion of Mg-Fe, Ni, and Mn in olivine can occur on relatively short time scales, typically <10 years, which means that most olivine compositions, even in relatively fast volcanic systems, do not record the entire history of the crystallization from initial precipitation through final rim formation (Costa and Dungan, 2005; Gordeychik *et al*., 2018). The timescales of crystallization are significantly longer in plutonic environments (i.e., thousands of years or more for individual magma batches), which means that there is sufficient time for primary compositional zonation in olivine to be erased by diffusion. During crystallization of olivine at Polaris and formation of a cumulate pile, which ultimately crystallizes to produce the range of observed lithologies (e.g., dunite, olivine wehrlite, wehrlite), olivine crystals would have been isolated from the parent melt. In principle, olivine at the bottom of a cumulate pile should have a higher forsterite content and higher Ni concentration than at the top. However, the relatively high diffusion rates of Ni and Mg-Fe in olivine means that individual olivine crystals will re-

equilibrate with other grains within the cumulate pile. This process, called “mush diffusion”, will result in a unimodal olivine composition distribution for a cumulate pile rather than a range from more magnesian to less magnesian olivine (Thomson and MacLennan, 2013). This process can account for the very limited range of forsterite contents in olivine from the Polaris intrusion. The most Mg-rich olivine preserved in dunite, olivine wehrlite, and wehrlite are likely slightly less magnesian than they were originally, and the least magnesian olivine (i.e., most Fe-rich) hosted in dunite, olivine wehrlite, and wehrlite are likely slightly more magnesian than they were originally (e.g., Thomson and MacLennan, 2013).

5.2. Origin of Ca-depleted olivine in the Polaris and other Alaskan-type intrusions

5.2.1. Ca-in-olivine variations in volcanic rocks

The Ca concentrations in olivine from the Polaris intrusion are, for the most part, substantially lower than Ca concentrations in olivine from volcanic rocks globally (Fig. 5.5). Komatiites from Barberton Greenstone Belt, South Africa, and Siqueiros MORB olivine compositions are derived from primary mantle melts and their olivine compositions overlap with model olivine compositions of primary melts from an anhydrous mantle (Gavrilenko *et al*., 2016). Olivine from primitive subduction zone-related Central American volcanos (Irazu, Barva, Platanar) and olivine from the Kamchatka arc range from about 500 to 3000 ppm Ca with most compositions in the range of 800 to 1900 ppm Ca (Gavrilenko *et al*., 2016). Olivine compositions from Mauna Loa, Hawaii, range from 1300 to 1900 ppm Ca (Gavrilenko *et al*., 2016). Although mostly higher than what is observed in the Polaris intrusion, the Ca concentrations in olivine from the subduction zone volcanoes are lower than what is expected by differentiation from a primary mantle melt (Gavrilenko *et al*., 2016).

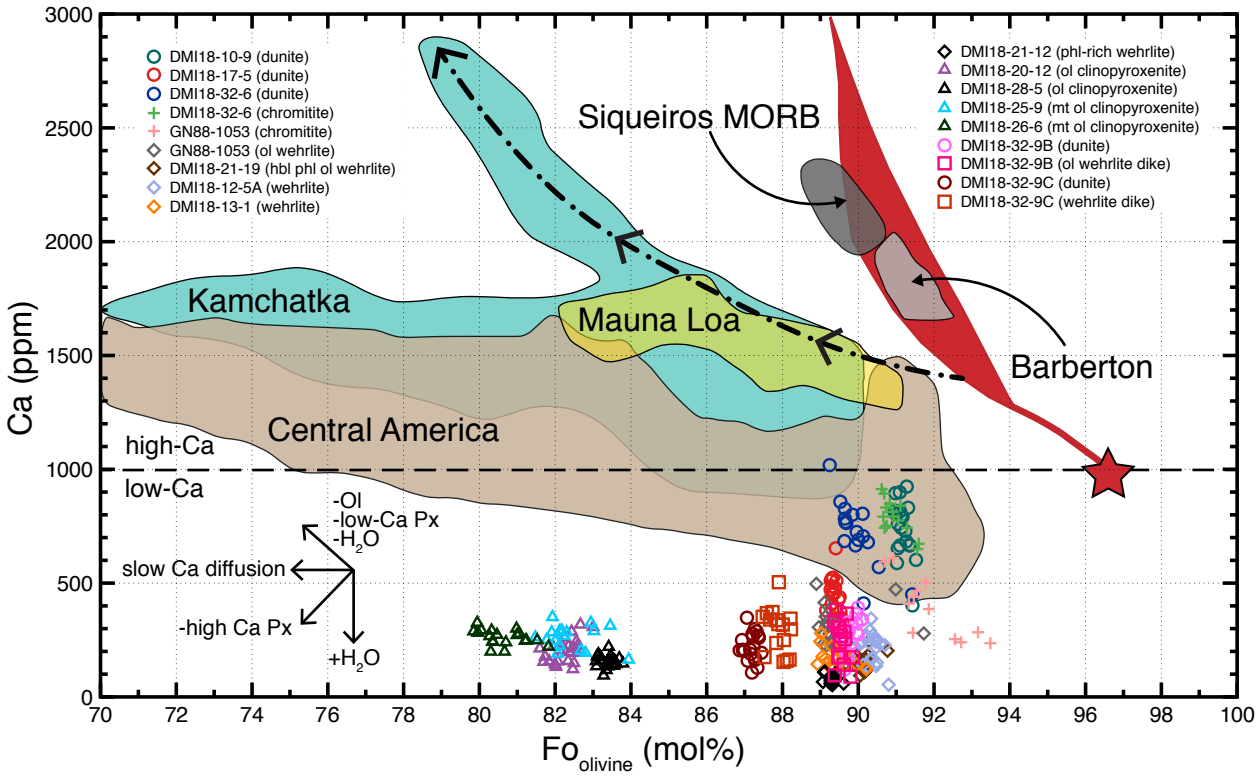

Figure 5.5. Ca concentrations (ppm) vs. forsterite content (mol. %) of olivine for representative olivine-bearing lithologies from the Polaris intrusion compared to olivine compositions from volcanic rocks from various tectonic settings. Fields and trends are modified from Gavrilenko et al. (2016). The red field indicates model olivine compositions of primary melts from an anhydrous mantle with the red star representing the olivine composition at total melting. The light-grey field represents olivine compositions from komatiites from Barberton Greenstone Belt, South Africa; Siqueiros MORB olivine compositions are shown in the dark-grey field. The beige field covers olivine compositions from three subduction zone-related Central American volcanos (Irazu, Barva, Platanar). The teal field represents olivine compositions from the Kamchatka arc. Olivine compositions from Mauna Loa (Hawaii) are represented by the yellow field for comparison. The black dash-dot line shows the trend of olivine compositions produced by fractional crystallization of olivine. Most olivine from arc volcanos has too little Ca to be explained by fractional crystallization trends – Gavrilenko et al. (2016) proposed that this is related to hydration of the mantle wedge. The vectors in the lower left show the relative influence of different processes that can lead to changes in the Ca content of olivine, including fractional crystallization of olivine (-Ol), low-Ca pyroxene (-low-Ca Px), or the removal of H_2O (-H2O), slow Ca diffusion, fractional crystallization of high-Ca pyroxene (clinopyroxene) (-high-Ca Px), and the addition of H_2O (+H_2O). Most of the analyzed olivine from the Polaris intrusion is characterized by very low Ca (<500 ppm) suggesting that Ca has been lost from olivine in plutonic rocks compared to olivine in volcanic rocks.

The partitioning of Ca between olivine and melt ($D_{CaO}^{Ol/L}$) is a function of the Ca content of the melt and the relative activity of iron in the melt (i.e., fayalite content of olivine) over a wide range of pressures, temperatures, and oxygen fugacity (Jurewicz and Watson, 1988; Libourel, 1999). This relationship suggests that in a system undergoing fractional crystallization, as the Fe in the melt increases (i.e., Fo content in olivine decreases), the Ca concentration of olivine should also increase. However, the addition of H_2O to the melt decreases Ca partitioning (Feig *et al*., 2006). In the case of Mauna Loa, relatively low-Ca olivine is likely representative of the pyroxenite mantle source rather than an H_2O-driven process (Herzberg, 2011). The relatively low-Ca olivine from the aforementioned arc volcanic rocks are not explained by a pyroxenite source and it has been proposed that they result from the introduction of magmatic H_2O during hydration partial melting of the mantle wedge above the subducting slab (Gavrilenko *et al*., 2016). As a result, most magmatic olivine found in arc settings is depleted in Ca relative to ideal fractional crystallization trends from magmas derived from anhydrous mantle.

5.2.2. Loss of Ca from olivine in the plutonic environment

The Polaris Alaskan-type intrusion likely crystallized from a primary hydrous arc magma as indicated by the crystallization of primary hydrous phases (i.e., phlogopite, hornblende) in both primitive and evolved lithologies. Olivine from the Polaris intrusion should thus have similar Ca contents as the relatively Ca-depleted olivine in its volcanic counterparts, however, Polaris olivine has remarkably low Ca concentrations (<1000 ppm, with most <500 ppm) (Fig. 5.5), a feature that appears to be typical of olivine compositions from ultramafic-mafic plutonic rocks globally (Fig. 5.6) (e.g., Simkin and Smith, 1970; Stormer, 1973; Morse, 1996; Li *et al*., 2012; Holness *et al*., 2015; Yao *et al*., 2017). The activation energy for Ca diffusion in olivine is

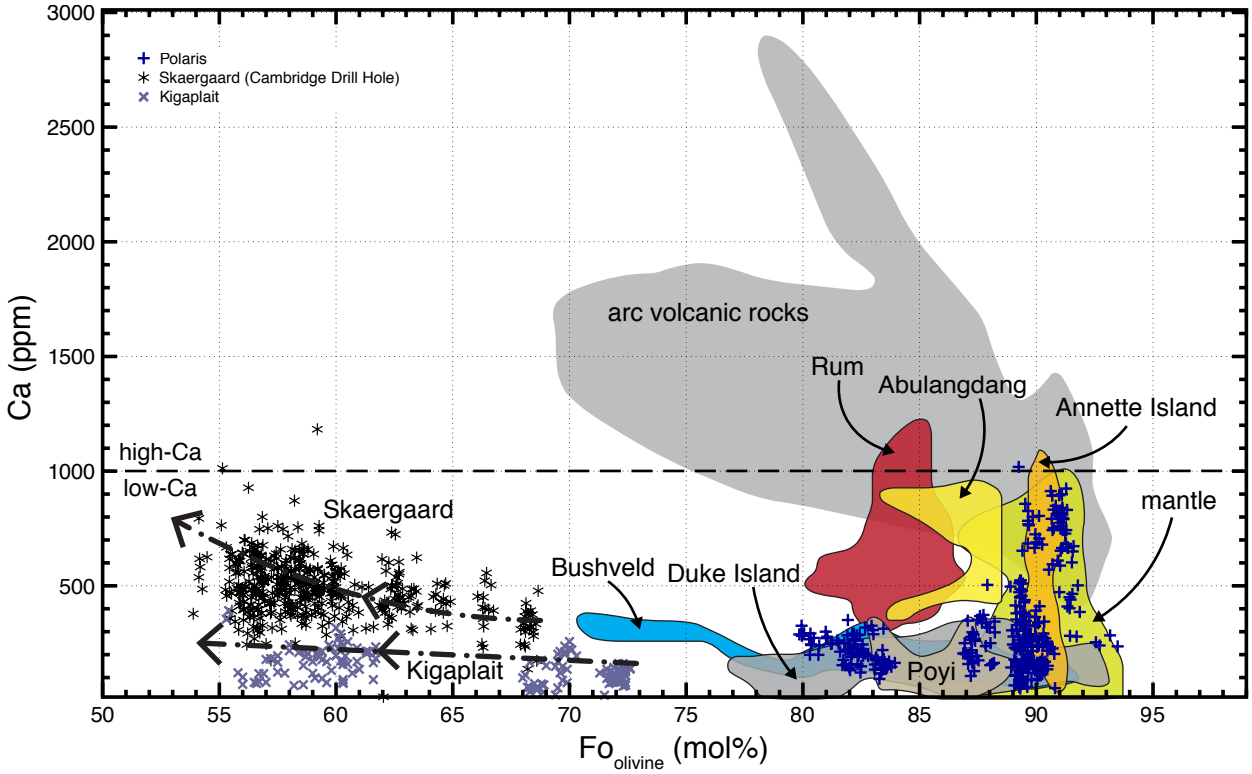

Figure 5.6. Ca concentrations (ppm) vs. forsterite content (mol. %) of olivine from the Polaris intrusion compared to olivine compositions from other ultramafic-mafic intrusions. High-precision Ca analyses are available from the Skaergaard intrusion (Greenland) from the Cambridge Drill Hole that intersects the earliest cumulates in the intrusion (Holness et al., 2015) and from the Kigaplait intrusion (Labrador) (June Cho, personal communication) – olivine compositions in both intrusions extend to endmember fayalite. Olivine compositional fields are modified from Yao et al. (2017) and show compositions of mantle periodite and xenoliths (green field), and from the Rum layered intrusion, Scotland (red field), Abulangdang intrusion, China (yellow field), Poyi intrusion, China (beige field), Bushveld Complex, South Africa (blue field), and Duke Island Alaskan-type intrusion, Alaska (grey field). Olivine compositions from the Annette Island Alaskan-type intrusion, Alaska (orange field) are modified from Li et al. (2011). Also shown is the field for olivine from arc volcanic rocks (grey) from Gavrilenko et al. (2016). Globally, olivine from plutonic rocks is depleted in Ca compared to olivine in volcanic rocks.

similar to that for other divalent cations in olivine (Fe-Mg, Ni, Mn, Co) and the diffusion of Ca in olivine has a similar timescale to that of Mg-Fe, Ni, and Mn (Costa and Dungan, 2005). The absolute value of the diffusion coefficient at 900°C, at an oxygen fugacity (fO_2) of 10^{-12} bars, is approximately one order of magnitude slower than that for Mg-Fe diffusion in olivine (Coogan *et al.*, 2005), however, at the extended timescales of crystallization and cooling of plutonic rocks compared to volcanic rocks, Ca should not behave significantly differently from the other major substituting cations. What process then has led to the near-universal loss of Ca from Polaris olivine and plutonic olivine in general?

The depletion of Ca in olivine was suggested to be an effect of crystallization pressure (Stormer, 1973), however, the effect of pressure is minimal on the partitioning of Ca between olivine and melt (Jurewicz and Watson, 1988). Morse (1996) evaluated different mechanisms for obtaining a "Ca sink" in cumulates in a plutonic environment for olivine for the Kigaplait layered intrusion of coastal Labrador. Olivine in the clinopyroxene-bearing lithologies (olivine gabbros) of the Upper Zone of the Kiglapait intrusion may have lost Ca through diffusion with co-existing clinopyroxene following the relationship: $0.8Ca_2SiO_4 + 1.2(Mg,Fe)_2SiO_4 + 2SiO_2 = 2Ca_{0.8}(Mg,Fe)_{1.2}Si_2O_6$. Such as process could potentially have operated in the clinopyroxene-bearing lithologies of the Polaris intrusion (wehrlite, olivine clinopyroxenite) and other clinopyroxene-bearing plutonic rocks. This diffusional process would not have been possible in the troctolitic Lower Zone of the Kiglapait intrusion, which is essentially devoid of clinopyroxene, and is similar to the situation for the dunitic cumulates in the Polaris intrusion where there is no mineral sink for the Ca released by olivine. Morse (1996) suggests that for these clinopyroxene-free rocks the only other mechanism that can account for Ca depletion in olivine is through the olivine-liquid diffusion of Ca to the intercumulus melt or the main magma

prior to compaction of the cumulate pile. This depletion is possible because $D_{CaO}^{Ol/L}$ is relatively low (<0.10 for high-Mg basalts and tholeiites with olivine forsterite contents ranging from Fo_{55-97}) (Libourel, 1999) such that Ca prefers the melt to olivine during crystallization. In Polaris olivine, Ca concentrations are higher in the cores than rims, especially in dunite and chromitite, which is the opposite of typical Ca zonation profiles in olivine from arc basalts that show Ca-rich rims (e.g., Gordeychick *et al*., 2018), and indicates that re-equilibration between olivine and some other phase has occurred. This phase was most likely the interstitial melt (Morse, 1996). It is unclear why this zonation was not overprinted by the process of mush diffusion within the cumulate pile, however, the process of Ca-loss to interstitial melt is sufficiently effective as to be a diagnostic feature of olivine from plutonic environments.

5.3. Significance of spatial variations of olivine compositions in the Polaris intrusion

The Polaris Alaskan-type intrusion is a crudely stratified sill-like body hosted within southwest dipping (40-50˚) rocks of the Lay Range Assemblage (Roots, 1954; Nixon *et al*., 1997; Nott *et al*., 2020). Olivine from the dunite, olivine wehrlite, and wehrlite-dominated eastern part of the intrusion has the highest forsterite contents that cover a range of Ni concentrations (Fig. 5.7). In contrast, olivine from the olivine clinopyroxenite and hornblende clinopyroxenite-dominated western part of the intrusion is characterized by the lowest forsterite contents and Ni concentrations. Dunites and wehrlites from the eastern margin of the intrusion are stratigraphically below the evolved lithologies of the western margin of the intrusion (Fig. 5.8). The most Fe-rich and Ni-poor olivine is found in the stratigraphically highest units, which is consistent with derivation through fractional crystallization from the less evolved magmas that produced the dunites, presumably in deeper-seated magma chambers of reservoirs. The average

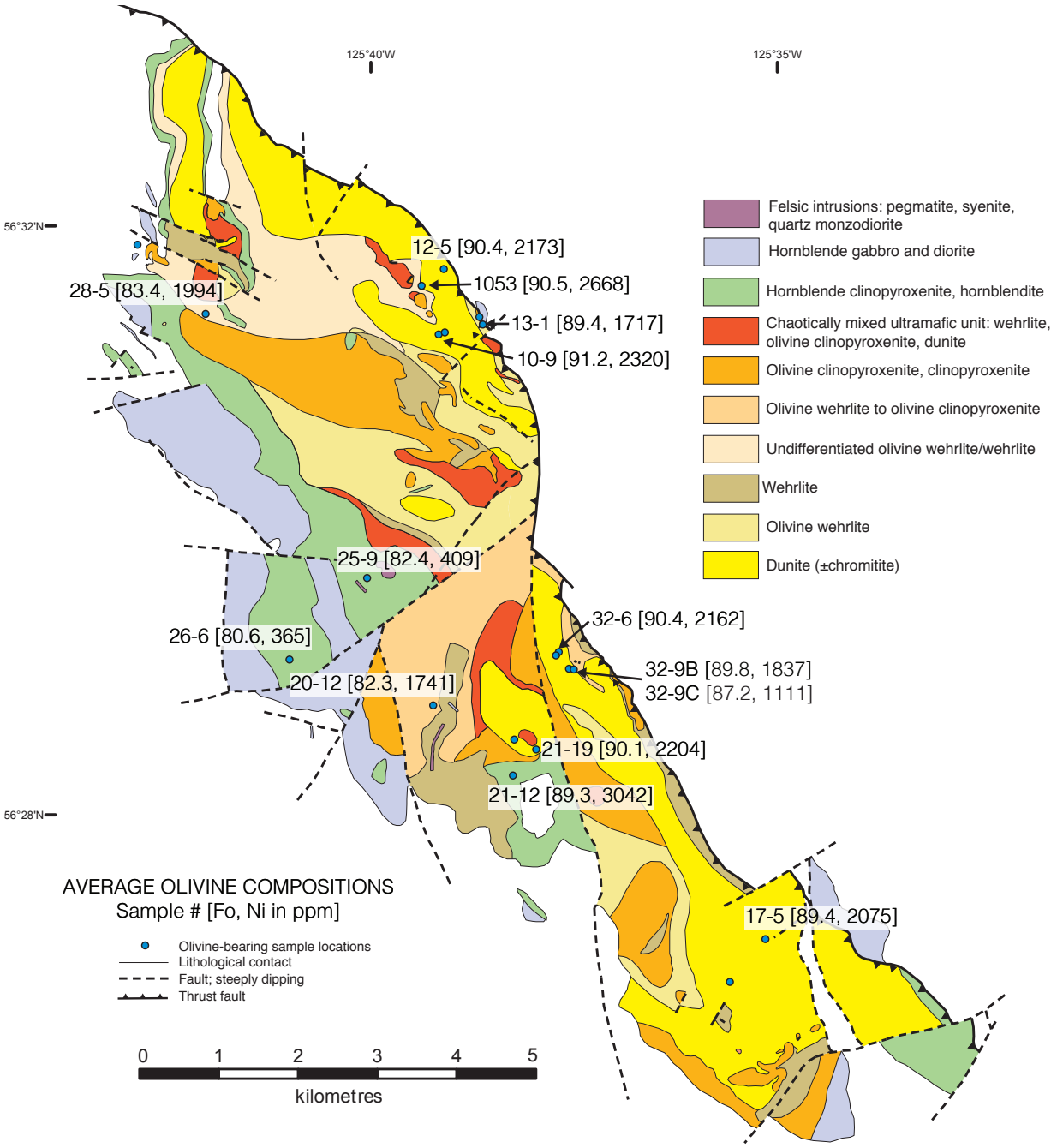

Figure 5.7. Geological map and olivine-bearing sample locations of the Polaris Alaskan-type ultramafic-mafic intrusion (from Nixon et al., 1997; revised and modified by Nott et al., 2020) illustrating host contact relationships, intrusive rock types, and average forsterite and Ni concentrations, [$Fo_{olivine}$, ppm [Ni]], for all samples analyzed by electronprobe microanalysis. The average forsterite content and Ni concentration of olivine is highest in the eastern part of the intrusion and most evolved to the west (FC trend).

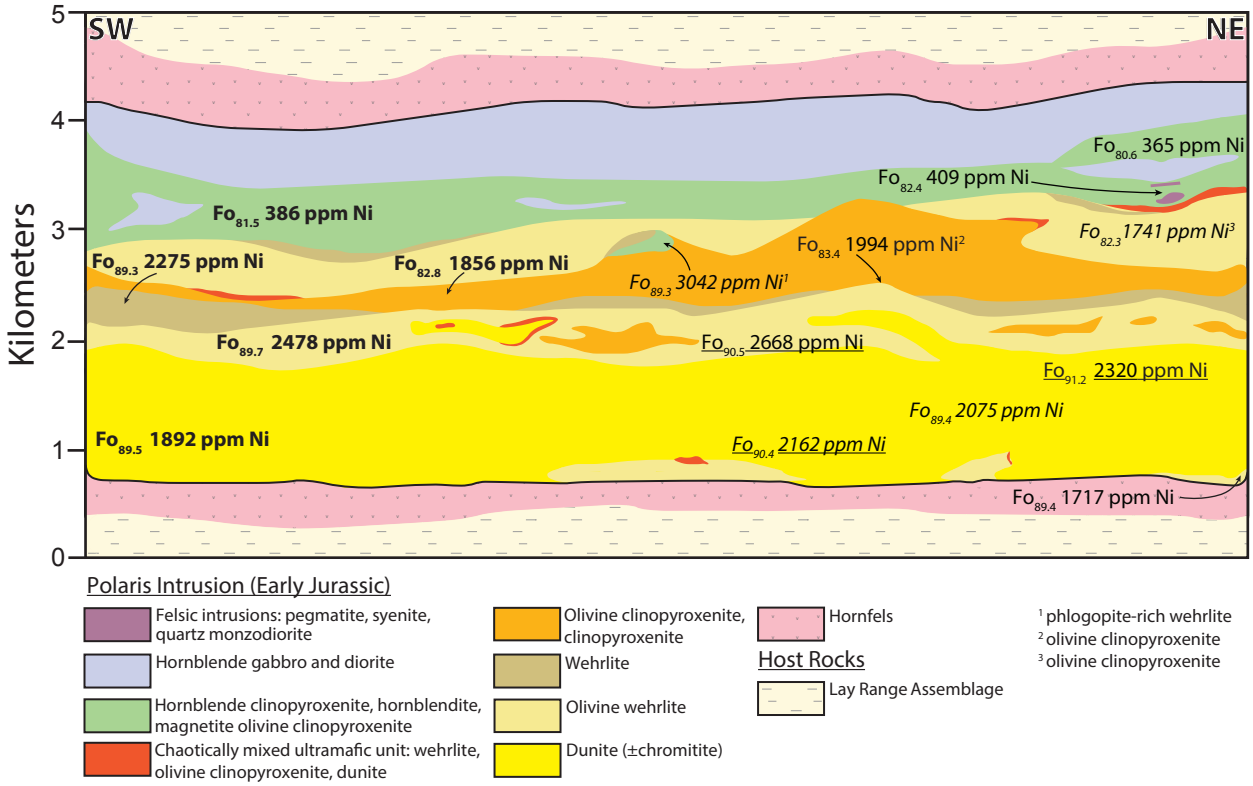

Figure 5.8. Schematic restored section trending NE-SW through the Polaris intrusion with average olivine forsterite content and Ni concentration plotted for representative olivine-bearing samples. Compositions from the south part of the intrusion were projected to the north assuming continuity of the units (italicized). Samples with chromitite schlieren are underlined. Complete averages for each lithology (i.e., all dunite) are indicated in bold text. The section was "restored" by assuming that the basal dunite units in the NW and SE were originally contiguous prior to faulting. The "true thickness" for each unit was determined by approximating the dip of each unit as 45˚ to the SW based on the dip of the Lay Range Assemblage (40-50˚W) and the sill-like nature of the Polaris intrusion (Nixon, 1997; Nott et al., 2020). Internal contact relations are schematic and based on map-scale relationships. Numbered superscripts indicate local rock types present within larger scale units (i.e., 1 = a phlogopite-rich wehrlite in hornblende clinopyroxenite unit). Note that the average forsterite content of olivine varies little in the lower ~1.5 km of the Polaris intrusion, yet average Ni concentrations vary widely indicating that multiple batches of magma likely containing entrained olivine, with distinct Fo-Ni relationships, were emplaced in the formation of the Polaris intrusion. The most Fe-rich and Ni-poor olivine (FC trend) is found in the stratigraphically highest units.

forsterite content of olivine from the Polaris intrusion varies little in the lower ~1.5 km of the intrusion, whereas average Ni concentrations vary widely. Ni variations or "spikes" in olivine with high forsterite contents are evidence for the emplacement of multiple batches of magma with distinct Ni-Fo relationships during the crystallization of the Polaris intrusion (e.g., Morse, 1996; de Maisonneuve *et al*., 2016).

5.4. Implications for the evolution of magma conduits in arc settings

5.4.1. Tectonic significance

Mafic-ultramafic magmatic conduits are found in various geological settings globally and are generally associated with crustal-scale fault features through which mantle-derived magmas ascended before emplacement or eruption (e.g., Song *et al*., 2011; Begg *et al*., 2018). Within the conduit, magma differentiation processes, including fractional crystallization, magma recharge, and crustal assimilation, occur and produce a range of lithologies, textures, and morphologies (e.g., Song *et al*., 2011; Barnes and Mungall, 2018). The most commonly accepted model for magma genesis in subduction zone settings (i.e., magmatic arcs) begins with hydration of the mantle wedge and the ascent of diapirs of partial melt separated from its mantle source (e.g., Ringwood, 1974; Marsh, 1979; Tamura, 1994; Ulmer, 2001; Stern, 2002). The resulting mafic magmas crystallize over a wide range of pressures (depths), fractionate out early-crystallized phases like olivine (+Cr-spinel), and assimilate crustal materials resulting in the large diversity of lithologies indicated by a wide compositional range of volcanic rocks derived from volcanic arcs (Stern, 2002; Cruz-Uribe *et al*., 2018).

The Polaris Alaskan-type ultramafic-mafic intrusion was emplaced in the Quesnellia magmatic arc during the Early Jurassic (Nixon *et al*., 1997; Nixon *et al*., 2019). Voluminous

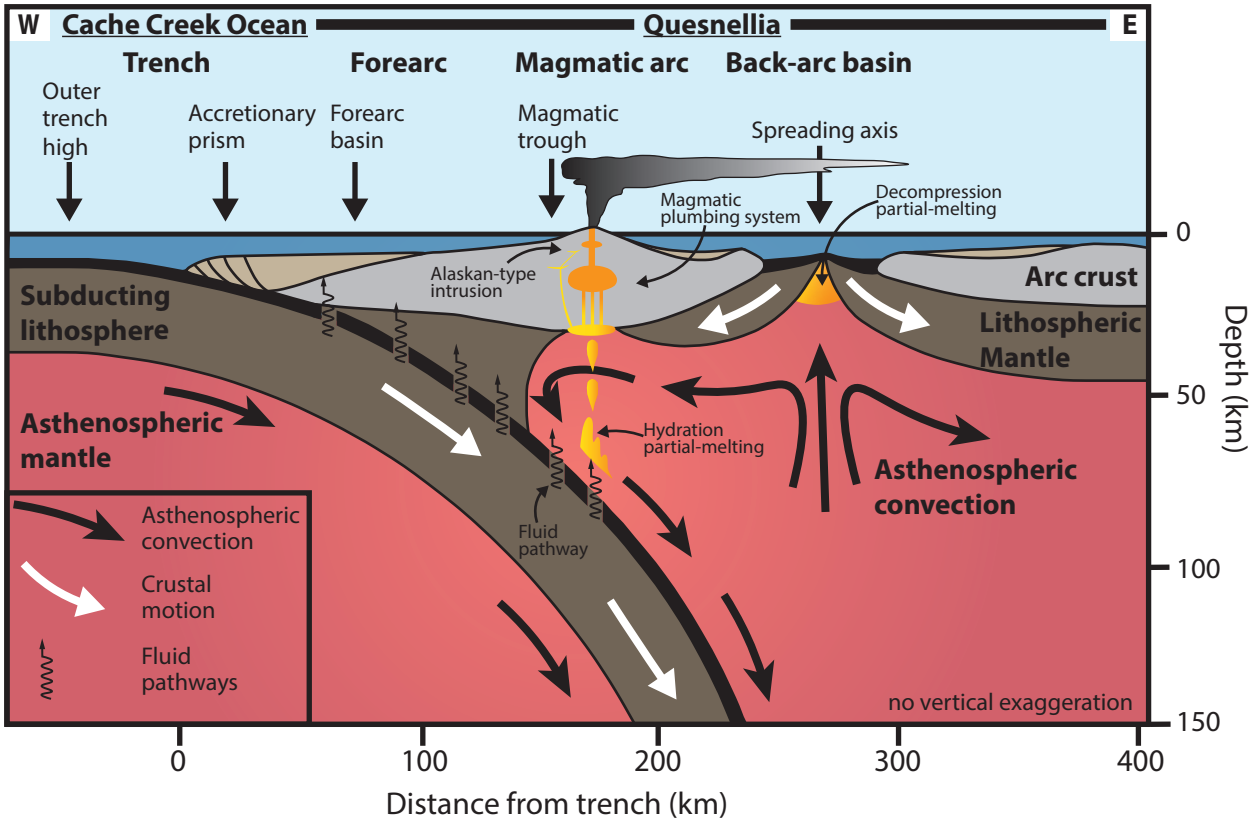

Figure 5.9. Schematic cross section through the upper 140 km of an idealized subduction zone (adapted and modified from Stern, 2002), representative of the Cache Creek Ocean plate subducting under the Quesnellia arc terrane in the Early Jurassic. Magma generation in the magmatic arc, including the parent magmas to Alaskan-type ultramafic-intrusions like the Polaris intrusion, is produced due to hydration partial melting of the subduction zone mantle wedge. Magmas then rise to the arc crust where the process of magma differentiation (fractional crystallization-mixing-assimilation) begins (orange regions on figure). In the case of the Polaris intrusions (yellow), the Fo-rich olivine compositions for dunites and olivine wehrlites from this study indicate that very little differentiation occurred between separation from the mantle wedge source and emplacement of magma in shallow crustal magma chambers (~12 km depth).

volcanism in the Quesnellia arc defined by the Late Triassic to Early Jurassic Takla, Nicola, and Stuhini groups and cogenetic plutonism in British Columbia is considered coeval with the emplacement of the Polaris intrusion (Nixon *et al*., 1997; Nelson and Colpron, 2007). During the Lower Jurassic, the Cache Creek Ocean was subducting westward beneath the Quesnellia arc (Nelson and Colpron, 2007). Partial melting in the mantle wedge induced by dehydration of the subducting Cache Creek Ocean resulted in ascent of primary magmas into the arc crust (Fig. 5.9). Maximum emplacement depths of 12 km (Nixon *et al*., 1997) of the Polaris Alaskan-type intrusion into the sedimentary, volcaniclastic, and volcanic rocks of the Lay Rang Assemblage suggest that relatively rapid ascent of primary magmas from the mantle wedge source to emplacement of magma was necessary to avoid significant magmatic differentiation at lower levels in the crust and to maintain the observed Mg-rich olivine compositions.

5.4.2. Convergent margin Ni-Cu-PGE ore-forming systems

Ultramafic-mafic magmatic conduit systems host Ni-Cu-PGE mineralization in various tectonic settings; however, they are most commonly associated with extensional settings (e.g., Naldrett, 2010; Song *et al*., 2011; Nixon *et al*., 2015; Barnes and Mungall, 2018; Begg *et al*., 2018). The Polaris Alaskan-type ultramafic-mafic intrusion does not host significant magmatic sulfide mineralization and the olivine compositions determined in this study do not reveal the characteristics Ni-depletion at high forsterite contents that may signal early segregation of immiscible sulfide melt (e.g., Li *et al*., 2007; Scheel, 2007; Thakurta *et al*., 2008; Li *et al*., 2013; Manor *et al*., 2016). The Polaris intrusion does, however, locally contain the characteristic ore minerals of Ni-Cu-PGE deposits (e.g., pentlandite, pyrrhotite, chalcopyrite, bornite) and it is broadly related spatially and temporally in the Cordilleran Mountains of British Columbia and

Alaska to known Ni-Cu-PGE deposits associated with Alaskan-type intrusions (e.g., Turnagain, Duke Island), thus petrogenetic trends determined for the Polaris intrusion have the potential to illuminate important magmatic processes in convergent margin Ni-Cu-PGE ore-forming systems. The Polaris intrusion shares common characteristics with Ni-Cu-PGE ore-forming conduit systems in other settings. The most significant Ni-Cu-PGE deposits globally are small (<10 km in length) and lensoidal or sill-like (Song *et al*., 2011). Ni-Cu-PGE deposits are commonly associated with magmas that were produced through relatively high degrees of partial melting that resulted in high Ni/Cu and relatively high PGE concentrations (Song *et al*., 2011). Fractional crystallization in ultramafic-mafic magmatic conduits prior to sulfide saturation can result in increased Pd concentrations and increased Cu/Ni (i.e., Ni is removed from the system through olivine crystallization) (Naldrett and Cabri, 1976; Song *et al*., 2011). Multiple pulses of magma are a common characteristic of magmatic conduit systems that produce Ni-Cu-PGE mineralization (Barnes and Mungall, 2018; Begg *et al*., 2018). The recharge of new unfractionated (i.e., undepleted) magmas following sulfide saturation can result in metal enrichment of the sulfide liquids (e.g., Barnes *et al.*, 2016b; Lesher, 2019). In this study, the Fo-Ni relationships of olivine from the Polaris Alaskan-type ultramafic-mafic intrusion highlight the importance of both fractional crystallization and magma recharge as differentiation processes and the similarity of some of the key processes that control Ni-Cu-PGE mineralization in extensional tectonic settings to those that operate in convergent margin settings.

6. Conclusions

The crystallization history of the Polaris Alaskan-type ultramafic-mafic intrusion in the Quesnel terrane of north-central British Columbia was evaluated through a systematic study of the petrography and chemistry of olivine, the dominant mineral in the intrusion. The main conclusions are:

1) The Mg-rich forsterite contents of olivine ($Fo_{87.5-92}$) from dunite, olivine wehrlite, and wehrlite indicate that the parent melts of the Polaris intrusion were primitive in composition and did not undergo significant degrees of differentiation from the mantle wedge source before emplacement in the crust.
2) Relationships between the forsterite content and Ni concentration of olivine from the Polaris intrusion show a fractional crystallization-controlled evolution from dunite-olivine werhlite-wehrlite ($Fo_{87.5-92}$, 1605-3108 ppm Ni) through magnetite-rich olivine clinopyroxenite (Fo_{79-84}, 275-550 ppm Ni). Other lithologies, such as magnetite-poor olivine clinopyroxenite ($Fo_{81.5-84}$, 1305-2090 ppm Ni), are accounted for by mixing between fractionated and primitive magmas.
3) Fractional crystallization trends are supported by a general evolution from Ni-rich, Mg-rich olivine to Ni-poor, Fe-rich olivine from lower to higher stratigraphic intervals in the Polaris intrusion, although fractional crystallization likely occurred in deeper-seated chambers, reservoirs, or conduits and not at the level of emplacement.
4) Recharge of primitive magmas is evidenced by “Ni-spikes” (i.e., Ni-rich olivine) over stratigraphic intervals with a limited range of forsterite values, as well as physically by the presence of chaotic mixing of dunite, olivine wehrlite, and olivine clinopyroxenite,

the common occurrence of ultramafic dikes, and localized sheared and disrupted chromitite throughout the intrusion.

5) The general absence of zoned olivine (e.g., no variation in Fo-Ni-Mn contents across individual crystals) in the Polaris intrusion is attributed to extensive crystal mush diffusion and re-equilibration at high temperatures at timescales significant enough to erase primary magmatic zonation during crystallization.
6) The Ca concentrations of olivine from the Polaris intrusion are low (<1000 ppm, with most analyses <500 ppm) and significantly lower than the Ca contents of olivine from volcanic arcs globally. Similar Ca-depleted olivine is found in other ultramafic-mafic intrusions worldwide (e.g., Skaergaard, Kiglapait, Bushveld, Duke Island) and is attributed to high-temperature diffusion of Ca from the olivine crystal lattice to either co-existing clinopyroxene (or some other Ca-bearing mineral) or interstitial melt when no other Ca-mineral phase is present (i.e., dunite).

The Polaris Alaskan-type ultramafic-mafic intrusion formed as a result of the hydrous partial melting of the mantle wedge above the subducting Cache Creek oceanic crust (Nixon *et al*., 1997; Nelson and Colpron, 2007). These primitive, high-MgO magmas ascended into the arc crust of Quesnellia during the Early Jurassic. A maximum emplacement depth of 12 km (Nixon *et al*., 1997) indicates that these magmas ascended relatively rapidly from their mantle source through the mantle lithosphere and lower crust to avoid significant differentiation and to retain their primitive initial compositions.

The Polaris Alaskan-type intrusion contains disseminated magmatic sulfides (e.g., pyrrhotite, chalcopyrite, pyrite and minor bornite) hosted mainly by hornblende clinopyroxenite and gabbro/diorite with some mineralization occurring in wehrlite in the central part of the

intrusion (Nixon et al., 2019). Alaskan-type intrusions can be prospective for magmatic Ni-Cu-PGE mineralization in the Cordillera (e.g., Turnagain – Scheel, 2007; Scheel *et al.,* 2009; Mudd and Jowitt, 2014; Nixon *et al*., 2015; Jackson-Brown, 2017; Nixon *et al*., 2019; Tulameen – Nixon *et al*., 2019; Duke Island – Thakurta, 2008). Many of the key processes that control magmatic Ni-Cu-PGE ore-forming systems globally, such as fractional crystallization and magma recharge and mixing of magmas, are shared by the Polaris Alaskan-type intrusion, which suggests that Ni-Cu-PGE mineralization in convergent margin settings may be controlled by similar processes to those in more conventional extensional settings.

6.1. Suggestions for further research

Several avenues of future research on the Polaris Alaskan-type intrusion of north-central British Columbia have been identified based on the work conducted in this study. The analysis of olivine from more olivine-bearing samples from a wider array of lithologies and locations across the intrusion could help better assess which units, or portions of units, are dominated by fractional crystallization processes vs. recharge and mixing processes. This may provide information on the relative rates of magma recharge or injection across the preserved stratigraphic thickness of the intrusion, and along-strike variations could be evaluated as well. Additional microanalytical studies utilizing electronprobe microanalysis (EPMA) could be conducted for the other major silicate and oxide phases in the Polaris intrusion, including chromite, clinopyroxene, hornblende, and magnetite. These mineral compositions would allow for evaluation of petrologic trends from across the entire Polaris intrusion, from the least fractionated to the most fractionated rocks, and encompass all the major rocks types in the intrusion (e.g., dunite, chromitite, olivine wehrlite, wehrlite, olivine clinopyroxenite,

clinopyroxenite, hornblende clinopyroxenite, hornblendite, hornblende gabbro-diorite, syenite) (Nott et al., 2020).

Relatively little is known about the compositions of melts parental to Alaskan-type intrusions globally, including the Polaris intrusion, except for their primitive nature based primarily on their Mg-rich olivine compositions. Use of trace element concentrations (e.g., Li, Na, Al, P, Ca, Sc, Ti, V, Cr, Mn, Co, Ni, Cu, Zn) in olivine determined by laser ablation-inductively coupled plasma-mass spectrometry (LA-ICP-MS) is becoming an increasingly important petrological tool for discriminating between petrologic processes and fingerprinting different mantle sources (e.g., Foley *et al.,* 2011; Batanova *et al.,* 2015; Rampone *et al.,* 2016; Bussweiler *et al.,* 2019; Ersoy *et al.,* 2019; Jankovics *et al.,* 2019). A follow-up study on the trace element variations in olivine from the Polaris intrusion is highly recommended and should provide new insights into the magmatic evolution of this remarkably well-exposed Alaskan-type ultramafic-mafic intrusion in the Canadian Cordillera.

Bibliography

Arai, S., and Ishimaru, S., 2008, Insights into petrological characteristics of the lithosphere of mantle wedge beneath arcs through peridotite xenoliths: A review: Journal of Petrology, v. 49(4), p. 665–695.

Armstrong, J.E., 1946, Aiken Lake (South Half), British Columbia: Geological Survey of Canada, Paper 46-11.

Armstrong, J.E. and Roots, E.F., 1948, Geology and Mineral Deposits of Aiken Lake Map Area, British Columbia: Geological Survey of Canada, Paper 48-5, 46 p.

Barnes, S. J., Mole, D. R., Le Vaillant, M., Campbell, M. J., Verrall, M. R., Roberts, M. P., and Evans, N. J., 2016a, Poikilitic textures, heteradcumulates and zoned orthopyroxenes in the Ntaka Ultramafic Complex, Tanzania: Implications for crystallization mechanisms of oikocrysts: Journal of Petrology, v. 57, p. 1171–1198.

Barnes, S. J., Cruden, A. R., Arndt, N., and Saumur, B. M., 2016b, The mineral system approach applied to magmatic Ni–Cu–PGE sulphide deposits: Ore Geology Reviews, v. 76, p. 296–316.

Barnes, S. J., and Mungall, J. E., 2018, Blade-shaped dikes and nickel sulfide deposits: A model for the emplacement of ore-bearing small intrusions: Economic Geology, v. 113, p. 789–798.

Batanova, V. G., Pertsev, A. N., Kamenetsky, V. S., Ariskin, A. A., Mochalov, A. G., and Sobolev, A. V., 2005, Crustal evolution of island-arc ultramafic magma: Galmoenan pyroxenite-dunite plutonic complex, Koryak Highland (Far East Russia): Journal of Petrology, v. 46, p. 1345–1366.

Batanova, V. G., Sobolev, A. V., and Kuzmin, D. V., 2015, Trace element analysis of olivine: High precision analytical method for JEOL JXA-8230 electron probe microanalyser: Chemical Geology, v. 419, p. 149–157.

Beattie, P., Ford, C., and Russell, D., 1991, Partition coefficients for olivine-melt and orthopyroxene-melt systems: Contributions to Mineralogy and Petrology, v. 109, p. 212–224.

Begg, G. C., Hronsky, J. M. A., Griffin, W. L., and O'Reilly, S. Y., 2018, Global- to Deposit-Scale Controls on Orthomagmatic Ni-Cu(-PGE) and PGE Reef Ore Formation: Elsevier Inc., 1–46 p.

Bowen, N.L., 1928, The Evolution of the Igneous Rocks: Princeton University Press, 334 p.

Bussweiler, Y., Giuliani, A., Greig, A., Kjarsgaard, B. A., Petts, D., Jackson, S. E., Barrett, N., Luo, Y., and Pearson, D. G., 2019, Trace element analysis of high-Mg olivine by LA-ICP-MS – Characterization of natural olivine standards for matrix-matched calibration and application to mantle peridotites: Chemical Geology, v. 524, p. 136–157.

Clark, T., 1978, Oxide Minerals in the Turnagain Ultramafic Complex, Northwestern British Columbia.: Can J Earth Sci, v. 15.

Clark, T., 1980, Petrology of the Turnagain ultramafic complex, northwestern British Columbia: Canadian Journal of Earth Sciences, v. 17, p. 744–757.

Coogan, L. A., Hain, A., Stahl, S., and Chakraborty, S., 2005, Experimental determination of the diffusion coefficient for calcium in olivine between 900°C and 1500°C: Geochimica et Cosmochimica Acta, v. 69, p. 3683–3694.

Costa, F., and Dungan, M., 2005, Short time scales of magmatic assimilation from diffusion modeling of multiple elements in olivine: Geology, v. 33, p. 837–840.

Cruz-Uribe, A. M., Marschall, H. R., Gaetani, G. A., and Le Roux, V., 2018, Generation of alkaline magmas in subduction zones by partial melting of mélange diapirs-An experimental study: Geology, v. 46, p. 343–346.
de Maisonneuve, C. B., Costa, F., Huber, C., Vonlanthen, P., Bachmann, O., and Dungan, M. A., 2016, How do olivines record magmatic events? Insights from major and trace element zoning: Contributions to Mineralogy and Petrology, v. 171, p. 1–20.
Ersoy, Ö., Nikogosian, I. K., van Bergen, M. J., and Mason, P. R. D., 2019, Phosphorous incorporation in olivine crystallized from potassium-rich magmas: Geochimica et Cosmochimica Acta, v. 253, p. 63–83.
Feig, S. T., Koepke, J., and Snow, J. E., 2006, Effect of water on tholeiitic basalt phase equilibria: An experimental study under oxidizing conditions: Contributions to Mineralogy and Petrology, v. 152, p. 611–638.
Ferri, F., 1997, Nina Creek Group and Lay Range Assemblage, north-central British Columbia: Remenants of late Paleozoic oceanic and arc terranes: Canadian Journal of Earth Sciences, v. 34, p. 854-874.
Ferri, F., Dudka, S., Rees, C., and Meldrum, D., 2001, Geology of the Aiken Lake Area, north-central British Columbia: British Columbia Geological Survey, Geoscience Map 2001-10, 1:50,000 scale.
Findlay, D.C., 1963, Petrology of the Tulameen ultramafic complex, Yale District, British Columbia: Ph.D. Thesis, Ontario, Canada, Queen's University, 415 p.
Findlay, D.C., 1969, Origin of the Tulameen ultramafic-gabbro complex, southern British Columbia: Canadian Journal of Earth Sciences, 6(3), p. 399–425.
Foley, S. F., Jacob, D. E., and O'Neill, H. S. C., 2011, Trace element variations in olivine phenocrysts from Ugandan potassic rocks as clues to the chemical characteristics of parental magmas: Contributions to Mineralogy and Petrology, v. 162, p. 1–20.
Foster, E., 1974, History and Origin of the Polaris Ultramafic Complex in the Aiken Lake Area of North-central British Columbia: unpublished B.Sc. thesis, Vancouver, British Columbia, University of British Columbia, 66 p.
Gavrilenko, M., Herzberg, C., Vidito, C., Carr, M. J., Tenner, T., and Ozerov, A., 2016, A Calcium-in-Olivine Geohygrometer and its Application to Subduction Zone Magmatism: Journal of Petrology, v. 57, p. 1811–1832.
Gordeychik, B., Churikova, T., Kronz, A., Sundermeyer, C., Simakin, A., and Wörner, G., 2018, Growth of, and diffusion in, olivine in ultra-fast ascending basalt magmas from Shiveluch volcano: Scientific Reports, v. 8, p. 1–15.
Hart, S. R., and Davis, K. E., 1978, Nickel partitioning between olivine and silicate melt: Earth and Planetary Science Letters, v. 40, p. 203–219.
Herzberg, C., 2011, Identification of source lithology in the Hawaiian and Canary Islands: Implications for origins: Journal of Petrology, v. 52, p. 113–146.
Herzberg, C., Asimow, P. D., Ionov, D. A., Vidito, C., Jackson, M. G., and Geist, D., 2013, Nickel and helium evidence for melt above the core-mantle boundary: Nature, v. 493, p. 393–397.
Herzberg, C., Vidito, C., and Starkey, N. A., 2016, Nickel-cobalt contents of olivine record origins of mantle peridotite and related rocks: American Mineralogist, v. 101, p. 1952–1966.

Himmelberg, G.R. and Loney, R.A., 1995, Characteristics and Petrogenesis of Alaskan-Type Ultramafic-Mafic Intrusions, Southeastern Alaska: U.S. Geological Survey, Professional Paper 1564, 47 p.

Holness, M., Tegner, C., Namur, O., Pilbeam, L., 2015, The Earliest History of the Skaergaard Magma Chamber: A Textural and Geochemical Study of the Cambridge Drill Core: Journal of Petrology, v. 56(6), p. 1199 - 1227.

Irvine, T.N., 1959, The ultramafic complex and related rocks of Duke Island, southeastern Alaska: Ph.D. thesis, Pasadena, California, California Institute of Technology, 320 p.

Irvine, T.N., 1974a, Ultramafic and Gabbroic Rocks in the Aiken Lake and McConnell Creek Map-areas, British Columbia: Geological Survey of Canada, Paper l4-lA, p. 149-152.

Irvine, T. N., 1974b, Petrology of the Duke Island Ultramafic Complex Southeastern Alaska, in Irvine, T. N. ed., Petrology of the Duke Island Ultramafic Complex Southeastern Alaska: Geological Society of America, v.138, 240 p.

Jackson-Brown, S., 2017, Origin of Cu-PGE-rich sulphide mineralization in the DJ/DB zone of the Turnagain Alaskan-type intrusion, British Columbia: M.Sc. thesis, Vancouver, British Columbia, University of British Columbia, 272 p.

Jankovics, M. É., Sági, T., Astbury, R. L., Petrelli, M., Kiss, B., Ubide, T., Németh, K., Ntaflos, T., and Harangi, S., 2019, Olivine major and trace element compositions coupled with spinel chemistry to unravel the magmatic systems feeding monogenetic basaltic volcanoes: Journal of Volcanology and Geothermal Research, v. 369, p. 203–223.

Jurewicz, A. J. G., and Watson, E. B., 1988, Cations in olivine, Part 1: Calcium partitioning and calcium-magnesium distribution between olivines and coexisting melts, with petrologic applications: Contributions to Mineralogy and Petrology, v. 99, p. 176–185.

Kamenetsky, V. S., Elburg, M., Arculus, R., and Thomas, R., 2006, Magmatic origin of low-Ca olivine in subduction-related magmas: Co-existence of contrasting magmas: Chemical Geology, v. 233, p. 346–357.

Kinzler, R. J., Grove, T. L., and Recca, S. I., 1990, An experimental study on the effect of temperature and melt composition on the partitioning of nickel between olivine and silicate melt: Geochimica et Cosmochimica Acta, v. 54, p. 1255–1265.

Krause, J., Brügmann, G. E., and Pushkarev, E. V., 2007, Accessory and rock forming minerals monitoring the evolution of zoned mafic-ultramafic complexes in the Central Ural Mountains: Lithos, v. 95, p. 19–42.

Langmuir C.H., and Hanson, G.N., 1981, Calculating mineral-melt equilibria with stoichiometry, mass balance and single component distribution coefficients (Newton R.C., Navrotsky A., Wood B.J., Eds.): Thermodynamics of minerals and melts, Springer, p. 247-271.

Le Maitre, R.W., 1989, A classification of igneous rocks and glossary of terms: Oxford, Blackwell Scientific Publications, 193 p.

Lesher, C. M., 2019, Up, down, or sideways: Emplacement of magmatic Fe–Ni–Cu–PGE sulfide melts in large igneous provinces: Canadian Journal of Earth Sciences, v. 56, p. 756–773.

Libourel, G., 1999, Systematics of calcium partitioning between olivine and silicate melt: Implications for melt structure and calcium content of magmatic olivines: Contributions to Mineralogy and Petrology, v. 136, p. 63–80.

Li, C., Naldrett, A.J., and Ripley, E.M., 2007, Controls on the Fo and Ni Contents of Olivine in Sulfide-bearing Mafic/Ultramafic Intrusions: Principles, Modeling, and Examples from Voisey's Bay: Earth Science Frontiers, v. 14, p. 177-185.

Li, C., Thakurta, J., and Ripley, E. M., 2012, Low-Ca contents and kink-banded textures are not unique to mantle olivine: Evidence from the Duke Island Complex, Alaska: Mineralogy and Petrology, v. 104, p. 147–153.
Li, C., Ripley, E. M., Thakurta, J., Stifter, E. C., and Qi, L., 2013, Variations of olivine Fo-Ni contents and highly chalcophile element abundances in arc ultramafic cumulates, southern Alaska: Chemical Geology, v. 351, p. 15–28.
Lynn, K. J., Shea, T., and Garcia, M. O., 2017, Nickel variability in Hawaiian olivine: Evaluating the relative contributions from mantle and crustal processes: American Mineralogist, v. 102, p. 507–518.
Manor, M. J., Scoates, J. S., Nixon, G. T., and Ames, D. E., 2016, The Giant Mascot Ni-Cu-PGE deposit, British Columbia: Mineralized conduits in a convergent margin tectonic setting: Economic Geology, v. 111, p. 57–87.
Marsh, B.D., 1979, Island Arc Development: Some Observations, Experiments and Speculations: Journal of Geology, vol. 87, p. 687-713.
Matzen, A. K., Baker, M. B., Beckett, J. R., Wood, B. J., and Stolper, E. M., 2017, The effect of liquid composition on the partitioning of Ni between olivine and silicate melt: Contributions to Mineralogy and Petrology, v. 172.
Morse, S. A., 1996, Kiglapait mineralogy III: Olivine compositions and Rayleigh fractionation models: Journal of Petrology, v. 37, p. 1037–1061.
Mudd, G.M. and Jowitt, S.M., 2014, A detailed assessment of global nickel resource trends and endowments: Economic Geology, v. 109, p. 1813–1841.
Murray, C. G., 1972, Zoned Ultramafic Complexes of the Alaskan Type: Feeder Pipes of Andesitic Volcanoes, in Shagam, R., Hargraves, R. B., Morgan, W. J., Van Houten, F. B., Burk, C. A., Holland, H. D., and Hollister, L. C. eds., Studies in Earth and Space Sciences: Geological Society of America, p. 313-335.
Naldrett, A. J., and Cabri, L. J., 1976, Ultramafic and Related Mafic Rocks: Their Classification and Genesis with Special Reference to the Concentration of Nickel Sulfides and Platinum-Group Element: Economic Geology, v. 71, p. 1131–1158.
Naldrett, A.J., 2004, Magmatic Sulfide Deposits: Geology, Geochemistry, and Exploration, Springer, Berlin, 728 p.
Naldrett, A. J., 2010, Secular Variation of Magmatic Sulfide Deposits and Their Source Magmas: Economic Geology, v. 105, p. 669–688.
Naldrett, A. J., 2011, Fundamentals of Magmatic Sulfide Deposits (C. Li & E. M. Ripley, Eds.), Magmatic Ni-Cu and PGE Deposits: Geology, Geochemistry, and Genesis, v. 17, p. 1-50.
Nandedkar, R. H., Ulmer, P., and Müntener, O., 2014, Fractional crystallization of primitive, hydrous arc magmas: An experimental study at 0.7 GPa: Contributions to Mineralogy and Petrology, v. 167, p. 1–27.
Nelson, J., and Colpron, M., 2007, Tectonics and metallogeny of the British Columbia, Yukon and Alaskan Cordillera, 1.8 Ga to the present: Mineral Deposits of Canada: A Synthesis of Major Deposit-Types, District Metallogeny, the Evolution of Geological Provinces, and Exploration Methods, v. 2703, p. 755–791.
Nelson, J., Colpron, M., and Israel, S., 2013, The Cordillera of British Columbia, Yukon, and Alaska: tectonics and metallogeny: Tectonics, Metallogeny, and Discovery–the North American Cordillera and Similar Accretionary Settings (Colpron, M., Bissig, T., Rusk, B., and Thomspon, J.F.H., Eds.): Society of Economic Geologists, Special Publication 17, p. 53-109.

Nixon, G.T., Hammack, J.L., Connelly, J.N., Case, G., and Paterson, W.P.E., 1990, Geology and Noble Metal Geochemistry of the Polaris Ultramafic Complex, North-Central British Columbia: British Columbia Geological Survey, Geological Fieldwork 1989, p. 387-404.
Nixon, G.T., Hammack, J.L., Ash, C.H., Cabri, L.J., Case, G., Connelly, J.N., Heaman, L.M., Laflamme, J.H.G., Nuttall, C., Paterson, W.P.E., and Wong, R.H., 1997, Geology and Platinum Group-Element Mineralization of Alaskan-type Ultramafic-Mafic Complexes in British Columbia: British Columbia Geological Survey, Bulletin 93, p. 1-113.
Nixon, G.T., Manor, M.J., Jackson-Brown, S., Scoates, J.S., and Ames, D.E., 2015, Magmatic Ni-Cu-PGE sulphide deposits at convergent margins: Geological Survey of Canada, Open File 7856, p. 19-30.
Nixon, G.T., Milidragovic, D., and Scoates, J.S., 2019, Convergent margin Ni-Cu-PGE-Cr ore systems: temporal and magmatic evolution: Targeted Geoscience Initiative 5, Grant Program Interim Reports 2018-2019, Geological Survey of Canada, Open File 8620, p. 49-61.
Nott, J., Milidragovic, D., Nixon, G.T., and Scoates, J.S., 2020, New geological investigations of the Early Jurassic Polaris ultramafic-mafic Alaskan-type intrusion, north-central British Columbia: Geological Fieldwork 2019, British Columbia Geological Survey, Paper 2020-01, p. 59-76.
Pouchou, J.L. and Pichoir, F., 1985, PAP $\phi(\rho Z)$ procedure for improved quantitative microanalysis: Microbeam Analysis, 1985, p. 104-106.
Putirka, K. D., 2005, Mantle potential temperatures at Hawaii, Iceland, and the mid-ocean ridge system, as inferred from olivine phenocrysts: Evidence for thermally driven mantle plumes: Geochemistry, Geophysics, Geosystems, v. 6, p. 1–14.
Putirka, K., Ryerson, F. J., Perfit, M., and Ridley, W. I., 2011, Mineralogy and composition of the oceanic mantle: Journal of Petrology, v. 52, p. 279–313.
Rampone, E., Borghini, G., Godard, M., Ildefonse, B., Crispini, L., and Fumagalli, P., 2016, Melt/rock reaction at oceanic peridotite/gabbro transition as revealed by trace element chemistry of olivine: Geochimica et Cosmochimica Acta, v. 190, p. 309–331.
Ringwood, A. E., 1974, The petrological evolution of island arc systems: Journal of the Geological Society, v. 130, p. 183–204.
Roeder, P. L. & Emslie, R. F., 1970, Olivine-liquid equilibrium: Contributions to Mineralogy and Petrology, v. 29, p. 275-289.
Roots, E.F., 1954, Geology and Mineral Deposits of Aiken Lake Map Area, British Columbia: Geological Survey of Canada, Memoir 274, 246 p.
Scheel, J.E., 2007, Age and Origin of the Turnagain Alaskan-type Intrusion and Associated Ni-Sulphide Mineralization, North-Central British Columbia, Canada: M.Sc. thesis, Vancouver, British Columbia, University of British Columbia, 201 p.
Scheel, J.E., Scoates, J. S., and Nixon, G. T., 2009, Chromian spinel in the Turnagain Alaskan-type ultramafic intrusion, northern British Columbia, Canada: Canadian Mineralogist, v. 47, p. 63–80.
Simkin, T., and Smith, J. V, 1970, Minor-Element Distribution in Olivine: The Journal of Geology, v. 78, p. 304–325.
Sobolev, A. V., Hofmann, A. W., Sobolev, S. V., and Nikogosian, I. K., 2005, An olivine-free mantle source of Hawaiian shield basalts: Nature, v. 434, p. 590–597.
Sobolev, A. V., Hofmann, A. W., Kuzmin, D. V., Yaxley, G. M., Arndt, N. T., Chung, S. L., Danyushevsky, L. V., Elliott, T., Frey, F. A., Garcia, M. O., Gurenko, A. A., Kamenetsky,

V. S., Kerr, A. C., Krivolutskaya, N. A., et al., 2007, The amount of recycled crust in sources of mantle-derived melts: Science, v. 316, p. 412–417.
Song, X., Wang, Y., and Chen, L., 2011, Magmatic Ni-Cu-(PGE) deposits in magma plumbing systems: Features, formation and exploration: Geoscience Frontiers, v. 2, p. 375–384.
Stern, R. J., 2002, Subduction zones: Reviews of Geophysics, v. 40(4), p. 3-1-3–38.
Stormer, J. C., 1973, Calcium zoning in olivine and its relationship to silica activity and pressure: Geochimica et Cosmochimica Acta, v. 37, p. 1815–1821.
Straub, S. M., LaGatta, A. B., Martin-Del Pozzo, A. L., and Langmuir, C. H., 2008, Evidence from high-Ni olivines for a hybridized peridotite/pyroxenite source for orogenic andesites from the central Mexican Volcanic Belt: Geochemistry, Geophysics, Geosystems, v. 9, 33 p.
Su, B. X., Qin, K. Z., Sakyi, P. A., Malaviarachchi, S. P. K., Liu, P. P., Tang, D. M., Xiao, Q. H., Sun, H., Ma, Y. G., and Mao, Q., 2012, Occurrence of an Alaskan-type complex in the Middle Tianshan Massif, Central Asian Orogenic Belt: Inferences from petrological and mineralogical studies: International Geology Review, v. 54, p. 249–269.
Tamura, Y., 1994, Genesis of island arc magmas by mantle-derived bimodal magmatism: Evidence from the Shirahama group, japan: Journal of Petrology, v. 35, p. 619–645.
Thakurta, J., Ripley, E. M., and Li, C., 2008, Geochemical constraints on the origin of sulfide mineralization in the Duke Island Complex, southeastern Alaska: Geochemistry, Geophysics, Geosystems, v. 9.
Thomson, A., and Maclennan, J., 2013, The distribution of olivine compositions in icelandic basalts and picrites: Journal of Petrology, v. 54, p. 745–768.
Ulmer, P., 1989, The dependence of the Fe^{2+}-Mg cation-partitioning between olivine and basaltic liquid on pressure, temperature and composition - An experimental study to 30 kbars: Contributions to Mineralogy and Petrology, v. 101, p. 261–273.
Ulmer, P., 2001, Partial melting in the mantle wedge - The role of H2O in the genesis of mantle-derived “arc-related” magmas: Physics of the Earth and Planetary Interiors, v. 127, p. 215–232.
Wager, L. R., Brown, G. M., and Wadsworth, W. J., 1960, Types of igneous cumulates: Journal of Petrology, v. 1, p. 73–85.
Wanless, R.K., Stevens, R.D., Lachance, G.R. and Edmonds, C.M., 1968, Age Determinations and Geologic Studies, K-Ar Isotopic Ages: Report 8, Geological Survey of Canada, paper 67-2A, 141 p.
Watson, E. B., 1979, Calcium content of forsterite coexisting with silicate liquid in the system Na_2O-CaO-MgO-Al_2O_3-SiO_2: American Mineralogist, v. 64, p. 824–829.
Yao, Z. sen, Qin, K. zhang, and Xue, S. chao, 2017, Genetic relationship between deformation and low-Ca content in olivine from magmatic systems: evidence from the Poyi ultramafic intrusion, NW China: Mineralogy and Petrology, v. 111, p. 909–919.

Appendix A: Thin Section Scans, Photomicrographs, and Petrographic Descriptions of Olivine-bearing Samples from the Polaris Alaskan-type Intrusion

1) DMI18-10-6B
Olivine wehrlite

Medium to coarse grained, heteradcumulate, clinopyroxene-poikilitic olivine wehrlite composed of 75% olivine, 23% clinopyroxene, 1% chromite, and 1% phlogopite. Olivine is subhedral to euhedral and 1-4 mm, and occasionally kink-banded. Clinopyroxene is found interstitially forming large oikocrysts around olivine and more rarely as small inclusions in individual grains of olivine. Chromite is euhedral, fine grained, and found both as inclusions in clinpyroxene and olivine. Olivine is 10-20% serpentinized and clinopyroxene is ~15% altered to fine-grained chlorite. Local carbonate veining is also present. Phlogopite (0.5-2 mm) is present as a trace phase interstitially and more rarely as inclusions in olivine.


TL

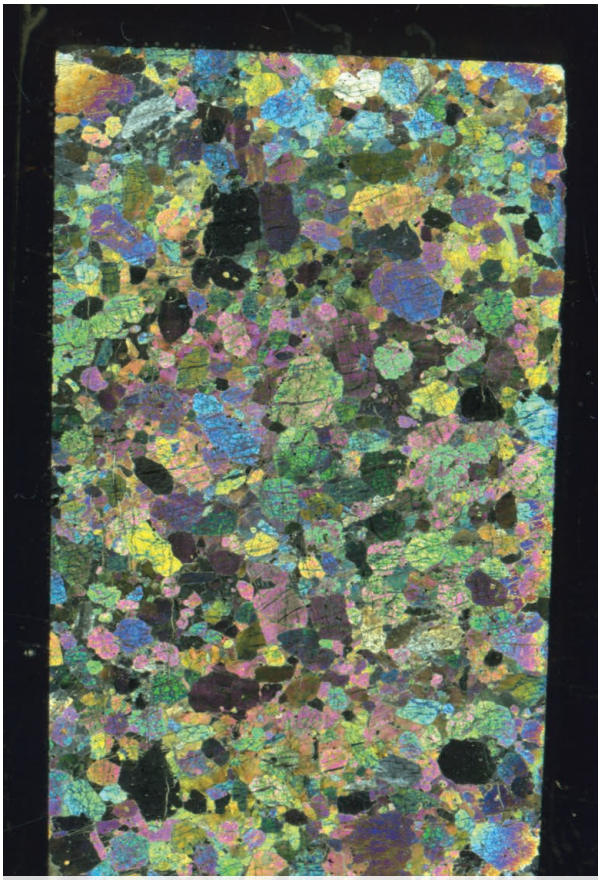
XPL

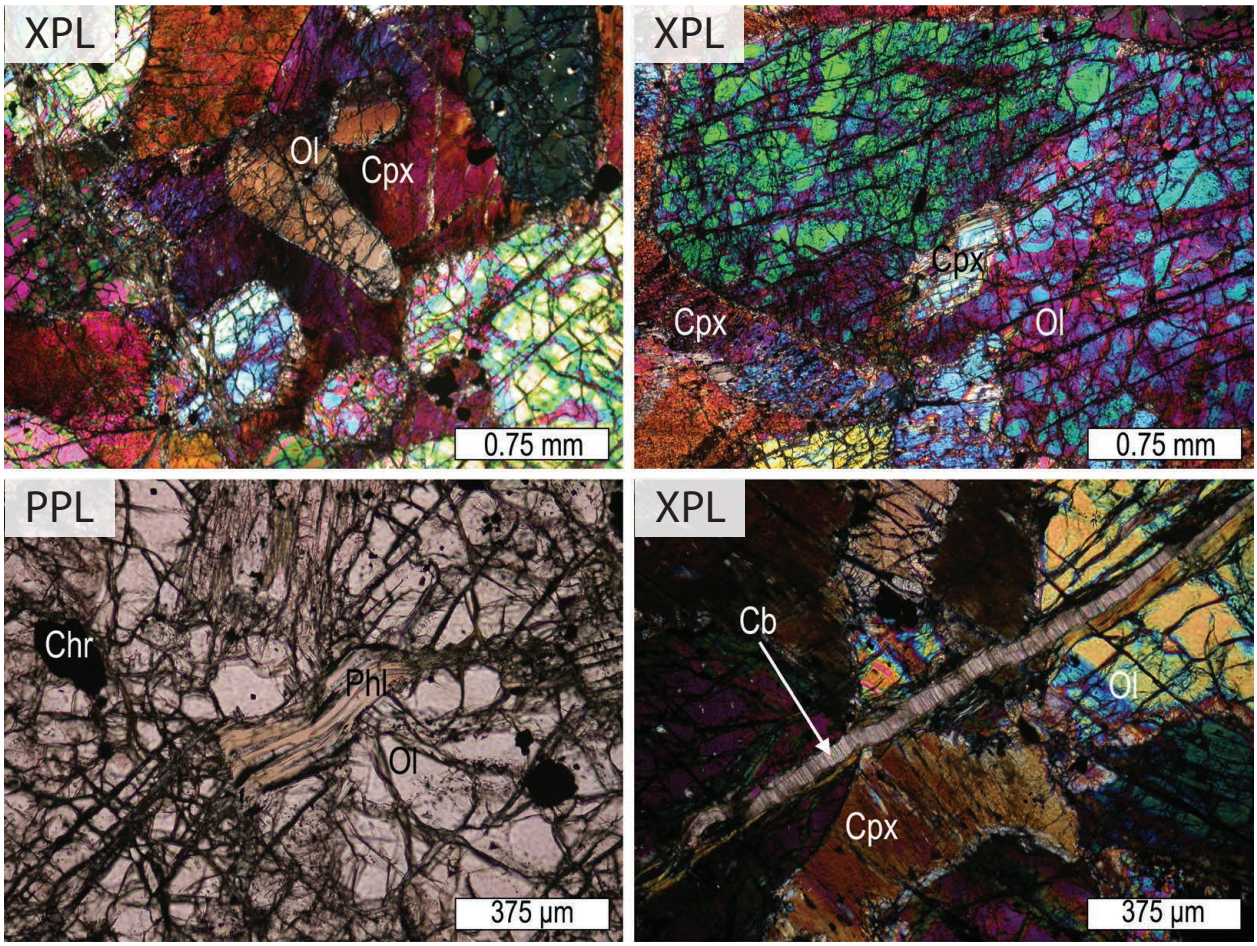
XPL
Ol
Cpx
0.75 mm
XPL
Cpx
Cpx
Ol
0.75 mm
PPL
Chr
Phl
Ol
375 µm
XPL
Cb
Ol
Cpx
375 µm

3) DMI18-10-10
Dunite

Medium to coarse grained, adcumulate dunite composed of 97% subhedral olivine (1-10 mm) and 3% euhedral fine-grained chromite. Larger olivine grains often exhibit kink-banding, whereas smaller grains are less likely to exhibit kink-banding and are generally more euhedral. Chromite is predominantly found as inclusions in olivine but is occasionally found interstitially as larger grains (~0.25 mm). Olivine crystals are approximately 20-40% serpentinized. However, the serpentinization is largely confined to individual grains and does not form vein networks across the rock.

TL

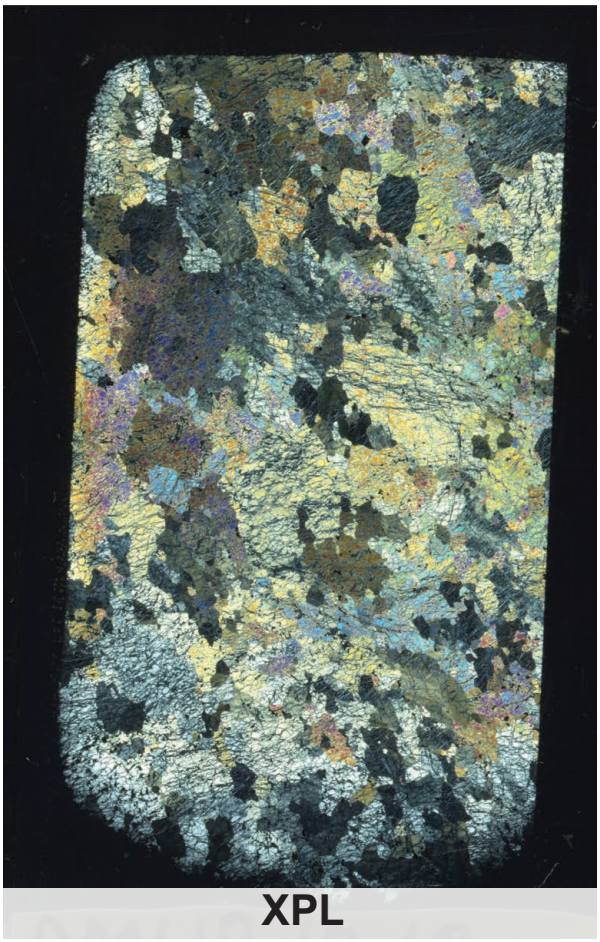

XPL

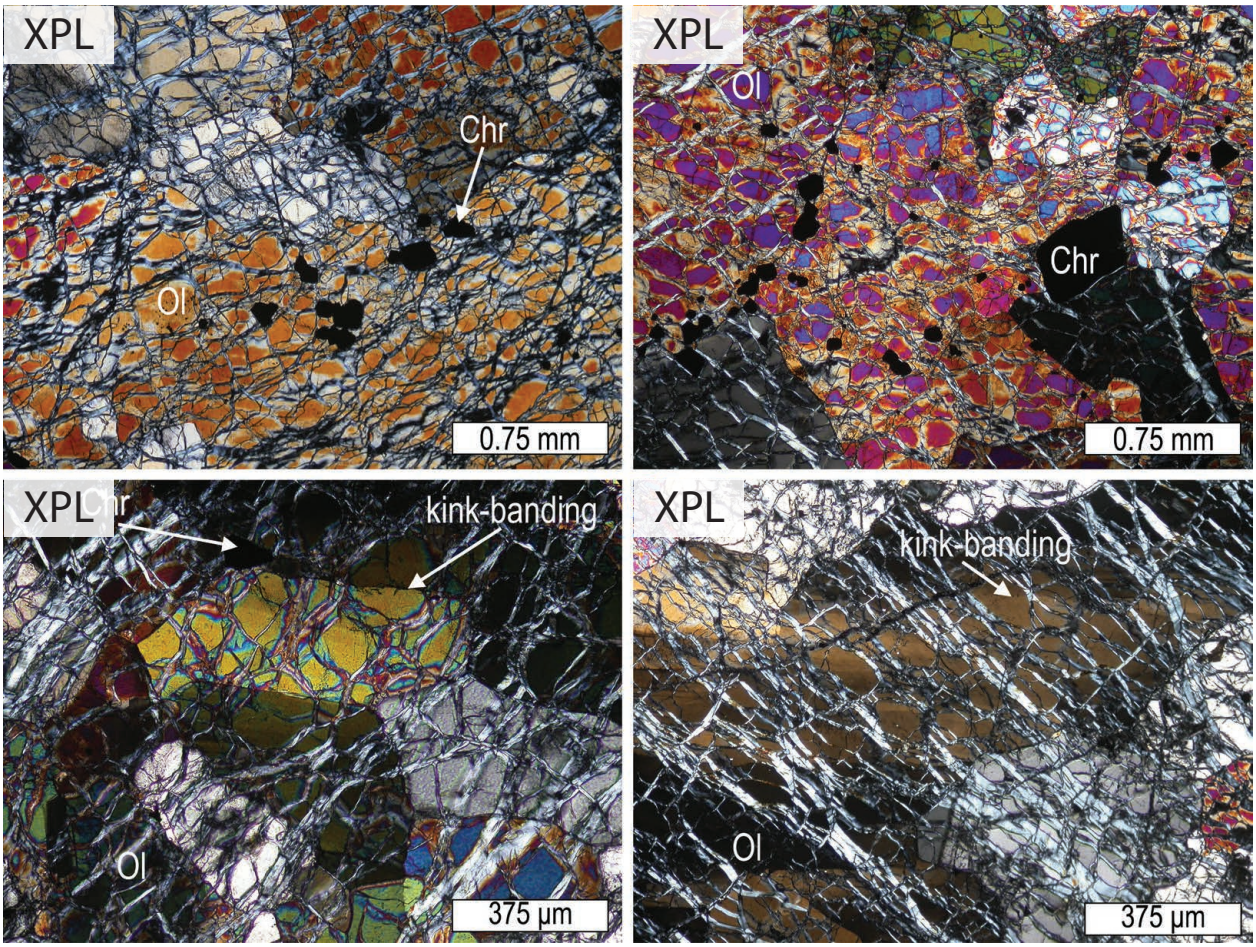
XPL
Chr
Ol
0.75 mm
XPL
Ol
Chr
0.75 mm
XPL
kink-banding
Ol
375 µm
XPL
kink-banding
Ol
375 µm

2) DMI18-10-9
Dunite, chromitite

Medium grained, chromitite schlieren-bearing adcumulate dunite. Adcumulate dunite is composed of 95% olivine and 5% chromite. Olivine is 0.5-2 mm, anhedral to subhedral, and appears to be aligned to some extent. As well, there are what appears to be subhedral olivine crystals found as “chadacrysts” in anhedral olivine oikocrysts. Chromite is euhedral, 0.1 to 0.25 mm, and found interstitially in the adcumulate dunite portion of this sample. Olivine is 20-60% serpentinized with an increase in alteration as olivine approaches chromitite boundary. Chromite is sutured and coarser grained when present in the chromitite schlieren. Chromitite is composed of 85-95% chromite and 5-15% serpentine (100% of the olivine in the chromitite has been altered to serpentine). Olivine is rarely found as inclusions within chromite grains.


TL


XPL

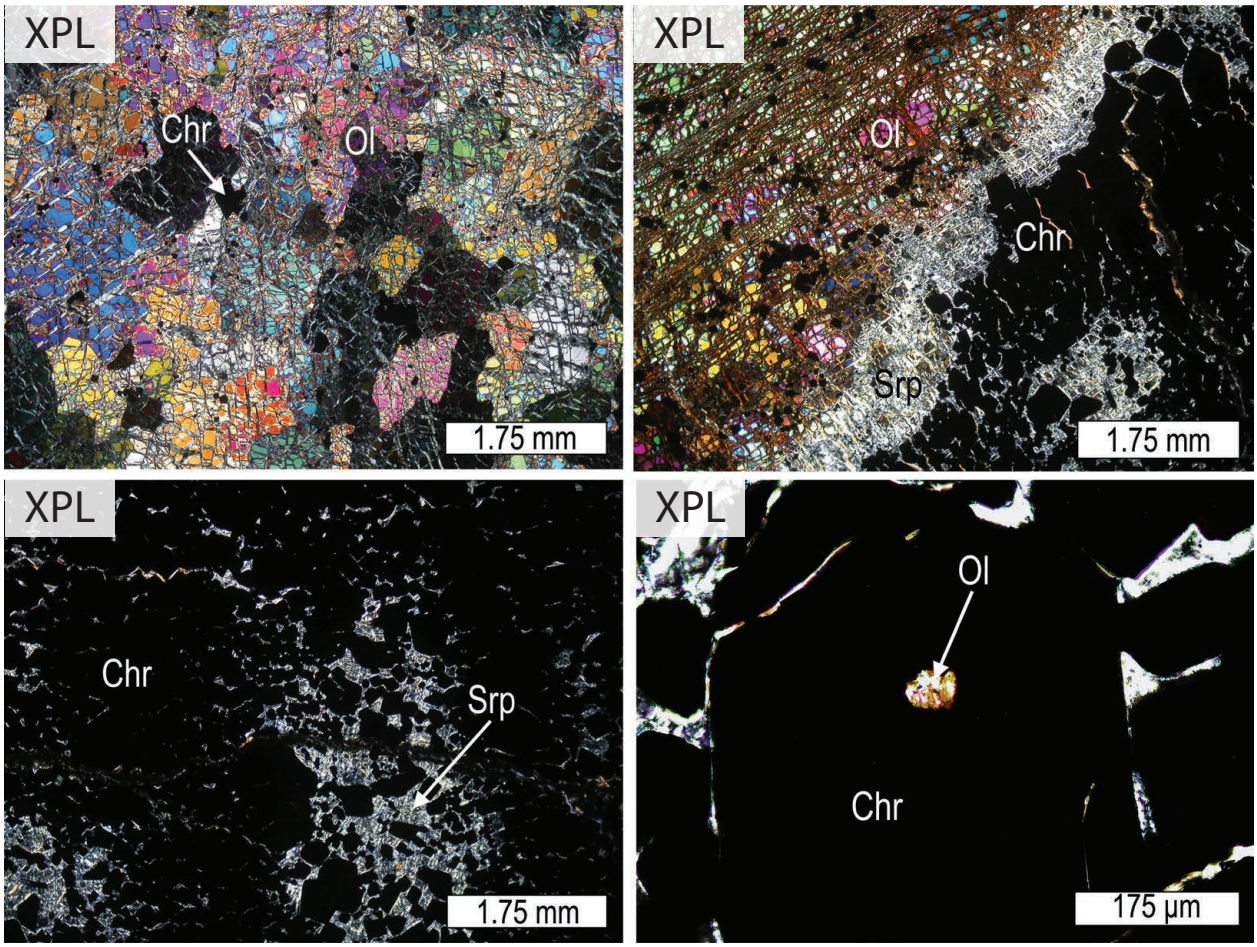
XPL
Chr
Ol
1.75 mm
XPL
Ol
Chr
Srp
1.75 mm
XPL
Chr
Srp
1.75 mm
XPL
Ol
Chr
175 µm

4) DMI18-12-5A
Wehrlite

Medium to coarse grained, heteradcumulate, clinopyroxene-poikilitic wehrlite composed of 55% olivine, 44% clinopyroxene, and 1% chromite. Olivine is 2-4 mm, mainly euhedral with some subhedral grains, and kink-banded. Clinopyroxene is found interstitially forming large oikocrysts. Chromite is 0.1 mm, euhedral, and found as inclusions in clinopyroxene and more rarely olivine. Olivine is 30-50% altered to serpentine, which forms pervasive vein networks that are often truncated by clinopyroxene grains. Olivine also exhibits local iddingsite alteration. Clinopyroxene is 5% altered to chlorite.


TL

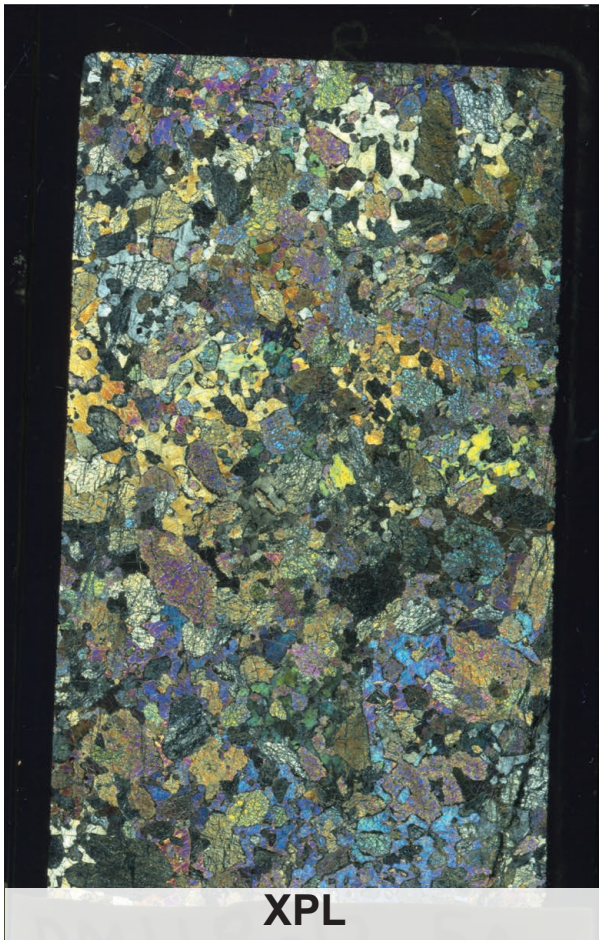
XPL

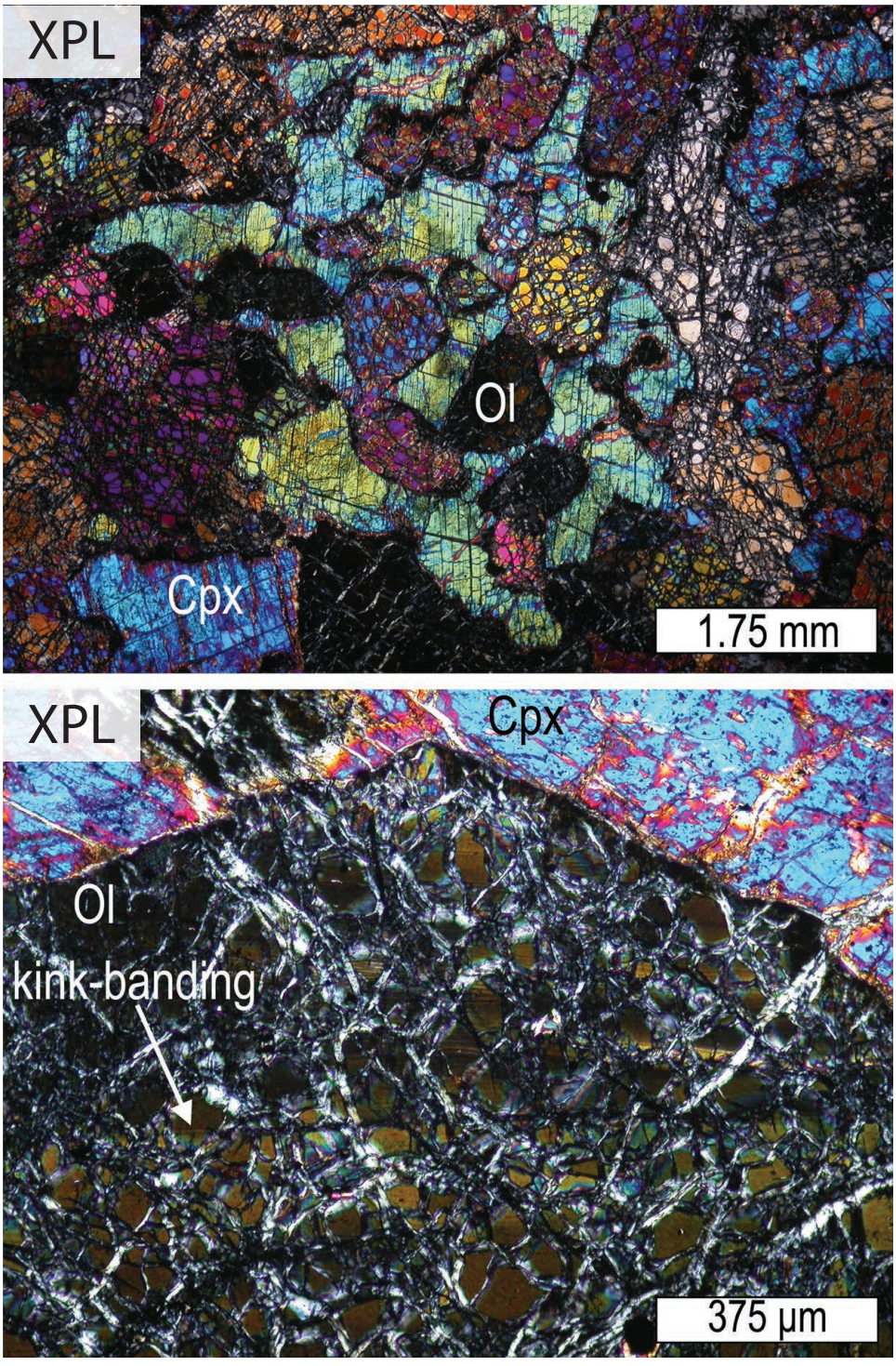
XPL
Ol
Cpx
1.75 mm
XPL
Cpx
Ol
kink-banding
375 µm

5) DMI18-13-1
Wehrlite

Medium to coarse grained, heteradcumulate, clinopyroxene-poikilitic wehrlite composed of 60% olivine, 38% clinopyroxene, and 2% chromite. Olivine is subhedral to euhedral, 2-4 mm, and not kink-banded. Clinopyroxene is interstitial and forms oikocrysts around olivine chadacrysts. Chromite is very fine grained (<0.1 mm), euhedral, and primarily forms clusters in clinopyroxene. Olivine is about 20% altered to serpentine, although a pervasive vein network does exist. Clinopyroxene is finely altered to chlorite and occasionally amphibole (~20%). Trace pentlandite is present.

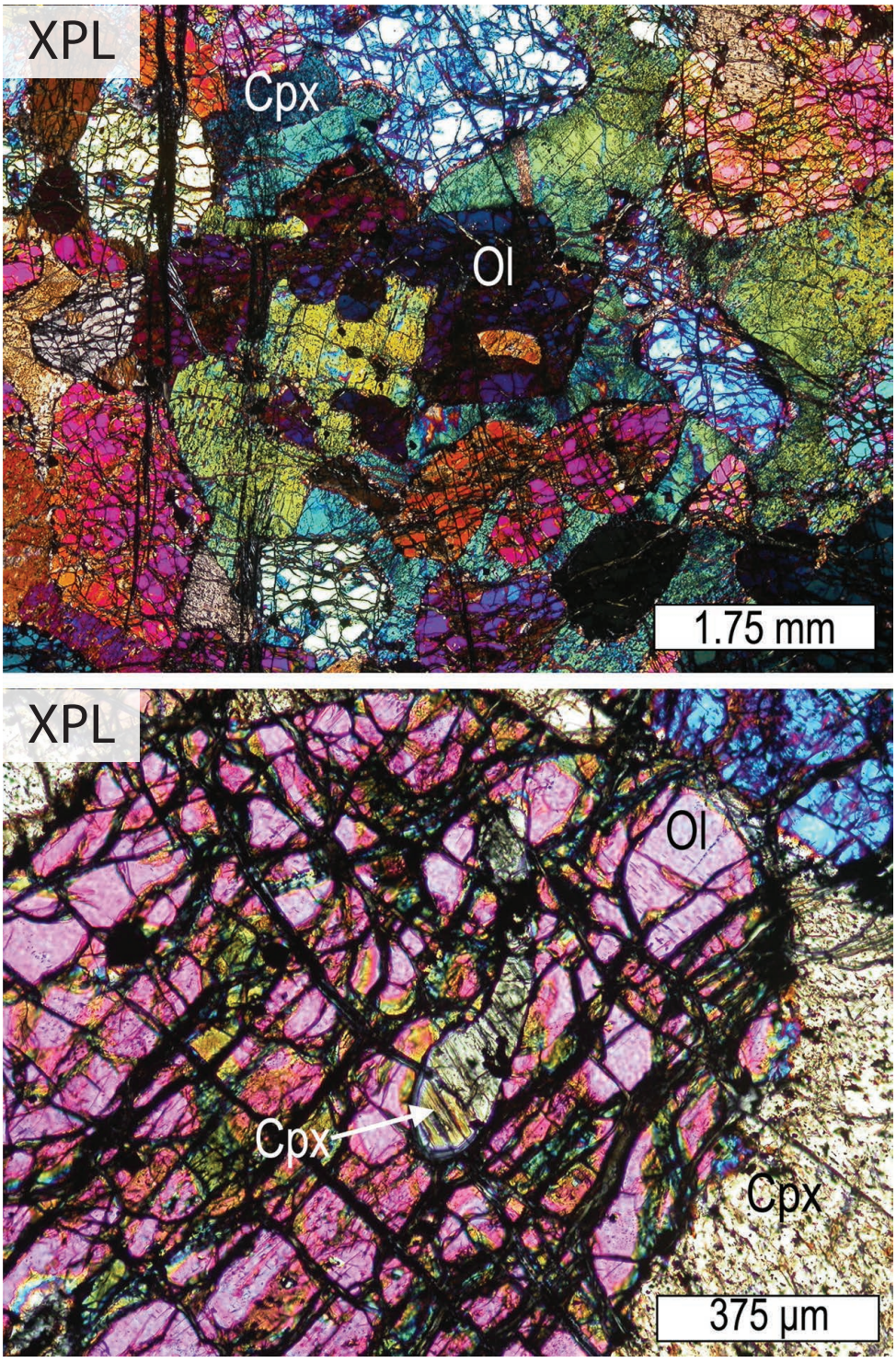
XPL
Cpx
Ol
1.75 mm
XPL
Ol
Cpx
Cpx
375 µm

6) DMI18-17-5
Dunite

Medium to coarse grained, adcumulate dunite composed of 97% olivine and 3% chromite. Olivine is 2-5 mm, subhedral, and occasionally kink-banded. In some cases, grain boundaries are quite irregular. Chromite is fine-grained, euhedral, and found as inclusions within olivine grains. Olivine is approximately 30-50% altered to serpentine. Serpentine does not form pervasive vein networks.

TL

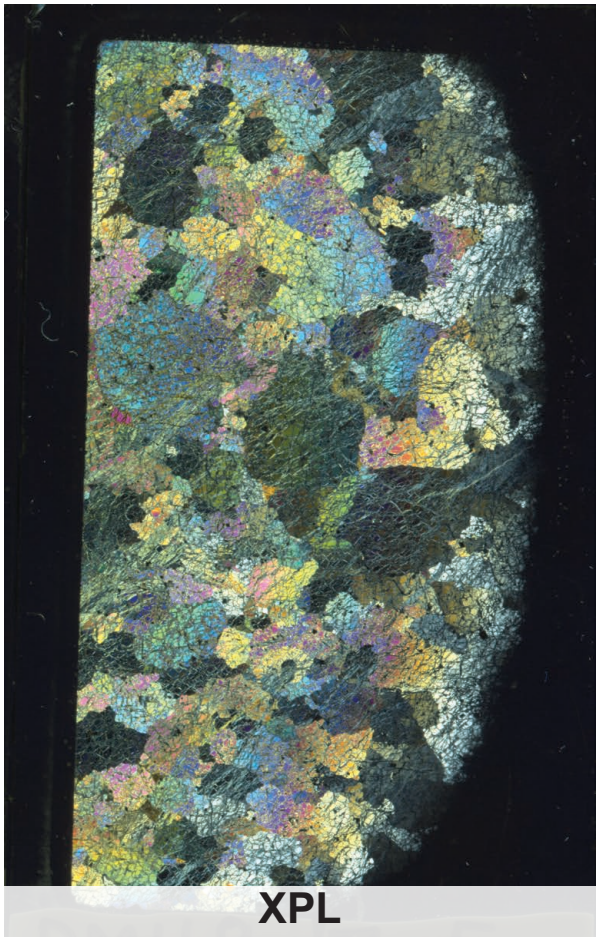

XPL

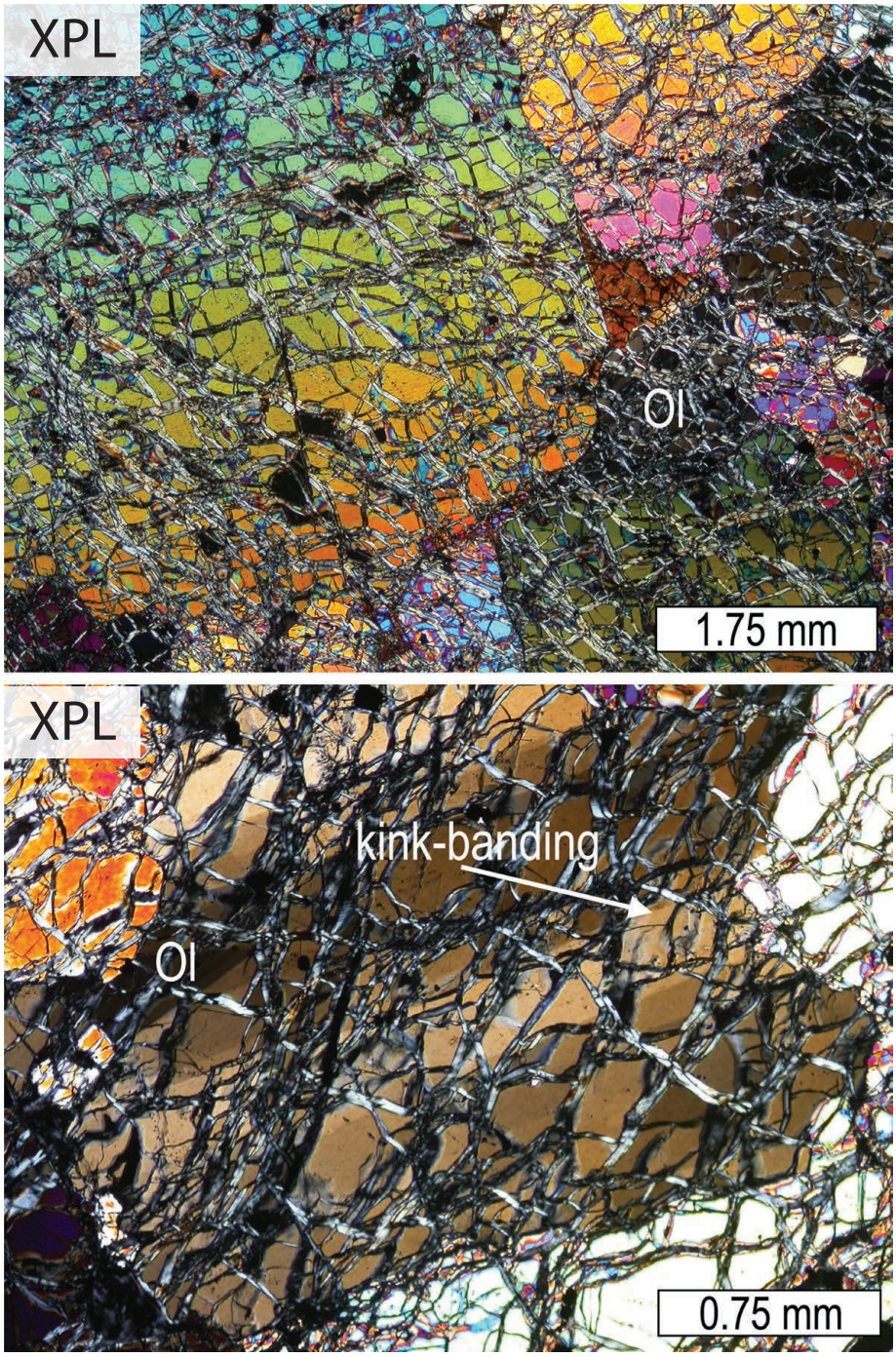
XPL
Ol
1.75 mm
XPL
kink-banding
Ol
0.75 mm

7) DMI18-18-7
Dunite, chromitite

Medium grained, chromitite stringer-bearing adcumulate dunite. Adcumulate dunite is composed of 95% olivine and 5% chromite. Olivine is 1-3 mm, subhedral to euhedral, and not kink-banded. Chromite is 0.1 mm, euhedral, and found interstitially to form stringers of chromitite, which occasionally wrap individual grains of olivine. Olivine is 40-70% serpentinized, which forms both a pervasive fabric and individually altered olivine grains.

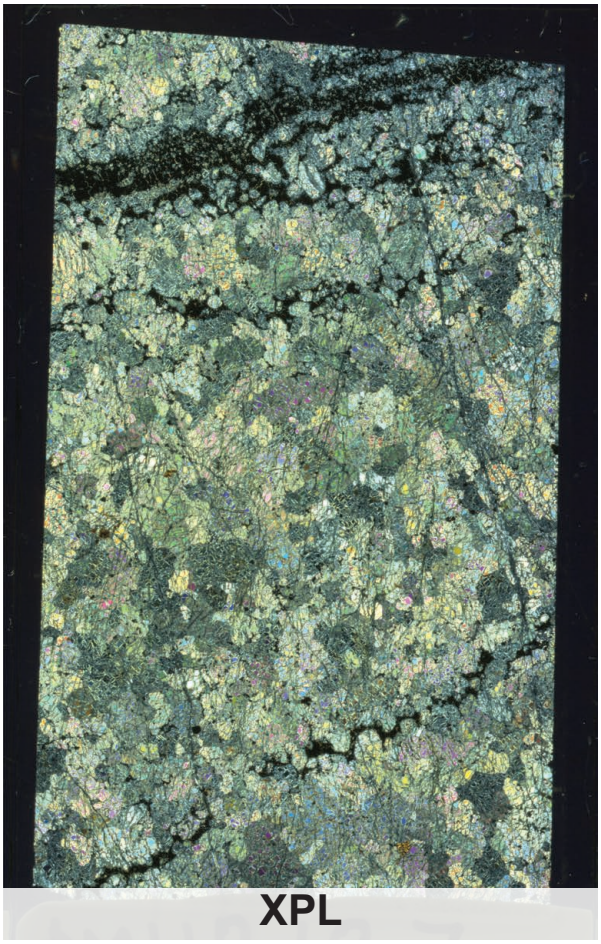

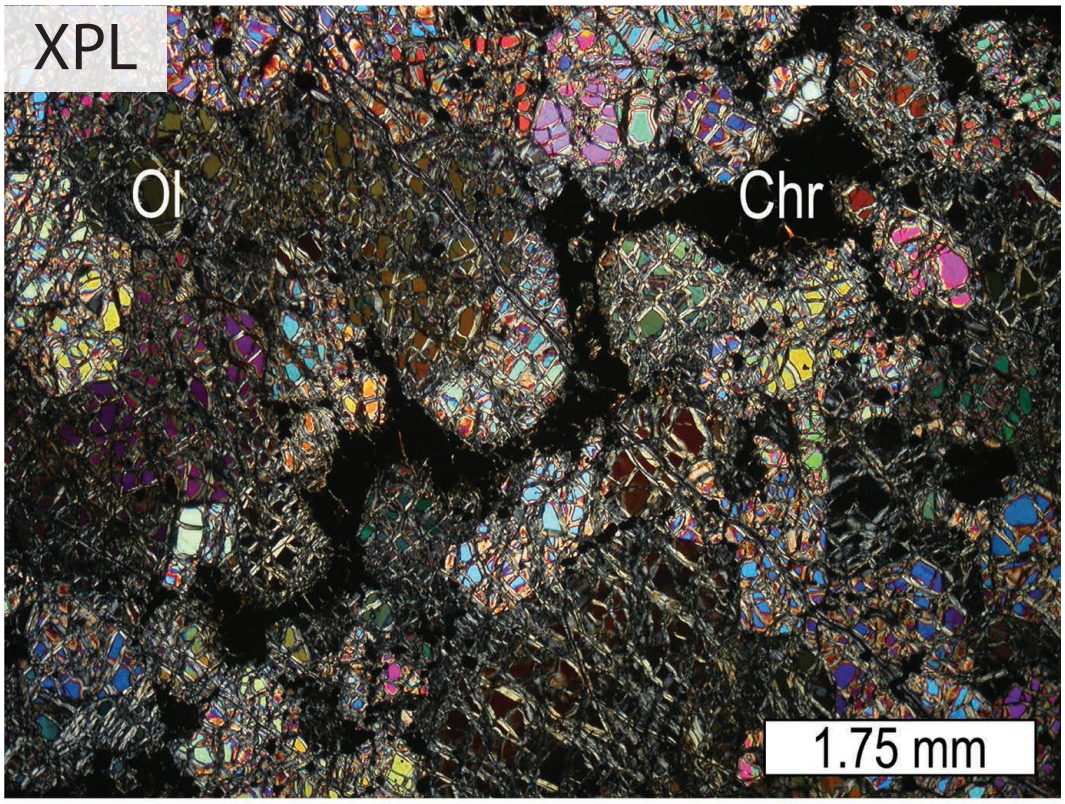
XPL
Ol
Chr
1.75 mm

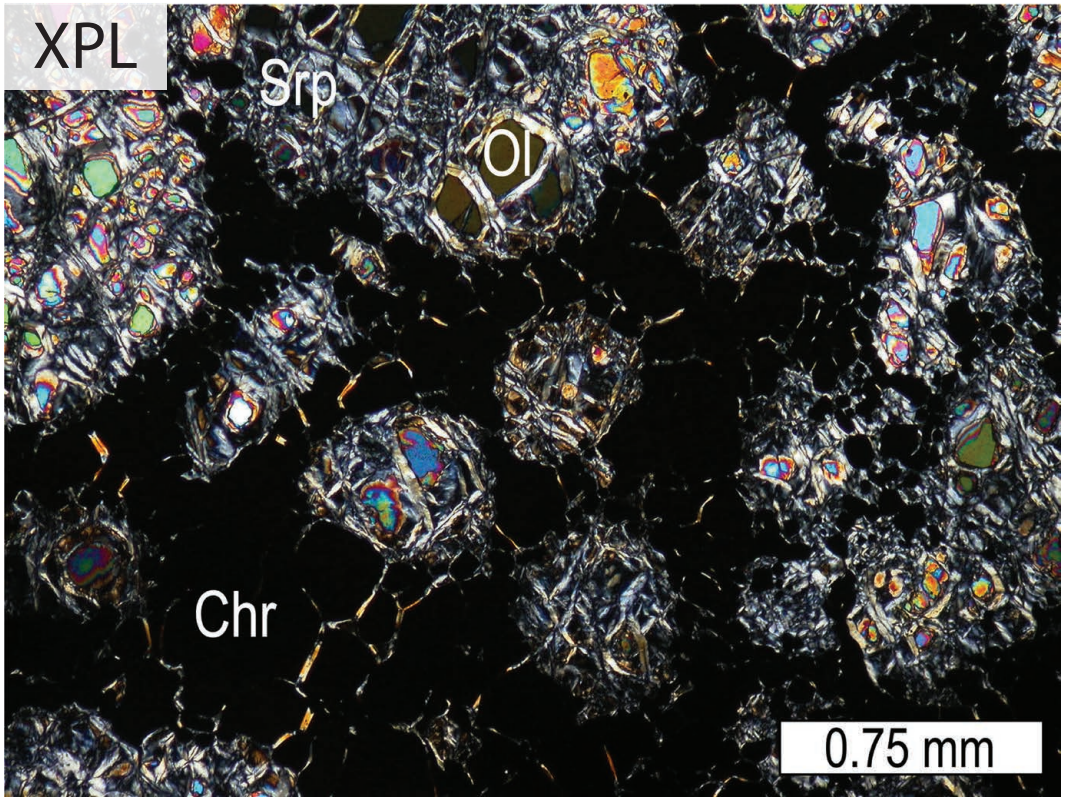
XPL
Srp
Ol
Chr
0.75 mm

8) DMI18-20-12
Olivine clinopyroxenite

Medium to coarse grained, olivine clinopyroxenite composed of 85% clinopyroxene, 12% olivine, 2% magnetite, 1% hornblende, and trace biotite and sulfide (Po+Cp+Pn). Clinopyroxene is subhedral, frequently twinned, and 2-4 mm. Olivine is 1 mm, anhedral to subhedral, is interstitially formed between clinopyroxene crystals, and is frequently kink-banded. Magnetite is anhedral, interstitial, and <0.5 mm. Hornblende is anhedral, interstitial, and about 1 mm. Olivine is approximately 0-5% serpentinized. However, there are small interstitial pockets of serpentine, which likely formed from 100% altered olivine.


TL

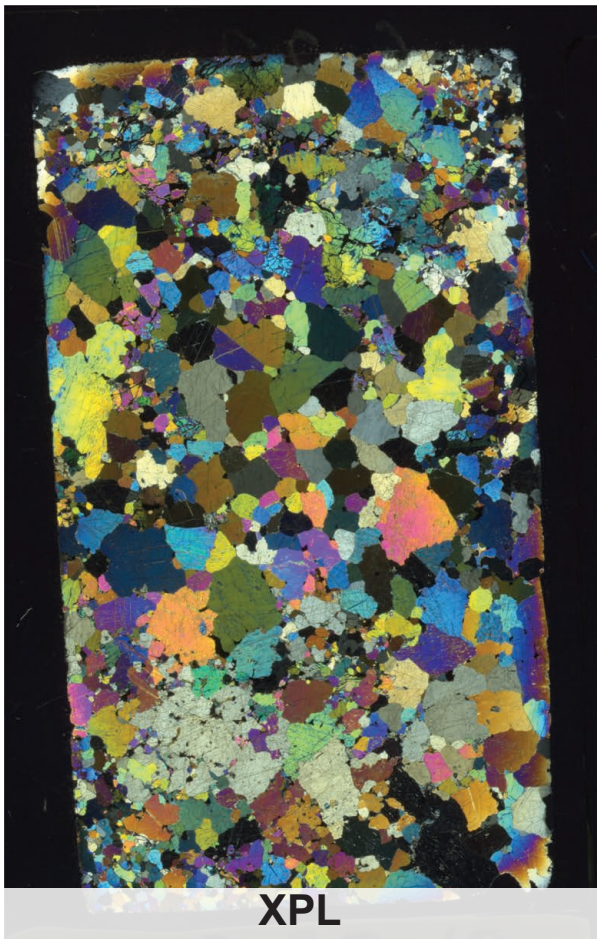
XPL

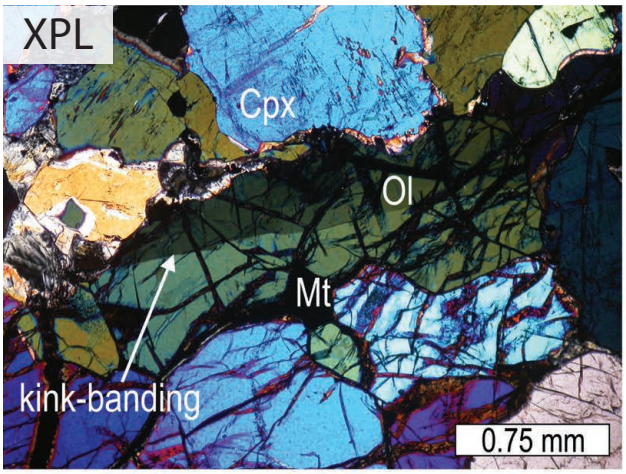
XPL
Cpx
Ol
Mt
kink-banding
0.75 mm

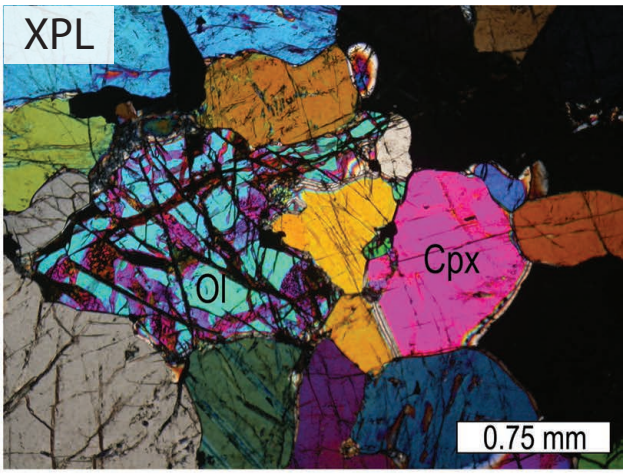
XPL
Ol
Cpx
0.75 mm

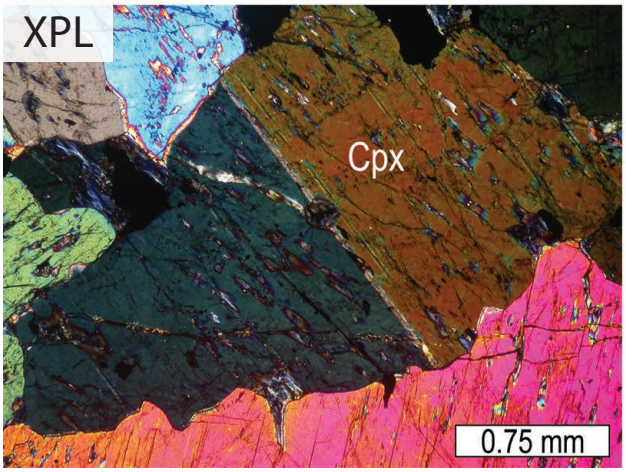
XPL
Cpx
0.75 mm

9) DMI18-21-12
Phlogopite-rich wehrlite

Medium to coarse grained, phlogopite-hornblende-clinopyroxene-poikilitic wehrlite composed of 47% clinopyroxene, 38% olivine, 10% biotite, and 5% hornblende. Clinopyroxene forms large oikocrysts around olivine and is about 3% altered to chlorite. Olivine is subhedral, 4-5 mm, is slightly kink-banded, and is 30-50% serpentinized. Phlogopite and hornblende form interstitially to make oikocrysts. Trace chromite is also present.

TL

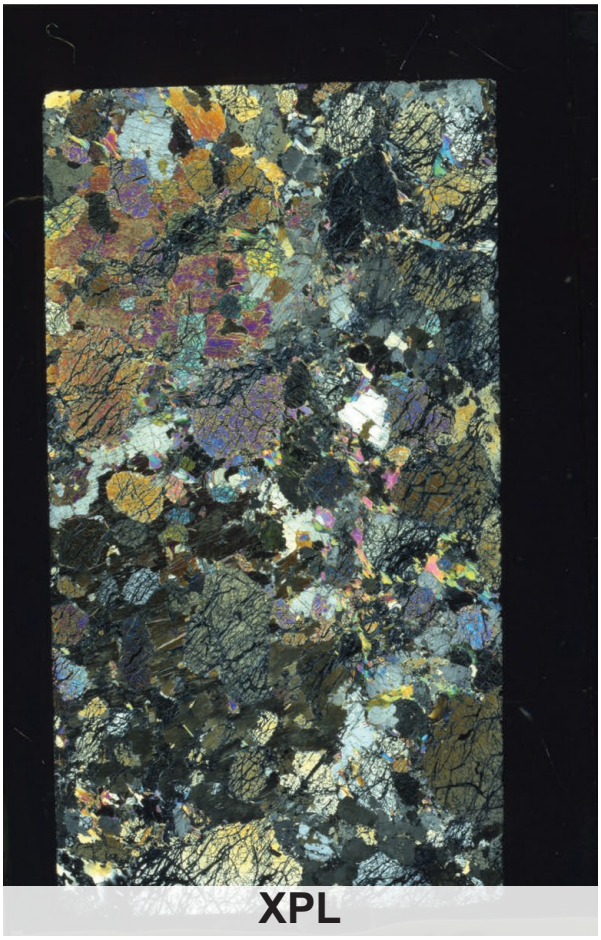

XPL

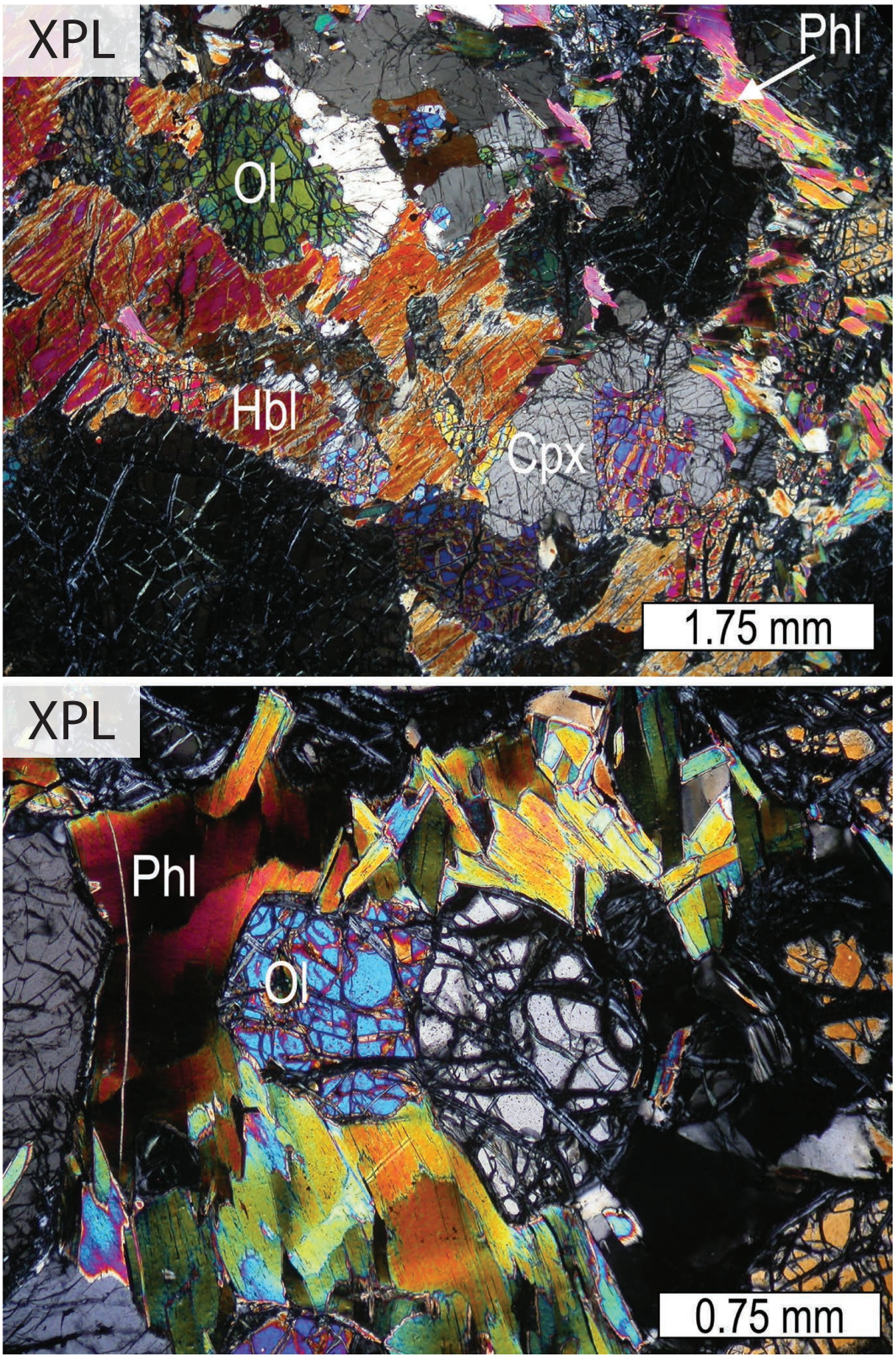
XPL
Phl
Ol
Hbl
Cpx
1.75 mm
XPL
Phl
Ol
0.75 mm

10) DMI18-21-15
Dunite

Medium grained, adcumulate dunite composed of 98% olivine, 2% chromite, and trace phlogopite. Olivine is 1-22 mm, subhedral to euhedral, rarely kink-banded, and forms polygonal sutures with other grains. Chromite is 0.2-0.5 mm, euhedral, and found preferentially between grains of olivine. However, chromite is also found as inclusions in olivine. Olivine is 20-40% altered to serpentine, which forms aligned, small pervasive veins. Phlogopite is found interstitially and is texturally primary.

TL

XPL

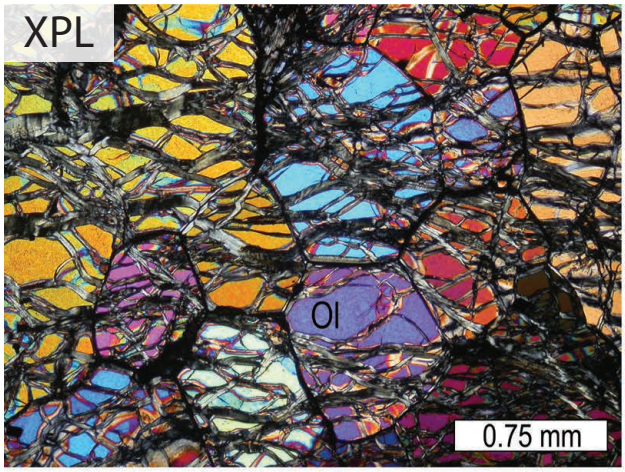
XPL
Ol
0.75 mm

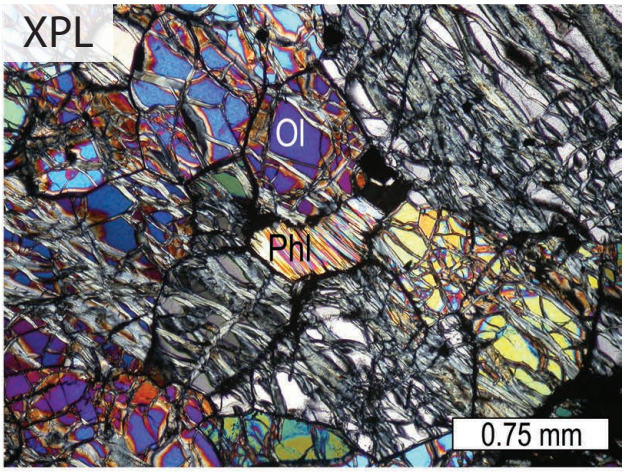
XPL
Ol
Phl
0.75 mm

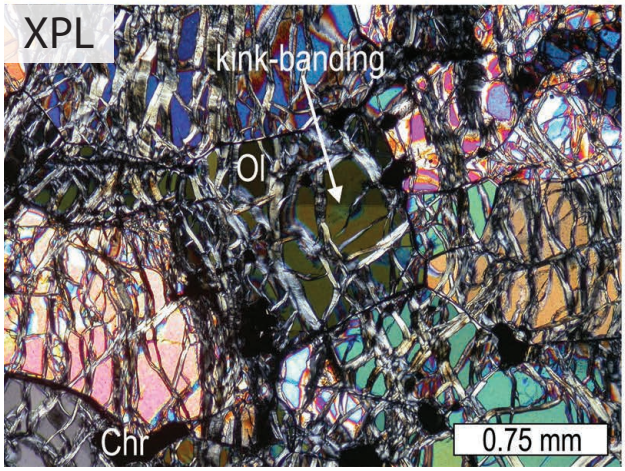
XPL
kink-banding
Ol
Chr
0.75 mm

11) DMI18-21-19
Hornblende-olivine wehrlite

Medium to coarse grained, heteradcumulate hornblende-olivine wehrlite composed of 73% olivine, 15% hornblende, 10% clinopyroxene, 1% phlogopite, and 1% chromite. Olivine is subhedral, 3-4 mm, and 50-70% altered to serpentine. Hornblende is anhedral to subhedral, 4 mm, and predominately primary texturally. Clinopyroxene is anhedral to subhedral, 3 mm, and 5% altered to chlorite. The rims of certain clinopyroxene grains have also been altered to uralite. Phlogopite is 1-2 mm and found interstitially. Chromite is <0.2 mm, euhedral, and has magnetite-altered rims. Trace apatite, pentlandite, and pyrrhotite are also present. Pentlandite (<0.1 mm) is found with tarnished pyrrhotite (<0.1mm), and both are broken up by magnetite found in veins of serpentinization.


TL


XPL

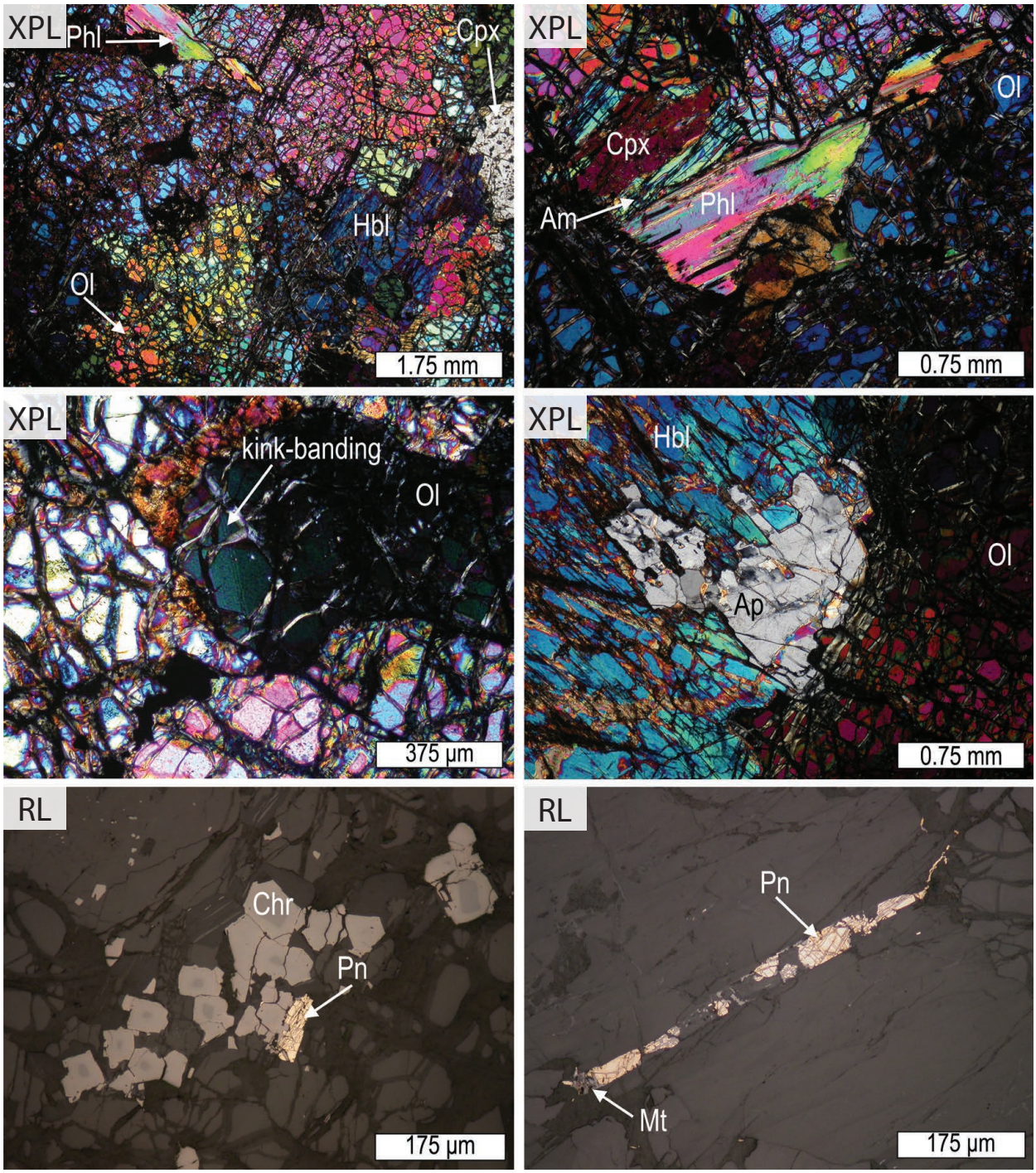
XPL
Phl
Cpx
Hbl
Ol
1.75 mm
XPL
Ol
Cpx
Am
Phl
0.75 mm
XPL
kink-banding
Ol
375 µm
XPL
Hbl
Ol
Ap
0.75 mm
RL
Chr
Pn
175 µm
RL
Pn
Mt
175 µm

12) DMI18-25-9
Magnetite-olivine clinopyroxenite

Medium grained, equigranular, magnetite-olivine clinopyroxenite composed of 47% clinopyroxene, 30% olivine, 20% magnetite, and 3% hornblende. Clinopyroxene is subhedral to euhedral, 1 mm, and predominantly unaltered. Olivine is subhedral, 1-2 mm, and virtually unaltered. Magnetite is subhedral to anhedral, 1 mm, and is found interstitially between clinopyroxene grains. Hornblende is <1 mm and is found interstitially as anhedral grains. Trace sulfides of chalcopyrite are present occasionally in conjunction with pyrrhotite and pentlandite.


TL

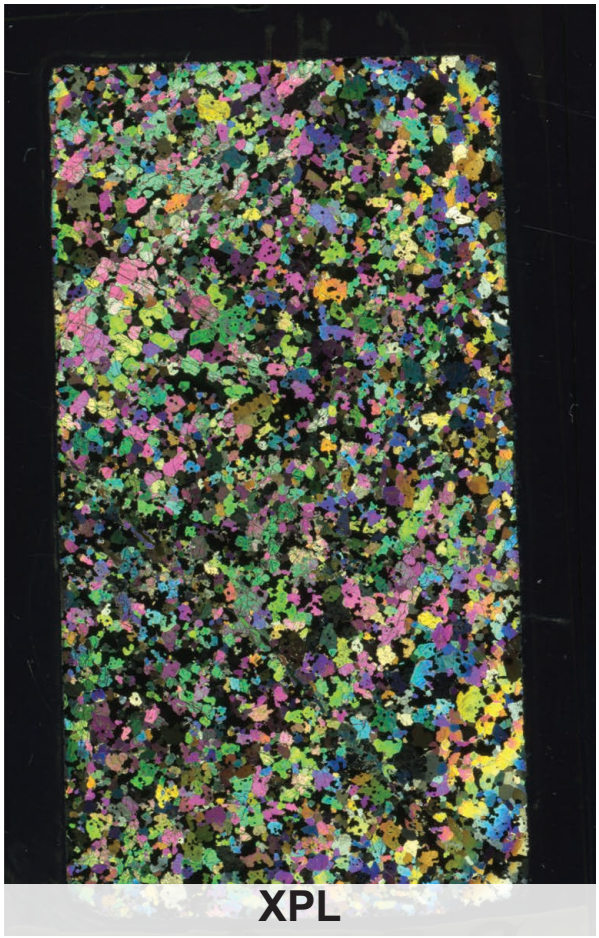
XPL

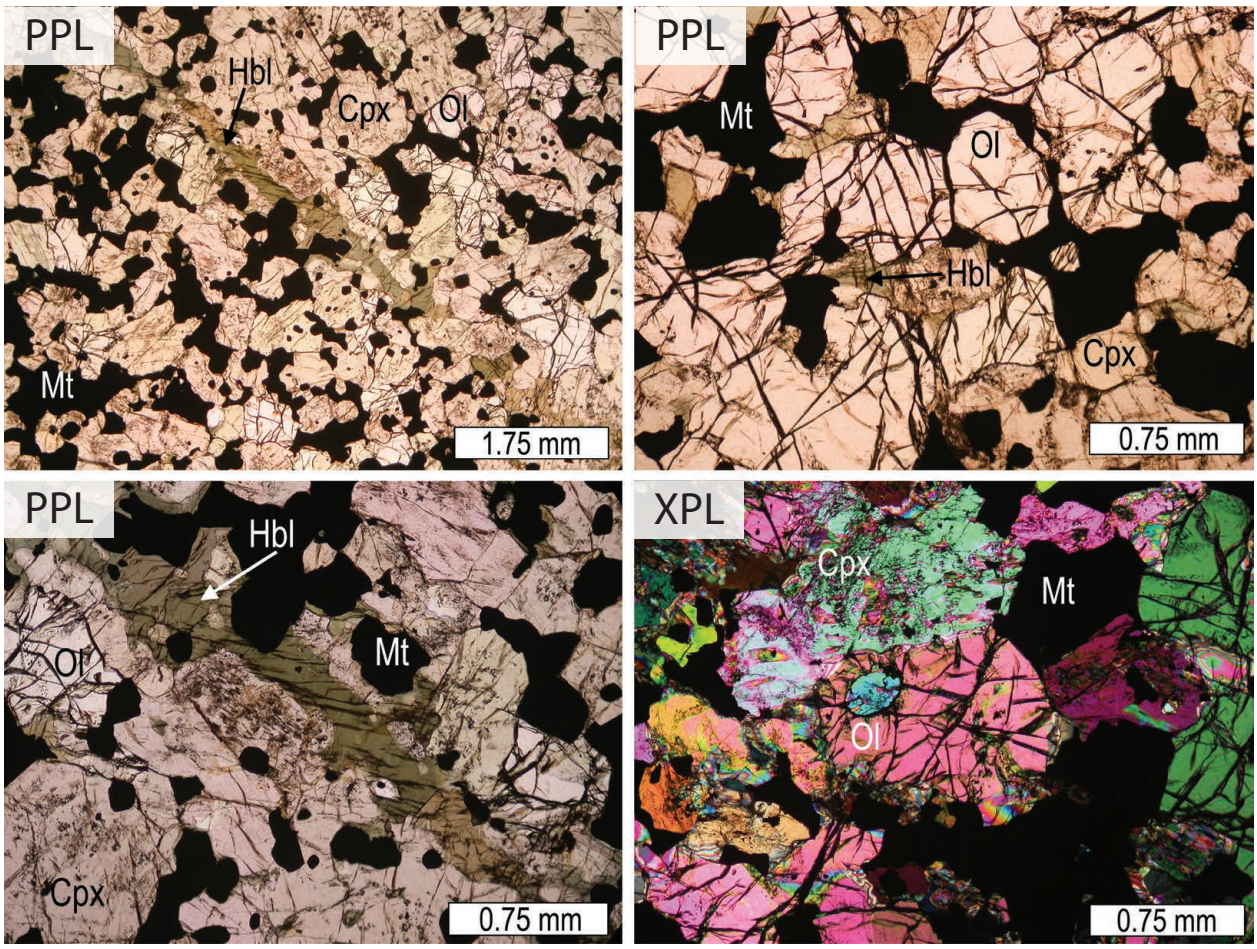
PPL
Hbl
Cpx
Ol
Mt
1.75 mm
PPL
Mt
Ol
Hbl
Cpx
0.75 mm
PPL
Hbl
Ol
Mt
Cpx
0.75 mm
XPL
Cpx
Mt
Ol
0.75 mm

13) DMI18-26-6
Magnetite-olivine clinopyroxenite

Medium to coarse grained, hornblende-phlogopite-magnetite olivine clinopyroxenite composed of 47% clinopyroxene, 30% magnetite, 15% olivine, 4% hornblende, and 4% phlogopite. Clinopyroxene is 1 mm, subhedral to euhedral, and often shows simple twins. Magnetite is subhedral, often rounded, and shows exsolution of ilmenite or another form of spinel. Rims of magnetite grains do not show this exsolution. Olivine is anhedral to subhedral, <10 mm, and locally kink-banded. Olivine is 10% serpentinized and locally altered to iddingsite. Both phlogopite and hornblende are found interstitially around olivine and clinopyroxene, and phlogopite occasionally forms oikocrysts. Trace ilmenite is present in magnetite-rich areas. Trace chalcopyrite is found as sulfide droplets interstitially and as inclusions in magnetite and has been supergene enriched to bornite and covellite.

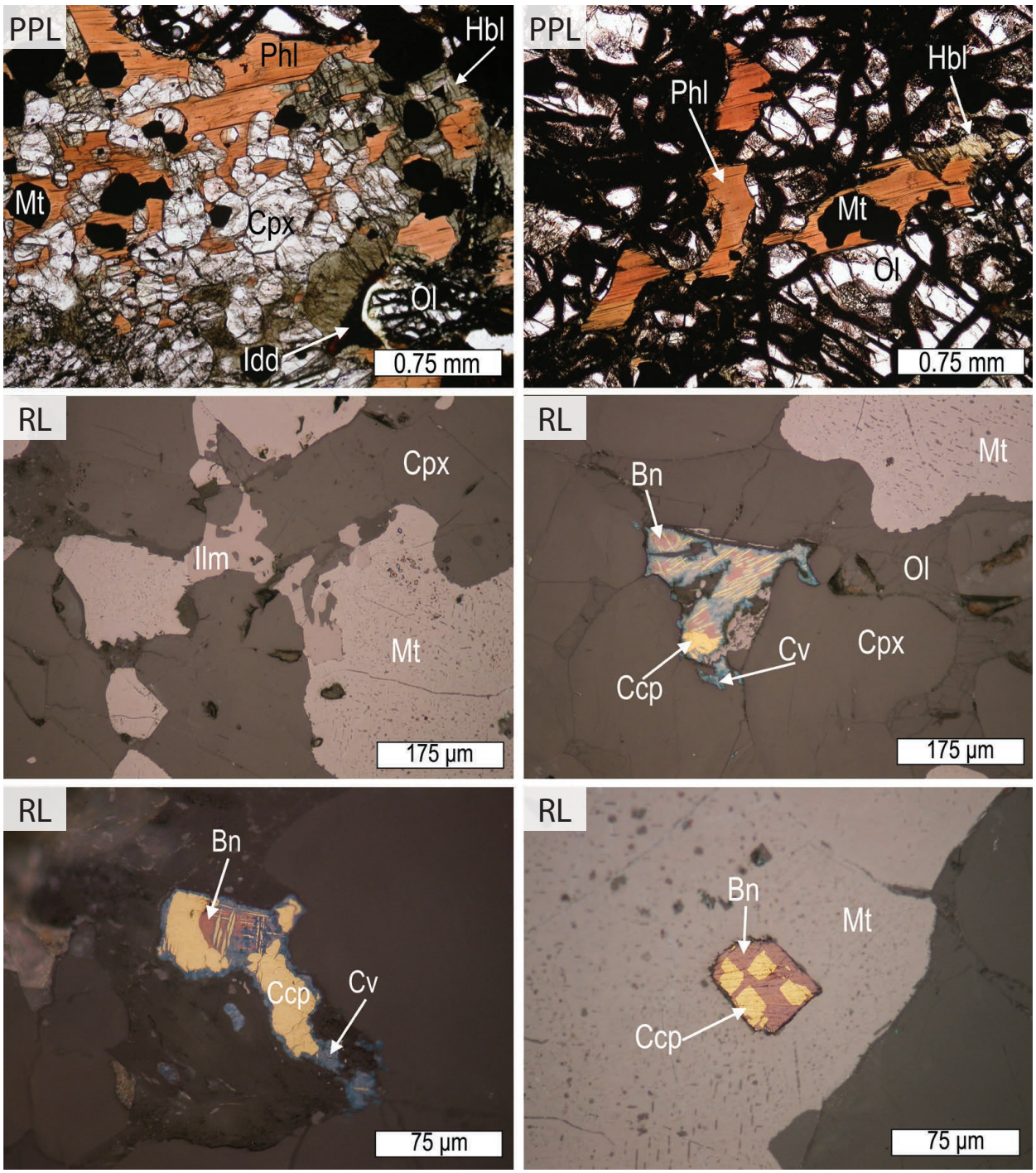
PPL
Hbl
Phl
Mt
Cpx
Ol
Idd
0.75 mm
PPL
Phl
Hbl
Mt
Ol
0.75 mm
RL
Cpx
Ilm
Mt
175 µm
RL
Mt
Bn
Ol
Cv
Cpx
Ccp
175 µm
RL
Bn
Ccp
Cv
75 µm
RL
Bn
Mt
Ccp
75 µm

14) DMI18-27-4
Wehrlite

Medium to coarse grained, clinopyroxene-poikilitic wehrlite with 50% olivine, 46% clinopyroxene, 2% phlogopite, 1% carbonate, and 1% amphibole. Olivine is 1-5mm, subhedral to euhedral, primarily occurs as chadacrysts, and is variably serpentinized (20-100%). Clinopyroxene forms very large oikocrysts up to 10 mm and shows alteration to amphibole and carbonate. Phlogopite is minor and is found interstitially. Trace chromite is also present.

TL

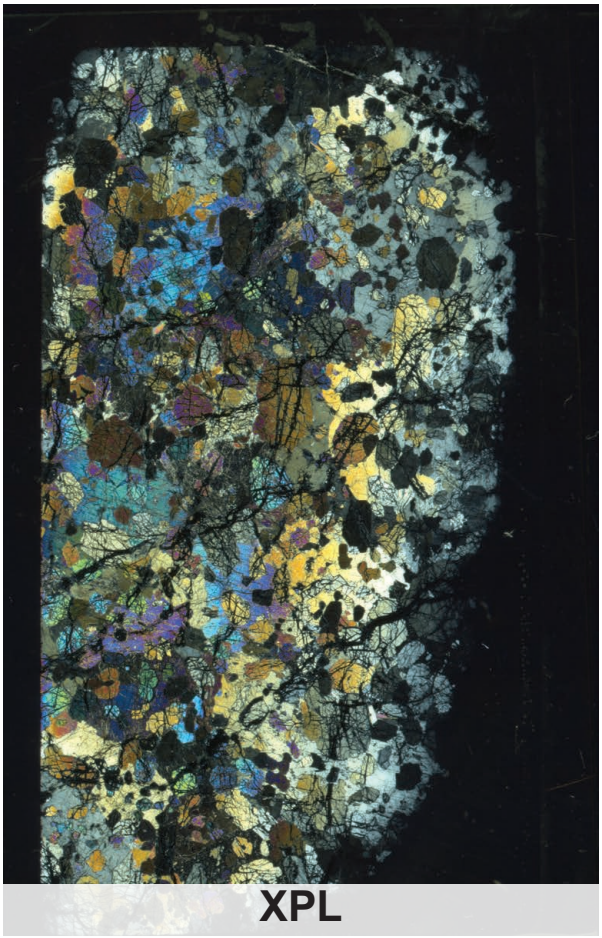

XPL

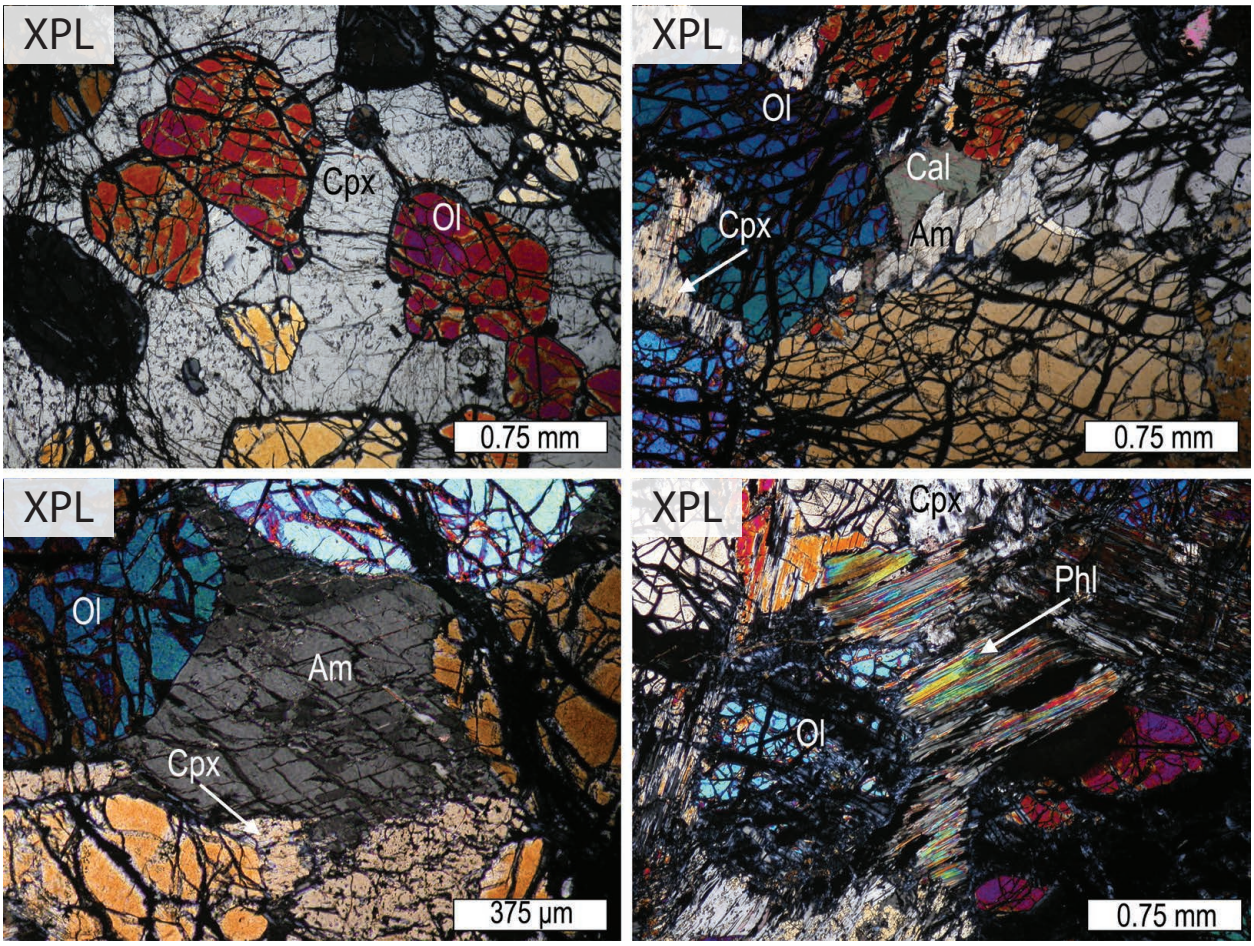
XPL
Cpx
Ol
0.75 mm
XPL
Ol
Cal
Cpx
Am
0.75 mm
XPL
Ol
Am
Cpx
375 µm
XPL
Cpx
Phl
Ol
0.75 mm

15) DMI18-28-5
Olivine clinopyroxenite

Medium grained, olivine clinopyroxenite composed of 69% clinopyroxene, 30% olivine, and 1% chromite. Clinopyroxene is 0.5-3 mm, subhedral to euhedral, and commonly twinned. Clinopyroxene is about 10% altered to chlorite. Olivine is anhedral to subhedral, 2-4 mm, and shows kink-banding. Olivine is 20-50% serpentinized and a vein network of serpentine is pervasive throughout the sample. Trace sulfide of pyrrhotite and pentlandite is also present, often found in conjunction with magnetite in veins of serpentine.


TL


XPL

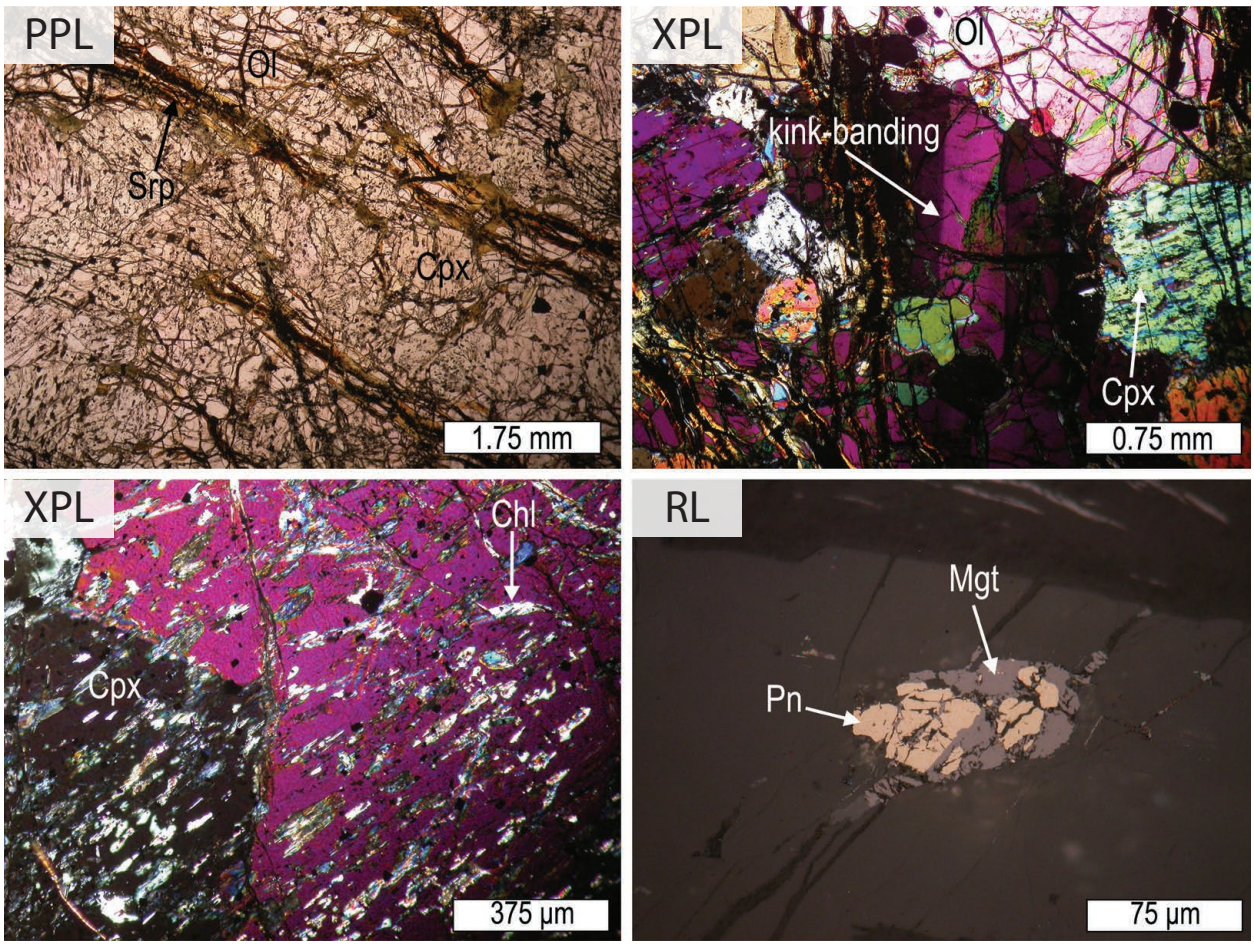
PPL
Ol
Srp
Cpx
1.75 mm
XPL
Ol
kink-banding
Cpx
0.75 mm
XPL
Chl
Cpx
375 µm
RL
Mgt
Pn
75 µm

16) DMI18-32-6
Dunite, chromitite

Medium to coarse grained, chromitite schlieren-bearing adcumulate dunite composed of 90% olivine and 10% chromite. Olivine is subhedral to euhedral, 2-4 mm, and kink-banded. Chromite is 0.1 mm, euhedral, and sutured in schlieren. Olivine is 30-50% serpentinized and olivine surrounded my chromite is more altered.

TL

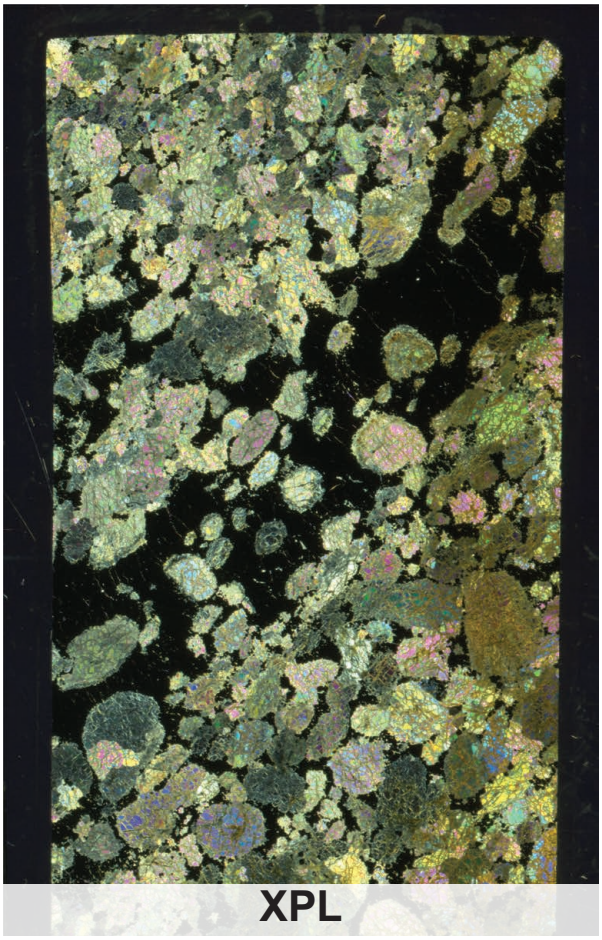

XPL

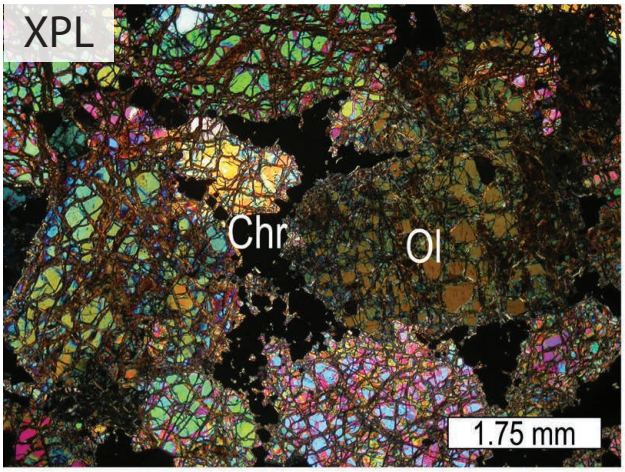
XPL
Chr
Ol
1.75 mm

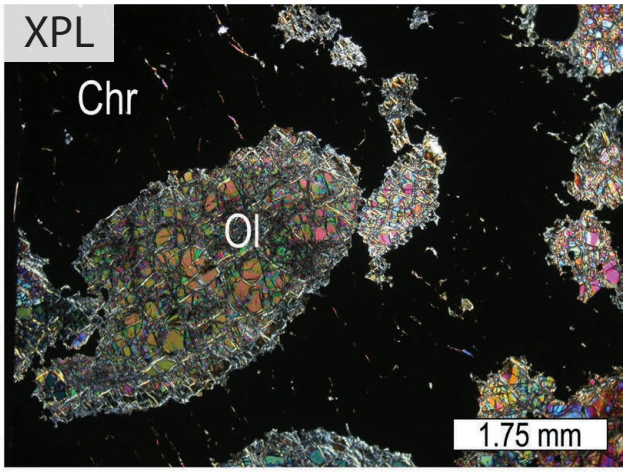
XPL
Chr
Ol
1.75 mm

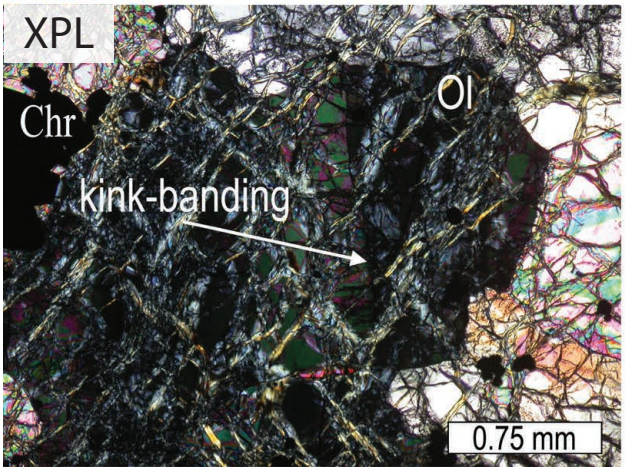
XPL
Chr
Ol
kink-banding
0.75 mm

17) DMI18-32-6
Dunite, chromitite

Medium to coarse grained, chromitite schlieren-bearing adcumulate dunite composed of 90% olivine and 10% chromite. Olivine is subhedral to euhedral, 2-4 mm, and kink-banded. Chromite is 0.1 mm, euhedral, and sutured in schlieren. Olivine is 30-50% serpentinized and olivine surrounded my chromite is more altered.

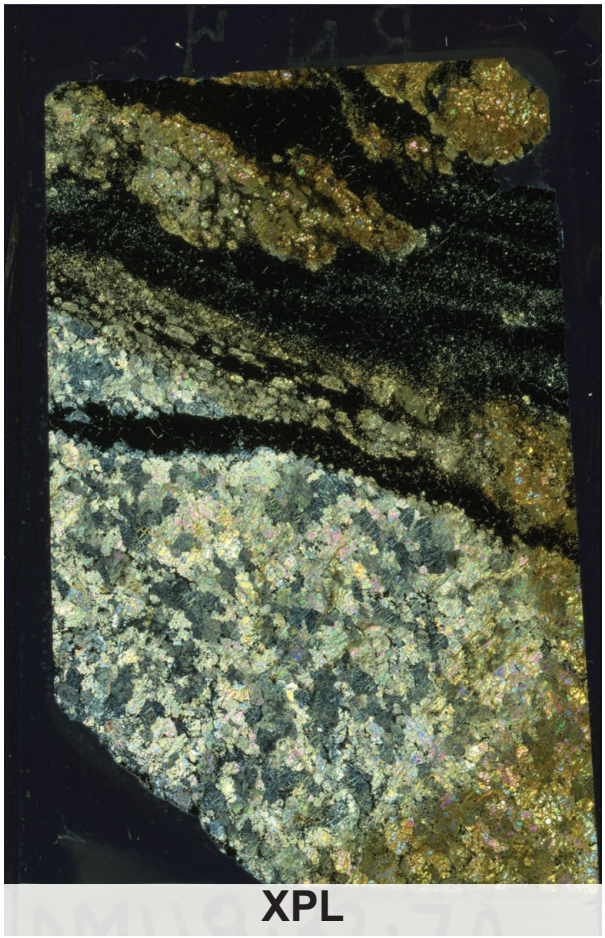

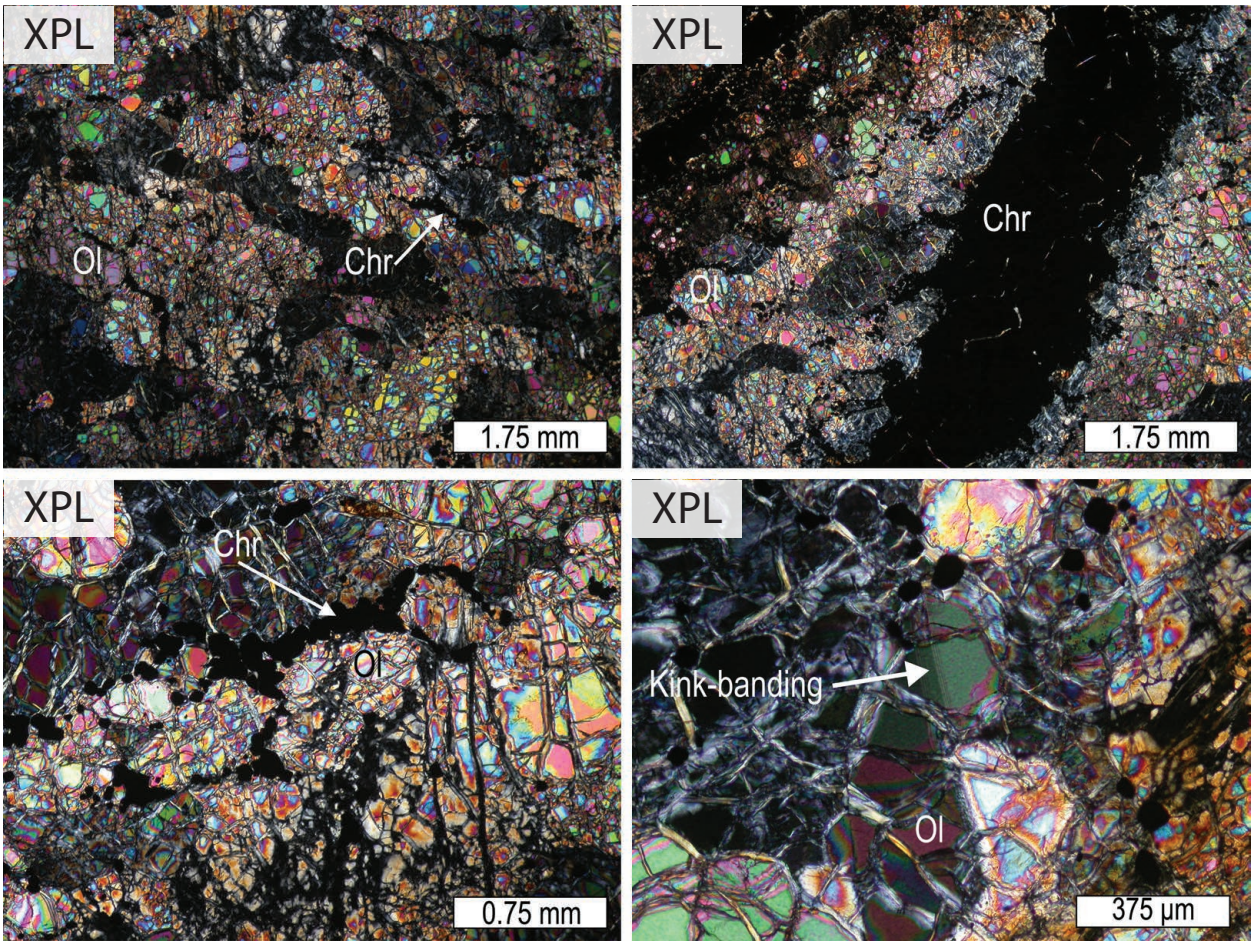
XPL
Ol
Chr
1.75 mm
XPL
Chr
Ol
1.75 mm
XPL
Chr
Ol
0.75 mm
XPL
Kink-banding
Ol
375 µm

18) DMI18-32-7C
Dunite, chromitite, dunite dike

Fine to medium grained, adcumulate dunite dike cross-cutting medium grained chromitite schlieren-bearing adcumulate dunite. Adcumulate dunite dike is composed of 98% 0.5-2 mm, subhedral olivine, and 2% <0.1 mm chromite. Chromitite is composed of 80-100% sutured chromite (0.2- 0.4 mm) and 0-20% subhedral to euhedral olivine (0.5-2mm). Adcumulate dunite host is composed of 90% anhedral to subhedral olivine (1-3mm) and 10% 0.1 mm, subhedral chromite that wraps olivine grains. Dunite dike is mainly visible because it sharply cross-cuts chromitite. In dunite, olivine is 50-60% altered to serpentine, whereas in chromitite, olivine is 70-100% serpentinized.

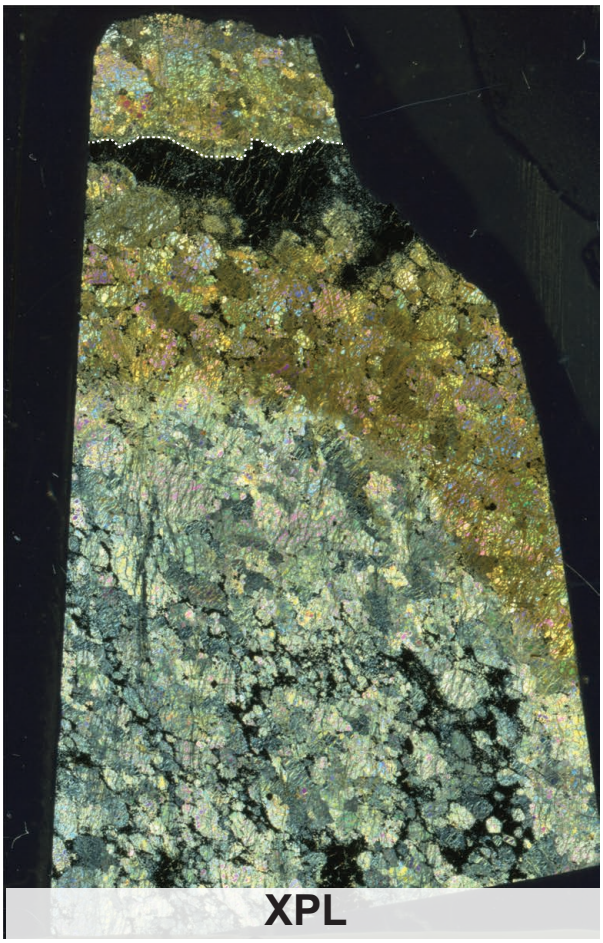

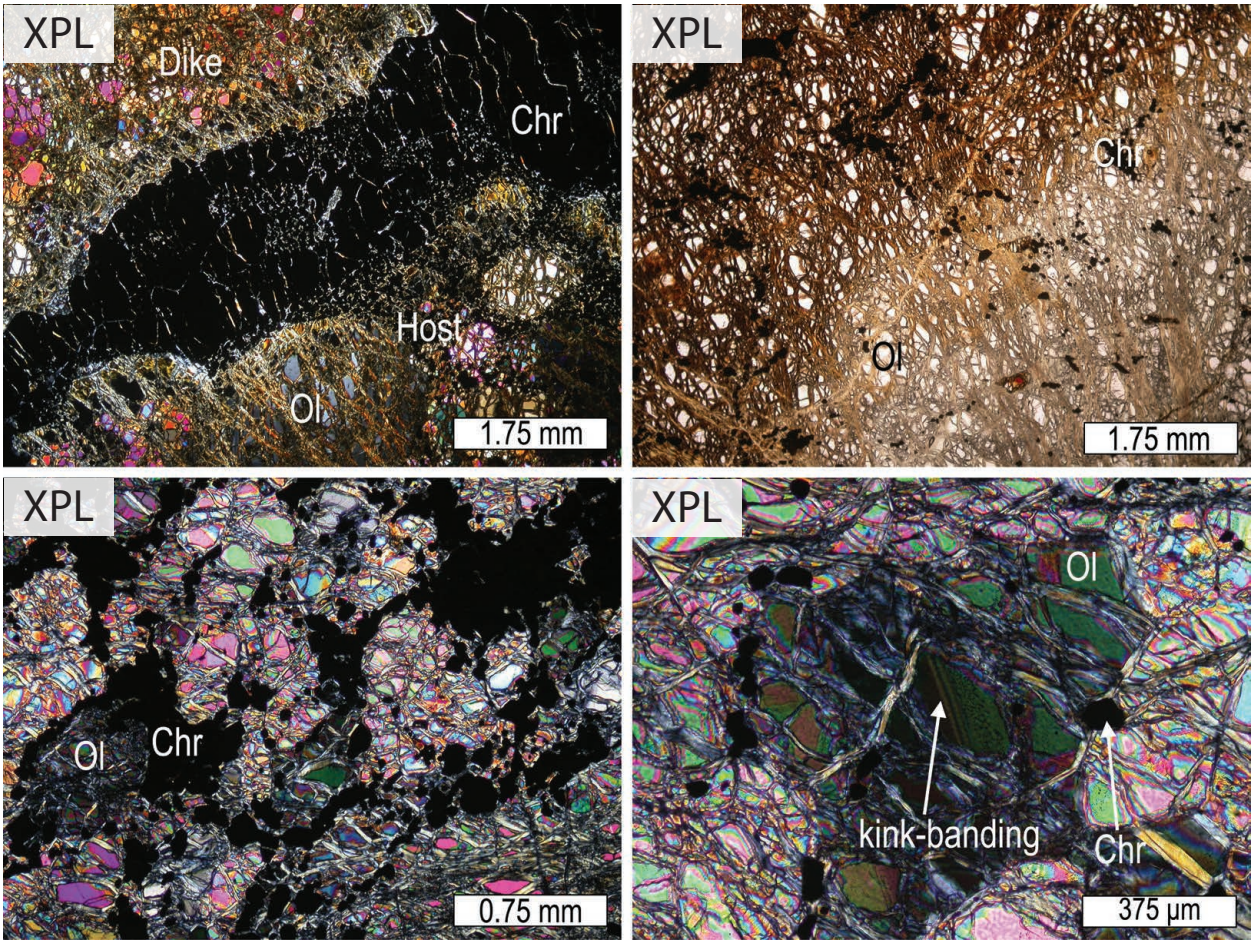
XPL
Dike
Chr
Host
Ol
1.75 mm
XPL
Chr
Ol
1.75 mm
XPL
Ol
Chr
0.75 mm
XPL
Ol
kink-banding
Chr
375 µm

19) DMI18-32-8
Dunite

Medium to coarse grained, adcumulate dunite composed of 95% olivine and 5% chromite. Olivine is anhedral to subhedral, 2-5 mm, rarely kink-banded. Anhedral olivine grains have same extinction angles implying alignment. Olivine is 20-40% serpentinized. Serpentine forms small parallel veins across thin-section as well as alteration networks in individual grains. Chromite is 0.2-0.5 mm, euhedral, and found mainly between grains of olivine.

TL

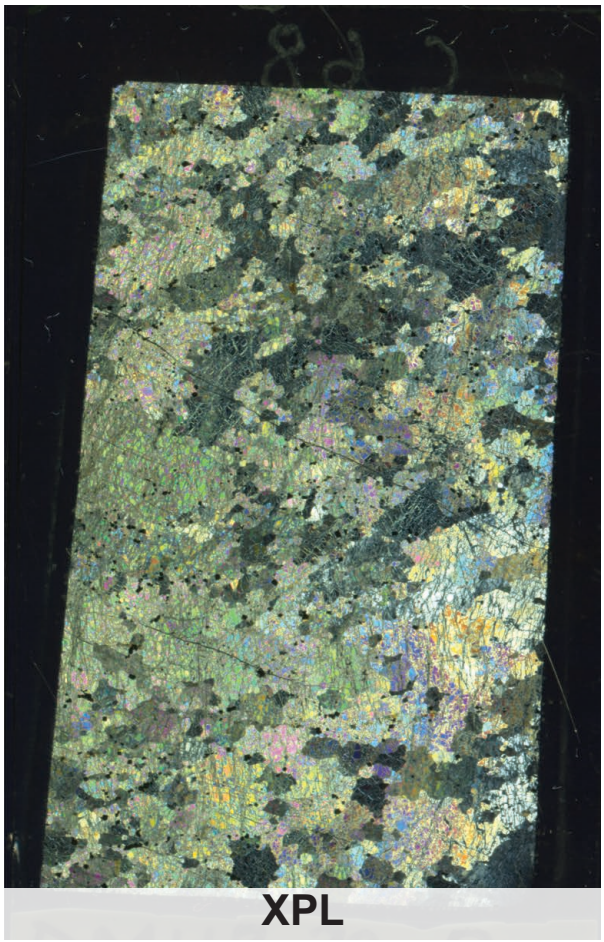

XPL

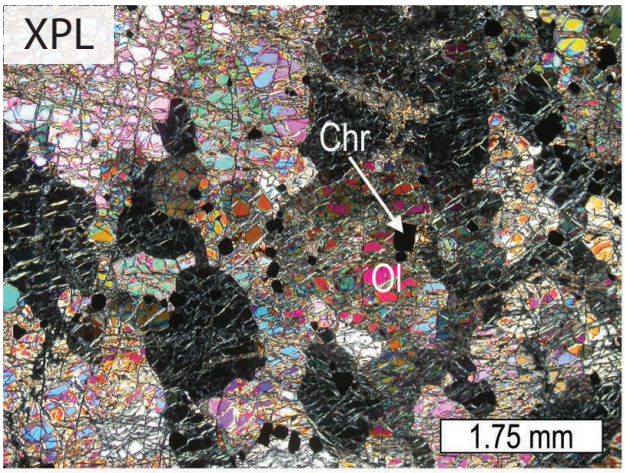
XPL
Chr
Ol
1.75 mm

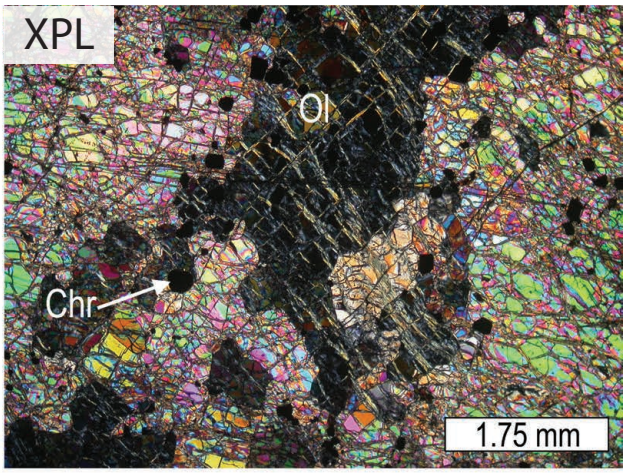
XPL
Ol
Chr
1.75 mm

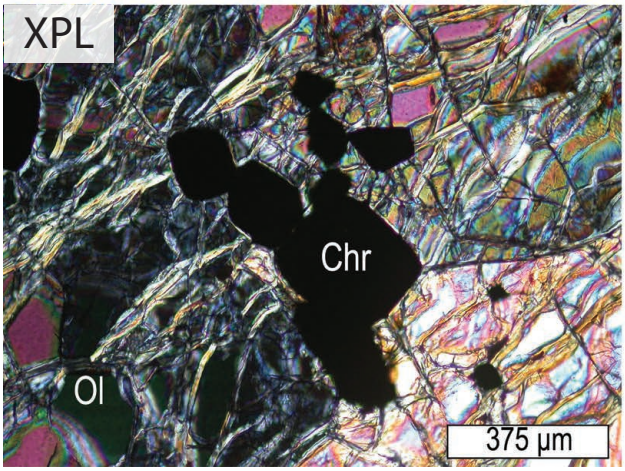
XPL
Chr
Ol
375 µm

20) DMI18-32-9A
Dunite, dunite dike

Fine to medium grained, adcumulate dunite dike cross-cutting fine to coarse grained adcumulate dunite. Adcumulate dunite dike is composed of 2% <0.5 mm chromite found as inclusions in olivine and 98% anhedral to subhedral, 1-3 mm olivine that becomes drastically finer grained at 0.2 mm near dike boundary. Olivine is frequently kink-banded in dike. Adcumulate dunite host is composed of 0.5-12 mm, subhedral to euhedral olivine (95%) that is occasionally kink-banded, <0.3 mm, euhedral chromite (4%) found between grains of olivine, and <1 mm, anhedral, interstitial grains of clinopyroxene (1%). Olivine is approximately 30% serpentinized.

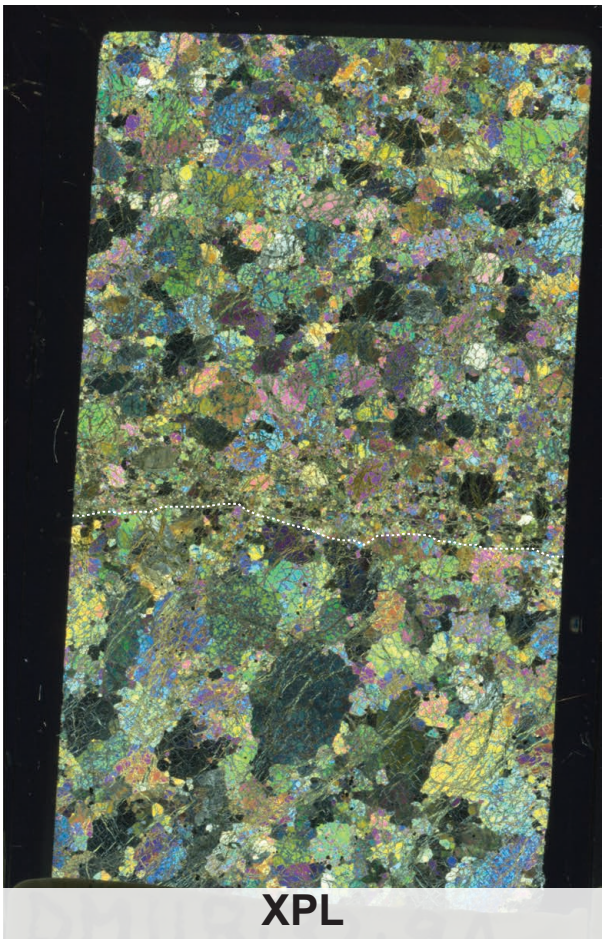

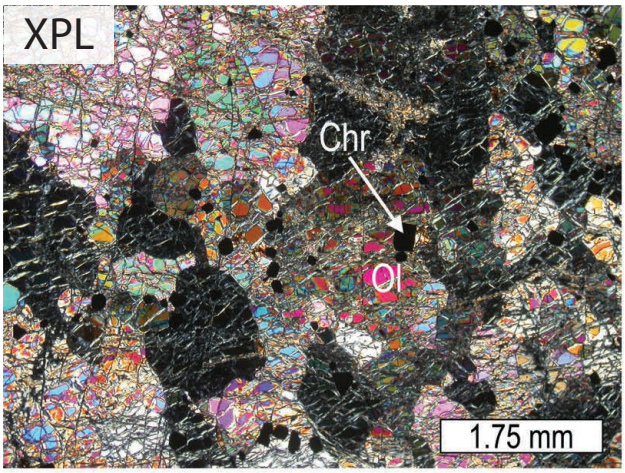
XPL
Chr
Ol
1.75 mm

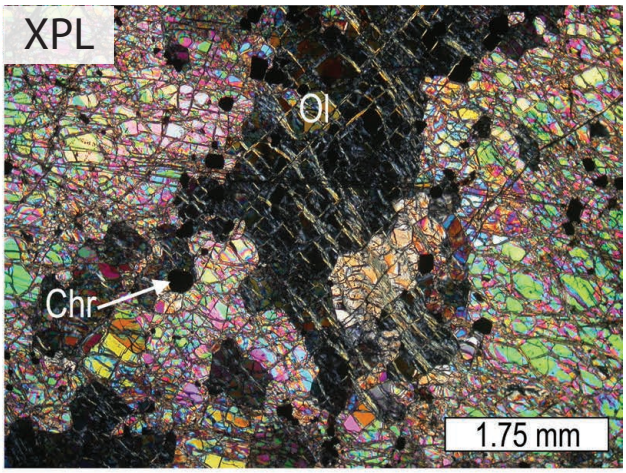
XPL
Ol
Chr
1.75 mm

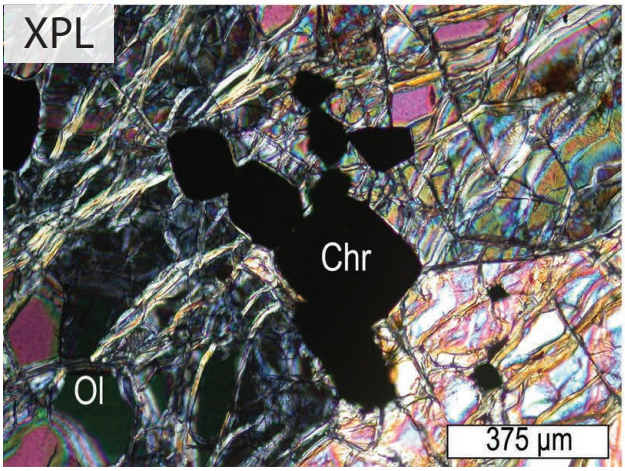
XPL
Chr
Ol
375 µm

21) DMI18-32-9B
Dunite, olivine wehrlite dike

Fine to medium grained olivine wehrlite dike cross-cutting medium to coarse grained, adcumulate dunite. Olivine wehrlite is composed of 0.5-3 mm, subhedral to euhedral, aligned olivine (72%), 2 mm, anhedral, interstitial clinopyroxene (20%), and <0.1 mm, euhedral chromite (3%). Adcumulate dunite is composed of 2-4 mm, subhedral olivine (90%), 2 mm, interstial clinopyroxene (5%), and <0.1 mm, euhedral chromite (5%). Olivine is 30-50% serpentinized with pervasive vein network across sample. Trace carbonate veins are also present.

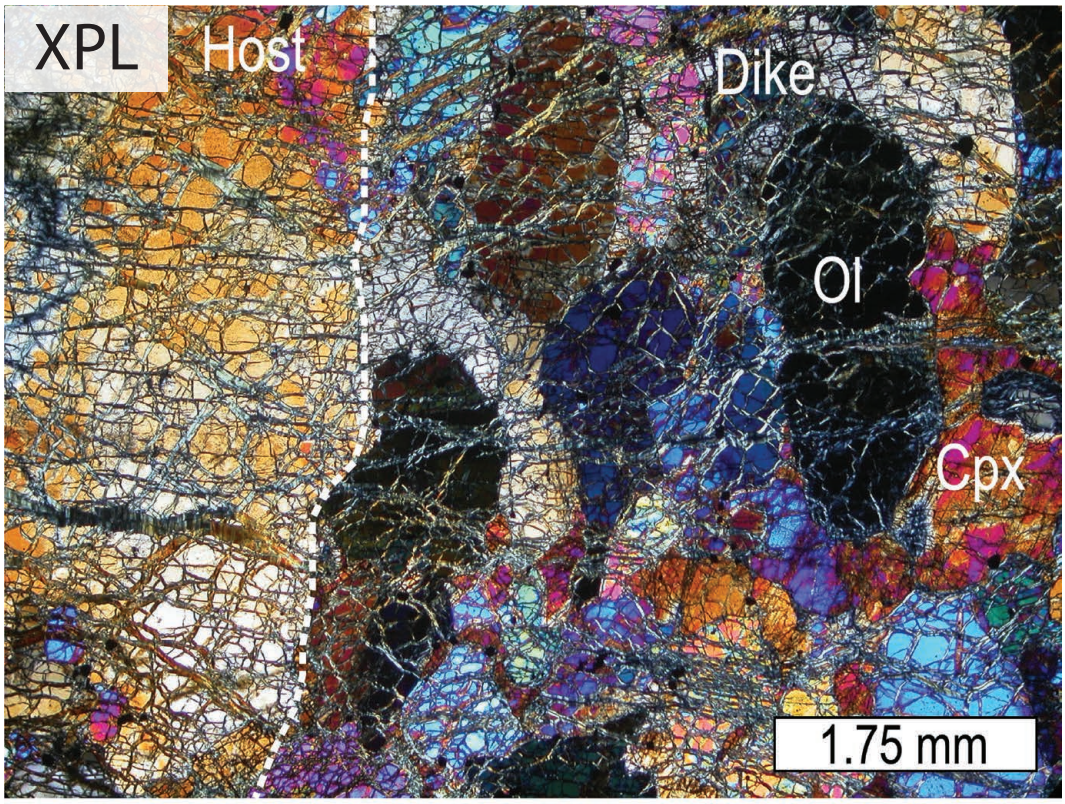
XPL
Host
Dike
Ol
Cpx
1.75 mm

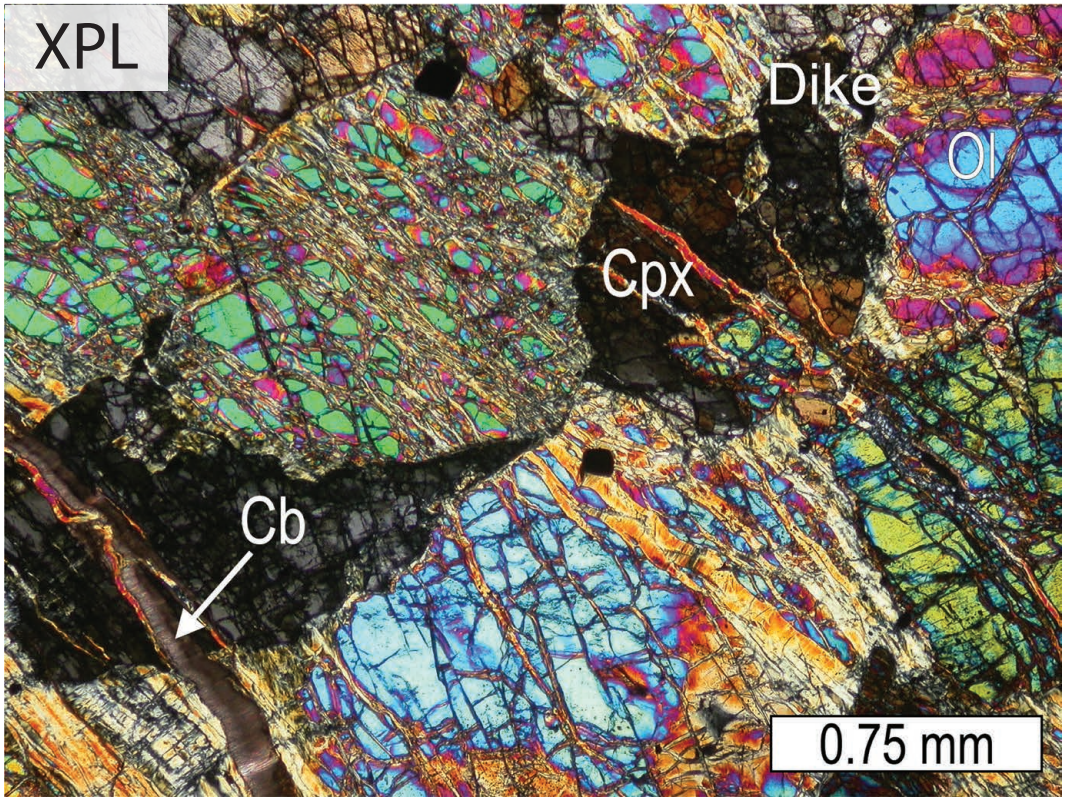
XPL
Dike
Ol
Cpx
Cb
0.75 mm

22) DMI18-32-9C
Dunite, wehrlite dike

Medium grained wehrlite dike cross-cutting medium grained, adcumulate dunite. Wehrlite dike is composed of 0.4-1.5 mm, subhedral to euhedral polygonally sutured clinopyroxene (40%), 1-4 mm (most commonly 3-4 mm), rounded olivine grains (60%), and <0.1 mm, euhedral chromite (<1%) found between grains of olivine. Adcumulate dunite is composed of 1-3 mm, subhedral to euhedral, kink-banded olivine (95%), 0.3 mm, euhedral chromite (5%) found between grains of olivine, and 0.5 mm, interstitial clinopyroxene (<1%). Olivine is 40-70% serpentinized.


TL


XPL

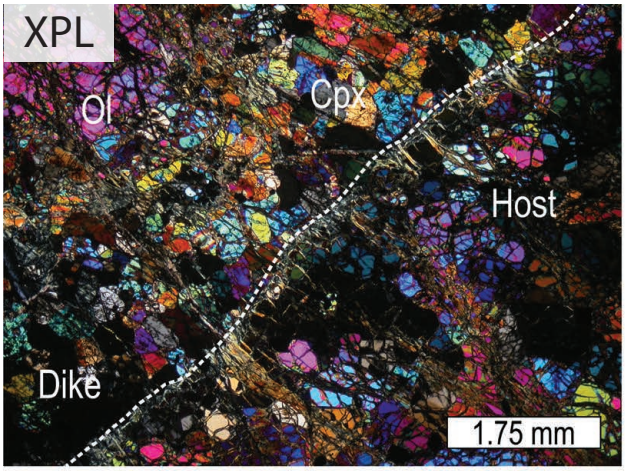
XPL
Ol
Cpx
Host
Dike
1.75 mm

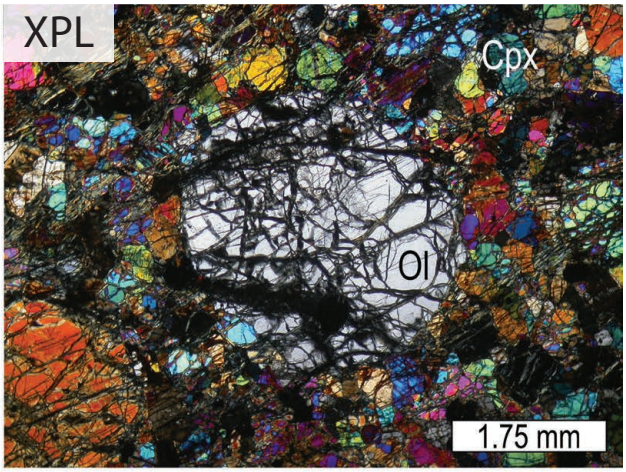
XPL
Cpx
Ol
1.75 mm

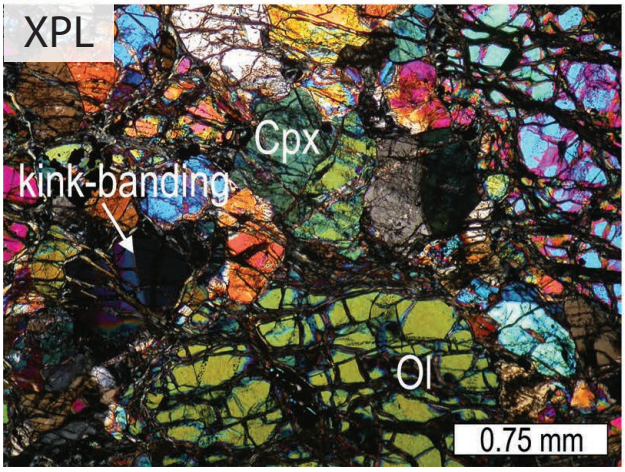
XPL
Cpx
kink-banding
Ol
0.75 mm

23) GN88-1053
Olivine wehrlite, chromitite

Medium to coarse grained, chromitite schlieren-bearing, clinopyroxene-poikilitic, olivine wehrlite. Chromitite is composed of 90% sutured chromite grains, 2-4 mm, subhedral olivine (5%) that shows polycrystalline textures, and very fine clinopyroxene (5%) in areas of less compact chromitite. Olivine wehrlite is composed of 2-4 mm, subhedral to euhedral, kink-banded olivine (82%), 2 mm, interstial oikocrysts of clinopyroxene (15%), and 3%, 0.1-0.4 mm, euhedral oikocrysts found interstitially. Along chromitite olivine is ~90% serpentinized, within chromitite olivine is 10-20% serpentinized, and in olivine wehrlite olivine is ~10% serpentinized

TL

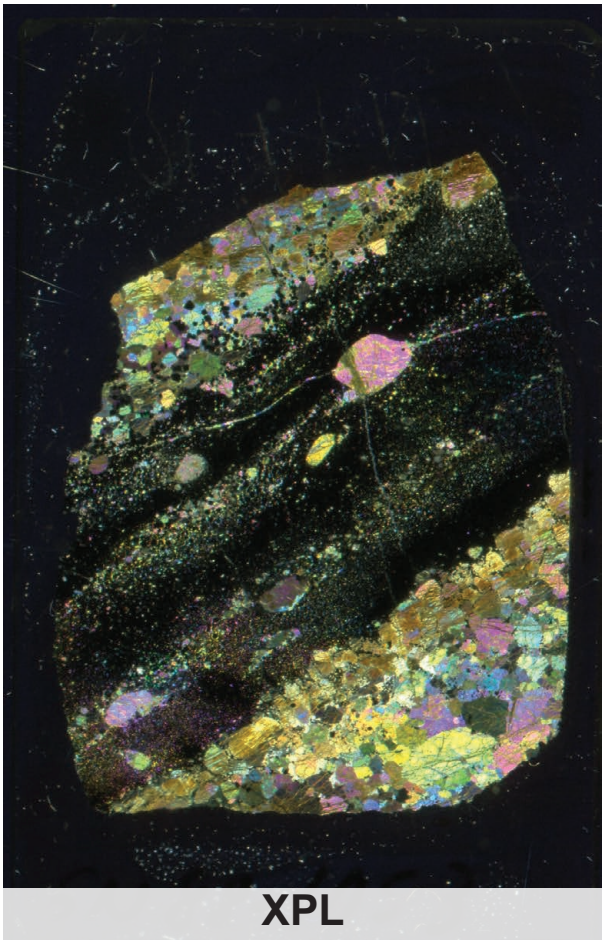

XPL

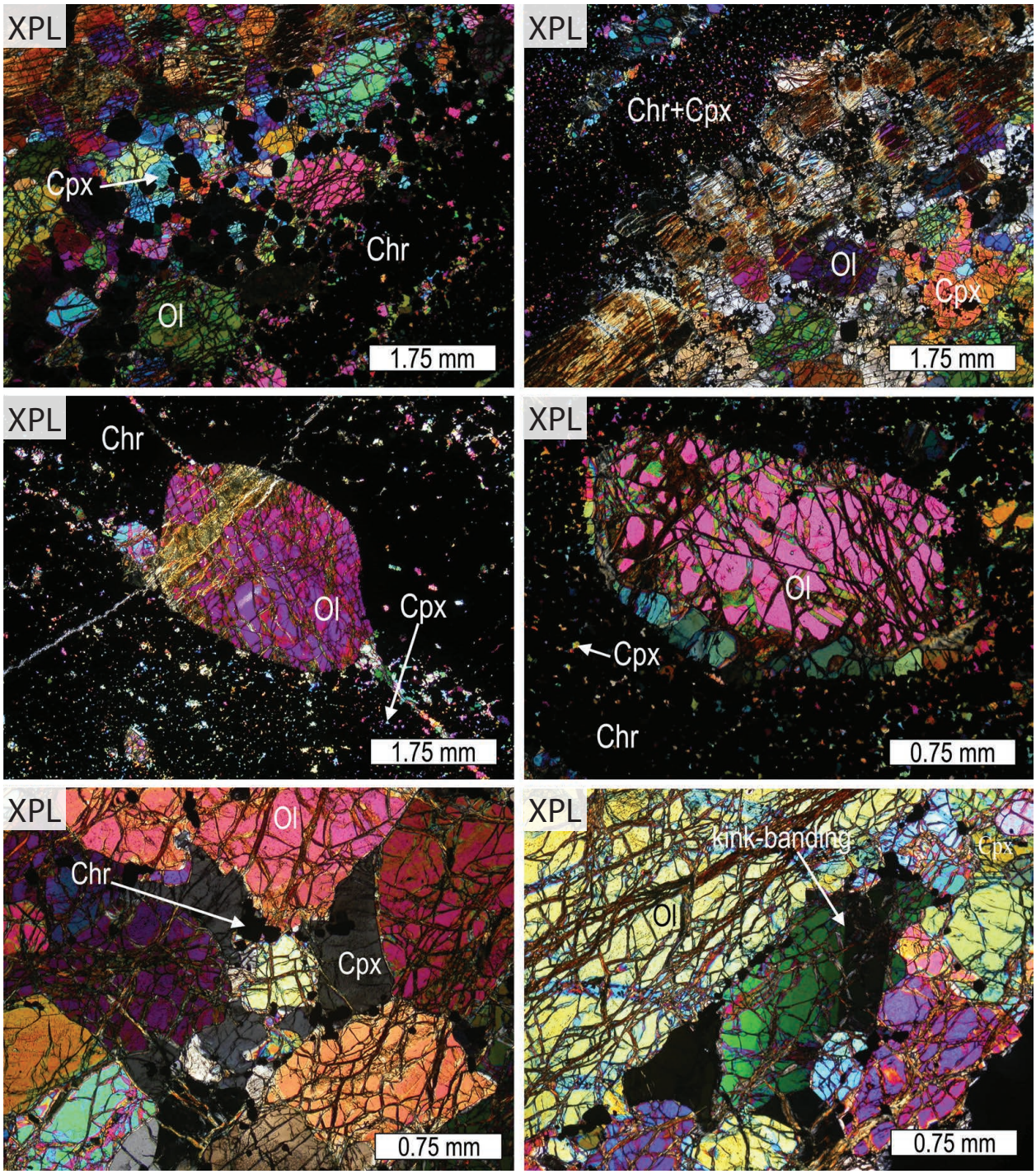
XPL
Cpx
Chr
Ol
1.75 mm
XPL
Chr+Cpx
Ol
Cpx
1.75 mm
XPL
Chr
Ol
Cpx
1.75 mm
XPL
Ol
Cpx
Chr
0.75 mm
XPL
Ol
Chr
Cpx
0.75 mm
XPL
kink-banding
Cpx
Ol
0.75 mm

Appendix B: Backscatter Electron (BSE) Micrographs of Samples from the Polaris Alaskan-type Intrusion Taken by Scanning Electron Microscope (SEM)

1) DMI18-13-1
Wehrlite

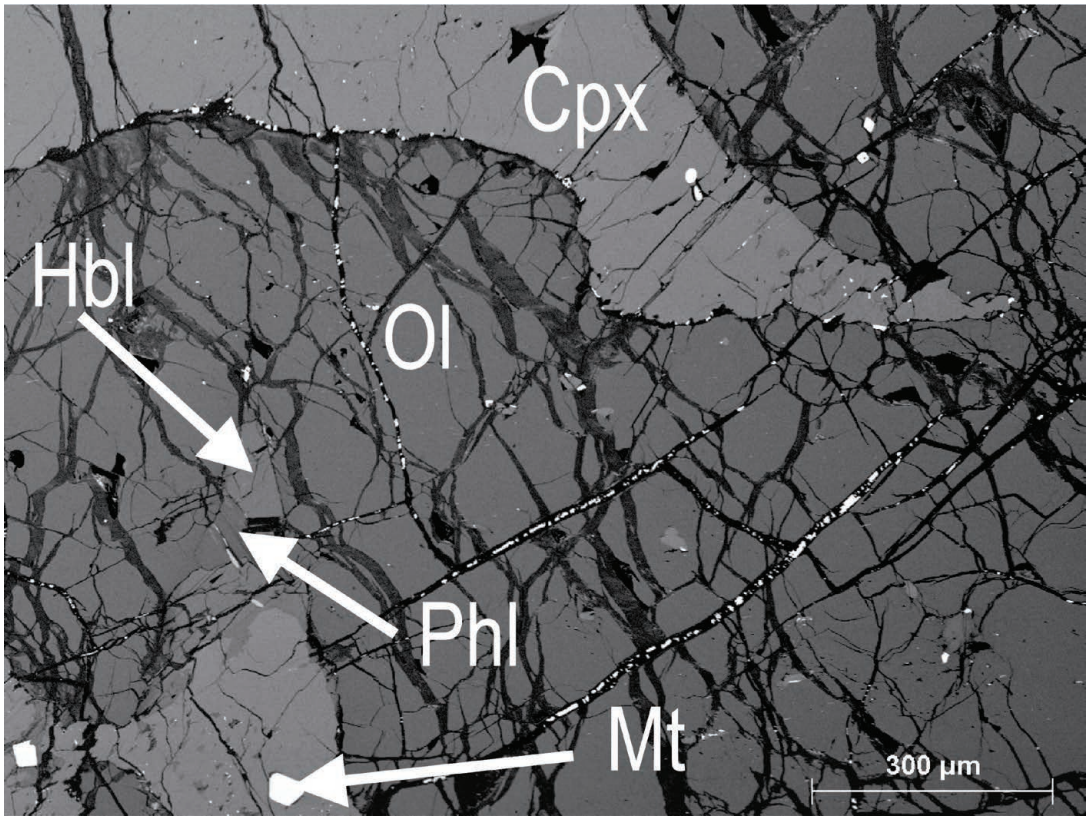

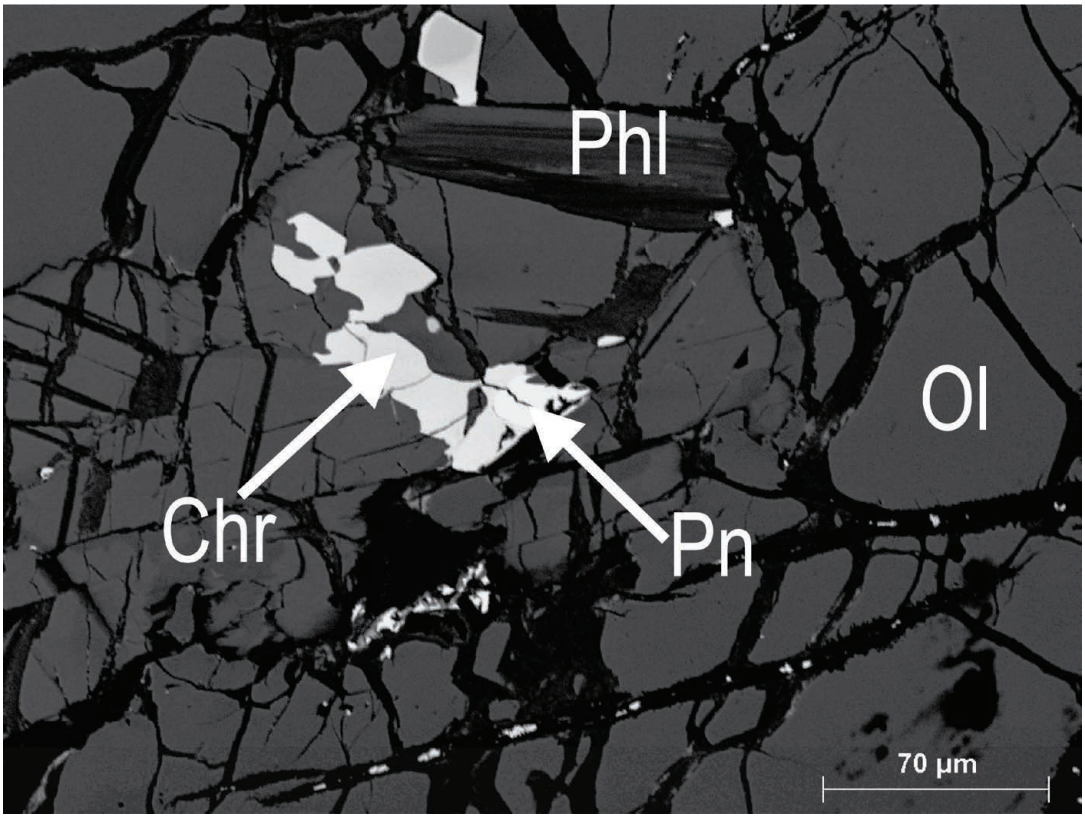

2) DMI18-20-12
Olivine clinopyroxenite

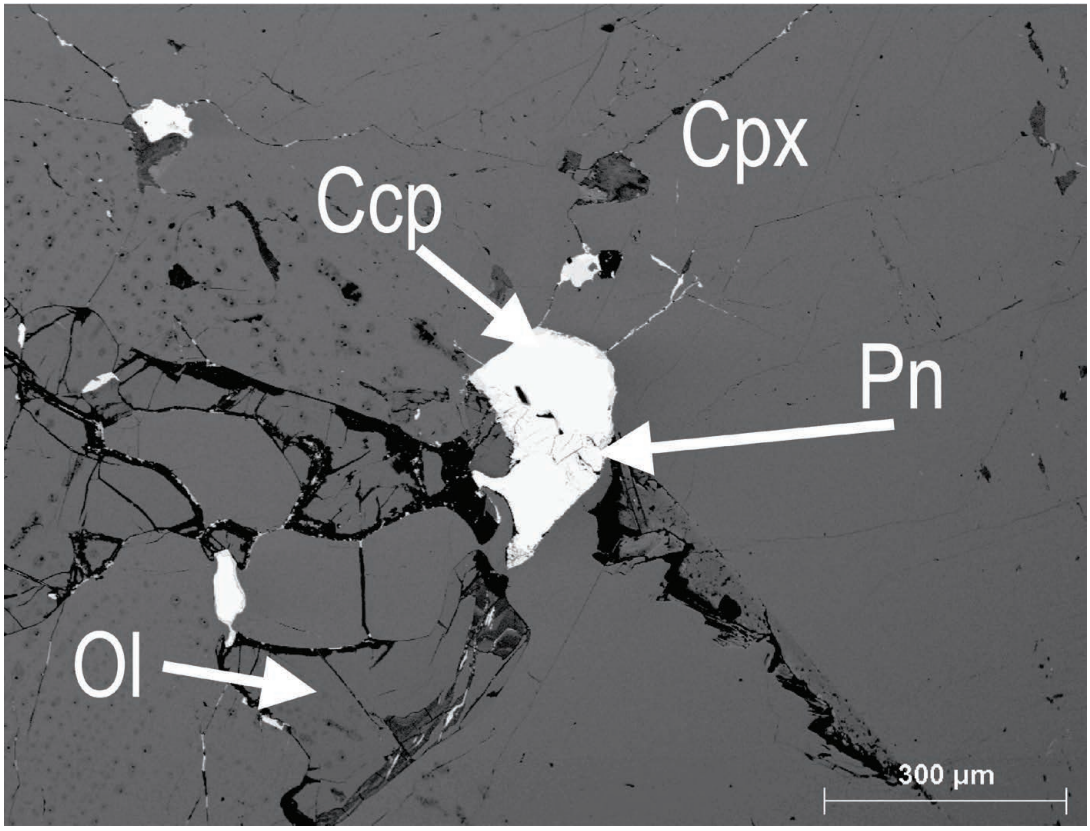

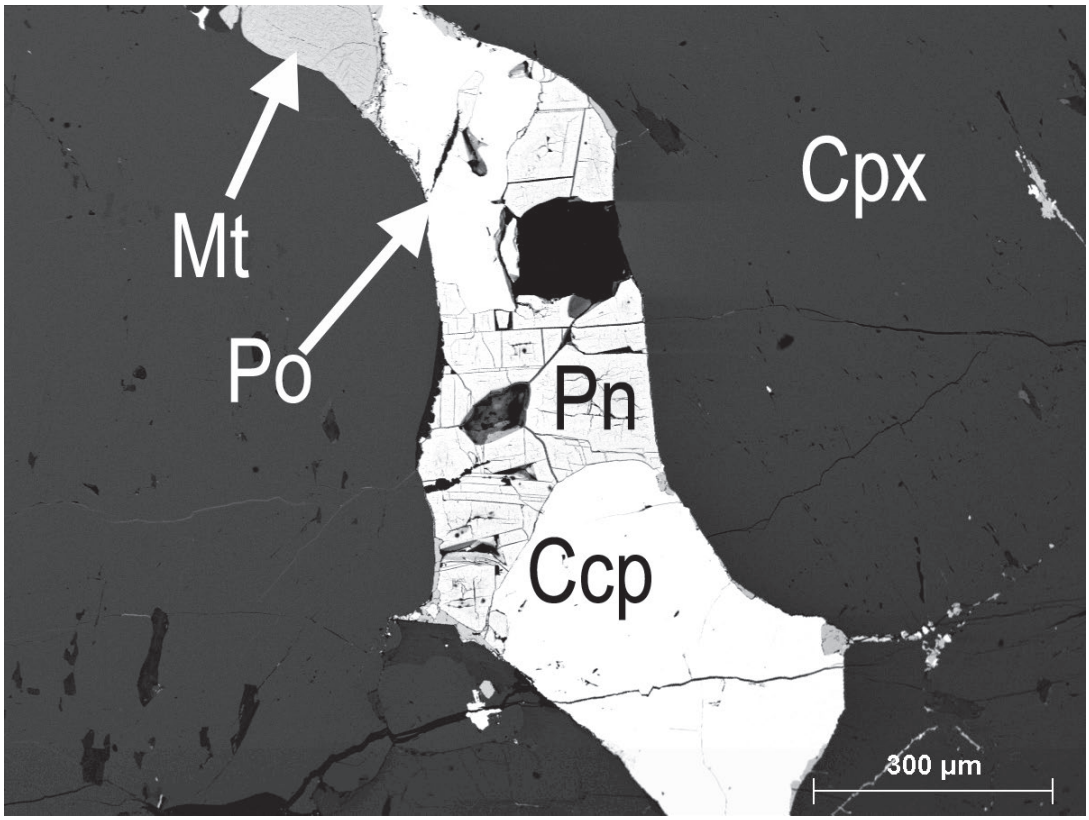

3) DMI18-21-12
Phlogopite-rich wehrlite

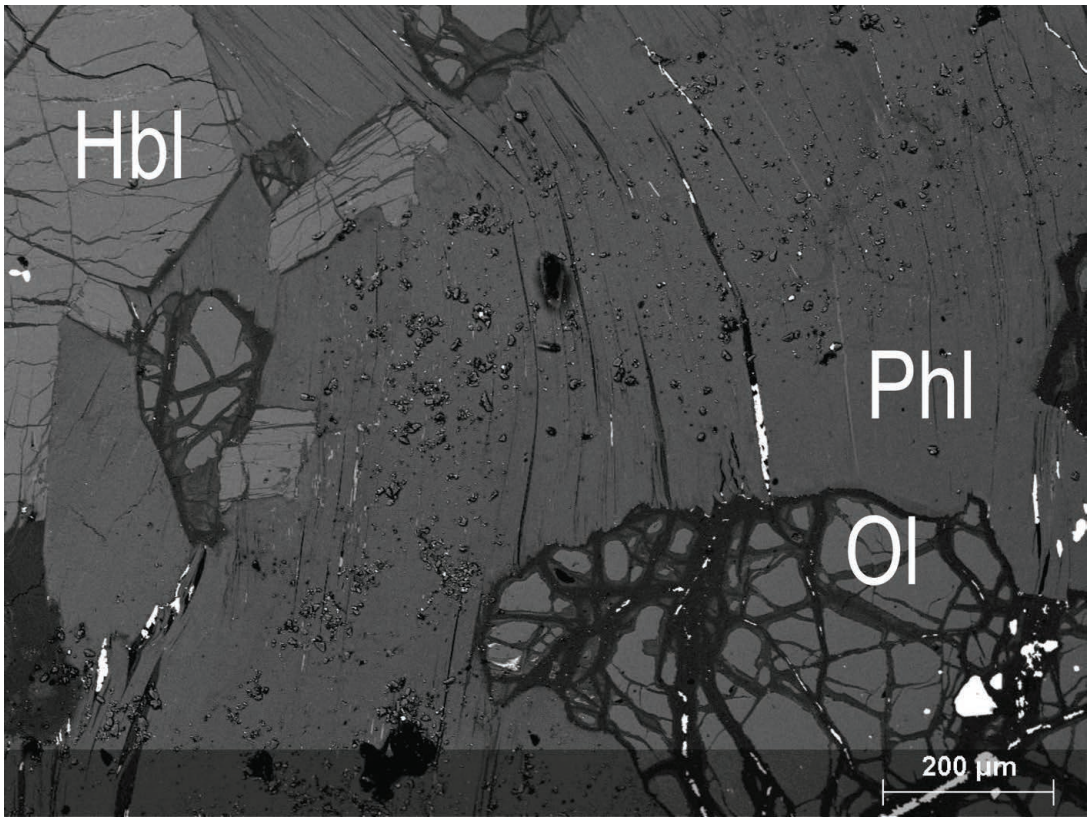

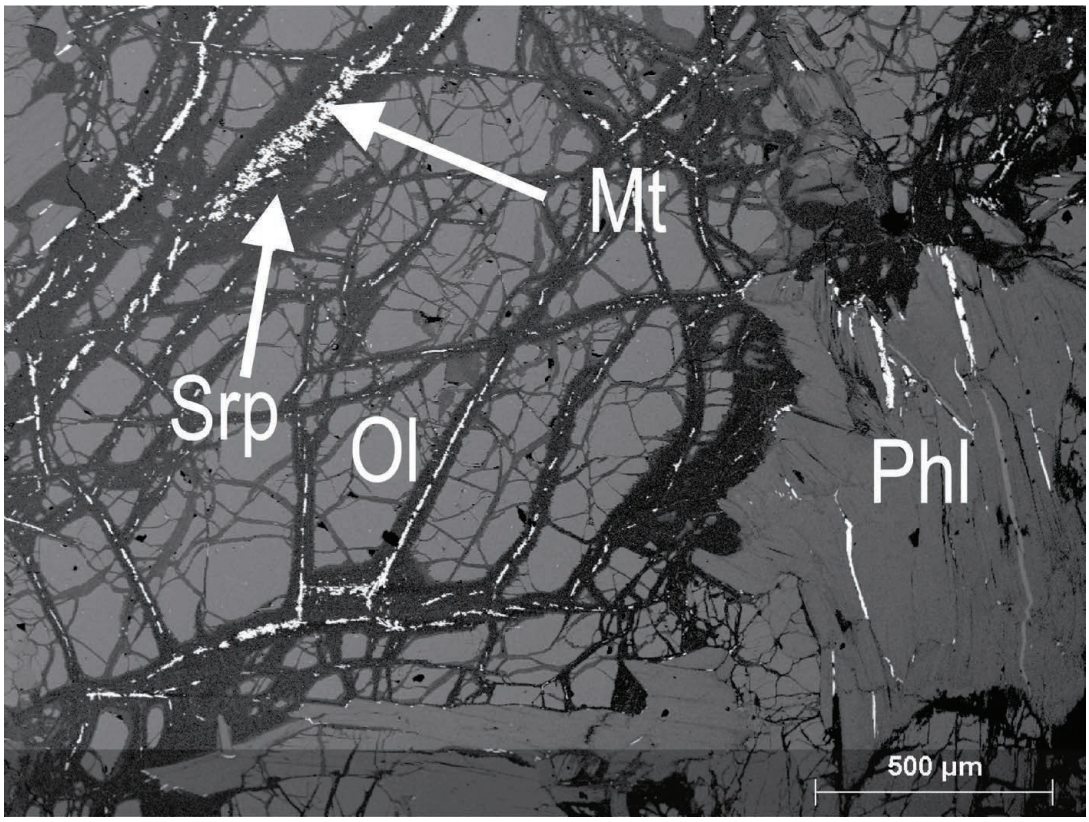

4) DMI18-21-19
Hornblende-olivine wehrlite

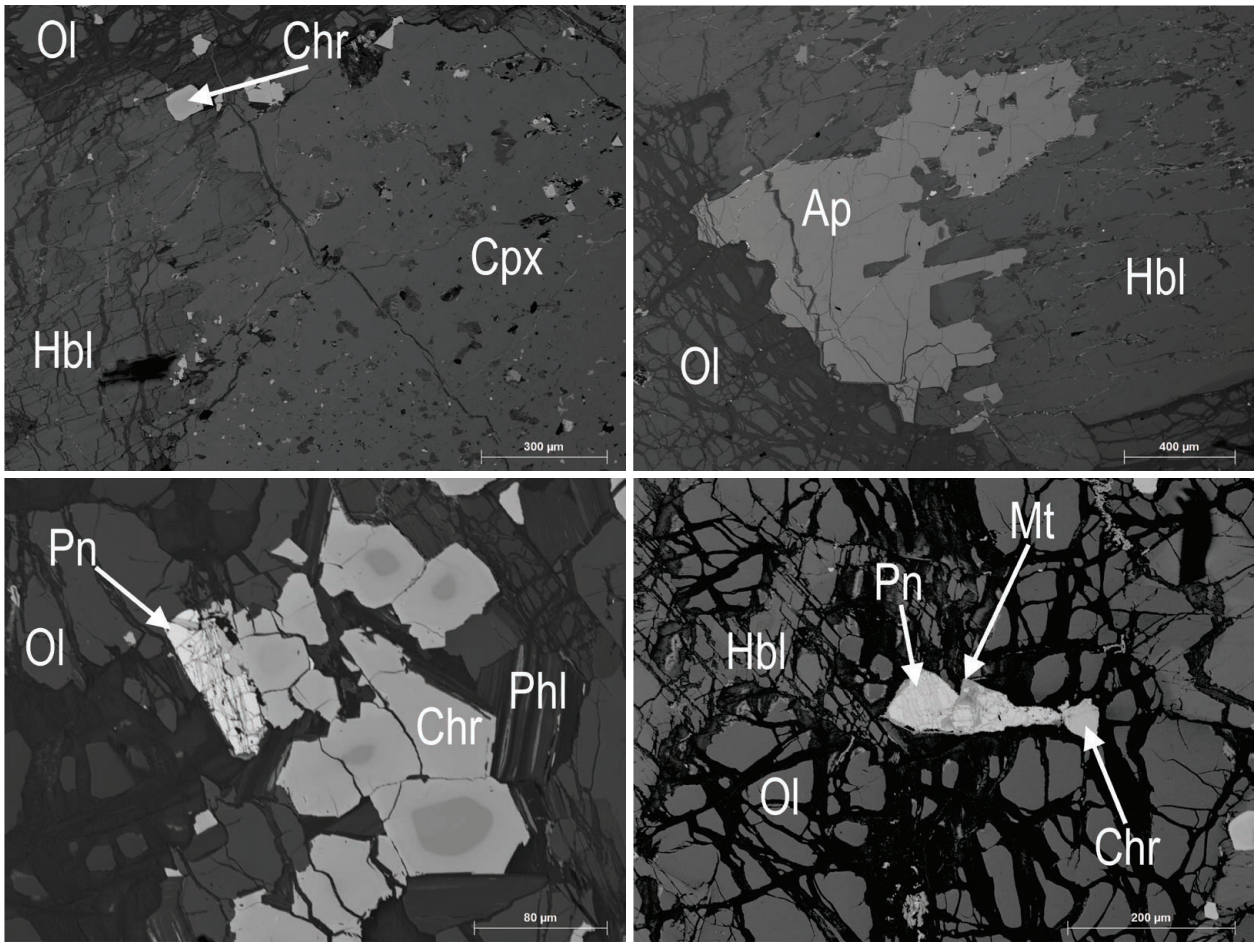

5) DMI18-26-6
Magnetite-olivine clinopyroxenite

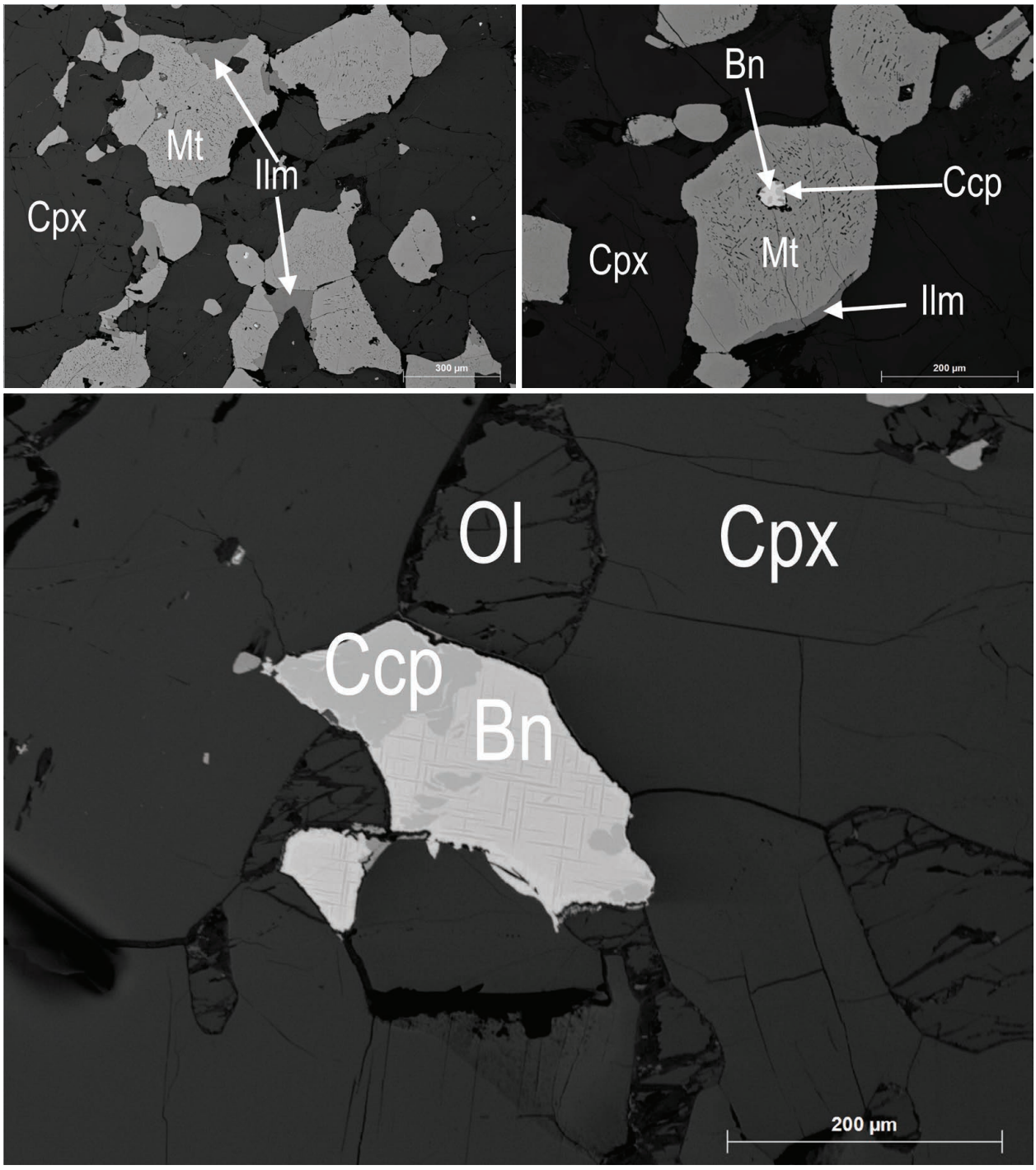

6) DMI18-28-5
Olivine clinopyroxenite

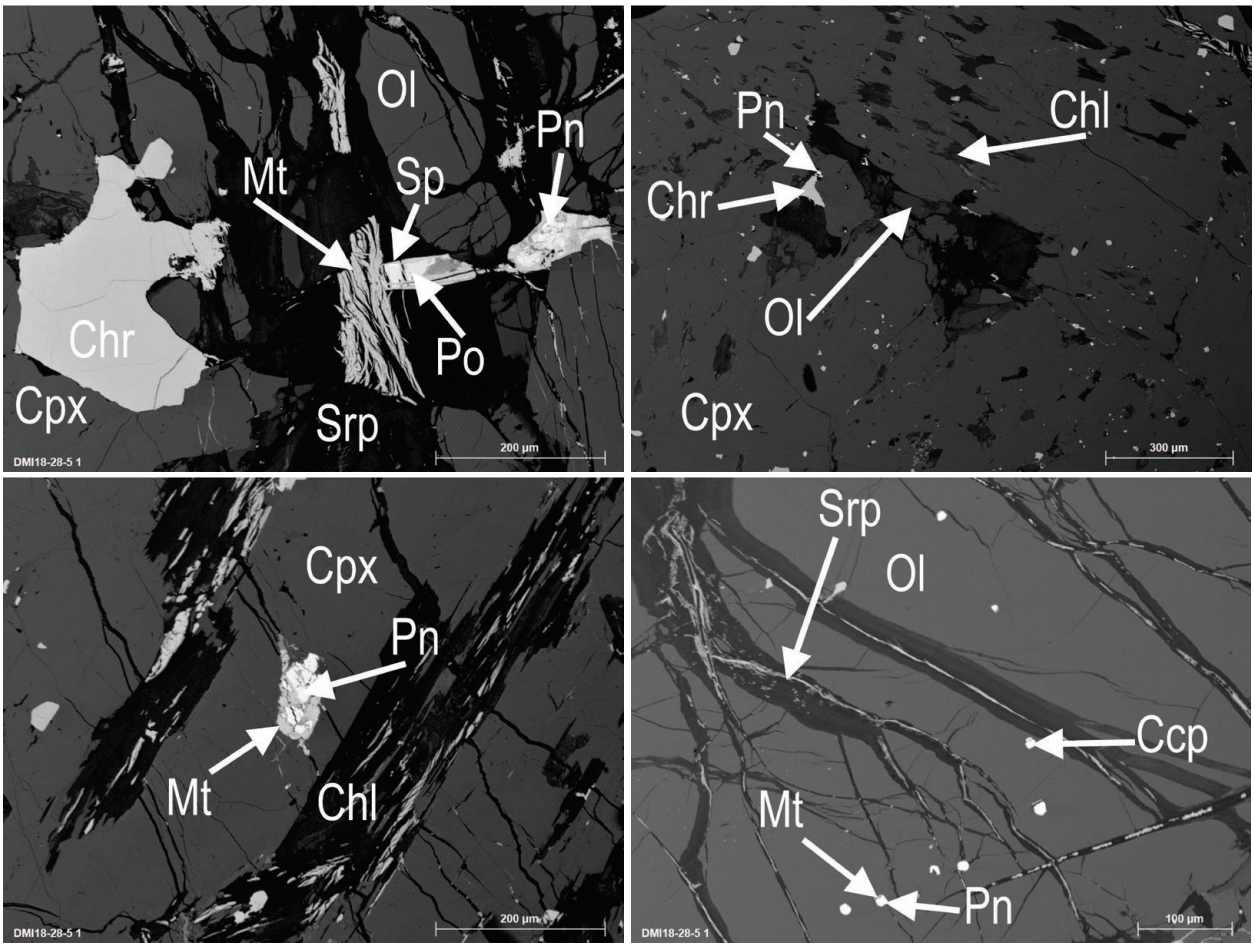

7) DMI18-32-6
Dunite, chromitite

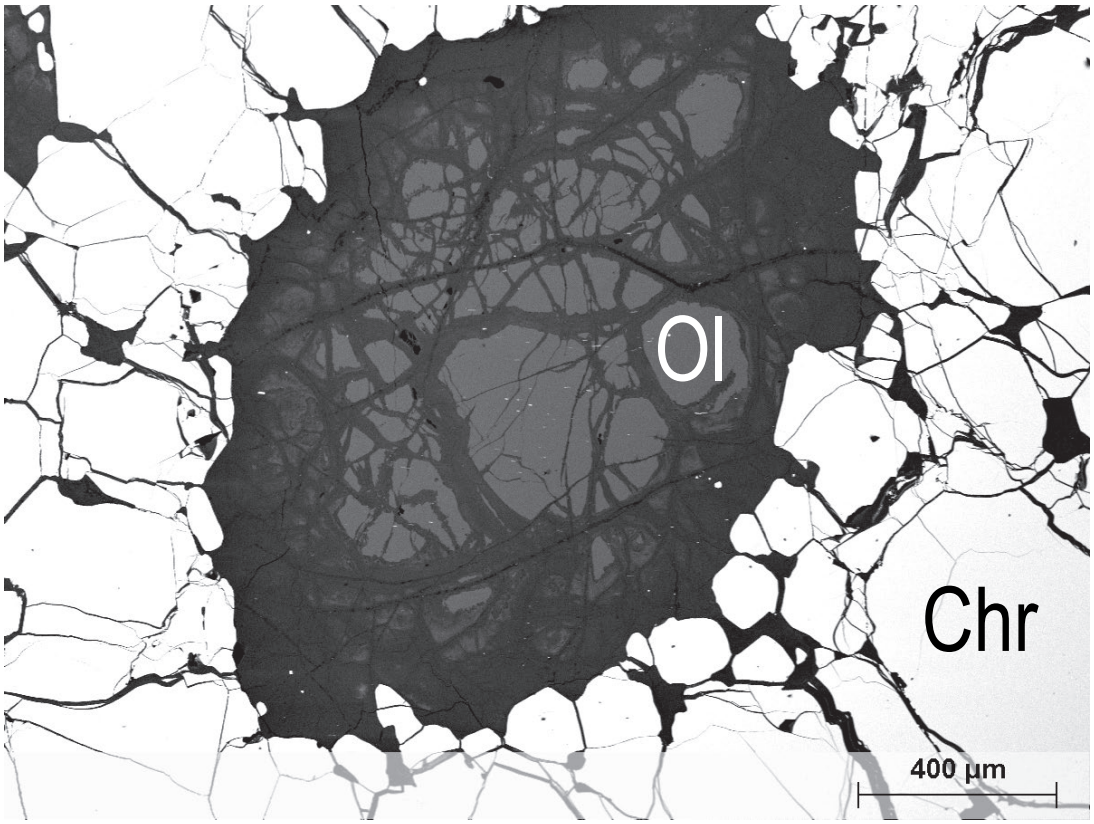

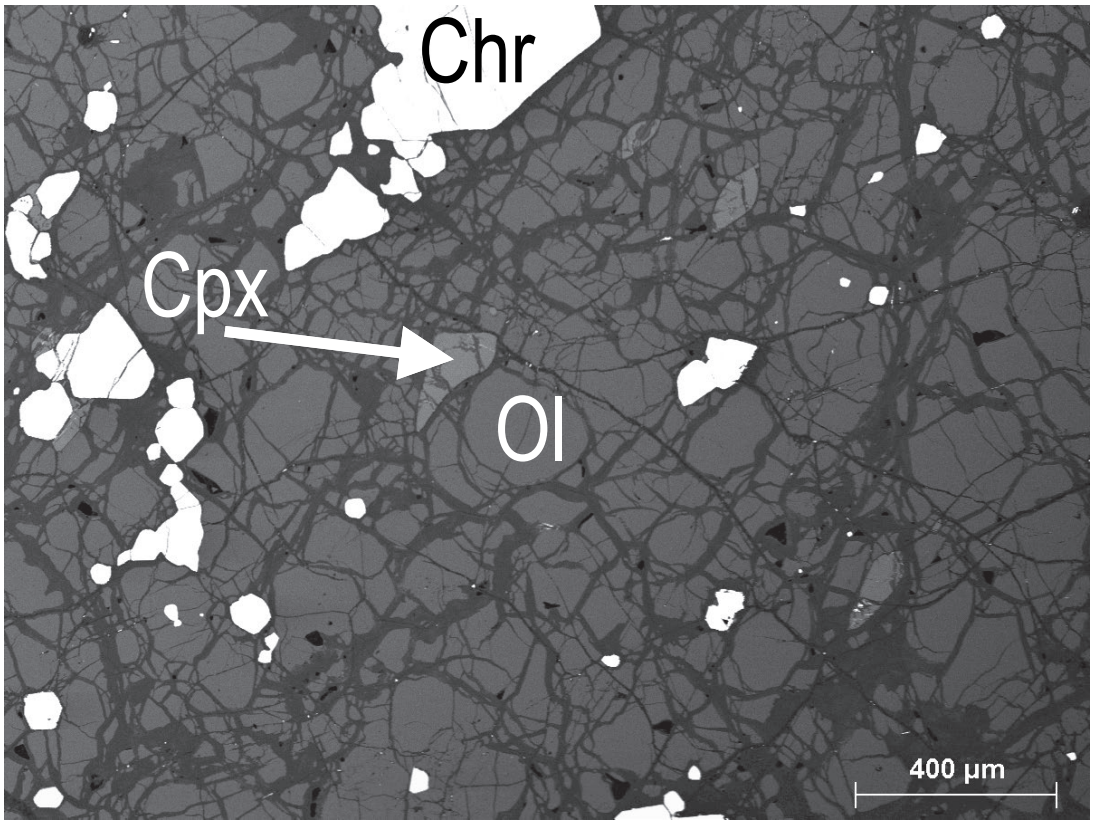

8) DMI18-32-7C
Dunite, chromitite, dunite dike

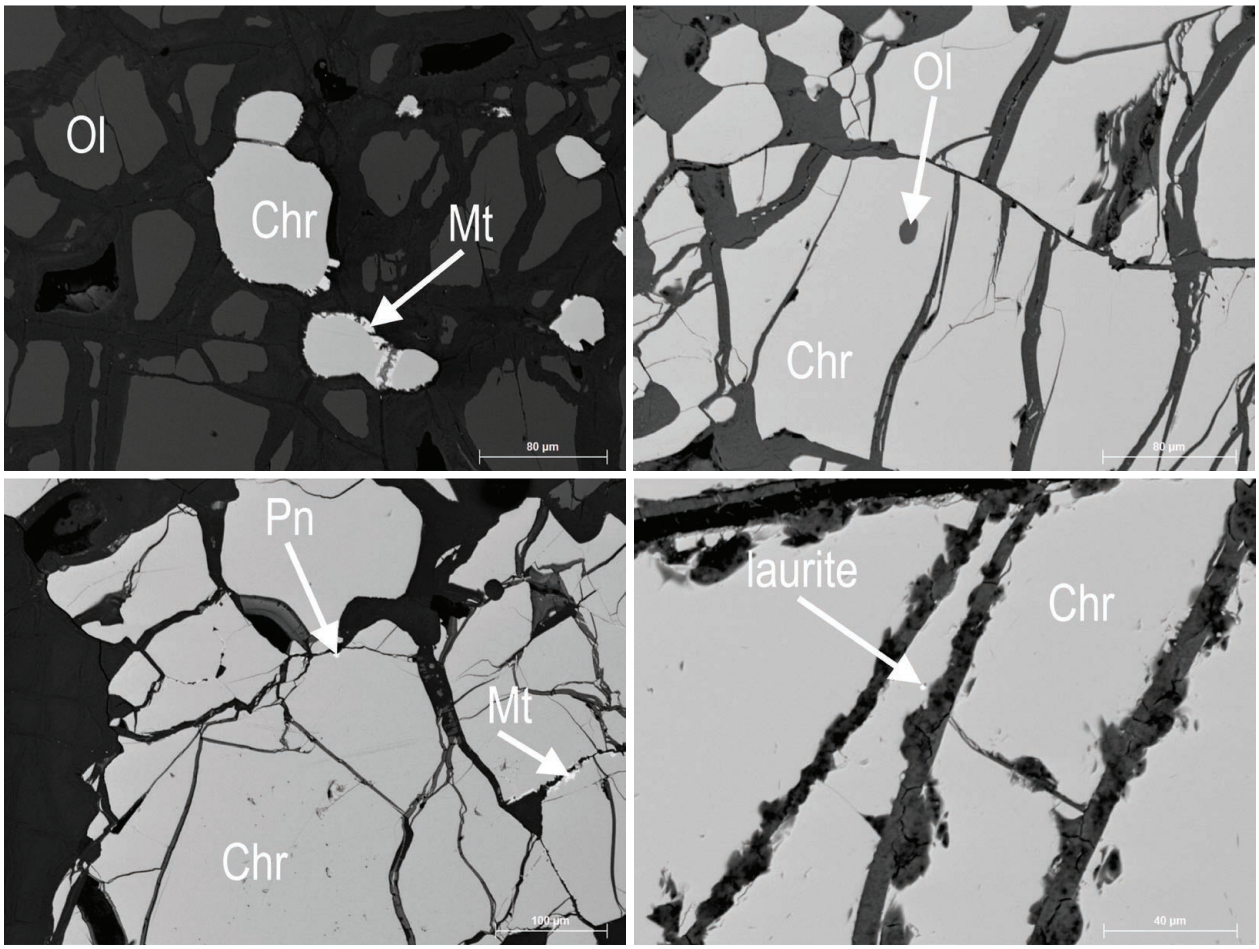

9) DMI18-32-8
Dunite

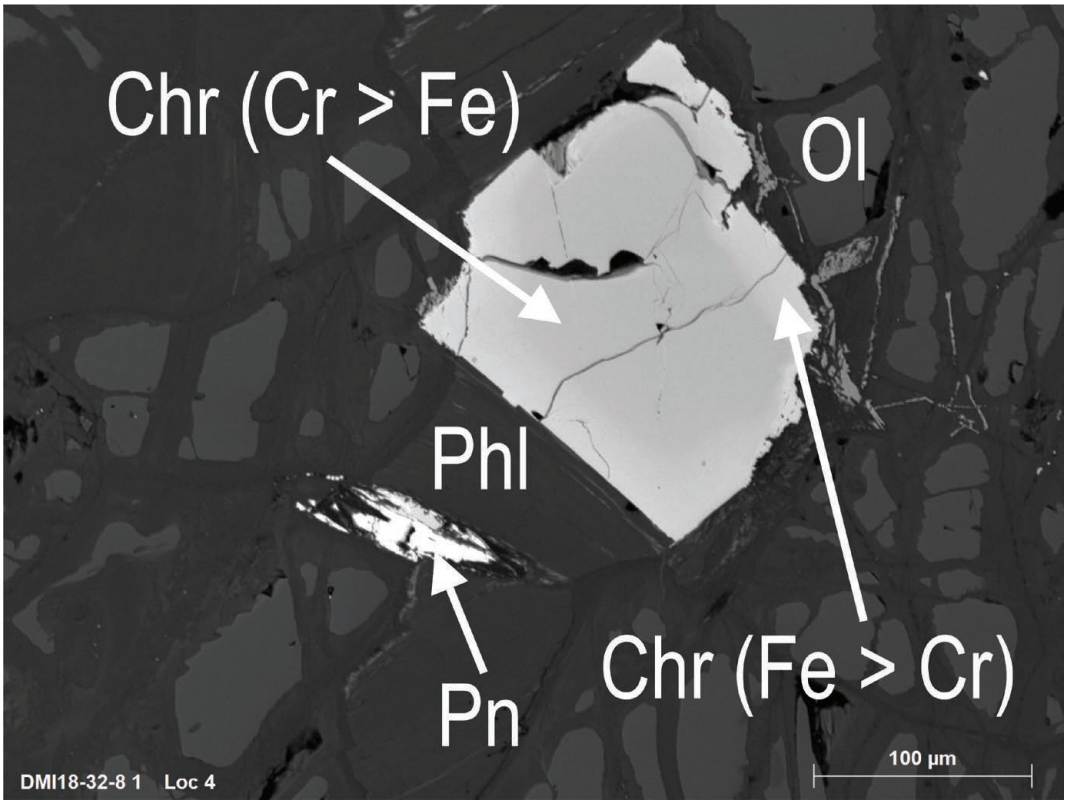

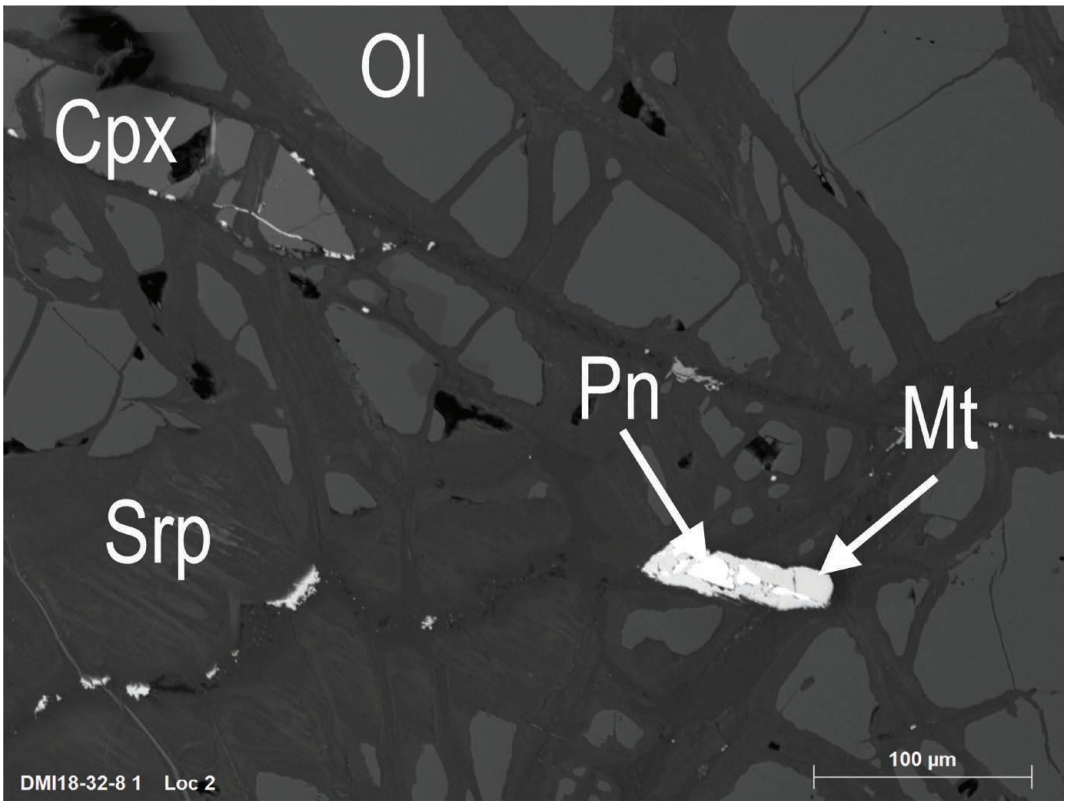

10) DMI18-32-9B
Dunite, olivine wehrlite dike

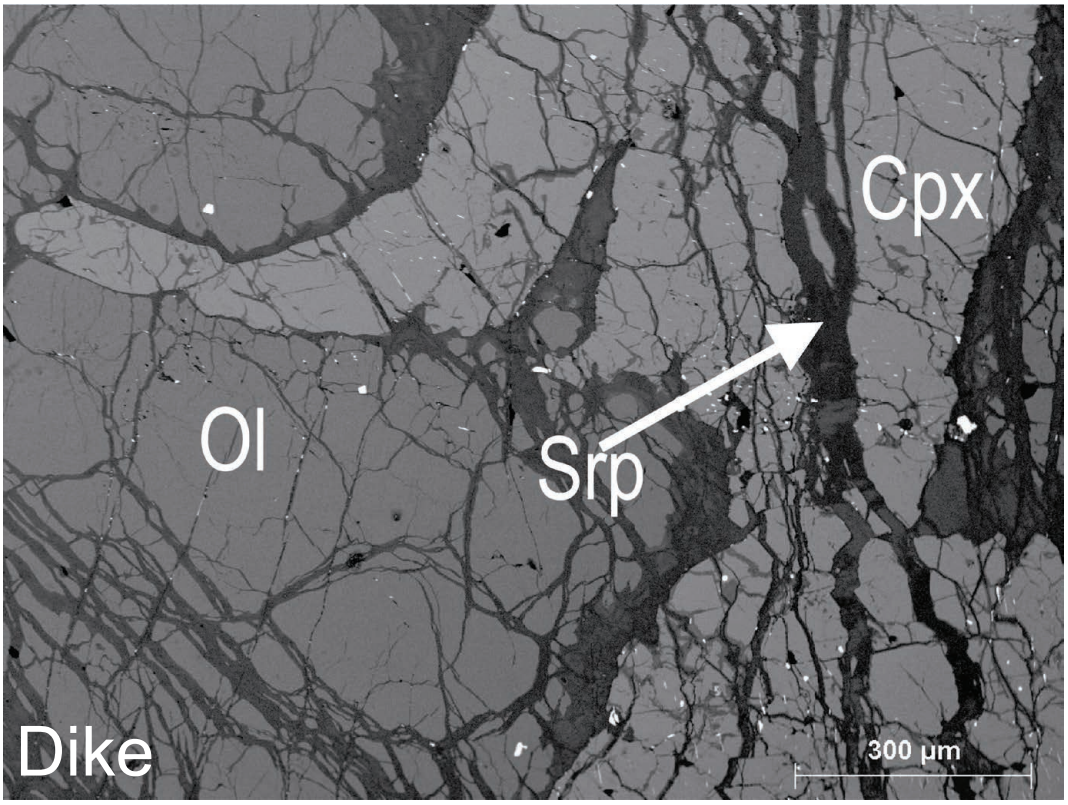

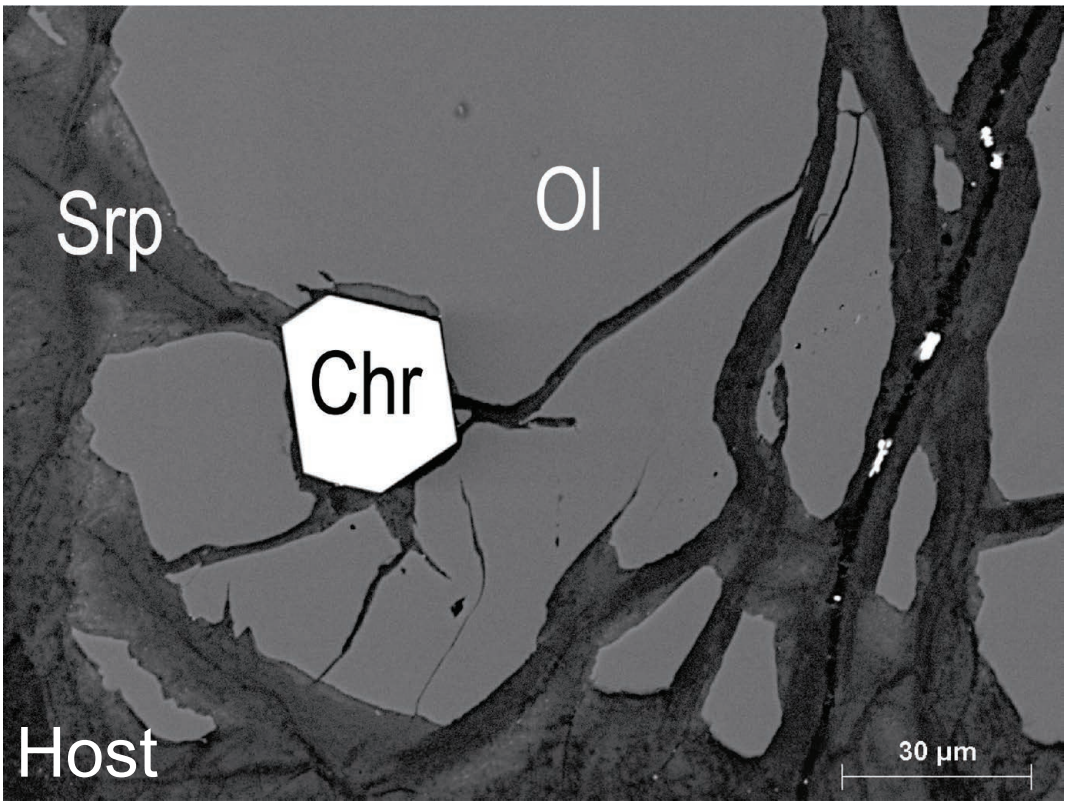

11) GN88-1053
Olivine wehrlite, chromitite

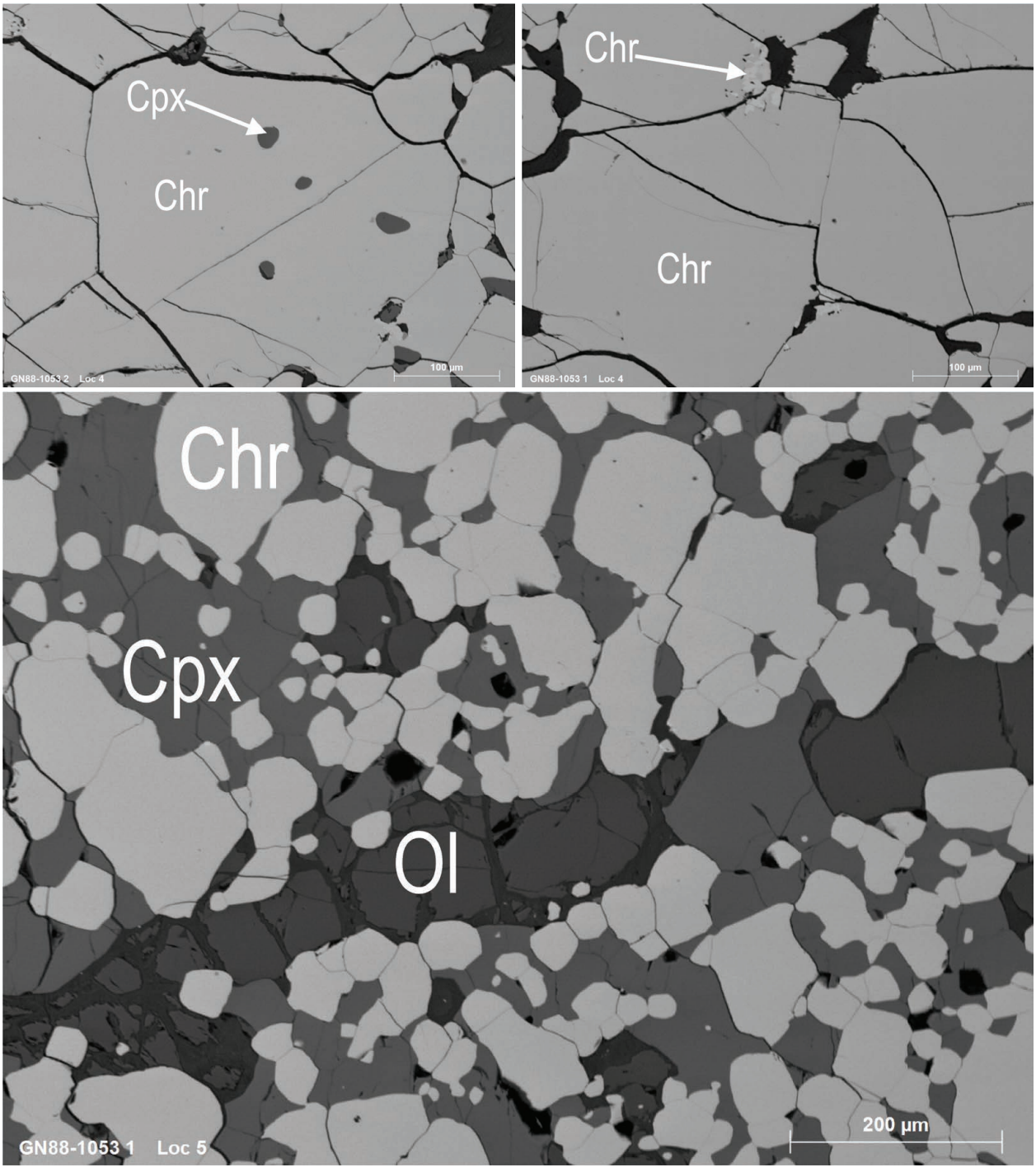

Appendix C: Electronprobe Microanalysis (EPMA) Spots for Olivine from the Polaris Alaskan-type Intrusion

1) DMI18-10-9
Dunite, chromitite

2) DMI18-12-5A
Wehrlite

4) DMI18-17-5
Wehrlite

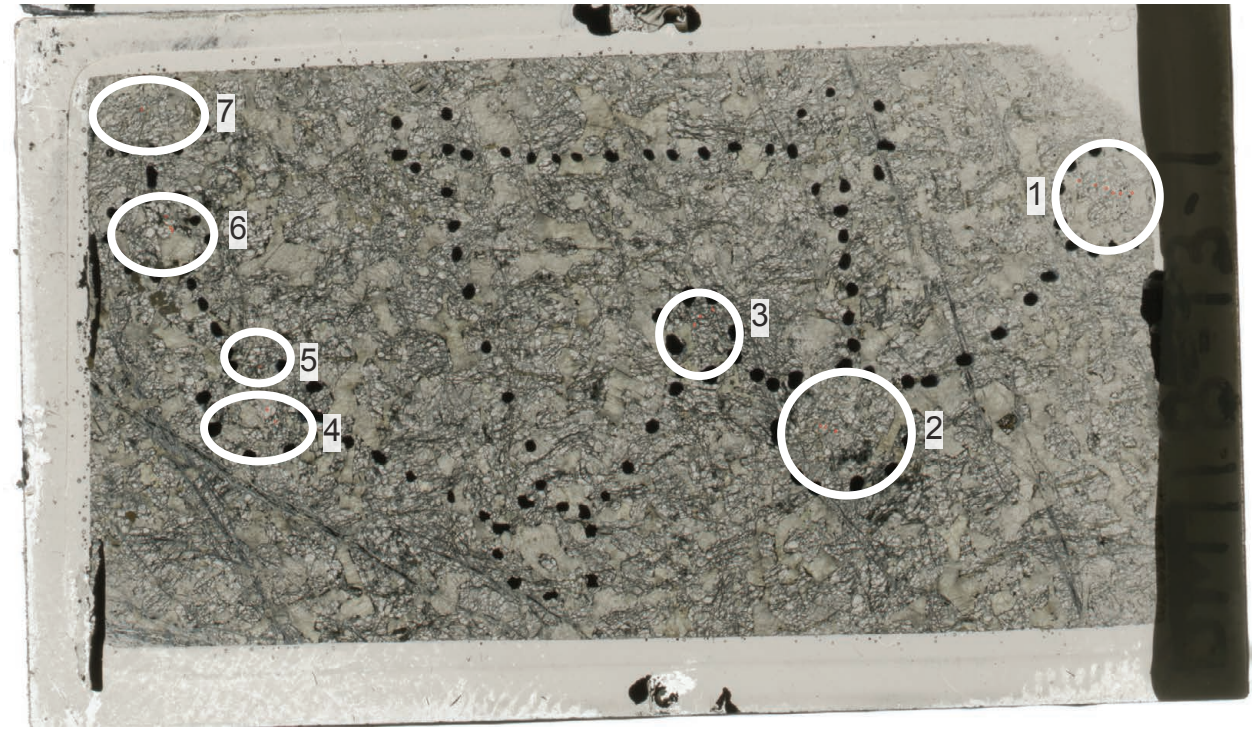

4) DMI18-17-5
Dunite

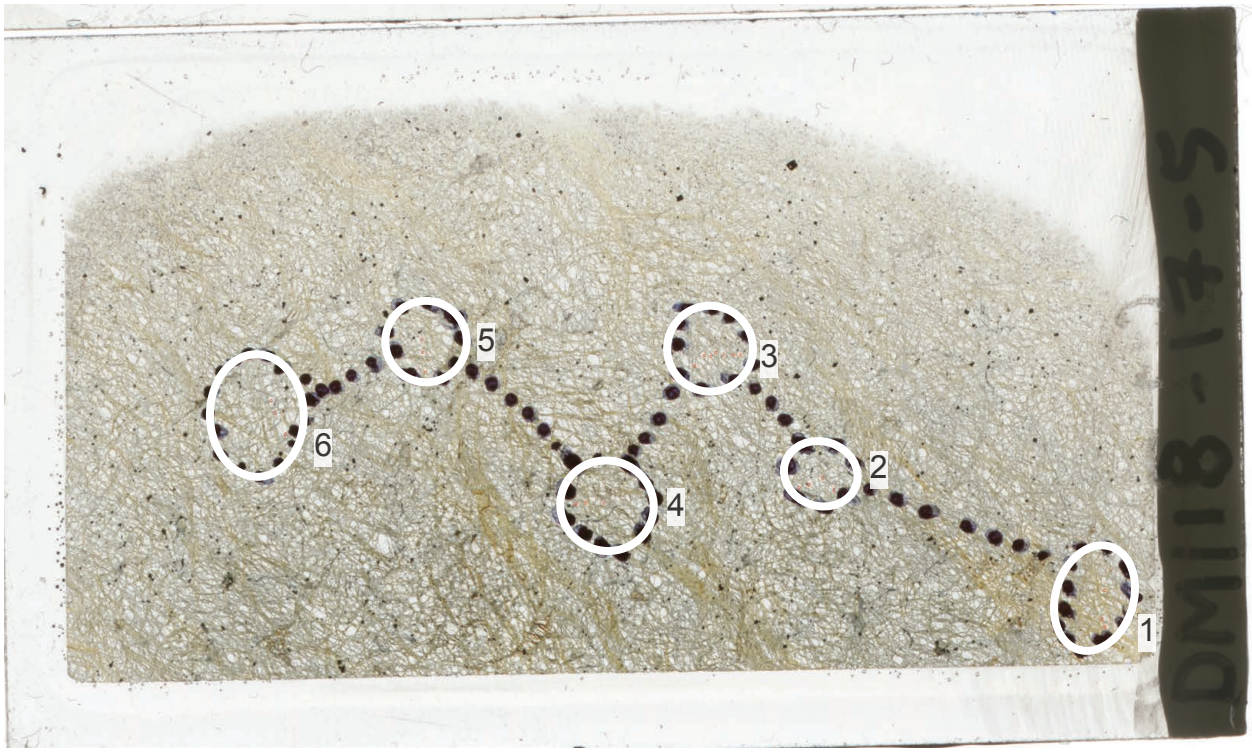

5) DMI18-20-12
Olivine clinopyroxenite

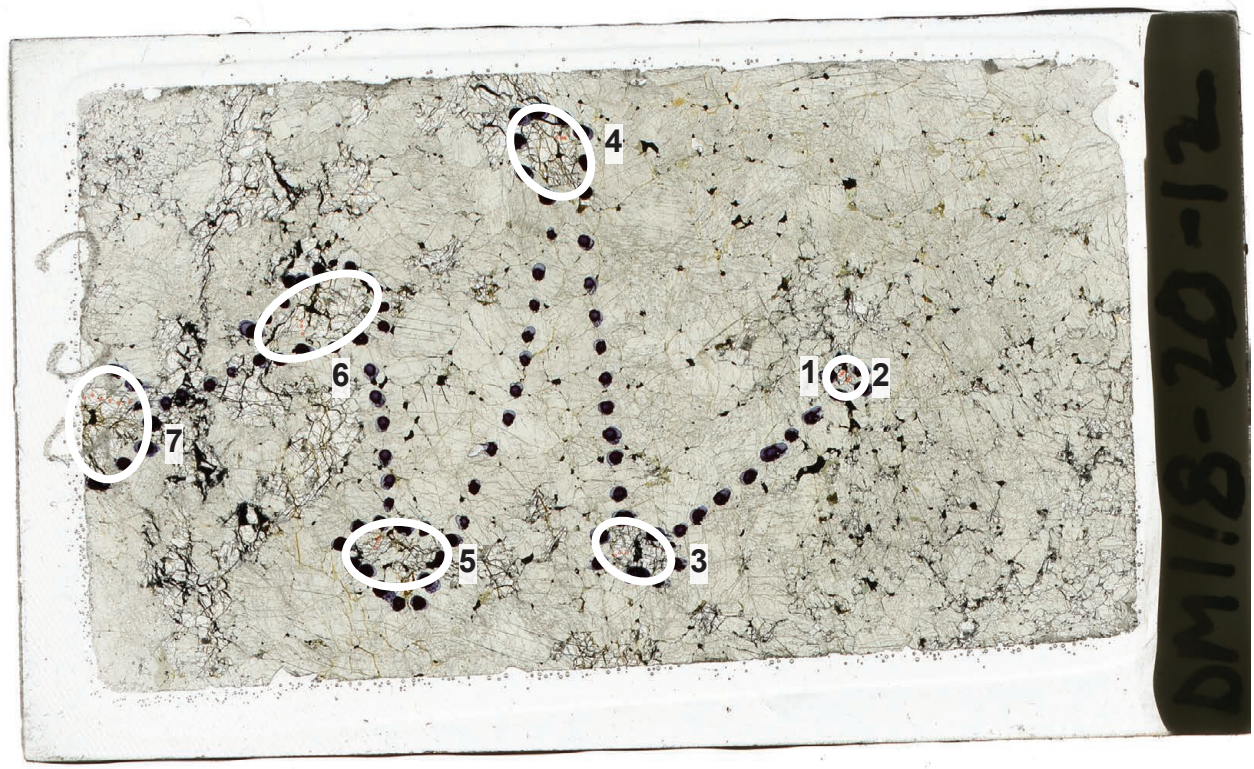

6) DMI18-21-12
Phlogopite-rich wehrlite

7) DMI18-21-19
Hornblende-olivine wehrlite

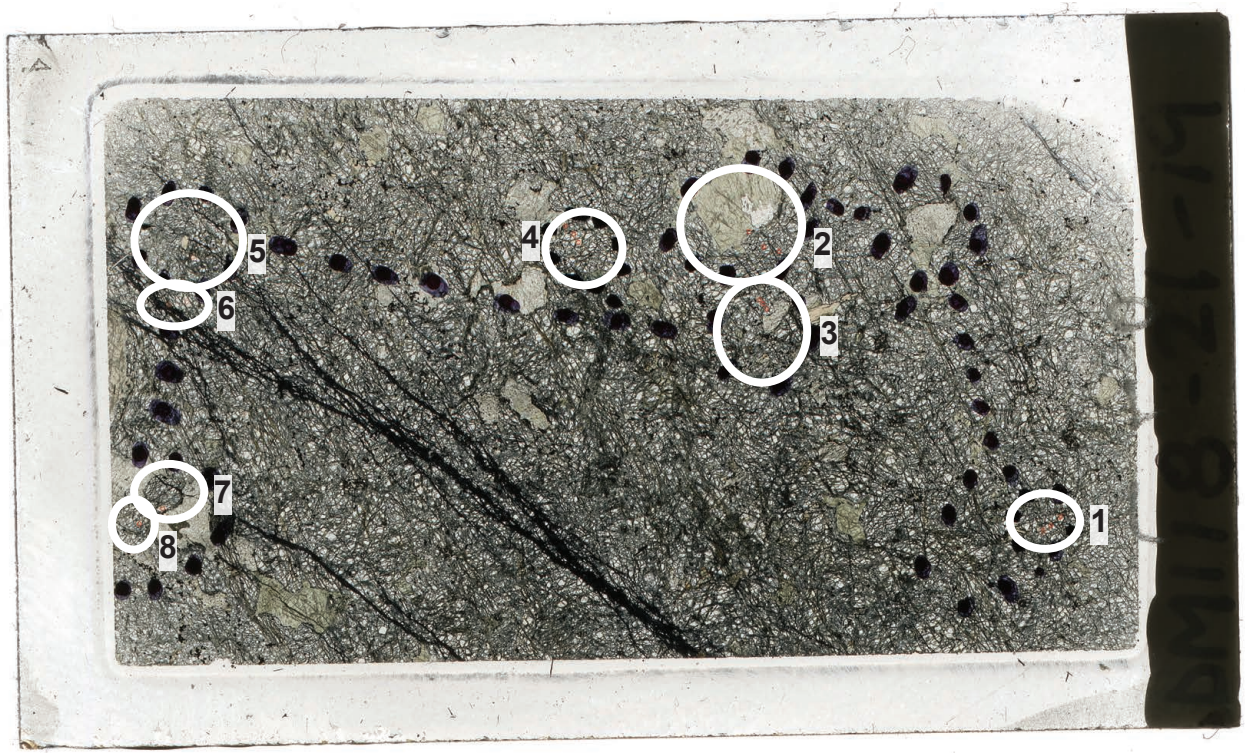

8) DMI18-25-9
Magnetite-olivine clinopyroxenite

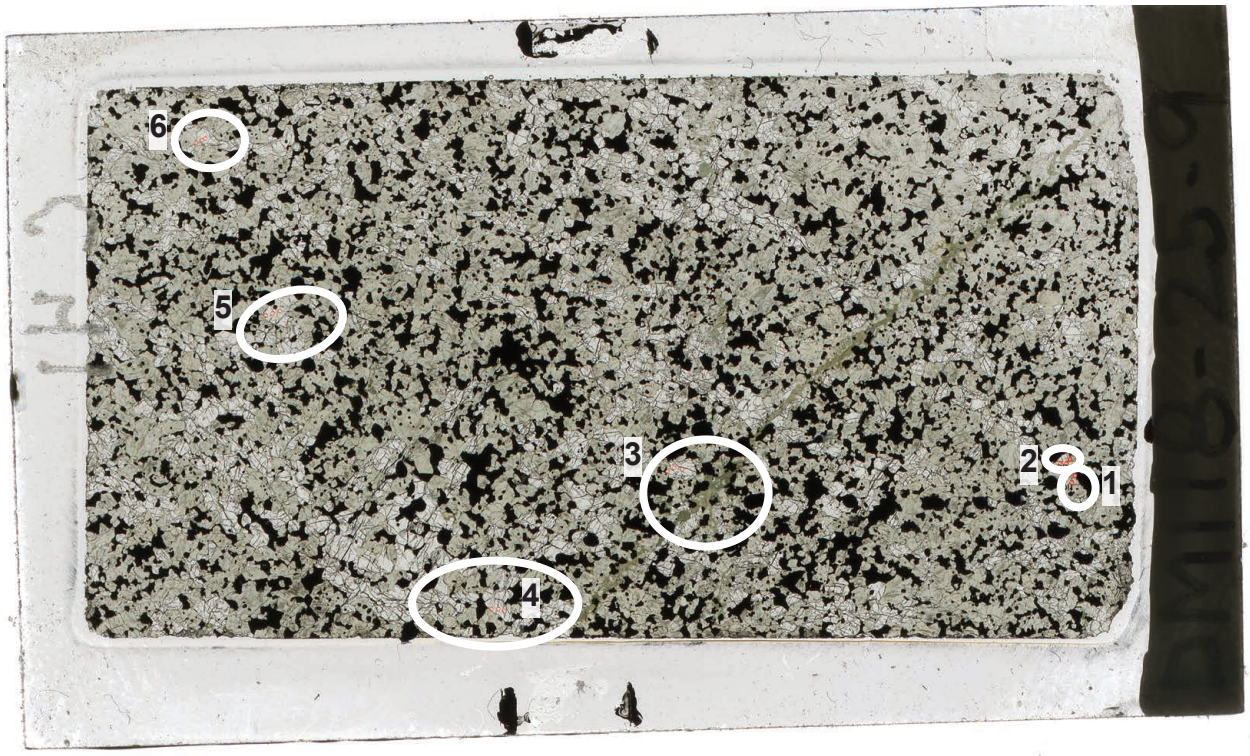

9) DMI18-26-6
Magnetite-olivine clinopyroxenite

10) DMI18-28-5
Olivine clinopyroxenite

11) DMI18-32-7
Dunite, chromitite

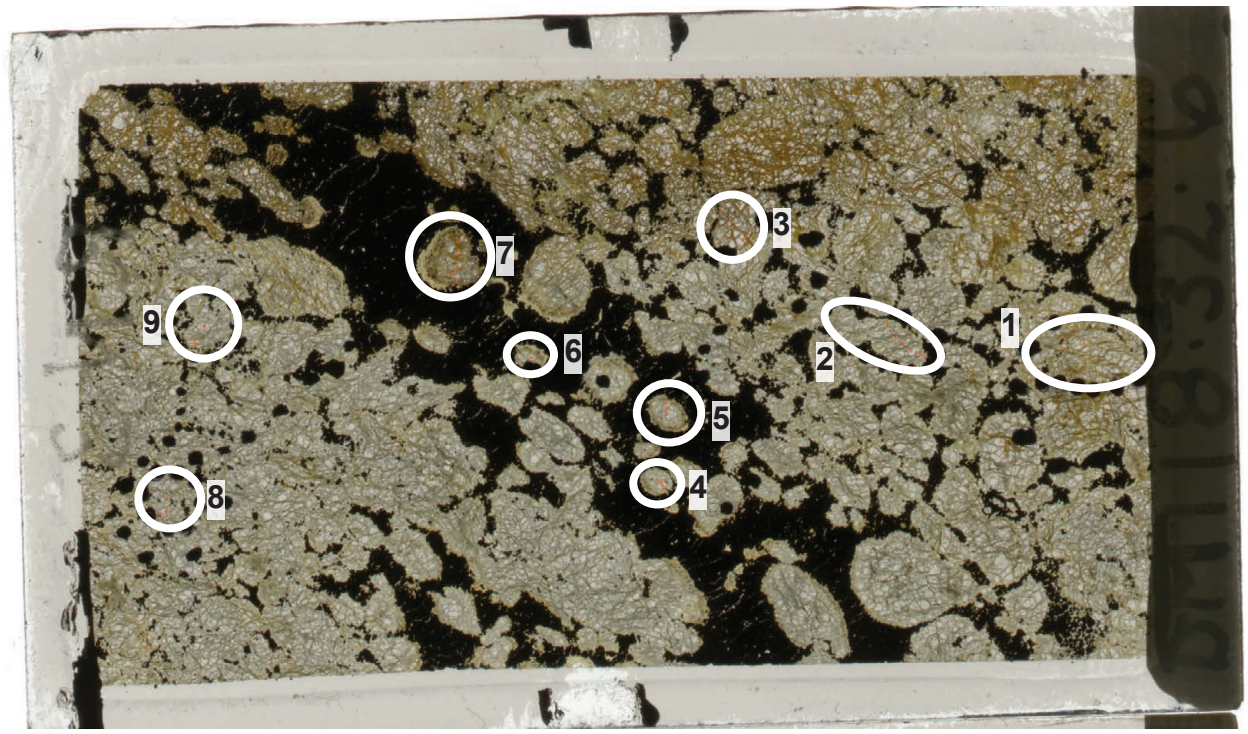

12) DMI18-32-9B
Dunite, olivine wehrlite dike

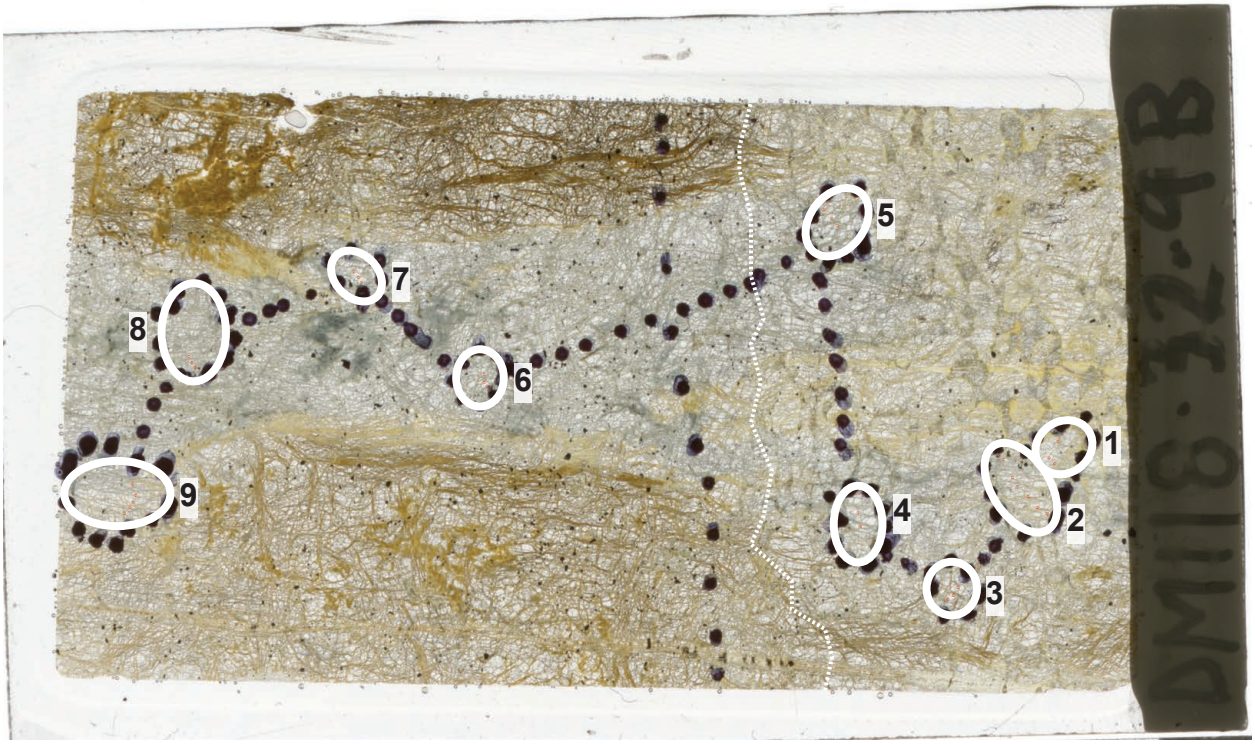

13) DMI18-32-9C
Dunite, wehrlite dike

14) GN88-1053
Olivine wehrlite, chromitite

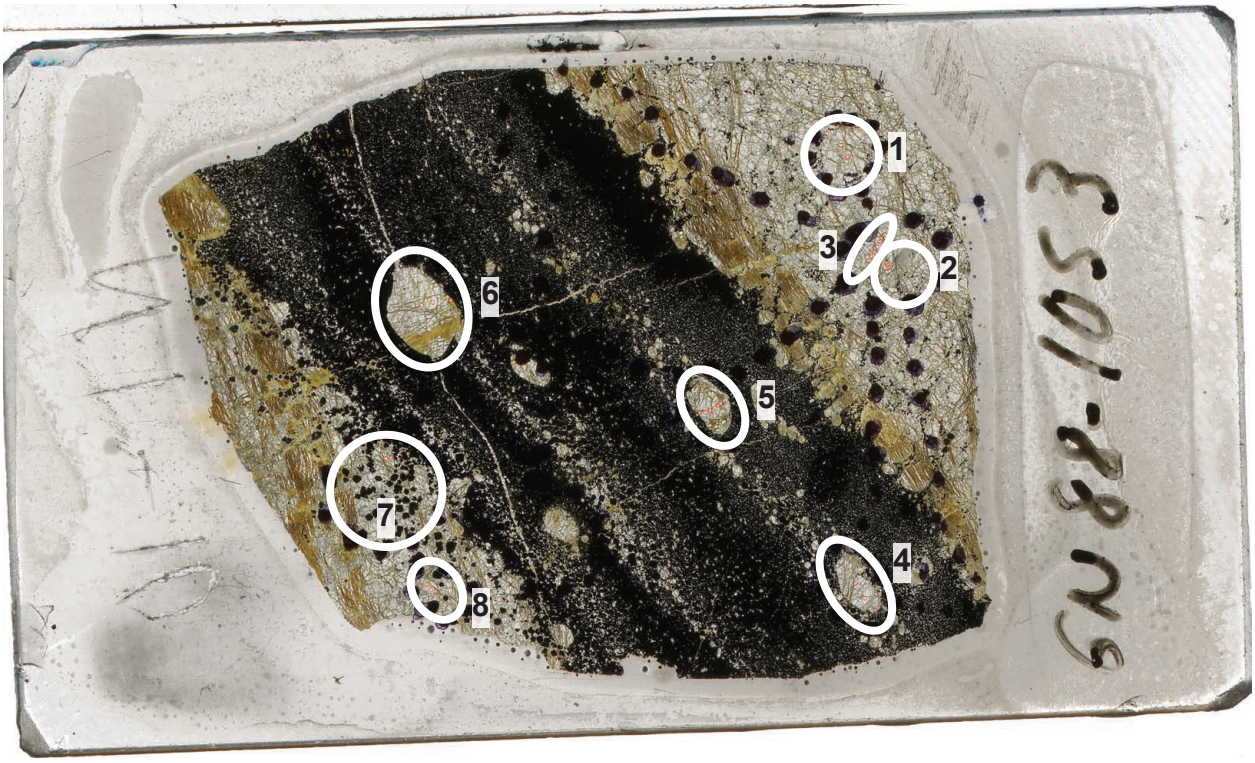

Appendix D: Major and Minor Element Oxide Compositions of Olivine from the Polaris Alaskan-type Intrusion determined by Electronprobe Microanalysis (EPMA)

Appendix D. Electronprobe microanalyses (EPMA) of olivine from the Polaris Alaskan-type intrusion

Spot	Oxides (wt.%)									Cations (p.f.u.)								End Members (mol. %)	
	Location	SiO_2	Cr_2O_3	MgO	MnO	FeO	CaO	NiO	Total	Si	Cr	Mg	Mn	Fe	Ca	Ni	Sum	Fo[1]	Fa[1]
DMI18-10-9-1-1-r1	rim	40.57	0.00	49.67	0.21	8.65	0.09	0.29	99.49	0.996	0.000	1.818	0.004	0.178	0.002	0.006	3.00	91.1	8.9
DMI18-10-9-1-1-m2	mid	41.02	0.00	50.05	0.16	8.82	0.11	0.29	100.46	0.997	0.000	1.814	0.003	0.179	0.003	0.006	3.00	91.0	9.0
DMI18-10-9-1-1-m3	mid	41.12	0.00	50.10	0.19	8.65	0.11	0.29	100.46	0.999	0.000	1.814	0.004	0.176	0.003	0.006	3.00	91.2	8.8
DMI18-10-9-1-1-m4	mid	41.27	0.01	49.92	0.17	8.84	0.11	0.29	100.62	1.001	0.000	1.805	0.003	0.179	0.003	0.006	3.00	91.0	9.0
DMI18-10-9-1-1-r5	rim	41.04	0.02	50.29	0.14	8.57	0.10	0.28	100.44	0.997	0.000	1.821	0.003	0.174	0.002	0.005	3.00	91.3	8.7
DMI18-10-9-2-1-c1	core	41.13	0.00	49.87	0.18	8.79	0.11	0.31	100.40	1.000	0.000	1.808	0.004	0.179	0.003	0.006	3.00	91.0	9.0
DMI18-10-9-2-1-m2	mid	40.90	0.02	49.79	0.19	8.80	0.13	0.30	100.12	0.998	0.000	1.811	0.004	0.180	0.003	0.006	3.00	91.0	9.0
DMI18-10-9-2-1-r3	rim	40.85	0.04	50.26	0.15	8.40	0.06	0.29	100.05	0.996	0.001	1.826	0.003	0.171	0.001	0.006	3.00	91.4	8.6
DMI18-10-9-3-1-c1	core	41.08	0.03	50.17	0.16	8.80	0.09	0.29	100.60	0.997	0.000	1.815	0.003	0.179	0.002	0.006	3.00	91.0	9.0
DMI18-10-9-3-1-r2	rim	40.75	0.02	49.68	0.13	8.62	0.10	0.30	99.59	0.998	0.000	1.815	0.003	0.177	0.003	0.006	3.00	91.1	8.9
DMI18-10-9-3-2-c1	core	40.97	0.01	49.94	0.22	8.76	0.11	0.30	100.31	0.998	0.000	1.813	0.005	0.178	0.003	0.006	3.00	91.0	9.0
DMI18-10-9-3-2-r2	rim	41.18	0.00	49.87	0.17	8.77	0.08	0.29	100.35	1.001	0.000	1.808	0.004	0.178	0.002	0.006	3.00	91.0	9.0
DMI18-10-9-4-1-c1	core	41.15	0.00	49.87	0.21	8.68	0.11	0.30	100.33	1.001	0.000	1.808	0.004	0.177	0.003	0.006	3.00	91.1	8.9
DMI18-10-9-4-1-m2	mid	41.14	0.00	49.98	0.17	8.67	0.11	0.30	100.36	1.000	0.000	1.811	0.003	0.176	0.003	0.006	3.00	91.1	8.9
DMI18-10-9-4-1-r3	rim	41.33	0.04	50.22	0.14	8.48	0.09	0.30	100.61	1.001	0.001	1.813	0.003	0.172	0.002	0.006	3.00	91.3	8.7
DMI18-10-9-5-1-c1	core	41.17	0.03	49.83	0.17	8.49	0.13	0.29	100.10	1.003	0.001	1.809	0.003	0.173	0.003	0.006	3.00	91.3	8.7
DMI18-10-9-5-1-m2	mid	41.08	0.01	49.88	0.11	8.69	0.13	0.29	100.18	1.000	0.000	1.811	0.002	0.177	0.003	0.006	3.00	91.1	8.9
DMI18-10-9-5-1-r3	rim	41.27	0.00	49.70	0.16	8.42	0.12	0.29	99.96	1.006	0.000	1.805	0.003	0.172	0.003	0.006	2.99	91.3	8.7
DMI18-10-9-6-1-c1	core	41.25	0.02	50.28	0.18	8.48	0.09	0.29	100.60	1.000	0.000	1.816	0.004	0.172	0.002	0.006	3.00	91.4	8.6
DMI18-10-9-6-1-m2	mid	41.09	0.00	50.22	0.16	8.59	0.10	0.30	100.48	0.998	0.000	1.818	0.003	0.174	0.003	0.006	3.00	91.2	8.8
DMI18-10-9-6-1-r3	rim	41.01	0.00	50.09	0.19	8.27	0.08	0.30	99.94	1.000	0.000	1.820	0.004	0.169	0.002	0.006	3.00	91.5	8.5
DMI18-12-5A-1-1-c1	core	41.07	0.01	50.14	0.17	9.56	0.05	0.27	101.27	0.994	0.000	1.809	0.004	0.193	0.001	0.005	3.01	90.3	9.7
DMI18-12-5A-1-1-m2	mid	40.64	0.07	49.56	0.21	9.51	0.03	0.27	100.29	0.994	0.001	1.806	0.004	0.194	0.001	0.005	3.01	90.3	9.7
DMI18-12-5A-1-1-r3	rim	40.84	0.00	49.86	0.16	9.47	0.02	0.26	100.63	0.994	0.000	1.809	0.003	0.193	0.001	0.005	3.01	90.4	9.6
DMI18-12-5A-2-1-r1	rim	40.57	0.00	49.73	0.17	9.34	0.02	0.27	100.09	0.993	0.000	1.814	0.003	0.191	0.000	0.005	3.01	90.5	9.5
DMI18-12-5A-2-1-m2	mid	40.75	0.00	50.01	0.22	9.57	0.04	0.29	100.88	0.991	0.000	1.813	0.005	0.195	0.001	0.006	3.01	90.3	9.7
DMI18-12-5A-2-1-m3	mid	41.22	0.02	49.76	0.17	9.34	0.03	0.29	100.83	1.000	0.000	1.800	0.003	0.189	0.001	0.006	3.00	90.5	9.5
DMI18-12-5A-2-1-m4	mid	41.03	0.02	50.30	0.15	9.20	0.03	0.27	101.00	0.994	0.000	1.816	0.003	0.186	0.001	0.005	3.01	90.7	9.3
DMI18-12-5A-2-1-m5	mid	40.70	0.00	49.71	0.18	9.35	0.03	0.28	100.26	0.994	0.000	1.810	0.004	0.191	0.001	0.006	3.01	90.5	9.5
DMI18-12-5A-2-1-r6	rim	40.93	0.01	49.86	0.19	9.45	0.04	0.28	100.77	0.995	0.000	1.807	0.004	0.192	0.001	0.005	3.00	90.4	9.6
DMI18-12-5A-3-1-c1	core	40.29	0.31	49.89	0.17	9.55	0.02	0.30	100.53	0.985	0.006	1.817	0.003	0.195	0.001	0.006	3.01	90.3	9.7
DMI18-12-5A-3-1-m2	mid	40.66	0.03	49.69	0.23	9.59	0.04	0.30	100.53	0.992	0.001	1.807	0.005	0.196	0.001	0.006	3.01	90.2	9.8
DMI18-12-5A-3-1-r3	rim	41.06	0.00	50.14	0.11	9.42	0.04	0.29	101.06	0.995	0.000	1.811	0.002	0.191	0.001	0.006	3.01	90.5	9.5
DMI18-12-5A-4-1-c1	core	40.96	0.05	49.90	0.21	9.76	0.03	0.26	101.17	0.993	0.001	1.804	0.004	0.198	0.001	0.005	3.01	90.1	9.9
DMI18-12-5A-4-1-m2	mid	40.77	0.04	50.09	0.16	9.83	0.03	0.25	101.19	0.989	0.001	1.812	0.003	0.200	0.001	0.005	3.01	90.1	9.9
DMI18-12-5A-4-1-r3	rim	40.91	0.02	49.70	0.20	9.79	0.03	0.27	100.93	0.995	0.000	1.801	0.004	0.199	0.001	0.005	3.01	90.0	10.0
DMI18-12-5A-5-1-c1	core	40.97	0.01	49.71	0.16	8.98	0.01	0.28	100.11	1.000	0.000	1.808	0.003	0.183	0.000	0.005	3.00	90.8	9.2
DMI18-12-5A-5-1-m2	mid	40.88	0.00	50.17	0.20	9.80	0.02	0.27	101.33	0.990	0.000	1.811	0.004	0.198	0.001	0.005	3.01	90.1	9.9
DMI18-12-5A-5-1-r3	rim	41.15	0.00	50.29	0.21	9.42	0.02	0.29	101.37	0.994	0.000	1.811	0.004	0.190	0.001	0.006	3.01	90.5	9.5
DMI18-12-5A-5-2-c1	core	40.65	0.00	49.68	0.12	9.60	0.02	0.28	100.34	0.993	0.000	1.809	0.003	0.196	0.000	0.005	3.01	90.2	9.8

[1] $Fo = Mg^{2+}/(Mg^{2+}+Fe^{2+}) \times 100$; Fa = 100-Fo

Appendix D. (continued) Electronprobe microanalyses (EPMA) of olivine from the Polaris Alaskan-type intrusion

Spot	Oxides (wt.%)								Cations (p.f.u.)								End Members (mol. %)	
	Location	SiO_2	Cr_2O_3	MgO	MnO	FeO	CaO	NiO	Total	Si	Cr	Mg	Mn	Fe	Ca	Ni	Sum	Fo[1]	Fa[1]
DMI18-12-5A-5-2-r2	rim	41.06	0.00	50.06	0.18	9.28	0.03	0.27	100.88	0.996	0.000	1.810	0.004	0.188	0.001	0.005	3.00	90.6	9.4
DMI18-13-1-1-1-r1	rim	40.68	0.03	48.66	0.18	9.68	0.02	0.23	99.49	1.002	0.001	1.787	0.004	0.199	0.001	0.005	3.00	90.0	10.0
DMI18-13-1-1-1-m2	mid	40.89	0.00	49.04	0.19	10.09	0.02	0.20	100.45	0.999	0.000	1.787	0.004	0.206	0.001	0.004	3.00	89.7	10.3
DMI18-13-1-1-1-m3	mid	40.80	0.02	48.59	0.14	10.29	0.02	0.22	100.09	1.001	0.000	1.777	0.003	0.211	0.001	0.004	3.00	89.4	10.6
DMI18-13-1-1-1-m4	mid	40.81	0.00	48.61	0.21	10.39	0.02	0.21	100.25	1.001	0.000	1.777	0.004	0.213	0.000	0.004	3.00	89.3	10.7
DMI18-13-1-1-1-m5	mid	40.87	0.00	48.68	0.17	10.42	0.02	0.22	100.38	1.001	0.000	1.777	0.004	0.213	0.000	0.004	3.00	89.3	10.7
DMI18-13-1-1-1-r6	rim	40.72	0.00	48.91	0.15	10.08	0.03	0.22	100.11	0.998	0.000	1.788	0.003	0.207	0.001	0.004	3.00	89.6	10.4
DMI18-13-1-2-1-c1	core	40.57	0.00	48.68	0.14	10.51	0.02	0.22	100.14	0.997	0.000	1.783	0.003	0.216	0.001	0.004	3.00	89.2	10.8
DMI18-13-1-2-1-m2	mid	40.97	0.00	48.83	0.19	10.52	0.02	0.23	100.75	1.000	0.000	1.777	0.004	0.215	0.001	0.005	3.00	89.2	10.8
DMI18-13-1-2-1-r3	rim	41.06	0.00	49.63	0.19	9.60	0.02	0.22	100.71	0.999	0.000	1.799	0.004	0.195	0.000	0.004	3.00	90.2	9.8
DMI18-13-1-3-1-c1	core	40.81	0.01	48.49	0.22	10.39	0.01	0.22	100.15	1.002	0.000	1.774	0.005	0.213	0.000	0.004	3.00	89.3	10.7
DMI18-13-1-3-1-m2	mid	40.71	0.00	48.62	0.22	10.65	0.02	0.22	100.45	0.998	0.000	1.776	0.005	0.218	0.001	0.004	3.00	89.1	10.9
DMI18-13-1-3-1-r3	rim	40.48	0.01	48.55	0.18	10.35	0.02	0.23	99.82	0.997	0.000	1.783	0.004	0.213	0.000	0.004	3.00	89.3	10.7
DMI18-13-1-4-1-c1	core	40.48	0.00	48.37	0.21	10.74	0.02	0.23	100.05	0.997	0.000	1.776	0.004	0.221	0.001	0.005	3.00	88.9	11.1
DMI18-13-1-4-1-r2	rim	40.55	0.05	48.68	0.20	10.08	0.02	0.20	99.79	0.998	0.001	1.786	0.004	0.207	0.001	0.004	3.00	89.6	10.4
DMI18-13-1-4-2-m1	mid	40.60	0.01	48.27	0.15	10.61	0.04	0.21	99.89	1.000	0.000	1.773	0.003	0.219	0.001	0.004	3.00	89.0	11.0
DMI18-13-1-5-1-m1	mid	40.67	0.00	48.46	0.19	10.35	0.03	0.21	99.91	1.000	0.000	1.777	0.004	0.213	0.001	0.004	3.00	89.3	10.7
DMI18-13-1-5-1-m2	mid	40.15	0.01	48.63	0.20	10.04	0.03	0.22	99.27	0.994	0.000	1.795	0.004	0.208	0.001	0.004	3.01	89.6	10.4
DMI18-13-1-5-1-m3	mid	40.46	0.01	48.14	0.22	10.61	0.03	0.21	99.69	0.999	0.000	1.772	0.005	0.219	0.001	0.004	3.00	89.0	11.0
DMI18-13-1-6-1-c1	core	40.36	0.00	48.30	0.20	10.50	0.02	0.21	99.60	0.997	0.000	1.779	0.004	0.217	0.001	0.004	3.00	89.1	10.9
DMI18-17-5-1-1-c1	core	40.82	0.00	48.78	0.13	10.45	0.07	0.27	100.51	0.999	0.000	1.779	0.003	0.214	0.002	0.005	3.00	89.3	10.7
DMI18-17-5-1-1-m2	mid	40.76	0.00	48.86	0.16	10.32	0.09	0.25	100.44	0.998	0.000	1.783	0.003	0.211	0.002	0.005	3.00	89.4	10.6
DMI18-17-5-1-1-r3	rim	40.55	0.00	48.35	0.17	10.13	0.06	0.26	99.53	1.001	0.000	1.779	0.004	0.209	0.002	0.005	3.00	89.5	10.5
DMI18-17-5-2-1-c1	core	41.13	0.00	48.84	0.19	10.46	0.07	0.27	100.95	1.002	0.000	1.773	0.004	0.213	0.002	0.005	3.00	89.3	10.7
DMI18-17-5-2-1-m2	mid	40.45	0.00	48.92	0.19	10.44	0.04	0.26	100.30	0.993	0.000	1.790	0.004	0.214	0.001	0.005	3.01	89.3	10.7
DMI18-17-5-2-1-r3	rim	40.65	0.00	48.75	0.20	10.12	0.05	0.27	100.04	0.998	0.000	1.785	0.004	0.208	0.001	0.005	3.00	89.6	10.4
DMI18-17-5-3-1-r1	rim	40.74	0.02	48.87	0.17	10.34	0.07	0.27	100.48	0.997	0.000	1.783	0.004	0.212	0.002	0.005	3.00	89.4	10.6
DMI18-17-5-3-1-m2	mid	40.88	0.00	48.87	0.19	10.42	0.07	0.26	100.69	0.998	0.000	1.779	0.004	0.213	0.002	0.005	3.00	89.3	10.7
DMI18-17-5-3-1-m3	mid	40.70	0.01	48.32	0.17	10.31	0.05	0.26	99.82	1.002	0.000	1.773	0.004	0.212	0.001	0.005	3.00	89.3	10.7
DMI18-17-5-3-1-m4	mid	40.50	0.01	48.43	0.18	10.34	0.06	0.26	99.79	0.998	0.000	1.780	0.004	0.213	0.002	0.005	3.00	89.3	10.7
DMI18-17-5-3-1-m5	mid	40.40	0.03	48.90	0.21	10.43	0.06	0.27	100.31	0.992	0.000	1.790	0.004	0.214	0.002	0.005	3.01	89.3	10.7
DMI18-17-5-3-1-m6	mid	40.65	0.03	48.82	0.16	10.18	0.05	0.27	100.16	0.997	0.000	1.786	0.003	0.209	0.001	0.005	3.00	89.5	10.5
DMI18-17-5-3-1-r7	rim	40.86	0.01	48.86	0.19	10.31	0.05	0.26	100.53	0.999	0.000	1.781	0.004	0.211	0.001	0.005	3.00	89.4	10.6
DMI18-17-5-4-1-c1	core	40.93	0.00	48.62	0.22	10.25	0.07	0.25	100.35	1.002	0.000	1.775	0.005	0.210	0.002	0.005	3.00	89.4	10.6
DMI18-17-5-4-1-m2	mid	40.50	0.00	48.85	0.20	10.36	0.06	0.27	100.24	0.994	0.000	1.788	0.004	0.213	0.002	0.005	3.01	89.4	10.6
DMI18-17-5-4-1-r3	rim	40.44	0.01	48.43	0.16	10.50	0.05	0.28	99.87	0.997	0.000	1.780	0.003	0.217	0.001	0.006	3.00	89.2	10.8
DMI18-17-5-5-1-c1	core	41.15	0.00	49.00	0.19	10.46	0.07	0.27	101.14	1.000	0.000	1.776	0.004	0.213	0.002	0.005	3.00	89.3	10.7
DMI18-17-5-5-1-m2	mid	40.40	0.00	48.73	0.19	10.37	0.07	0.25	100.02	0.994	0.000	1.787	0.004	0.213	0.002	0.005	3.01	89.3	10.7
DMI18-17-5-5-1-r3	rim	40.34	0.00	48.89	0.17	10.21	0.06	0.26	99.94	0.993	0.000	1.794	0.004	0.210	0.002	0.005	3.01	89.5	10.5
DMI18-17-5-6-1-c1	core	40.30	0.01	48.54	0.20	10.36	0.06	0.27	99.74	0.995	0.000	1.786	0.004	0.214	0.002	0.005	3.01	89.3	10.7

[1] $Fo = Mg^{2+}/(Mg^{2+}+Fe^{2+}) \times 100$; Fa = 100-Fo

Appendix D. (continued) Electronprobe microanalyses (EPMA) of olivine from the Polaris Alaskan-type intrusion

Spot	Oxides (wt.%)								Cations (p.f.u.)								End Members (mol. %)	
	Location	SiO_2	Cr_2O_3	MgO	MnO	FeO	CaO	NiO	Total	Si	Cr	Mg	Mn	Fe	Ca	Ni	Sum	Fo[1]	Fa[1]
DMI18-17-5-6-1-m2	mid	40.47	0.00	48.71	0.16	10.13	0.05	0.26	99.77	0.997	0.000	1.788	0.003	0.209	0.001	0.005	3.00	89.6	10.4
DMI18-17-5-6-1-r3	rim	40.57	0.01	48.70	0.19	10.20	0.05	0.26	99.99	0.997	0.000	1.785	0.004	0.210	0.001	0.005	3.00	89.5	10.5
DMI18-20-12-1-1-c1	core	39.04	0.02	43.09	0.27	17.17	0.02	0.24	99.86	0.994	0.000	1.635	0.006	0.365	0.001	0.005	3.01	81.7	18.3
DMI18-20-12-1-1-m2	mid	38.93	0.00	43.25	0.31	17.28	0.02	0.25	100.04	0.990	0.000	1.640	0.007	0.367	0.001	0.005	3.01	81.7	18.3
DMI18-20-12-1-1-r3	rim	39.66	0.00	44.03	0.30	16.69	0.02	0.25	100.94	0.995	0.000	1.647	0.006	0.350	0.000	0.005	3.00	82.5	17.5
DMI18-20-12-1-2-c1	core	38.96	0.00	43.27	0.30	16.91	0.02	0.25	99.72	0.992	0.000	1.643	0.006	0.360	0.001	0.005	3.01	82.0	18.0
DMI18-20-12-1-2-r2	rim	39.11	0.00	43.32	0.28	16.82	0.03	0.26	99.81	0.994	0.000	1.642	0.006	0.358	0.001	0.005	3.01	82.1	17.9
DMI18-20-12-2-1-c1	core	39.22	0.00	43.66	0.30	17.00	0.02	0.19	100.39	0.992	0.000	1.646	0.006	0.360	0.001	0.004	3.01	82.1	17.9
DMI18-20-12-2-1-m2	mid	39.29	0.00	43.78	0.27	16.73	0.02	0.18	100.27	0.993	0.000	1.650	0.006	0.354	0.001	0.004	3.01	82.3	17.7
DMI18-20-12-2-1-r3	rim	39.31	0.00	43.44	0.25	16.43	0.02	0.19	99.64	0.998	0.000	1.644	0.005	0.349	0.001	0.004	3.00	82.5	17.5
DMI18-20-12-3-1-r1	rim	38.92	0.02	42.99	0.32	17.00	0.02	0.25	99.52	0.994	0.000	1.636	0.007	0.363	0.001	0.005	3.01	81.8	18.2
DMI18-20-12-3-1-c2	core	39.33	0.00	43.06	0.30	17.32	0.03	0.25	100.29	0.997	0.000	1.627	0.006	0.367	0.001	0.005	3.00	81.6	18.4
DMI18-20-12-3-1-r3	rim	39.25	0.01	42.97	0.31	16.82	0.02	0.26	99.63	0.999	0.000	1.631	0.007	0.358	0.001	0.005	3.00	82.0	18.0
DMI18-20-12-4-1-c1	core	39.75	0.00	43.77	0.29	16.48	0.03	0.17	100.49	1.000	0.000	1.642	0.006	0.347	0.001	0.003	3.00	82.6	17.4
DMI18-20-12-4-1-m2	mid	39.07	0.00	43.76	0.26	16.56	0.03	0.17	99.85	0.992	0.000	1.656	0.006	0.352	0.001	0.003	3.01	82.5	17.5
DMI18-20-12-4-1-r3	rim	39.20	0.00	43.40	0.29	16.33	0.03	0.19	99.44	0.998	0.000	1.647	0.006	0.347	0.001	0.004	3.00	82.6	17.4
DMI18-20-12-5-1-c1	core	39.23	0.00	43.57	0.27	17.11	0.03	0.21	100.42	0.992	0.000	1.643	0.006	0.362	0.001	0.004	3.01	81.9	18.1
DMI18-20-12-5-1-m2	mid	39.21	0.01	43.54	0.29	16.59	0.03	0.21	99.87	0.995	0.000	1.647	0.006	0.352	0.001	0.004	3.00	82.4	17.6
DMI18-20-12-5-1-r3	rim	39.27	0.02	43.88	0.33	16.02	0.04	0.21	99.77	0.995	0.000	1.657	0.007	0.339	0.001	0.004	3.00	83.0	17.0
DMI18-20-12-6-1-r1	rim	39.26	0.00	43.47	0.31	16.51	0.04	0.26	99.85	0.996	0.000	1.644	0.007	0.350	0.001	0.005	3.00	82.4	17.6
DMI18-20-12-6-1-m2	mid	39.40	0.02	43.45	0.29	16.33	0.03	0.25	99.77	0.999	0.000	1.643	0.006	0.346	0.001	0.005	3.00	82.6	17.4
DMI18-20-12-6-1-m3	mid	39.07	0.00	43.55	0.27	16.64	0.03	0.22	99.78	0.993	0.000	1.650	0.006	0.354	0.001	0.004	3.01	82.4	17.6
DMI18-20-12-6-1-m4	mid	39.47	0.00	43.67	0.25	16.90	0.03	0.20	100.52	0.996	0.000	1.642	0.005	0.356	0.001	0.004	3.00	82.2	17.8
DMI18-20-12-6-1-m5	mid	39.45	0.00	43.63	0.28	16.78	0.04	0.21	100.39	0.996	0.000	1.642	0.006	0.354	0.001	0.004	3.00	82.3	17.7
DMI18-20-12-6-1-r6	rim	39.19	0.01	43.57	0.32	16.29	0.04	0.22	99.64	0.996	0.000	1.650	0.007	0.346	0.001	0.005	3.00	82.7	17.3
DMI18-21-12-1-1-c1	core	40.36	0.00	48.77	0.22	10.38	0.01	0.39	100.14	0.993	0.000	1.788	0.005	0.213	0.000	0.008	3.01	89.3	10.7
DMI18-21-12-1-1-m2	mid	40.66	0.00	48.81	0.15	10.41	0.01	0.40	100.44	0.996	0.000	1.783	0.003	0.213	0.000	0.008	3.00	89.3	10.7
DMI18-21-12-1-1-r3	rim	41.12	0.02	48.67	0.15	10.06	0.01	0.39	100.41	1.005	0.000	1.773	0.003	0.206	0.000	0.008	2.99	89.6	10.4
DMI18-21-12-2-1-c1	core	40.62	0.06	48.30	0.10	10.63	0.27	0.38	100.35	0.998	0.001	1.768	0.002	0.218	0.007	0.007	3.00	89.0	11.0
DMI18-21-12-2-1-m2	mid	40.79	0.00	48.63	0.17	10.42	0.01	0.38	100.40	0.999	0.000	1.776	0.004	0.213	0.000	0.008	3.00	89.3	10.7
DMI18-21-12-2-1-r3	rim	40.65	0.00	48.64	0.16	10.29	0.01	0.39	100.14	0.998	0.000	1.781	0.003	0.211	0.000	0.008	3.00	89.4	10.6
DMI18-21-12-3-1-r1	rim	40.76	0.00	49.06	0.20	10.49	0.01	0.37	100.90	0.995	0.000	1.785	0.004	0.214	0.000	0.007	3.01	89.3	10.7
DMI18-21-12-3-1-m2	mid	40.55	0.00	48.59	0.16	10.39	0.01	0.40	100.10	0.997	0.000	1.781	0.003	0.214	0.000	0.008	3.00	89.3	10.7
DMI18-21-12-3-1-m3	mid	40.59	0.00	48.74	0.16	10.45	0.01	0.39	100.34	0.996	0.000	1.782	0.003	0.214	0.000	0.008	3.00	89.3	10.7
DMI18-21-12-3-1-m4	mid	40.36	0.01	49.02	0.20	10.73	0.01	0.38	100.71	0.989	0.000	1.790	0.004	0.220	0.000	0.007	3.01	89.1	10.9
DMI18-21-12-3-1-r5	rim	40.69	0.00	49.21	0.20	10.71	0.02	0.37	101.19	0.991	0.000	1.787	0.004	0.218	0.000	0.007	3.01	89.1	10.9
DMI18-21-12-4-1-c1	core	40.85	0.02	49.00	0.19	10.49	0.01	0.39	100.96	0.996	0.000	1.781	0.004	0.214	0.000	0.008	3.00	89.3	10.7
DMI18-21-12-4-1-r2	rim	40.58	0.02	48.67	0.14	10.41	0.01	0.39	100.23	0.997	0.000	1.782	0.003	0.214	0.000	0.008	3.00	89.3	10.7
DMI18-21-12-5-1-c1	core	40.58	0.00	48.87	0.17	10.66	0.02	0.39	100.68	0.993	0.000	1.783	0.003	0.218	0.000	0.008	3.01	89.1	10.9
DMI18-21-12-5-1-r2	rim	40.43	0.01	48.77	0.16	10.30	0.01	0.39	100.07	0.994	0.000	1.788	0.003	0.212	0.000	0.008	3.01	89.4	10.6

[1] $Fo = Mg^{2+}/(Mg^{2+}+Fe^{2+}) \times 100$; Fa = 100-Fo

Appendix D. (continued) Electronprobe microanalyses (EPMA) of olivine from the Polaris Alaskan-type intrusion

Spot	Oxides (wt.%)								Cations (p.f.u.)								End Members (mol. %)	
	Location	SiO_2	Cr_2O_3	MgO	MnO	FeO	CaO	NiO	Total	Si	Cr	Mg	Mn	Fe	Ca	Ni	Sum	Fo[1]	Fa[1]
DMI18-21-12-6-1-c1	core	40.70	0.01	48.84	0.18	10.32	0.01	0.39	100.44	0.997	0.000	1.783	0.004	0.211	0.000	0.008	3.00	89.4	10.6
DMI18-21-12-6-1-m2	mid	40.02	0.00	48.81	0.20	10.42	0.01	0.39	99.85	0.988	0.000	1.797	0.004	0.215	0.000	0.008	3.01	89.3	10.7
DMI18-21-12-6-1-c3	core	40.71	0.02	48.82	0.19	10.41	0.01	0.39	100.56	0.997	0.000	1.781	0.004	0.213	0.000	0.008	3.00	89.3	10.7
DMI18-21-19-1-1-1c	core	40.76	0.01	50.01	0.18	9.76	0.02	0.29	101.03	0.990	0.000	1.811	0.004	0.198	0.000	0.006	3.01	90.1	9.9
DMI18-21-19-1-1-2m	mid	40.58	0.00	49.51	0.14	9.57	0.02	0.29	100.10	0.994	0.000	1.807	0.003	0.196	0.000	0.006	3.01	90.2	9.8
DMI18-21-19-1-1-3r	rim	40.35	0.00	49.19	0.20	9.85	0.02	0.29	99.91	0.992	0.000	1.803	0.004	0.202	0.001	0.006	3.01	89.9	10.1
DMI18-21-19-2-1-1c	core	41.26	0.00	50.20	0.23	9.63	0.03	0.28	101.63	0.995	0.000	1.805	0.005	0.194	0.001	0.005	3.00	90.3	9.7
DMI18-21-19-2-1-2m	mid	40.62	0.00	50.08	0.16	9.86	0.01	0.27	101.01	0.988	0.000	1.815	0.003	0.201	0.000	0.005	3.01	90.0	10.0
DMI18-21-19-2-1-3r	rim	40.35	0.00	49.79	0.17	9.67	0.02	0.25	100.26	0.988	0.000	1.817	0.003	0.198	0.001	0.005	3.01	90.2	9.8
DMI18-21-19-3-1-1c	core	40.42	0.00	49.41	0.18	9.91	0.02	0.28	100.22	0.991	0.000	1.806	0.004	0.203	0.001	0.006	3.01	89.9	10.1
DMI18-21-19-3-1-2m	mid	40.27	0.01	49.34	0.15	9.57	0.02	0.29	99.65	0.991	0.000	1.811	0.003	0.197	0.001	0.006	3.01	90.2	9.8
DMI18-21-19-3-1-3r	rim	40.93	0.02	50.26	0.18	9.11	0.03	0.27	100.80	0.993	0.000	1.818	0.004	0.185	0.001	0.005	3.01	90.8	9.2
DMI18-21-19-4-1-2m	mid	40.49	0.03	49.88	0.22	9.69	0.02	0.28	100.59	0.988	0.000	1.815	0.004	0.198	0.000	0.006	3.01	90.2	9.8
DMI18-21-19-4-1-1c	core	40.78	0.00	49.65	0.19	10.19	0.02	0.28	101.10	0.992	0.000	1.800	0.004	0.207	0.001	0.006	3.01	89.7	10.3
DMI18-21-19-4-1-3r	rim	40.70	0.00	49.83	0.21	9.59	0.03	0.28	100.64	0.992	0.000	1.810	0.004	0.195	0.001	0.006	3.01	90.3	9.7
DMI18-21-19-5-1-1c	core	40.36	0.01	49.24	0.20	9.93	0.02	0.28	100.04	0.991	0.000	1.803	0.004	0.204	0.001	0.006	3.01	89.8	10.2
DMI18-21-19-5-2-1c	core	39.93	0.00	49.33	0.18	9.75	0.02	0.28	99.50	0.986	0.000	1.816	0.004	0.201	0.001	0.006	3.01	90.0	10.0
DMI18-21-19-5-2-2r	rim	40.17	0.00	49.21	0.20	9.69	0.02	0.28	99.57	0.991	0.000	1.809	0.004	0.200	0.001	0.006	3.01	90.1	9.9
DMI18-21-19-6-1-1c	core	40.85	0.00	49.45	0.17	9.62	0.02	0.28	100.38	0.997	0.000	1.799	0.003	0.197	0.001	0.005	3.00	90.2	9.8
DMI18-21-19-6-2-1c	core	40.76	0.04	49.77	0.17	9.68	0.02	0.29	100.72	0.993	0.001	1.807	0.004	0.197	0.000	0.006	3.01	90.2	9.8
DM118-25-9-1-1-1c	core	39.24	0.03	43.97	0.32	16.42	0.03	0.05	100.06	0.993	0.001	1.658	0.007	0.347	0.001	0.001	3.01	82.7	17.3
DM118-25-9-1-1-2r	rim	39.29	0.00	44.55	0.36	15.19	0.02	0.05	99.48	0.994	0.000	1.681	0.008	0.322	0.001	0.001	3.01	83.9	16.1
DM118-25-9-1-2-1c	core	39.41	0.05	44.57	0.36	16.51	0.03	0.05	100.98	0.988	0.001	1.666	0.008	0.346	0.001	0.001	3.01	82.8	17.2
DM118-25-9-1-2-2m	mid	39.17	0.00	43.69	0.36	16.82	0.04	0.05	100.13	0.992	0.000	1.650	0.008	0.356	0.001	0.001	3.01	82.2	17.8
DM118-25-9-1-2-3r	rim	39.58	0.02	44.52	0.37	16.23	0.04	0.06	100.82	0.992	0.000	1.664	0.008	0.340	0.001	0.001	3.01	83.0	17.0
DM118-25-9-2-1-1c	core	39.15	0.03	44.01	0.29	17.01	0.04	0.05	100.57	0.988	0.001	1.656	0.006	0.359	0.001	0.001	3.01	82.2	17.8
DM118-25-9-2-1-2m	mid	38.77	0.01	43.81	0.32	16.79	0.04	0.06	99.79	0.986	0.000	1.661	0.007	0.357	0.001	0.001	3.01	82.3	17.7
DM118-25-9-2-1-3r	rim	39.01	0.00	44.76	0.29	15.82	0.04	0.04	99.96	0.986	0.000	1.686	0.006	0.334	0.001	0.001	3.01	83.5	16.5
DM118-25-9-3-1-1c	core	39.20	0.00	43.49	0.32	16.89	0.03	0.07	100.00	0.994	0.000	1.644	0.007	0.358	0.001	0.001	3.01	82.1	17.9
DM118-25-9-3-1-2m	mid	38.98	0.05	43.39	0.31	16.79	0.04	0.04	99.60	0.993	0.001	1.647	0.007	0.358	0.001	0.001	3.01	82.2	17.8
DM118-25-9-3-1-3r	rim	38.97	0.00	43.46	0.32	17.09	0.05	0.06	99.95	0.990	0.000	1.647	0.007	0.363	0.001	0.001	3.01	81.9	18.1
DM118-25-9-4-1-1c(mt)	core	38.87	0.04	43.79	0.32	17.13	0.03	0.05	100.24	0.986	0.001	1.655	0.007	0.363	0.001	0.001	3.01	82.0	18.0
DM118-25-9-4-1-2c	core	39.11	0.00	43.56	0.30	17.15	0.04	0.05	100.21	0.991	0.000	1.646	0.006	0.363	0.001	0.001	3.01	81.9	18.1
DM118-25-9-4-1-3m	mid	39.34	0.02	43.27	0.34	16.80	0.04	0.05	99.85	0.998	0.000	1.637	0.007	0.356	0.001	0.001	3.00	82.1	17.9
DM118-25-9-4-1-4r	rim	39.23	0.00	43.81	0.35	16.06	0.05	0.05	99.54	0.996	0.000	1.658	0.008	0.341	0.001	0.001	3.00	82.9	17.1
DM118-25-9-5-1-1c	core	39.05	0.01	43.49	0.40	17.63	0.04	0.06	100.67	0.988	0.000	1.640	0.009	0.373	0.001	0.001	3.01	81.5	18.5
DM118-25-9-5-1-2m	mid	39.39	0.01	43.74	0.37	17.37	0.04	0.05	100.97	0.991	0.000	1.641	0.008	0.366	0.001	0.001	3.01	81.8	18.2
DM118-25-9-5-1-3r	rim	39.08	0.04	43.49	0.35	16.94	0.03	0.06	99.99	0.992	0.001	1.646	0.008	0.360	0.001	0.001	3.01	82.1	17.9
DMI18-26-6-1-1-c1	core	39.38	0.00	42.42	0.42	17.68	0.04	0.05	99.98	1.002	0.000	1.609	0.009	0.376	0.001	0.001	3.00	81.0	19.0

[1]Fo = $Mg^{2+}/(Mg^{2+}+Fe^{2+})$ x 100; Fa = 100-Fo

Appendix D. (continued) Electronprobe microanalyses (EPMA) of olivine from the Polaris Alaskan-type intrusion

Spot	Oxides (wt.%)								Cations (p.f.u.)								End Members (mol. %)	
	Location	SiO_2	Cr_2O_3	MgO	MnO	FeO	CaO	NiO	Total	Si	Cr	Mg	Mn	Fe	Ca	Ni	Sum	Fo[1]	Fa[1]
DMI18-26-6-1-1-m2	mid	39.61	0.02	42.60	0.38	17.84	0.04	0.05	100.53	1.002	0.000	1.607	0.008	0.377	0.001	0.001	3.00	81.0	19.0
DMI18-26-6-1-1-r3	rim	39.29	0.00	42.84	0.43	17.67	0.03	0.05	100.31	0.997	0.000	1.620	0.009	0.375	0.001	0.001	3.00	81.2	18.8
DMI18-26-6-2-1-r1	rim	39.11	0.00	42.07	0.44	18.37	0.04	0.04	100.08	0.998	0.000	1.600	0.010	0.392	0.001	0.001	3.00	80.3	19.7
DMI18-26-6-2-1-m2	mid	39.17	0.05	42.27	0.42	18.88	0.04	0.05	100.87	0.994	0.001	1.599	0.009	0.401	0.001	0.001	3.01	80.0	20.0
DMI18-26-6-2-1-m3	mid	39.25	0.01	41.97	0.46	18.77	0.05	0.04	100.55	0.998	0.000	1.592	0.010	0.399	0.001	0.001	3.00	79.9	20.1
DMI18-26-6-2-1-m4	mid	39.29	0.00	42.03	0.44	18.67	0.04	0.06	100.53	0.999	0.000	1.593	0.010	0.397	0.001	0.001	3.00	80.1	19.9
DMI18-26-6-2-1-m5	mid	39.39	0.02	42.21	0.41	18.99	0.04	0.05	101.11	0.997	0.000	1.592	0.009	0.402	0.001	0.001	3.00	79.8	20.2
DMI18-26-6-2-1-m6	mid	39.29	0.03	42.44	0.47	18.49	0.03	0.04	100.80	0.996	0.001	1.604	0.010	0.392	0.001	0.001	3.00	80.4	19.6
DMI18-26-6-2-1-r7	rim	39.37	0.02	42.33	0.36	18.51	0.03	0.05	100.67	0.999	0.000	1.600	0.008	0.393	0.001	0.001	3.00	80.3	19.7
DMI18-26-6-3-1-c1	core	39.38	0.00	42.10	0.39	18.45	0.04	0.05	100.41	1.001	0.000	1.595	0.008	0.392	0.001	0.001	3.00	80.3	19.7
DMI18-26-6-3-1-m2	mid	39.34	0.01	42.91	0.37	17.95	0.04	0.04	100.67	0.996	0.000	1.619	0.008	0.380	0.001	0.001	3.00	81.0	19.0
DMI18-26-6-3-1-r3	rim	39.49	0.01	42.42	0.44	18.09	0.03	0.05	100.53	1.001	0.000	1.603	0.009	0.383	0.001	0.001	3.00	80.7	19.3
DMI18-26-6-4-1-c1	core	38.85	0.00	42.20	0.43	18.40	0.03	0.04	99.96	0.993	0.000	1.609	0.009	0.394	0.001	0.001	3.01	80.3	19.7
DMI18-26-6-4-1-m2	mid	39.20	0.00	42.31	0.40	18.31	0.04	0.05	100.32	0.997	0.000	1.605	0.009	0.390	0.001	0.001	3.00	80.5	19.5
DMI18-26-6-4-1-r3	rim	39.23	0.00	42.30	0.47	18.07	0.03	0.05	100.14	0.999	0.000	1.606	0.010	0.385	0.001	0.001	3.00	80.7	19.3
DMI18-26-6-5-1-c1	core	39.48	0.00	42.74	0.38	17.59	0.03	0.04	100.27	1.001	0.000	1.615	0.008	0.373	0.001	0.001	3.00	81.2	18.8
DMI18-26-6-5-1-m2	mid	39.40	0.00	43.15	0.40	17.08	0.03	0.04	100.11	0.999	0.000	1.630	0.009	0.362	0.001	0.001	3.00	81.8	18.2
DMI18-26-6-5-1-r3	rim	39.37	0.00	42.63	0.38	17.22	0.03	0.04	99.68	1.003	0.000	1.618	0.008	0.367	0.001	0.001	3.00	81.5	18.5
DMI18-28-5-1-1-c1	core	39.23	0.00	44.47	0.31	15.92	0.01	0.25	100.20	0.990	0.000	1.673	0.007	0.336	0.000	0.005	3.01	83.3	16.7
DMI18-28-5-1-1-m2	mid	38.95	0.05	44.12	0.27	16.02	0.02	0.27	99.70	0.989	0.001	1.669	0.006	0.340	0.001	0.005	3.01	83.1	16.9
DMI18-28-5-1-1-r3	rim	39.61	0.00	44.87	0.27	15.47	0.02	0.25	100.50	0.993	0.000	1.677	0.006	0.325	0.001	0.005	3.01	83.8	16.2
DMI18-28-5-2-1-c1	core	39.36	0.01	44.72	0.29	15.63	0.02	0.26	100.28	0.991	0.000	1.678	0.006	0.329	0.001	0.005	3.01	83.6	16.4
DMI18-28-5-2-1-m2	mid	38.77	0.01	44.48	0.30	16.08	0.03	0.25	99.92	0.983	0.000	1.681	0.006	0.341	0.001	0.005	3.02	83.1	16.9
DMI18-28-5-2-1-r3	rim	39.13	0.03	44.54	0.21	15.60	0.02	0.25	99.78	0.990	0.001	1.679	0.004	0.330	0.001	0.005	3.01	83.6	16.4
DMI18-28-5-3-1-r1	rim	39.37	0.01	44.55	0.26	15.68	0.02	0.25	100.15	0.992	0.000	1.674	0.006	0.330	0.001	0.005	3.01	83.5	16.5
DMI18-28-5-3-1-m2	mid	39.35	0.00	44.20	0.28	15.67	0.02	0.25	99.77	0.995	0.000	1.666	0.006	0.332	0.001	0.005	3.00	83.4	16.6
DMI18-28-5-3-1-m3	mid	39.19	0.02	44.68	0.28	15.78	0.03	0.27	100.24	0.988	0.000	1.679	0.006	0.333	0.001	0.005	3.01	83.5	16.5
DMI18-28-5-3-1-m4	mid	38.92	0.04	44.40	0.21	15.81	0.02	0.26	99.66	0.987	0.001	1.679	0.005	0.335	0.000	0.005	3.01	83.3	16.7
DMI18-28-5-3-1-m5	mid	39.05	0.00	44.67	0.22	15.68	0.02	0.24	99.88	0.987	0.000	1.684	0.005	0.332	0.001	0.005	3.01	83.5	16.5
DMI18-28-5-3-1-m6	mid	39.24	0.04	44.20	0.28	16.04	0.02	0.26	100.07	0.992	0.001	1.665	0.006	0.339	0.001	0.005	3.01	83.1	16.9
DMI18-28-5-3-1-r7	rim	38.64	0.02	44.74	0.32	15.76	0.02	0.24	99.75	0.980	0.000	1.692	0.007	0.334	0.001	0.005	3.02	83.5	16.5
DMI18-28-5-4-1-c1	core	39.12	0.02	44.55	0.29	16.14	0.03	0.26	100.40	0.986	0.000	1.674	0.006	0.340	0.001	0.005	3.01	83.1	16.9
DMI18-28-5-4-1-m2	mid	39.15	0.01	44.86	0.29	16.15	0.02	0.26	100.75	0.984	0.000	1.681	0.006	0.339	0.001	0.005	3.02	83.2	16.8
DMI18-28-5-4-1-r3	rim	39.33	0.01	44.79	0.25	15.56	0.02	0.25	100.20	0.990	0.000	1.681	0.005	0.328	0.001	0.005	3.01	83.7	16.3
DMI18-28-5-5-1-c1	core	39.04	0.04	44.18	0.24	15.66	0.03	0.24	99.44	0.991	0.001	1.672	0.005	0.333	0.001	0.005	3.01	83.4	16.6
DMI18-28-5-5-1-m2	mid	38.84	0.00	44.20	0.32	15.71	0.02	0.26	99.35	0.988	0.000	1.677	0.007	0.334	0.001	0.005	3.01	83.4	16.6
DMI18-28-5-5-1-r3	rim	39.22	0.03	44.40	0.20	15.75	0.02	0.26	99.88	0.992	0.001	1.673	0.004	0.333	0.001	0.005	3.01	83.4	16.6
DMI18-32-6-1-1-c1	core	40.84	0.02	48.86	0.19	10.06	0.11	0.29	100.36	0.999	0.000	1.782	0.004	0.206	0.003	0.006	3.00	89.6	10.4
DMI18-32-6-1-1-m2	mid	40.67	0.03	48.84	0.18	10.01	0.11	0.28	100.12	0.998	0.001	1.786	0.004	0.205	0.003	0.005	3.00	89.7	10.3
DMI18-32-6-2-1-r(chr)1	rim	41.10	0.06	50.20	0.11	8.40	0.06	0.27	100.21	0.999	0.001	1.820	0.002	0.171	0.002	0.005	3.00	91.4	8.6

[1] $Fo = Mg^{2+}/(Mg^{2+}+Fe^{2+}) \times 100$; Fa = 100-Fo

Appendix D. (continued) Electronprobe microanalyses (EPMA) of olivine from the Polaris Alaskan-type intrusion

Spot	Oxides (wt.%)								Cations (p.f.u.)								End Members (mol. %)	
	Location	SiO_2	Cr_2O_3	MgO	MnO	FeO	CaO	NiO	Total	Si	Cr	Mg	Mn	Fe	Ca	Ni	Sum	Fo[1]	Fa[1]
DMI18-32-6-2-1-m2	mid	40.31	0.00	48.57	0.16	9.48	0.10	0.29	98.92	0.999	0.000	1.794	0.003	0.197	0.003	0.006	3.00	90.1	9.9
DMI18-32-6-2-1-m4	mid	40.53	0.01	48.80	0.20	9.83	0.11	0.28	99.76	0.997	0.000	1.790	0.004	0.202	0.003	0.006	3.00	89.8	10.2
DMI18-32-6-2-1-m5	mid	41.01	0.00	49.00	0.18	10.22	0.12	0.27	100.80	1.000	0.000	1.780	0.004	0.208	0.003	0.005	3.00	89.5	10.5
DMI18-32-6-2-1-m6	mid	40.62	0.01	48.99	0.17	10.07	0.11	0.28	100.25	0.996	0.000	1.790	0.004	0.206	0.003	0.006	3.00	89.7	10.3
DMI18-32-6-2-1-r7	rim	41.05	0.00	49.37	0.21	9.50	0.10	0.27	100.51	1.000	0.000	1.793	0.004	0.194	0.002	0.005	3.00	90.3	9.7
DMI18-32-6-3-1-c1	core	40.57	0.01	48.94	0.16	10.51	0.14	0.27	100.59	0.993	0.000	1.786	0.003	0.215	0.004	0.005	3.01	89.2	10.8
DMI18-32-6-3-1-m2	mid	40.66	0.01	49.02	0.16	10.09	0.12	0.28	100.33	0.996	0.000	1.790	0.003	0.207	0.003	0.005	3.00	89.6	10.4
DMI18-32-6-3-1-r3	rim	40.92	0.00	49.47	0.26	9.64	0.06	0.28	100.63	0.997	0.000	1.797	0.005	0.197	0.002	0.006	3.00	90.1	9.9
DMI18-32-6-4-1-c1	core	41.00	0.03	50.21	0.17	9.13	0.11	0.28	100.92	0.994	0.001	1.814	0.003	0.185	0.003	0.005	3.01	90.7	9.3
DMI18-32-6-4-1-m2	mid	41.36	0.04	50.13	0.15	8.53	0.10	0.28	100.59	1.002	0.001	1.811	0.003	0.173	0.003	0.006	3.00	91.3	8.7
DMI18-32-6-4-1-r3	rim	40.90	0.04	50.14	0.15	8.20	0.09	0.27	99.80	0.998	0.001	1.824	0.003	0.167	0.002	0.005	3.00	91.6	8.4
DMI18-32-6-4-2-c1	core	41.21	0.03	49.89	0.20	9.16	0.11	0.28	100.89	0.999	0.001	1.803	0.004	0.186	0.003	0.005	3.00	90.7	9.3
DMI18-32-6-4-2-m2	mid	41.24	0.00	50.05	0.21	9.15	0.10	0.28	101.04	0.998	0.000	1.806	0.004	0.185	0.003	0.005	3.00	90.7	9.3
DMI18-32-6-4-2-r3	rim	41.35	0.01	50.24	0.14	8.79	0.11	0.27	100.91	1.000	0.000	1.811	0.003	0.178	0.003	0.005	3.00	91.1	8.9
DMI18-32-6-5-1-c1	core	40.79	0.02	49.57	0.18	8.62	0.12	0.28	99.57	1.000	0.000	1.811	0.004	0.177	0.003	0.005	3.00	91.1	8.9
DMI18-32-6-6-1-r1	rim	41.32	0.00	49.95	0.13	8.90	0.11	0.27	100.69	1.002	0.000	1.805	0.003	0.181	0.003	0.005	3.00	90.9	9.1
DMI18-32-6-6-1-m2	mid	40.88	0.00	49.80	0.16	9.12	0.13	0.28	100.36	0.996	0.000	1.809	0.003	0.186	0.003	0.005	3.00	90.7	9.3
DMI18-32-6-6-1-m3	mid	40.85	0.00	50.27	0.14	9.28	0.13	0.27	100.93	0.991	0.000	1.818	0.003	0.188	0.003	0.005	3.01	90.6	9.4
DMI18-32-6-6-1-m4	mid	40.95	0.00	49.45	0.16	9.00	0.12	0.28	99.95	1.001	0.000	1.802	0.003	0.184	0.003	0.005	3.00	90.7	9.3
DMI18-32-6-6-1-m5	mid	40.87	0.00	49.97	0.19	8.99	0.12	0.27	100.40	0.995	0.000	1.814	0.004	0.183	0.003	0.005	3.00	90.8	9.2
DMI18-32-6-6-1-m6	mid	40.81	0.00	50.27	0.20	8.94	0.11	0.28	100.60	0.992	0.000	1.822	0.004	0.182	0.003	0.005	3.01	90.9	9.1
DMI18-32-6-6-1-r7	rim	41.20	0.01	50.64	0.13	8.32	0.09	0.28	100.69	0.997	0.000	1.827	0.003	0.168	0.002	0.006	3.00	91.6	8.4
DMI18-32-6-7-1-c1	core	41.06	0.05	49.04	0.19	9.59	0.11	0.26	100.30	1.003	0.001	1.785	0.004	0.196	0.003	0.005	3.00	90.1	9.9
DMI18-32-6-7-1-m2	mid	40.82	0.01	49.14	0.16	9.78	0.10	0.26	100.26	0.998	0.000	1.792	0.003	0.200	0.003	0.005	3.00	90.0	10.0
DMI18-32-6-7-1-r3	rim	41.08	0.00	48.98	0.18	9.78	0.09	0.26	100.37	1.003	0.000	1.783	0.004	0.200	0.002	0.005	3.00	89.9	10.1
DMI18-32-6-8-1-c1	core	40.51	0.00	48.77	0.19	10.05	0.10	0.26	99.88	0.997	0.000	1.788	0.004	0.207	0.003	0.005	3.00	89.6	10.4
DMI18-32-6-8-1-m2	mid	40.93	0.00	49.35	0.21	9.77	0.10	0.26	100.62	0.998	0.000	1.793	0.004	0.199	0.003	0.005	3.00	90.0	10.0
DMI18-32-6-8-1-r3	rim	40.86	0.04	49.66	0.21	9.25	0.08	0.28	100.37	0.996	0.001	1.806	0.004	0.189	0.002	0.005	3.00	90.5	9.5
DMI18-32-9B-1-1-c1	core	40.65	0.03	48.47	0.18	10.13	0.02	0.23	99.72	1.001	0.001	1.779	0.004	0.209	0.001	0.005	3.00	89.5	10.5
DMI18-32-9B-1-1-m2	mid	40.70	0.00	49.06	0.15	10.39	0.01	0.23	100.55	0.996	0.000	1.788	0.003	0.213	0.000	0.005	3.00	89.4	10.6
DMI18-32-9B-1-1-r3	rim	40.45	0.00	48.69	0.21	10.21	0.02	0.24	99.83	0.996	0.000	1.788	0.004	0.210	0.001	0.005	3.00	89.5	10.5
DMI18-32-9B-1-2-r1	rim	40.75	0.03	49.35	0.18	9.93	0.02	0.22	100.48	0.995	0.000	1.797	0.004	0.203	0.001	0.004	3.00	89.9	10.1
DMI18-32-9B-1-2-m2	mid	40.65	0.00	48.97	0.21	10.40	0.05	0.25	100.52	0.995	0.000	1.787	0.004	0.213	0.001	0.005	3.00	89.4	10.6
DMI18-32-9B-1-2-m3	mid	40.45	0.01	49.02	0.16	10.30	0.04	0.23	100.20	0.993	0.000	1.794	0.003	0.211	0.001	0.004	3.01	89.5	10.5
DMI18-32-9B-1-2-m4	mid	40.53	0.02	48.99	0.19	10.24	0.04	0.23	100.23	0.994	0.000	1.791	0.004	0.210	0.001	0.004	3.01	89.5	10.5
DMI18-32-9B-1-2-m5	mid	40.55	0.00	49.04	0.17	10.24	0.03	0.23	100.27	0.994	0.000	1.792	0.003	0.210	0.001	0.005	3.01	89.5	10.5
DMI18-32-9B-1-2-r6	rim	40.67	0.03	49.21	0.20	9.97	0.01	0.24	100.35	0.995	0.001	1.795	0.004	0.204	0.000	0.005	3.00	89.8	10.2
DMI18-32-9B-2-1-c1	core	41.32	0.00	48.95	0.20	10.07	0.04	0.24	100.81	1.005	0.000	1.775	0.004	0.205	0.001	0.005	2.99	89.7	10.3
DMI18-32-9B-2-1-m2	mid	40.04	0.00	49.11	0.15	10.22	0.04	0.24	99.79	0.987	0.000	1.806	0.003	0.211	0.001	0.005	3.01	89.5	10.5
DMI18-32-9B-2-1-r3	rim	40.93	0.03	49.20	0.18	10.16	0.02	0.23	100.74	0.998	0.000	1.788	0.004	0.207	0.001	0.005	3.00	89.6	10.4
DMI18-32-9B-3-1-c1	core	40.62	0.05	48.60	0.18	9.95	0.05	0.23	99.69	1.000	0.001	1.784	0.004	0.205	0.001	0.005	3.00	89.7	10.3

[1] $Fo = Mg^{2+}/(Mg^{2+}+Fe^{2+}) \times 100$; Fa = 100-Fo

Appendix D. (continued) Electronprobe microanalyses (EPMA) of olivine from the Polaris Alaskan-type intrusion

Spot	Oxides (wt.%)								Cations (p.f.u.)								End Members (mol. %)	
	Location	SiO_2	Cr_2O_3	MgO	MnO	FeO	CaO	NiO	Total	Si	Cr	Mg	Mn	Fe	Ca	Ni	Sum	Fo[1]	Fa[1]
DMI18-32-9B-3-1-m2	mid	40.85	0.00	49.19	0.19	10.37	0.05	0.23	100.89	0.996	0.000	1.787	0.004	0.211	0.001	0.005	3.00	89.4	10.6
DMI18-32-9B-3-1-r3	rim	40.81	0.03	49.38	0.20	10.18	0.04	0.23	100.87	0.994	0.000	1.793	0.004	0.207	0.001	0.005	3.01	89.6	10.4
DMI18-32-9B-4-1-c1	core	40.52	0.00	49.28	0.18	10.04	0.04	0.23	100.30	0.993	0.000	1.800	0.004	0.206	0.001	0.004	3.01	89.7	10.3
DMI18-32-9B-4-1-m2	mid	40.69	0.00	49.36	0.16	9.83	0.05	0.24	100.34	0.995	0.000	1.799	0.003	0.201	0.001	0.005	3.00	89.9	10.1
DMI18-32-9B-4-1-r3	rim	40.83	0.00	49.39	0.13	10.17	0.02	0.24	100.78	0.995	0.000	1.795	0.003	0.207	0.000	0.005	3.00	89.6	10.4
DMI18-32-9B-5-1-c1	core	40.75	0.00	49.42	0.19	9.71	0.05	0.24	100.35	0.996	0.000	1.800	0.004	0.198	0.001	0.005	3.00	90.1	9.9
DMI18-32-9B-5-1-m2	mid	40.40	0.00	49.54	0.14	9.82	0.05	0.22	100.19	0.990	0.000	1.810	0.003	0.201	0.001	0.004	3.01	90.0	10.0
DMI18-32-9B-5-1-r3	rim	40.80	0.01	49.32	0.16	9.82	0.04	0.23	100.37	0.997	0.000	1.796	0.003	0.201	0.001	0.005	3.00	89.9	10.1
DMI18-32-9B-6-1-c1	core	40.55	0.02	49.16	0.25	9.79	0.05	0.23	100.05	0.995	0.000	1.798	0.005	0.201	0.001	0.005	3.01	89.9	10.1
DMI18-32-9B-6-1-m2	mid	40.57	0.03	48.75	0.17	10.13	0.04	0.23	99.92	0.998	0.000	1.787	0.004	0.208	0.001	0.005	3.00	89.6	10.4
DMI18-32-9B-6-1-r3	rim	40.56	0.02	48.75	0.17	10.09	0.04	0.23	99.86	0.998	0.000	1.787	0.004	0.208	0.001	0.005	3.00	89.6	10.4
DMI18-32-9B-7-1-c1	core	40.78	0.00	49.06	0.18	10.02	0.05	0.23	100.32	0.998	0.000	1.790	0.004	0.205	0.001	0.005	3.00	89.7	10.3
DMI18-32-9B-7-1-m2	mid	40.42	0.00	49.30	0.14	9.66	0.05	0.24	99.81	0.993	0.000	1.806	0.003	0.199	0.001	0.005	3.01	90.1	9.9
DMI18-32-9B-7-1-r3	rim	40.64	0.01	49.29	0.16	10.10	0.03	0.23	100.45	0.994	0.000	1.797	0.003	0.206	0.001	0.005	3.01	89.7	10.3
DMI18-32-9B-8-1-r1	rim	40.84	0.01	48.95	0.20	9.71	0.04	0.23	99.99	1.001	0.000	1.789	0.004	0.199	0.001	0.005	3.00	90.0	10.0
DMI18-32-9B-8-1-m2	mid	40.65	0.01	48.98	0.21	10.06	0.04	0.22	100.17	0.997	0.000	1.790	0.004	0.206	0.001	0.004	3.00	89.7	10.3
DMI18-32-9B-8-1-m3	mid	40.83	0.01	49.16	0.12	10.01	0.04	0.24	100.41	0.998	0.000	1.791	0.003	0.205	0.001	0.005	3.00	89.7	10.3
DMI18-32-9B-8-1-m4	mid	40.58	0.05	49.22	0.17	9.95	0.03	0.24	100.24	0.994	0.001	1.797	0.003	0.204	0.001	0.005	3.01	89.8	10.2
DMI18-32-9B-8-1-r5	rim	40.77	0.02	48.91	0.19	9.97	0.02	0.24	100.11	0.999	0.000	1.787	0.004	0.204	0.001	0.005	3.00	89.7	10.3
DMI18-32-9C-1-1-1c	core	40.57	0.00	47.45	0.25	12.24	0.04	0.16	100.71	0.999	0.000	1.741	0.005	0.252	0.001	0.003	3.00	87.4	12.6
DMI18-32-9C-1-1-m2	mid	40.36	0.00	47.47	0.26	12.38	0.03	0.15	100.65	0.995	0.000	1.745	0.005	0.255	0.001	0.003	3.00	87.2	12.8
DMI18-32-9C-1-1-r3	rim	40.23	0.02	47.65	0.25	12.53	0.03	0.17	100.88	0.991	0.000	1.750	0.005	0.258	0.001	0.003	3.01	87.1	12.9
DMI18-32-9C-2-1-c1	core	40.10	0.00	47.47	0.26	12.41	0.04	0.14	100.43	0.992	0.000	1.750	0.006	0.257	0.001	0.003	3.01	87.2	12.8
DMI18-32-9C-2-1-m2	mid	40.36	0.00	47.45	0.23	12.29	0.04	0.15	100.52	0.996	0.000	1.746	0.005	0.254	0.001	0.003	3.00	87.3	12.7
DMI18-32-9C-2-1-r3	rim	40.39	0.00	47.68	0.31	12.32	0.02	0.13	100.86	0.994	0.000	1.749	0.007	0.254	0.000	0.003	3.01	87.3	12.7
DMI18-32-9C-3-1-c1	core	40.28	0.00	47.17	0.22	12.49	0.05	0.15	100.35	0.997	0.000	1.740	0.005	0.259	0.001	0.003	3.00	87.1	12.9
DMI18-32-9C-3-1-m2	mid	40.21	0.00	47.46	0.25	12.34	0.04	0.14	100.46	0.994	0.000	1.748	0.005	0.255	0.001	0.003	3.01	87.3	12.7
DMI18-32-9C-3-1-r3	rim	40.34	0.02	47.31	0.24	12.30	0.02	0.15	100.38	0.997	0.000	1.743	0.005	0.254	0.001	0.003	3.00	87.3	12.7
DMI18-32-9C-4-1-c1	core	40.24	0.00	47.45	0.23	12.14	0.03	0.13	100.21	0.995	0.000	1.750	0.005	0.251	0.001	0.002	3.00	87.4	12.6
DMI18-32-9C-4-1-m2	mid	40.54	0.02	47.55	0.19	12.42	0.04	0.14	100.90	0.997	0.000	1.743	0.004	0.255	0.001	0.003	3.00	87.2	12.8
DMI18-32-9C-4-1-r3	rim	40.26	0.00	47.44	0.20	12.33	0.02	0.14	100.39	0.995	0.000	1.748	0.004	0.255	0.001	0.003	3.00	87.3	12.7
DMI18-32-9C-4-2-c1	core	40.35	0.00	47.38	0.24	12.63	0.03	0.14	100.77	0.995	0.000	1.741	0.005	0.260	0.001	0.003	3.01	87.0	13.0
DMI18-32-9C-4-2-m2	mid	40.13	0.01	47.34	0.23	12.75	0.03	0.15	100.63	0.992	0.000	1.744	0.005	0.264	0.001	0.003	3.01	86.9	13.1
DMI18-32-9C-4-2-r3	rim	40.15	0.00	47.10	0.25	12.56	0.03	0.14	100.23	0.995	0.000	1.740	0.005	0.260	0.001	0.003	3.00	87.0	13.0
DMI18-32-9C-4-3-r1	rim	40.14	0.00	47.19	0.17	12.62	0.03	0.13	100.29	0.994	0.000	1.743	0.004	0.262	0.001	0.003	3.01	87.0	13.0
DMI18-32-9C-4-3-m2	mid	40.22	0.04	47.18	0.23	12.35	0.02	0.12	100.17	0.996	0.001	1.742	0.005	0.256	0.000	0.002	3.00	87.2	12.8
DMI18-32-9C-4-3-m3	mid	40.04	0.00	47.41	0.25	12.45	0.03	0.14	100.32	0.992	0.000	1.750	0.005	0.258	0.001	0.003	3.01	87.2	12.8
DMI18-32-9C-4-3-m4	mid	40.42	0.00	47.36	0.20	12.53	0.02	0.13	100.67	0.997	0.000	1.741	0.004	0.258	0.001	0.003	3.00	87.1	12.9
DMI18-32-9C-4-3-m5	mid	40.10	0.00	47.57	0.24	12.25	0.04	0.13	100.32	0.992	0.000	1.754	0.005	0.253	0.001	0.003	3.01	87.4	12.6
DMI18-32-9C-4-3-r6	rim	40.01	0.00	47.42	0.24	12.71	0.04	0.14	100.56	0.990	0.000	1.749	0.005	0.263	0.001	0.003	3.01	86.9	13.1
DMI18-32-9C-5-1-r1	rim	40.44	0.00	48.03	0.27	11.64	0.02	0.28	100.69	0.994	0.000	1.760	0.006	0.239	0.001	0.006	3.01	88.0	12.0

[1] $Fo = Mg^{2+}/(Mg^{2+}+Fe^{2+}) \times 100$; Fa = 100-Fo

Appendix D. (continued) Electronprobe microanalyses (EPMA) of olivine from the Polaris Alaskan-type intrusion

Spot	Oxides (wt.%)								Cations (p.f.u.)								End Members (mol. %)	
	Location	SiO_2	Cr_2O_3	MgO	MnO	FeO	CaO	NiO	Total	Si	Cr	Mg	Mn	Fe	Ca	Ni	Sum	Fo[1]	Fa[1]
DMI18-32-9C-5-1-m2	mid	40.27	0.03	47.72	0.23	11.71	0.07	0.29	100.32	0.994	0.001	1.756	0.005	0.242	0.002	0.006	3.01	87.9	12.1
DMI18-32-9C-5-1-m3	mid	40.36	0.00	47.98	0.20	11.42	0.04	0.29	100.29	0.995	0.000	1.763	0.004	0.235	0.001	0.006	3.00	88.2	11.8
DMI18-32-9C-5-1-m4	mid	40.39	0.01	47.92	0.17	11.41	0.05	0.30	100.25	0.996	0.000	1.761	0.003	0.235	0.001	0.006	3.00	88.2	11.8
DMI18-32-9C-5-1-m5	mid	40.24	0.00	48.21	0.22	11.51	0.02	0.29	100.49	0.991	0.000	1.770	0.005	0.237	0.001	0.006	3.01	88.2	11.8
DMI18-32-9C-5-1-m6	mid	40.21	0.02	47.38	0.20	11.97	0.05	0.29	100.12	0.996	0.000	1.749	0.004	0.248	0.001	0.006	3.00	87.6	12.4
DMI18-32-9C-5-1-r7	rim	40.56	0.02	48.32	0.16	11.70	0.04	0.29	101.09	0.993	0.000	1.763	0.003	0.240	0.001	0.006	3.01	88.0	12.0
DMI18-32-9C-6-1-c1	core	40.72	0.02	47.53	0.22	11.72	0.05	0.26	100.52	1.002	0.000	1.743	0.004	0.241	0.001	0.005	3.00	87.8	12.2
DMI18-32-9C-6-1-m2	mid	40.66	0.00	47.82	0.17	12.20	0.05	0.26	101.17	0.996	0.000	1.747	0.004	0.250	0.001	0.005	3.00	87.5	12.5
DMI18-32-9C-6-1-r3	rim	40.18	0.00	47.47	0.23	12.06	0.02	0.26	100.23	0.994	0.000	1.751	0.005	0.250	0.001	0.005	3.01	87.5	12.5
DMI18-32-9C-7-1-c1	core	40.25	0.03	47.65	0.19	11.57	0.04	0.29	100.03	0.996	0.001	1.757	0.004	0.239	0.001	0.006	3.00	88.0	12.0
DMI18-32-9C-7-1-m2	mid	40.19	0.21	47.90	0.22	12.01	0.05	0.31	100.88	0.989	0.004	1.757	0.005	0.247	0.001	0.006	3.01	87.7	12.3
DMI18-32-9C-7-1-r3	rim	40.29	0.00	48.04	0.16	11.86	0.03	0.29	100.67	0.992	0.000	1.762	0.003	0.244	0.001	0.006	3.01	87.8	12.2
DMI18-32-9C-8-1-c1	core	40.18	0.07	47.65	0.16	11.87	0.05	0.30	100.28	0.993	0.001	1.756	0.003	0.245	0.001	0.006	3.01	87.7	12.3
DMI18-32-9C-8-1-m2	mid	40.49	0.01	47.76	0.19	11.73	0.04	0.28	100.51	0.997	0.000	1.753	0.004	0.242	0.001	0.006	3.00	87.9	12.1
DMI18-32-9C-8-1-r3	rim	40.31	0.00	48.24	0.22	11.60	0.02	0.27	100.67	0.991	0.000	1.768	0.005	0.239	0.001	0.005	3.01	88.1	11.9
GN88-1053-1-1-c1	core	41.15	0.00	48.85	0.28	10.88	0.07	0.34	101.57	0.999	0.000	1.768	0.006	0.221	0.002	0.007	3.00	88.9	11.1
GN88-1053-1-1-m2	mid	40.31	0.04	48.52	0.20	10.57	0.06	0.35	100.03	0.993	0.001	1.782	0.004	0.218	0.002	0.007	3.01	89.1	10.9
GN88-1053-1-1-r3	rim	40.82	0.07	49.24	0.17	10.22	0.04	0.35	100.91	0.995	0.001	1.789	0.004	0.208	0.001	0.007	3.00	89.6	10.4
GN88-1053-2-1-c1	core	40.19	0.29	48.54	0.21	10.74	0.04	0.35	100.36	0.989	0.006	1.780	0.004	0.221	0.001	0.007	3.01	89.0	11.0
GN88-1053-2-1-m2	mid	39.68	0.01	48.55	0.17	10.53	0.03	0.37	99.34	0.986	0.000	1.798	0.004	0.219	0.001	0.007	3.01	89.1	10.9
GN88-1053-2-1-r3	rim	40.53	0.00	48.39	0.16	10.31	0.04	0.36	99.78	0.999	0.000	1.778	0.003	0.213	0.001	0.007	3.00	89.3	10.7
GN88-1053-2-2-r1	rim	41.00	0.01	49.39	0.19	10.44	0.03	0.36	101.41	0.995	0.000	1.787	0.004	0.212	0.001	0.007	3.01	89.4	10.6
GN88-1053-2-2-m2	mid	40.13	0.00	48.86	0.18	10.50	0.04	0.35	100.05	0.989	0.000	1.794	0.004	0.216	0.001	0.007	3.01	89.2	10.8
GN88-1053-2-2-m3	mid	40.51	0.00	49.04	0.18	10.65	0.05	0.36	100.78	0.991	0.000	1.788	0.004	0.218	0.001	0.007	3.01	89.1	10.9
GN88-1053-2-2-m4	mid	40.44	0.04	48.94	0.23	10.61	0.04	0.35	100.65	0.991	0.001	1.787	0.005	0.217	0.001	0.007	3.01	89.2	10.8
GN88-1053-2-2-m5	mid	40.58	0.00	49.05	0.17	10.47	0.05	0.35	100.66	0.993	0.000	1.789	0.004	0.214	0.001	0.007	3.01	89.3	10.7
GN88-1053-2-2-m6	mid	41.21	0.00	48.79	0.16	10.56	0.05	0.35	101.12	1.002	0.000	1.769	0.003	0.215	0.001	0.007	3.00	89.2	10.8
GN88-1053-2-2-r7	rim	40.61	0.05	49.13	0.18	10.49	0.03	0.35	100.84	0.992	0.001	1.789	0.004	0.214	0.001	0.007	3.01	89.3	10.7
GN88-1053-3-1-c1	core	40.85	0.01	50.78	0.16	8.36	0.07	0.34	100.57	0.991	0.000	1.836	0.003	0.170	0.002	0.007	3.01	91.5	8.5
GN88-1053-3-1-m2	mid	40.80	0.01	50.90	0.19	8.13	0.07	0.35	100.44	0.990	0.000	1.842	0.004	0.165	0.002	0.007	3.01	91.8	8.2
GN88-1053-3-1-r3	rim	41.41	0.05	51.83	0.12	7.26	0.03	0.33	101.03	0.994	0.001	1.855	0.002	0.146	0.001	0.006	3.01	92.7	7.3
GN88-1053-4-1-cpx-r1	rim	41.39	0.00	51.19	0.14	8.54	0.04	0.32	101.63	0.993	0.000	1.832	0.003	0.171	0.001	0.006	3.01	91.4	8.6
GN88-1053-4-1-m2	mid	40.59	0.07	50.56	0.17	8.55	0.06	0.33	100.33	0.988	0.001	1.836	0.004	0.174	0.001	0.006	3.01	91.3	8.7
GN88-1053-4-1-m3	mid	41.10	0.03	50.63	0.09	8.42	0.06	0.33	100.65	0.995	0.000	1.828	0.002	0.171	0.002	0.006	3.00	91.5	8.5
GN88-1053-4-1-m4	mid	41.14	0.00	51.22	0.16	8.09	0.05	0.34	100.99	0.992	0.000	1.841	0.003	0.163	0.001	0.007	3.01	91.9	8.1
GN88-1053-4-1-m5	mid	41.38	0.00	51.49	0.09	7.39	0.04	0.34	100.72	0.997	0.000	1.849	0.002	0.149	0.001	0.007	3.00	92.6	7.4
GN88-1053-4-1-chr-r6	rim	41.27	0.00	52.29	0.08	6.49	0.03	0.33	100.50	0.993	0.000	1.875	0.002	0.131	0.001	0.006	3.01	93.5	6.5
GN88-1053-5-1-c1	core	40.68	0.00	50.15	0.19	8.93	0.09	0.30	100.33	0.992	0.000	1.823	0.004	0.182	0.002	0.006	3.01	90.9	9.1
GN88-1053-5-1-m2	mid	40.93	0.01	50.00	0.12	9.14	0.08	0.30	100.59	0.995	0.000	1.812	0.003	0.186	0.002	0.006	3.00	90.7	9.3
GN88-1053-5-1-r3	rim	40.99	0.05	51.90	0.11	6.79	0.04	0.31	100.19	0.991	0.001	1.870	0.002	0.137	0.001	0.006	3.01	93.2	6.8
GN88-1053-6-1-c1	core	40.51	0.02	50.05	0.16	8.84	0.07	0.34	99.97	0.991	0.000	1.825	0.003	0.181	0.002	0.007	3.01	91.0	9.0

[1] $Fo = Mg^{2+}/(Mg^{2+}+Fe^{2+}) \times 100$; Fa = 100-Fo

Appendix D. (continued) Electronprobe microanalyses (EPMA) of olivine from the Polaris Alaskan-type intrusion

Spot	Oxides (wt.%)									Cations (p.f.u.)								End Members (mol. %)	
	Location	SiO_2	Cr_2O_3	MgO	MnO	FeO	CaO	NiO	Total	Si	Cr	Mg	Mn	Fe	Ca	Ni	Sum	Fo[1]	Fa[1]
GN88-1053-6-1-r2	rim	40.86	0.05	51.03	0.14	8.20	0.04	0.33	100.65	0.990	0.001	1.843	0.003	0.166	0.001	0.007	3.01	91.7	8.3
GN88-1053-7-1-c1	core	40.37	0.00	48.72	0.20	10.65	0.03	0.35	100.31	0.992	0.000	1.785	0.004	0.219	0.001	0.007	3.01	89.1	10.9
GN88-1053-7-1-m2	mid	40.38	0.00	48.79	0.20	10.37	0.03	0.34	100.11	0.993	0.000	1.789	0.004	0.213	0.001	0.007	3.01	89.3	10.7
GN88-1053-7-1-r3	rim	40.46	0.00	49.44	0.20	9.97	0.03	0.34	100.44	0.990	0.000	1.804	0.004	0.204	0.001	0.007	3.01	89.8	10.2

[1]Fo = $Mg^{2+}/(Mg^{2+}+Fe^{2+})$ x 100; Fa = 100-Fo